UNIVERSIDADE ESTADUAL PAULISTA
"JULIO DE MESQUITA FILHO"
INSTITUTO DE GEOCIÊNCIAS E CIÊNCIAS EXATAS

DISSERTAÇÃO DE MESTRADO

Programa de Pós-Graduação em Geociências e Meio Ambiente

(Recursos Naturais)

TRACE ELEMENT GEOCHEMISTRY OF APATITE AND MAGNETITE IN GOLD SYSTEMS OF THE ALTA FLORESTA MINERAL PROVINCE: PETROGENETIC AND METALLOGENIC IMPLICATIONS

PEDRO AUGUSTO FERREIRA LEITE

Prof. Dr. Rafael Rodrigues de Assis
(Orientador)

RIO CLARO (SP)

2020

UNIVERSIDADE ESTADUAL PAULISTA
Instituto de Geociências e Ciências Exatas
Câmpus de Rio Claro

PEDRO AUGUSTO FERREIRA LEITE

GEOQUÍMICA DE ELEMENTOS-TRAÇO DE APATITA E MAGNETITA EM SISTEMAS AURÍFEROS DA PROVÍNCIA MINERAL DE ALTA FLORESTA: IMPLICAÇÕES PETROGENÉTICAS E METALOGENÉTICAS

Dissertação de Mestrado apresentada ao Instituto de Geociências e Ciências Exatas do Câmpus de Rio Claro, da Universidade Estadual Paulista Júlio de Mesquita Filho, como parte dos requisitos para obtenção do título de mestre em Geociências e Meio Ambiente.

Orientador: Prof. Dr. Rafael Rodrigues de Assis

RIO CLARO (SP)
2020

L533t

Leite, Pedro Augusto Ferreira
Trace element geochemistry of apatite and magnetite in gold systems of the Alta Floresta mineral province : Petrogenetic and metallogenic implications / Pedro Augusto Ferreira Leite. -- Rio Claro, 2020
187 p. : il., tabs., fotos, mapas + 1 CD-ROM

Dissertação (mestrado) - Universidade Estadual Paulista (Unesp), Instituto de Geociências e Ciências Exatas, Rio Claro
Orientadora: Rafael Rodrigues de Assis

1. Alta Floresta mineral province. 2. Mineral chemistry. 3. Apatite. 4. Magnetite. 5. Trace elements. I. Título.

Sistema de geração automática de fichas catalográficas da Unesp. Biblioteca do Instituto de Geociências e Ciências Exatas, Rio Claro. Dados fornecidos pelo autor(a).

Essa ficha não pode ser modificada.

PEDRO AUGUSTO FERREIRA LEITE

GEOQUÍMICA DE ELEMENTOS-TRAÇO DE APATITA E MAGNETITA EM SISTEMAS AURÍFEROS DA PROVÍNCIA MINERAL DE ALTA FLORESTA: IMPLICAÇÕES PETROGENÉTICAS E METALOGENÉTICAS

Dissertação de Mestrado apresentada ao Instituto de Geociências e Ciências Exatas do Câmpus de Rio Claro, da Universidade Estadual Paulista Júlio de Mesquita Filho, como parte dos requisitos para obtenção do título de mestre em Geociências e Meio Ambiente.

Orientador: Prof. Dr. Rafael Rodrigues de Assis

Comissão examinadora

_____

Prof. Dr. Rafael Rodrigues de Assis
Instituto de Geociências
USP

_____

Prof. Dr. George Luiz Luvizotto
Instituto de Geociências e Ciências Exatas
Unesp, Câmpus Rio Claro

_____

Profª. Drª. Carolina Penteado Natividade Moreto
Instituto de Geociências
Unicamp

Conceito: APROVADO

05 de agosto de 2020, Rio Claro, SP

"The ship on which Theseus sailed with the youths and returned in safety, the thirty-oared galley, was preserved by the Athenians down to the time of Demetrius Phalereus. They took away the old timbers from time to time, and put new and sound ones in their places, so that the vessel became a standing illustration for the philosophers in the mooted question of growth, some declaring that it remained the same, others that it was not the same vessel."

Plutarch, *Lives*, c. 75 BC. Translated by Bernadotte Perrin.

Agradecimentos

Primeiramente, quero expressar gratidão ao meu orientador, Prof. Rafael Assis, por me aceitar como estudante de mestrado e por me guiar durante todo o trabalho. Ao pessoal da Coogavepe, em especial a Rael Cavalli e Gilson Camboim, que tanto ajudaram nas viagens de campo. Aos grandes Daniel Godoy, do laboratório de microssonda da Unesp, e Vinicius Martins, do laboratório de LA-ICP-MS da USP, por toda a assistência durante os experimentos. A Maria José de Mesquita e George Luiz Luvizotto pela valiosas sugestões e críticas. A todos do Grupo de Estudo GEOLIT, em especial a Vinicius Louro, Andrey Meyer, Andrez Perez, Danilo Pineschi, Ivan Souza, Lucas Ranolfi, Rômulo Bortolozzo, e muitos outros colegas da USP deste grupo que só cresce.

O presente trabalho foi realizado com apoio da Coordenação de Aperfeiçoamento de Pessoal de Nível Superior (CAPES) – código de financiamento 001. Igualmente, meus sinceros agradecimentos à SEGF (Society of Economic Geologists Foundation) pelo financiamento do projeto através do Fundo McKinstry.

Table of contents

List of Figures

List of tables

ABSTRACT

Indicator minerals, such as apatite and magnetite, are useful for discriminating between barren igneous rocks and hydrothermal alteration halos, since they display contrasting chemical compositions that allow us to infer the distance to a mineral deposit, and to know which type of deposit it is. In this study, textural and compositional patterns in apatite and magnetite were evaluated in the Paleoproterozoic mineral deposits of the Alta Floresta mineral province, in the Amazon Craton, to appraise whether there are unrealised metallogenic potentials in the region. Samples were collected from the barren host rocks and from the hydrothermally altered zones of three intrusion-hosted gold deposits (Luizão, Pé Quente and X1 deposits), one epithermal Au + base metals deposit (Francisco deposit), and one barren granitic unit (Teles Pires Intrusive Suite). Thin sections of these units were analysed by transmitted and reflected light microscopy, scanning electron microscope (SEM) and cathodoluminescence (CL). Apatite and magnetite compositions were measured by electron microprobe (EMP) and laser ablation-inductively coupled plasma-mass spectrometry (LA-ICP-MS). Geochemical data was treated, statistically evaluated, analysed for principal components (PCA), and applied to linear discriminant functions (LDA). Apatite displays textural variations depending on which type of hydrothermal alteration it is associated with: (1) yellow-green-luminescent apatite in barren host rocks, (2) brightly saturated green-luminescent apatite in phyllic-altered rocks, and (3) dull grey-luminescent apatite in potassic-/propylitic-altered rocks. These different apatite types are progressively enriched in REE, Mn, and Ge, from (1) to (3), which indicates that they interacted with hydrothermal fluids. In the X1 deposit, phyllic-related apatite displays high Mn and HREE concentrations, similar to porphyry Cu-Au deposits. Mn-in-apatite oxybarometer reveals slightly lower oxygen fugacity (fO_2 -10 to -14) during hydrothermal alteration in the Pé Quente deposit and strongly reducing conditions (fO_2 -35 to -23) during sulphide precipitation in the X1 deposit. Mn-in-apatite oxybarometer was compared to V/Ga relative redox ratio in magnetite based on literature experimental data. Magnetite recorded lower fO_2 values (-8.93 to -10.30) only for titanite alteration (sphenitisation) during deuteric and propylitic alteration. Otherwise, the relative redox ratio in magnetite seemed to retain fO_2 values from magmatic fractionation. Magnetite is mostly absent from hydrothermal zones, such as in the X1 deposit, where pyrite precipitates instead. In the X1 deposit, ilmenite-magnetite intergrowths endorse the assumption that sulphides crystallised under reducing conditions. Apatite offers incisive information about the nature of magmatic-hydrothermal systems through elements such as F, Cl, Mn, REE, Sr, and Ge that might serve as proxies for the . On the other hand, magnetite has several drawbacks as an indicator mineral: (1) pseudomorphic alteration into hematite (martitisation), (2) alteration into titanite (sphenitisation), and (3) trace element variance mostly coordinated by Ti concentrations (11 ppm to 4.64 wt. %), which hinders the evaluation of trace elements that vary independently from Ti. Even though apatite and magnetite co-precipitate in the magma and are closely assembled as part of the accessory phase, they further bifurcate into distinct crystallisation paths that are differently affected by deuteric and hydrothermal processes.

Keywords: Alta Floresta mineral province, mineral chemistry, apatite, magnetite, trace elements, gold deposits

RESUMO

Minerais indicadores, como apatita e magnetita, são úteis para discriminação entre rochas estéreis e halos de alteração hidrotermal, visto que eles apresentam composições químicas contrastantes que permitem-nos inferir a distância de um prospecto mineral e que tipo de depósito se trata. Neste estudo, foram avaliados os padrões texturais e composicionais em apatita e magnetita em depósitos minerais Paleoproterozoicos da Província Mineral de Alta Floresta, no Cráton Amazônico, para estimar se há potenciais metalogenéticos não realizados na região. Amostras foram coletadas de rochas hospedeiras estéreis e de zonas alteradas de três depósitos auríferos hospedados em intrusões graníticas (depósitos Luizão, Pé Quente e X1), um depósito epitermal de ouro e metais base (depósito Francisco), e uma unidade granítica estéril (Suíte Intrusiva Teles Pires). Seções delgadas destas unidades foram analisadas por microscopia de luz transmitida e refletida, microscópio eletrônico de varredura (MEV) e catodoluminescência (CL). Em seguida, composições da apatita e magnetita foram medidas por microssonda eletrônica (EMP) e ablação a laser associada a um espectrômetro de massas com plasma indutivamente acoplado (LA-ICP-MS). Os dados geoquímicos foram tratados, avaliados estatisticamente, analisados para componentes principais (PCA) e aplicados a funções discriminantes lineares (LDA). Apatita apresenta variações texturais que dependem do tipo de alteração hidrotermal com que ela está associada: (1) apatita com luminescência amarelo-verde em rochas hospedeiras estéreis, (2) apatita com luminescência verde fortemente saturada em rochas com alteração fílica, e (3) apatita com luminescência cinza, de brilho desbotado, em rochas com alteração potássica e propilítica. Estes tipos diferentes de apatita são progressivamente enriquecidos em REE, Mn e Ge, de (1) a (3), o que indica interação com fluidos hidrotermais. No depósito X1, apatita relacionada à alteração fílica apresenta altas concentrações de Mn e HREE, similares a depósitos de Cu-Au pórfiro. Oxibarometria da apatita baseada em Mn revela uma fugacidade de oxigênio relativamente mais baixa durante a alteração hidrotermal (fO_2 -10 e -14) do depósito Pé Quente, e condições fortemente redutoras durante a precipitação do sulfeto (fO_2 -35 a -23) no depósito X1. O oxibarômetro da apatita foi comparado a uma razão redox relativa (V/Ga) em magnetita, baseada em dados experimentais da literatura. A magnetita registrou valores menores de fO_2 (-8.93 a -10.30) apenas para alteração com titanita (esfenitização) durante alteração deutérica ou propilítica. Em outros casos, a razão redox relativa em magnetita aparenta reter os valores de fO_2 do fracionamento magmático. Magnetita é majoritariamente ausente das zonas hidrotermais, como no depósito X1, aonde, ao invés de magnetita, ocorre a precipitação de pirita. No depósito X1, intercrescimentos de ilmenita-magnetita endossam a hipótese de que sulfetos cristalizaram sob condições redutoras. Apatita oferece informações incisivas sobre a natureza dos sistemas magmático-hidrotermais, através de elementos como F, Cl, Mn, REE, Sr e Ge. Por sua vez, magnetita apresenta diversas desvantagens como um mineral indicador: (1) alteração pseudomórfica para hematita (martitização), (2) alteração em titanita (esfenitização), e (3) variância de elementos-traço coordenada pelas concentrações de Ti (11 ppm a 4.64 wt. %), o que impede a avaliação de elementos-traço que variam independentemente do Ti. Ainda que apatita e magnetita coprecipitem no magma e sejam associadas como parte da fase acessório, elas posteriormente se bifurcam em duas trajetórias de cristalização distintas.

Palavras-chave: Província Mineral de Alta Floresta, química mineral, apatita, magnetita, elementos-traço, depósitos auríferos.

Chapter 1

Introduction

Trace elements in apatite and magnetite are important petrogenetic and metallogenic indicators. Apatite and magnetite are accessory phases in many magmatic, sedimentary and metamorphic rocks, and their chemical fingerprinting may indicate the presence of nearby mineral deposits and their metallogenic fertility. Recently, mineral exploration has turned its gaze upon the recognition of chemical diversity in indicator minerals, such as apatite and magnetite, from different deposit types by implementing electron microprobe analysis (EMPA) and laser ablation inductively coupled plasma mass spectrometry (LA-ICP-MS). For examples of the use of apatite as an indicator mineral, the reader is referred to Belousova et al. (2001), Belousova et al. (2002), Cao et al. (2012), Ding et al. (2015), Mao et al. (2016), Pan et al. (2016), Duan and Jiang (2019), Xie et al. (2018) and Zafar et al. (2019); and for examples regarding magnetite as an indicator mineral, see Dupuis and Beaudoin (2011), Boutroy et al. (2014), Dare et al. (2014), Nadoll et al. (2014a, b), Hu et al. (2015), Canil et al. (2016), Pisiak et al. (2017), Huang et al. (2019) and Duan et al. (2019).

Over the last few decades, scientific research has also improved our understanding of the Alta Floresta mineral province (AFMP), in the southernmost portion of the Amazon Craton, Brazil (Santos et al., 2001; Moreton and Martins, 2005; Moura et al., 2006; Silva and Abram, 2008). The AFMP extends for 500 km in a NW-SE lineament (Miguel Jr., 2011). Four deposit types are distinguished in the AFMP, according to their occurrence, mineral paragenesis and geochemical signature (Xavier et al., 2011; Assis, 2011): (1) disseminated Au±Cu deposits (e.g. Luizão, Pé Quente, Serrinha, X1 and Juruena deposits) (Moura et al., 2006; Paes de Barros, 2007; Assis, 2011 Rodrigues, 2012; Serrato, 2014); (2) structurally controlled vein-type Au±Cu deposits (e.g. Edu, Peteca and Paraíba deposits) (Trevisan, 2012); (3) disseminated Au±Mo±Cu deposits (e,g, Ana and Jaca); and (4) structurally controlled vein-type Au+Zn+Pb±Cu deposits (e.g. Francisco, Bigode and Luiz) (Assis, 2011; Trevisan, 2015).

Artisan mining started in the Alta Floresta mineral province in 1973, and it still represents the main method of gold extraction today. Between the 1980s and 1990s, the

AFMP remained one of the most productive gold provinces in Brazil, with an annual production of 60-80 t (Santos et al., 2001). Gold is mainly extracted from secondary sources (placer deposits), and primary sources are relinquished due to lack of investment and economic uncertainty. In this context, indicator minerals may be used to discover primary mineral deposits, or to lead exploration towards areas of higher ore grade (McClenaghan, 2005, 2011; Averill, 2011), because both apatite and magnetite have traits such as: (1) sensitivity to their crystallising environment, so that they can record the chemical interactions of their surrounding melt and fluid; (2) resistance, so that they can avoid weathering; (3) abundance and density, so that they can remain in the sedimentary record; and (4) discernibility, so that they are easy to identify and separate (Mao et al., 2016). There are also other non-resistant indicator minerals, such as chlorite, epidote and allanite, that do not remain in the sedimentary record – and will not be the subject of this study – but that may be used as indicator minerals in the propylitic zone of porphyry ore deposits, as vectoring tools towards the porphyry centres (Cooke et al., 2014, 2020; Wilkinson et al., 2015). Exploration geologists may superpose geochemical vectors and use indicator minerals as ore pathfinders (Cook et al., 2016; Cooke et al., 2017). This may be feasible in porphyry systems and other intrusion-hosted systems that have predictable anatomies (Corbett, 2009; Sillitoe, 2010).

Apatite and magnetite, on the other hand, behave as key indicators of magma evolution and ore formation (Dare et al, 2014; Webster and Piccoli, 2015). They are potential fertility proxies for the extent of the mineralisation because they occur at both the ore-related and the barren granitic rocks (Pisiak et al., 2017; Duan and Jiang et al., 2018). Fertility proxies may aid the exploration targeting in the AFMP. The Alta Floresta mineral province has shown promising tectonic and metallogenic triggers for epithermal-porphyry systems (Moura et al., 2006; Sillitoe, 2010; Assis et al., 2012), orogenic Au systems (Groves et al., 1998; Santos et al., 2001) and intrusion-related gold systems (IRGS; Thompson et al., 1999; Hart et al., 2005; Paes de Barros, 2007).

In this study, we present trace element compositions of apatite and magnetite by EMPA and LA-ICP-MS analysis from three disseminated Au±Cu deposits (Pé Quente, Luizão and X1 deposits), from a structurally controlled vein-type Au+Zb+Pb±Cu deposit (Francisco deposit), and from the barren A-type Teles Pires granite. We evaluate the metallogenic potential of the region by discriminating between the barren and hydrothermal zones. Herein, barren zones are defined as unaltered magmatic rocks or

magmatic rocks weakly altered by incipient autometasomatism and/or propylitic alteration, which indicate that these rocks are distal from the mineralised cores. Concurrently, hydrothermal zones were sampled directly from the strongly altered mineral deposits and exhibit strongly pervasive potassic and phyllic alteration, generally overprinted by propylitic alteration. Finally, we will integrate trace element compositions to descriptive data such as mineral parageneses, mineral textures, and petrologic constraints. The objective is to evaluate whether apatite and magnetite are useful for fertility assessment in the region, and what these indicator minerals can reveal about the igneous and hydrothermal processes that generated the deposits in the Alta Floresta mineral province.

Chapter 2

Structural Chemistry of Apatite and Magnetite – A review

2.1 Trace elements in apatite

Apatite has a chemical composition of $Ca_5(PO_4)_3[F, Cl, OH]$. The F^-, Cl^- and OH^- anions are different chemical substitutions that respectively represent the end-members fluorapatite, chlorapatite and hydroxylapatite. Fluorapatite is widely distributed in igneous rocks, in Ca-rich metamorphic rocks, and as a residual mineral in lateritic soils. Apatite is also a common secondary mineral in hydrothermal alteration zones, with a wide range of homogenisation temperatures, from 450º C to 150º C, as indicated by isotopic and fluid inclusion data (Broman et al., 1999; Jami et al., 2007). Hydrothermal apatite typically occurs in potassic and propylitic alteration zones of porphyry systems, associated with a variety of mafic to felsic intrusive rocks (Thompson and Thompson, 1996). Apatite is also an ore mineral in iron oxide-apatite deposits (IOA, or 'Kiruna-type') that may be considered a phosphorus-rich type of iron oxide-copper-gold (IOCG) deposit (Pirajno, 2009; Groves et al., 2010; Knipping et al., 2015). Similarly, magnetite corresponds to the iron-rich ore mineral in IOA deposits (Jonsson et al., 2013; Knipping et al., 2015; Simon et al., 2018).

Apatite is a mineral supergroup that can be divided up to 40 mineral species (Hughes and Rakovan, 2015) with substitutions in Ca, P and halogen ions. Apatite pure end-members – fluor-, chlor- and hydroxylapatite – are rarely found in nature in their ideal form, because halogen ions easily diffuse through apatite due to its open structural channel along the c axis (Dong, 2005). Therefore, a better way to represent apatite is by the general formula $A_5(XO_4)_3[Z]$. Apatite has hexagonal bipyramidal $P6_3/m$ symmetry (space group number 176) and could adopt other symmetries such as $P6_3$, $P\text{-}3$, $P\text{-}6$, $P2_1/m$ (with only chlorapatite being monoclynic).

Crystal structure of apatite allows for two structural channels in an hexagonal system, one inside the other (Fig. 2.1): the larger structural channel arranges forty percent of the Ca atoms in a nine-fold coordination (Ca(I) site) with the tetrahedral PO_3^- [4] groups; while a smaller structural channel converges within that larger one, containing the other sixty percent of Ca atoms arranged in a seven-fold coordination (Ca(II) site);

whereas inside the smaller structural channel, the monovalent anion site for F, Cl or OH occupies the center of it all (Fig. 2.1; Deer et al., 2013).

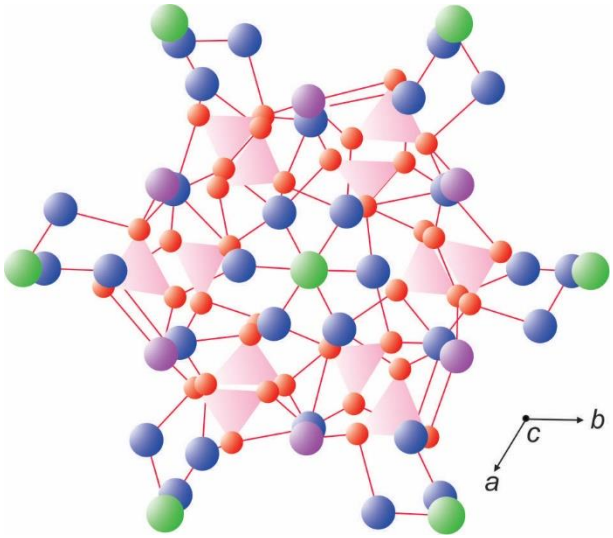

Figure 2.1 – Crystal structure of apatite, projected from the [001] plane. Purple spheres are Ca(I) cations, blue spheres are Ca(II) cations, and pink tetrahedrons are P site cations. Green spheres are channel anions and red spheres are oxygen atoms. The continuous red lines connecting the spheres represent atomic bonds. Sketch based on Skinner et al. (2003).

Apatite has a highly variable major and trace element composition, and these chemical compositions are sensible to its crystallising environment (Sha and Chappell, 1999; Belousova et al., 2001). Trace elements are easily lodged in apatite crystal structure, especially in the larger Ca(I) site. Apatite can accommodate elements with different charges and sizes, and it can deviate from the hexagonal symmetry while maintaining the same crystalline topology. This means that apatite has a high mineral-melt and mineral-fluid partition coefficient, even though it still relies on coupled substitution to maintain balance of cations of different charges (Hughes and Rakovan, 2002; Pan and Fleet, 2002; Prowatke and Klemme, 2006).

The prevailing trace element substitutes in apatite are divalent cations, such as Mg^{2+}, Mn^{2+}, Fe^{2+}, Sr^{2}+, Ba^{2+}, Eu^{2+} and Pb^{2+} that have the same valence state and similar ionic radius of Ca^{2+}, which allows these cations to occur in apatite from parts per million (ppm) to weight percentage (wt. %) range. These cations will prefer either the Ca(I) site (1.18 Å radii) or the Ca(II) site (1.06 Å), depending on their size (Fig. 2.2). Each cation might prefer one vacancy to the other depending on external factors such as pH, element competition, and oxygen fugacity. Mg^{2+}, Mn^{2+}, Fe^{2+} and Na^{+} prefer the larger Ca(I) site. Sr^{2+}, Ba^{2+}, Eu^{2+}, REE^{3+}, Y^{3+} prefer the smaller Ca(II) site. U^{4+} and Th^{4+}

do not have a particular preference (Cherniak, 2005). Rare earth elements (REE) together with Y (REE+Y) also fit into the Ca site (Sha and Chappell, 1999). REE+Y are among the elements most severely affected by melt compositional changes, which makes them a good proxy for detecting changes in melt/fluid regime (Watson and Green, 1981; Prowatke and Klemme, 2006). Likewise, the PO_4^{3-} group in apatite can be replaced by SiO_4^{3-}, AsO_4^{3-}, VO_4^{3-}, CrO_4^{3-}, CrO_4^{2-}, MnO_4^{3-} and SO_4^{2-}. The SiO_4^{-4} group is the commonest impurity at the PO_3^{-4} site, and it can be a charge compensator for REE^{3+} and Y^{3+} substitution at the Ca(II) site (Comodi et al. 1999).

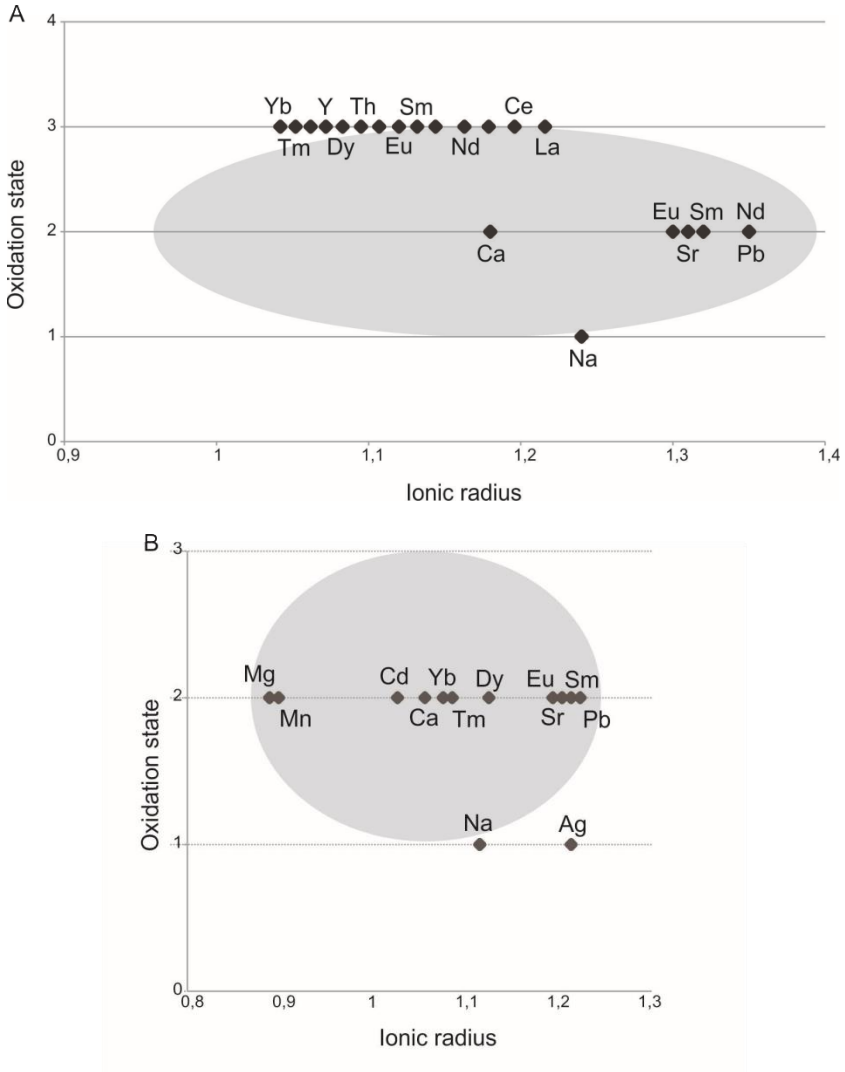

Figure 2.2 – Common cations that can substitute in the apatite crystal structure. Those diagrams show ionic radius vs. positive charge for the (A) Ca(I) site and the (B) Ca(II) site. Coupled substitution is necessary to maintain balance of cations of different charges. Ionic radius is plotted in a nine-fold coordination for Ca(I) sites and in a seven-fold coordination for Ca(II) sites. Data from Shannon (1976).

Chemical heterogeneities will be expressed as different textures and morphologies in apatite. Apatite may display complex zonation and patchiness (Zirner et al., 2015; Krneta et al., 2016). In apatite crystals, enrichments in REE+Y will tend to accumulate in crystal overgrowths and in the interface between core and rim (Rakovan and Reeder, 1994). Overgrowth and resorption textures are common in hydrothermal overprint, while concentric, oscillatory and sector zonation indicate crystal growth under magmatic conditions (Dempster et al., 2003; Zirner et al., 2015). If enough REE+Y are available, then the soluble phosphate will destabilize apatite and replace it with monazite and xenotime (Heinrich et al., 1997; Gratz and Heinrich, 1997).

Apatite crystallizes early in silicate melts and remains stable during nearly the whole range of magma evolution (Watson, 1980; Hoskin et al. 2000; Webster and Piccoli, 2015). Therefore, apatite may record the dynamical interactions between rock and fluidat the last stages of magmatic differentiation and during hydrothermal alteration, which makes it a valuable proxy (Webster and Piccoli, 2015). In granitic magmas, accessory phases (that include Fe-Ti-oxides, monazite, titanite, apatite, and so on) are primarily formed by heterogeneous nucleation inside hydrous mafic silicates, such as hornblende and biotite. Those small accessory minerals might be undistinguishable from inclusions in the hornblende or biotite (Parsons et al., 2015; Ferrero and Angel, 2018). These accessory minerals may either break down in the partial melting reactions, or may be liberated and remain stable or metastable within the surrounding melt (Clemens and Stevens, 2012). Thereupon, both iron oxides and phosphate phases have their formation history entangled together.

2.2 Trace elements in magnetite

Magnetite (Fe_3O_4) is a ferrimagnetic mineral that contains iron in both valence states, Fe^{2+} and Fe^{3+}. Magnetite has an inverse spinel structure (AB_2O_4, as $Fe^{2+}Fe_2{}^{3+}O_4{}^{2}$) and belongs to space group Fd_3m (Fig. 2.3). The O anions are arranged in a face-centred cubic (isometric) close-packed lattice along [111]. The A site represents divalent cations, such as Fe^{2+}, Mg, Ni, Mn, Co or Zn, that occupy one-eighth of the tetrahedral sites. The B sites represent trivalent cations, such as Fe^{3+}, Al, Ti, Cr, V, Mn and Ga, which occupy half of the octahedral sites.

Magnetite displays various phase transitions with other spinel group minerals, such as spinel ($MgAl_2O_4$), ulvöspinel (Fe_2TiO_4) and chromite ($FeCr_2O_4$).

Titanomagnetite is a solid solution Ti_xFe_3-xO_4 (Buddington and Lindsley, 1964) with coupled substitution of Ti^4+ for Fe^{3+} in the octahedral sites and Fe^{2+} for Fe^{3+} in the tetrahedral sites. Above 600ºC, there is continuous solid solution between magnetite and ulvöspinel, and their oxidation products, such as titanomaghemite (Buddington and Lindsley, 1964). Below 600ºC, extensive miscibility gaps may dissolute and re-precipitate the Fe-Ti-Al oxides as exsolution lamellae with different trace element compositions (Buddington and Lindsley, 1964).

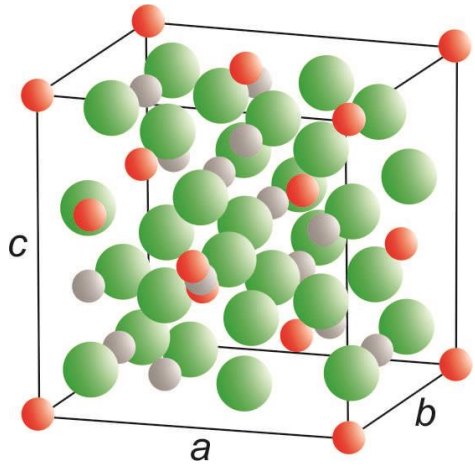

Figure 2.3 – Cubic inverse spinel structure of magnetite. Red spheres are Fe^{3+} cations (tetrahedral sites), grey spheres are Fe^{2+} / Fe^{3+} cations (octahedral sites), and green spheres are oxygen atoms. Sketch based on Nadoll et al. (2014).

Magnetite is formed under a wide variety of conditions. These conditions coordinate cation substitutions in magnetite, as a function of temperature, cooling rate, fO_2, and silica activity (Shishin et al., 2015). Magnetite accommodates a large range of cation substitutions, including Co, Ni and Zn; and also encrustations of Cu, Mn and Cd on its surface (Sidhu et al., 1978). Cation substitutions, and chiefly Al-substitution, make magnetite structure frequently non-stoichiometric (Murad et al., 2004). In stoichiometric magnetite (Fe^{2+}/Fe^{3+}=0.5), the divalent ion is frequently replaced by Mn^{2+} and Zn^{2+} (Cornell and Schwertmann, 2003).

The radius of Fe^{3+} in four-fold coordination is 0.49 Å, (Fig. 2.4a), while the radius of Fe^{2+} in four- and eight-fold coordination is 0.63 and 0.92 Å, respectively (Shannon, 1976) (Fig. 2.4b). Both these Fe^{3+} and Fe^{2+} coordination sites are for Fe ions in high spin (HS) state (Shannon, 1976). HS arises when all electrons are unpaired – thus each electron occupies one orbital. Orbital is the region in space occupied by a single electron or a pair of electrons. The electrons of Fe ions interact with those of the

other bound ions and this interaction leads to changes in the energy of states of ion (Cornell and Schwertmann, 2003). The electrical and magnetic properties of magnetite emerge out of this.

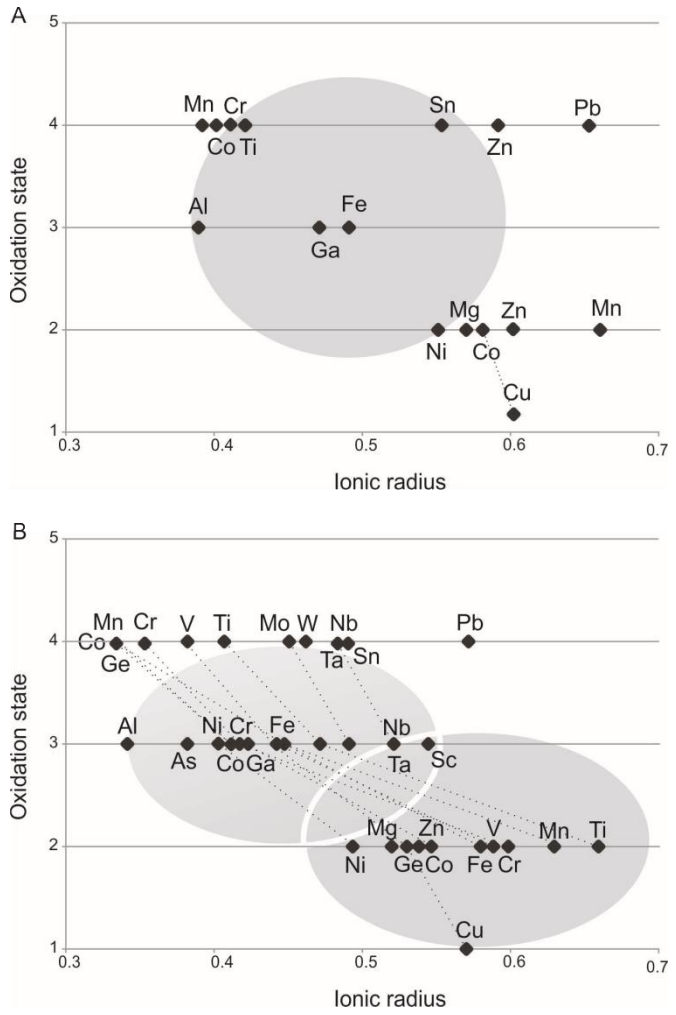

Figure 2.4 – Common cations that can substitute in the magnetite crystal structure. Diagrams display ionic radius (in Å) vs. positive charge for the (A) Fe(IV) site and the (B) Fe(VIII) site. Coupled substitution is necessary to maintain balance of cations of different charges. Adapted from Nadoll et al. (2014). Data from Shannon (1976).

Magnetite is an important iron ore and, along with other iron-titanium oxide minerals, it is the oldest known example of a ferrimagnetic substance. Crystal field stabilization energy (CFSE) of Fe^{2+} is greater for octahedral than for tetrahedral coordination, so Fe^{2+} preferentially occupies the octahedral sites (Burns, 2003). For Fe^{3+} the CFSE is zero for both octahedral and tetrahedral coordination, so that Fe^{3+} has no preference for either type of coordination (Burns, 2003). The two different cation sites in the structure – tetrahedral (A) occupied by Fe^{3+} and octahedral (B) occupied by Fe^{3+} and Fe^{2+} – form the basis for two interpenetrating magnetic sublattices. These two

interpenetrating sublattices have opposing magnetic moments – the alignment of the spins on the A and B sites are antiparallel and the magnitudes of the two types of spins are unequal (Burns, 2003). This generates an overall net magnetic moment, a large magnetic permeability and a large, positive magnetic susceptibility that causes ferrimagnetism (Cornell and Schwertmann, 2003).

Magnetite is a typical proxy for evaluating oxygen fugacity in magmas (Ishihara, 1977; Ishihara et al., 1979; Ishihara, 2004). Oxygen fugacity, fO_2, is also an important parameter in magmatic-hydrothermal systems (Simon et al., 2004). Oxygen fugacity is equivalent to the effective partial pressure of oxygen, and it relates thermodynamic activity (e.g., the effective concentration of a mineral phase in the melt) to the redox reactions (e.g., transfer of electrons between reacting species) of a melt (Ballhaus et al., 1990). Knowledge of redox conditions is attained to certain mineral assemblages in the rock that serve as oxygen redox buffers. Magnetite is among these mineral redox buffers. Some experiments calibrate the activity of magnetite by measuring the intrinsic fO_2 values relative to a magnetite-contained synthetic solid solution that serves as an oxygen redox buffer (e.g. Wijbrans et al., 2015; Sievwright et al., 2017; Sossi et al., 2018). Magnetite is present in redox buffer assemblages such as MH (magnetite-hematite) and FMQ (fayalite-magnetite-quartz), which means that it remains stoichiometrically stable (Ohmoto and Goldhaber, 1997). Such redox buffer assemblages remain reacting for long periods of time as metastable phases – that is, magnetite composition remains the same, while fO_2 changes.

Magnetite precipitates at oxidizing conditions, but trace element substitutions in magnetite generally occur during cooling of igneous rocks, at lower oxygen fugacity (Buddington and Lindsley, 1964; Nadoll et al. 2014). Several studies have used statistical methods to discriminate magnetite by trace element composition in different kinds of ore-related tectonic settings (e.g., Dupuis and Beaudoin, 2011; Dare et al., 2012, 2014; Nadoll et al., 2012; Nadoll et al., 2014; Canil et al., 2016; Pisiak et al, 2017). Fe^{2+} can be substituted by Mg, Mn, Zn and Ti, while Fe^{3+} can be substituted by Al, V and Cr (Nadoll et al., 2014). Other uncommon substitutions include Si, Ca, Mo, Ni, Cu, Co, and Ga that may be detected by LA-ICP-MS analysis (Nadoll and Koenig, 2011; Canil et al, 2016; Pisiak et al., 2017). Element concentration in magnetite varies with the element concentration in the melt from which it crystallized. This concentration

changes if other minerals are crystallizing at the same time and competing for the same elements.

In this context, it is important to understand how magnetite behaves during ore-forming processes. Several physical parameters may change the partition coefficient (the rate of transfer) of trace elements into magnetite. Overall, magnetite composition is controlled by seven main factors: (1) source rock or melt composition, (2) temperature, (3) pressure, (4) cooling rate, (5) oxygen fugacity, fO_2, (6) sulfur fugacity, fS_2, and (7) silica and sulfide activity (Buddington and Lindsley, 1964; Whalen and Chappel, 1988; Ghiorso and Evans, 2008; Mollo et al., 2013; Nadoll et al., 2014).

Chapter 3

Geological settings

3.2 Amazon Craton

The Amazon Craton is one of the largest cratons in the world. It was assembled through global tectonic events from 3.05 to 0.99 Ga (Santos et al., 2000; Tassinari and Macambira, 1999; Cordani et al., 2009). Its central portion is covered by the Phanerozoic Amazon sedimentary basin that splits the craton into two blocks: (1) the northern Guiana Shield and (ii) the southern Guaporé Shield (Almeida et al., 1981).

The assembly history of the Amazon Craton underwent at least two supercontinent cycles: the Paleo-Mesoproterozoic Columbia supercontinent (1.8-1.3 Ga; Rogers and Santosh, 2002; Zhao et al. 2003, 2004), and the Neoproterozoic Rodinia supercontinent (1.1–0.6 Ga; Hoffman, 1991). Columbia was an equatorial supercontinent composed of North American, East European, West African, and proto-Amazon Cratons (Bispo-Santos, 2008). It is argued that during the assembly of Rodinia, the Amazon Craton was attached to the North American Craton by the Grenville and Sunsás orogenic belts (Cordani and Teixeira, 2007). The Amazon and the North American cratons remained attached until the breakup of Rodinia at ~600 Ma (Cordani et al., 2009), while the Amazon and the West African cratons stood together until the breakup of Gondwana at ~173 Ma (Golonka and Bocharova, 2000). Other reconstructions are possible for either supercontinent (Pisarevsky et al. 2014, Cawood et al., 2016).

The geological and tectonic evolution of the Amazon Craton comprises several collisional orogenies that amount for some significant crustal growth. Two eminent models have been proposed in these terms: Tassinari & Macambira (1999) and Santos et al. (2000). These models differ in their methods and nomenclature. Tassinari and Macambira (1999) mainly used Rb-Sr dating, whereas Santos et al. (2000) additionally used a more robust U-Pb and Sm-Nd dating. This resulted in conflicting nomenclature for these tectono-geochronological models, and correlation between them is tentative. In this work, we opt for the nomenclature of Santos et al. (2000) for pragmatic reasons only, since the general outline for both models are knowingly similar. Both models agree that the Amazon Craton is an assembly of several orogenic belts, and both sustain

a collisional paradigm. A third model proposes an extensional paradigm, which assumes that the bulk of the Amazon Craton grew from post-collisional granitic magmatism (Almeida et al., 1981; Dall'Agnol et al. 1999; Kroonenberg and Roever, 2011).

The eastern segment of the Amazon Craton has an Archean nucleus (namely, the Central Amazon block) that is bordered by Proterozoic accretionary belts (Figure 3.1). The northeastern portion of this Archean nucleus is engulfed by the Paleoproterozoic Transamazon Orogen (2.26-2.01 Ga). In its southernmost part, this Archean nucleus is accreted by subduction-related juvenile magmatic arcs of Tapajós-Parima (2.03-1.88 Ga) and Rondônia-Juruena orogenic belts (2.03-1.88 Ga). The Rio Negro Orogen (1.82-1.52) records the Sthatherian collage (Brito Neves, 2011), responsible for establishing a cratonic landmass to the region. It was also an important metallogenic epoch concerning the craton evolution, since the gold ore-forming processes took place during Moreover, the presence of ophiolites in the Mesoproterozoic Alto Guaporé belt indicates further continental collision and crustal recycling (Rizzotto and Hartmann, 2012). These accretionary processes then generated the 1.45-1.1 Ga Sunsás belt, related to the collision of the Amazon craton towards the Paraguá block.

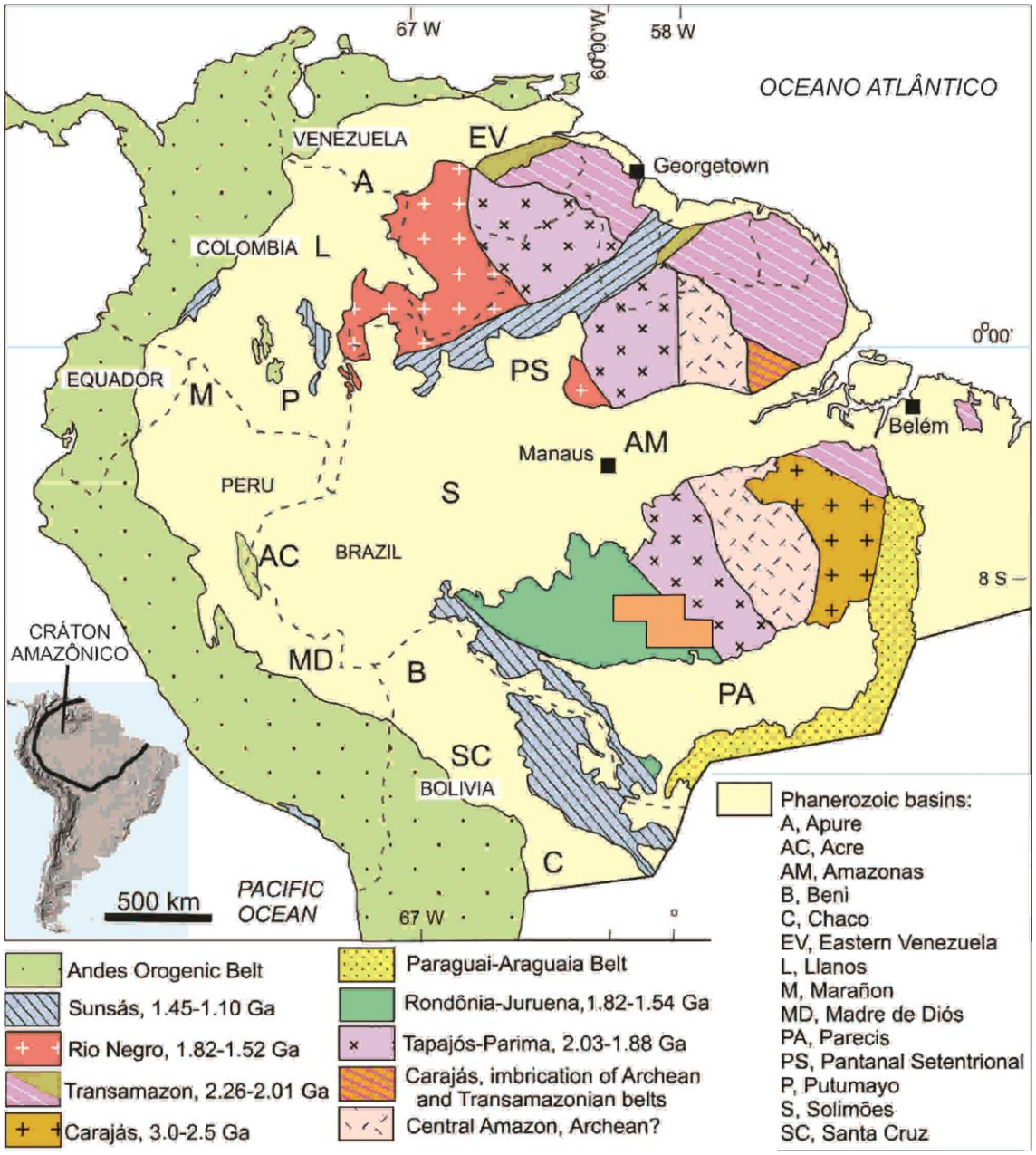

Figure 3.1 – Location of the Alta Floresta mineral province within the Amazon Craton, adapted from Santos et al. (2008). Grid boundaries of the AFMP between the Tapajós-Parima and Rondônia-Juruena provinces are according to Souza et al. (2005).

3.2 Alta Floresta mineral province

Our study area is located at the eastern segment of the Alta Floresta Mineral province (AFMP) (Fig. 3.1), at the municipalities of Peixoto de Azevedo, Matupá, Novo Mundo and Guarantã do Norte. This area concentrates most of the known gold deposits in the province. The AFMP is also known as Juruena-Teles Pires mineral province (Botelho and Moura, 2002; Moura et al., 2006; Silva and Abram, 2008; Alves et al.,

2019). The AFMP occurs as a Paleoproterozoic magmatic arc disposed in a NW-trending lineament (Miguel-Jr., 2011) that comprises several mineral deposits hosted in plutonic, volcanic and sedimentary rocks (Figure 3.2). Southward, the AFMP is bounded by the Caiabis graben and the Juruena terrane (Scandolara et al., 2017). Northward, it is bordered by the Cachimbo graben, which separates it from the Tapajós mineral province (Coutinho et al., 2008). The AFMP is located in the Tapajós-Parima province (2.03-1.88 Ga), next to the limit with the Rondônia-Juruena province (1.82-1.54 Ga)[1]. Both these tectonic provinces represent different crustal blocks merged as successive orogenic belts (Tassinari and Macambira, 1999; Santos et al., 2000; Assis, 2015; Scandolara et al., 2017). In this sense, because the AFMP is a place of interaction between these two orogenic belts, it consists of a "Tapajós"-like crust that interacted with the southward Juruena terrane (Assis, 2015; Scandolara et al., 2017; Duarte et al., 2019).

The Tapajós-Parima orogenic belt is divided by Santos et al. (2001) in four domains: Parima, Uaumiri, Tapajós and Alta Floresta[2]. From 2.03 to 1.87 Ga, the Tapajós and the Alta Floresta domains shared much of the same lithostratigraphical units as they were part of the same Tapajós-Parima orogenic belt. However, these domains started to differentiate from 1.82 onwards, when the Tapajós-like crust of the Alta Floresta domain began to accommodate the Paranaíta intrusive suite and the Colíder Group (1.82-1.77 Ga), which are products of the evolution of the Juruena magmatic arc[3] (Scandolara et al., 2017; Duarte et al., 2019). Moreover, the Tapajós domain also holds the namesake mineral province that shows substantial lithostratigraphical correlations with the Alta Floresta mineral province (Table 3.1).

[1] Some authors classify the location of the AFMP as "between the Tapajós-Parima and Rondônia-Juruena provinces" (e.g. Assis et al., 2017) because it contains elements of both provinces.

[2] The Alta Floresta domain, which comprises the homonym mineral province, is also referred to as Peixoto de Azevedo domain in Santos et al. (2004). This labelling was most likely opted because the area surrounding the city of Peixoto de Azevedo has a larger concentration of gold mines than the Alta Floresta area, and hence the Peixoto area is considered more significant in a metallogenetic perspective.

[3] The Colíder group and the Paranaíta intrusive suite are known in the works of Duarte (2015) and Duarte et al. (2012, 2019) as the "Volcanic Domain".

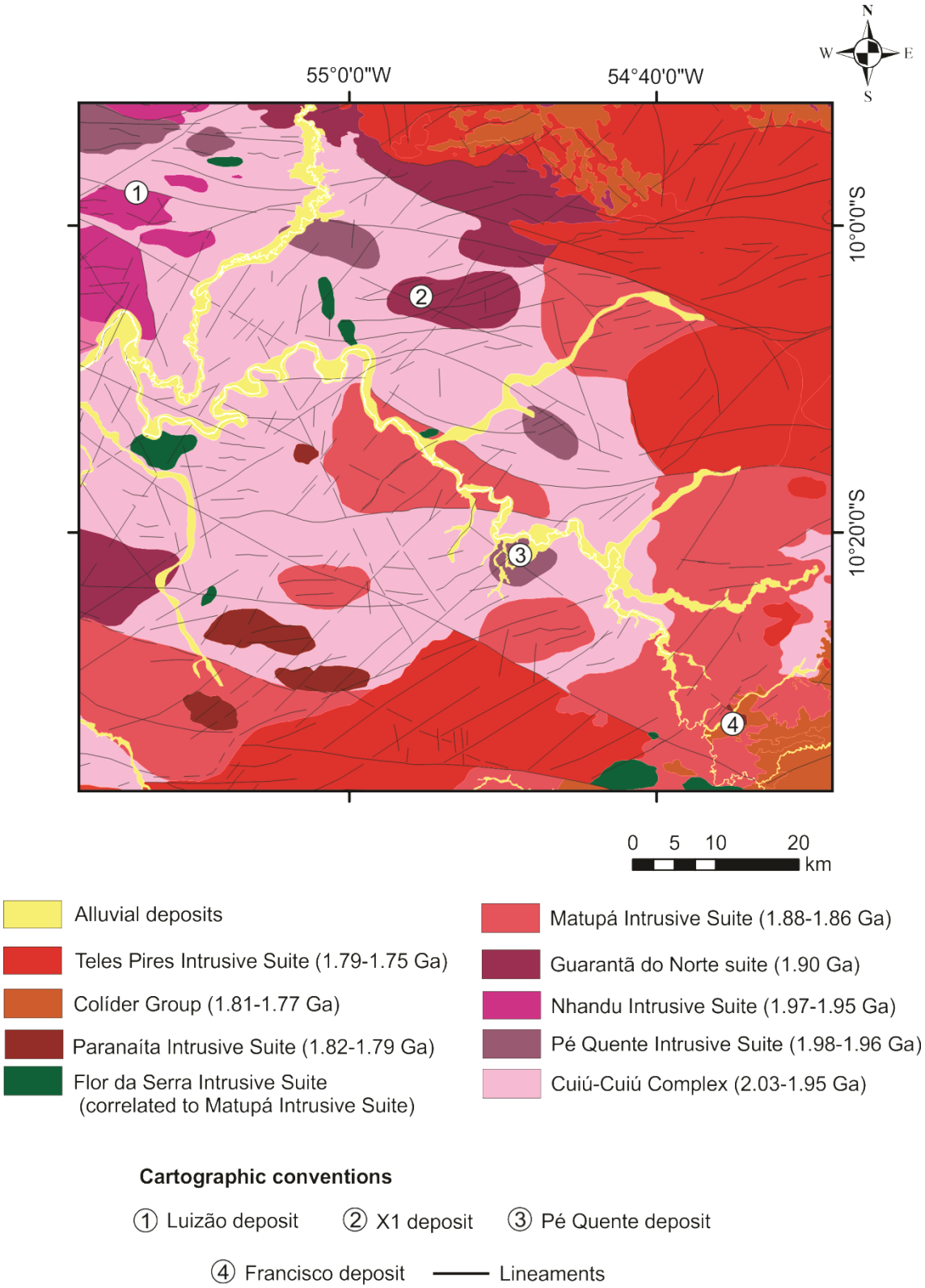

Figure 3.2 – Geological map of the easternmost segment of the Alta Floresta mineral province. From Alves et al. (2019).

Table 3.1 Summary of the main geologic units in the eastern portion of the Alta Floresta mineral province.

Geologic domains	Geologic units	Ages (Ma)	Tectonic settings (T_{DM} ages reported in Ga)	References
Sedimentary sequences	Alluvial deposits Gravel, sand, silt and clay	Quaternary	Intracratonic unconsolidated sediments	Souza et al. (2005)
Anorogenic magmatism: A-type plutonic-volcanic groups	Teles Pires Intrusive Suite Alkali-feldspar granite, monzogranite, granodiorite, porphyritic and rapakivi granite	1782 ± 17–1757[2,3]	Late-stage extensional back-arc ($1.94 < T_{DM} < 2.28$; $-3.4 < \varepsilon_{Nd(t)} < +3$)	Santos (2000); Pinho et al. (2001); Souza et al. (2005); Paes de Barros (2007); Silva and Abram (2008); Silva et al. (2014); Assis (2015)
Juruena magmatic arc: Syn to late orogenic plutonic-volcanic units	Colíder group: Intermediate to acid epiclastic, pyroclastic, subvolcanic and volcanic rocks	1812 ± 12; 1786 ± 17; 1785 ± 6.3; 1781 ± 8[2]	Calc-alkaline volcanic arc to synorogenic setting ($1.94 < T_{DM} < 2.34$; $-3.4 < \varepsilon_{Nd(t)} < +3$). Correlated to the forearc Roosevelt magmatism in the Juruena Domain	Japan International Cooperation Agency (2000); Pimentel (2001); Silva and Abram (2008); Assis (2011); Miguel Jr. (2011); Duarte et (2019)
	Paranaíta Intrusive Suite: Monzogranite, quartz-monzonite, epizonal and porphyrytic granodiorite to monzonite intrusions	1815 ± 10; 1780 ± 5[2] União do Norte porphyry: 1774 ± 7.5[2] Peixoto granite: 1792 ± 2[5]; 1781 ± 10 Ma[3]	Continental arc setting ($1.9 < T_{DM} < 2.3$; $-1.5 < \varepsilon_{Nd(t)} < +1.0$)	Santos (2000); Souza et al. (2005); Duarte et al. (2019)
Cuiú-Cuiú magmatic arc: postorogenic plutonic-volcanic units and volcano-sedimentary sequences	Flor da Serra Intrusive Suite: Diabase dykes and gabbro stocks	Unknown age; intruded into Matupá intrusive suite	Correlated to the Ingarana intrusive suite (1980-1860 Ma) in the Tapajós Domain	Moura (1998); Souza et al. (2005)

Table 3.1 *(Cont.)*

Geologic domains	Geologic units	Ages (Ma)	Tectonic settings (T_{DM} ages reported in Ga)	References
	Matupá Intrusive Suite: Monzogranite, monzonite, monzodiorite, granodiorite, tonalite and porphyritic-rapakivi granite	1888 ± 9; 1872 ± 12; 1863 ± 4.8[3,5] União granodiorite: 1853 ± 23[2]	Synorogenic to postorogenic volcanic arc ($2.34 < T_{DM} < 2.47$; $-2.6 < \varepsilon_{Nd(t)} < -4.9$). Correlated to the Parauari and the Maloquinha intrusive suites (1880-1860 Ma) in the Tapajós Domain	Moura (1998); Souza et al. (2005); Assis (2011); Assis (2015); Lima Jr. (2017)
	Guarantã do Norte suite: Granodiorite, monzonite, quartz-monzonite, quartz-monzodiorite, monzodiorite, aplitic granodiorite, and biotite tonalite	1904 ± 4.6–1901 ± 6.8[2]	Calc-alkaline volcanic arc ($2.36 < T_{DM} < 2.29$; $-5.49 < \varepsilon_{Nd(t)} < -4.46$). Correlated to the Tropas Intrusive Suite (1900-1907 Ma) in the Tapajós Domain	Assis (2015)
Cuiú-Cuiú magmatic arc: Syn to late orogenic plutonic sequences	Aragão granite: Syenogranite, monzogranite with porphyritic and microgranite facies	1931 ± 12[2]	Restricted postsubduction / postorogenic magmatism (no isotopic data available)	Vitório (2010); Miguel Jr. (2011); Ramos (2011)
	Nhandu Intrusive Suite: Syenogranite, monzogranite granodiorite, quartz-monzonite, and monzonite, with subordinate subvolcanic facies	1953 ± 6 Ma; 1962 ± 7[2,3] Novo Mundo granite[4]: 1970 ± 3; 1964 ± 1[5]	Calc-alkaline volcanic arc ($2.36 < T_{DM} < 2.29$; $-5.49 < \varepsilon_{Nd(t)} < -4.46$). Correlated to the Creporizão intrusive suite (1980-1960 Ma) in the Tapajós Domain	Paes de Barros (2007); Ramos (2011); Barros et al. (2015); Dezula (2016); Alves et al. (2019)
	Pé Quente suite: Monzonite, quartz-monzonite, monzodiorite, fine-coarse-albitite, aplitic granodiorite, and tonalite	1979 ± 31 Ma; 1978 ± 8.1[2] Pezão monzogranite: 1987 ± 4.2[2]	Calc-alkaline volcanic arc ($2.30 < T_{DM} < 2.51$; $-3.36 < \varepsilon_{Nd(t)} < -0.96$). Correlated to the Cumaru intrusive suite (2000-1980 Ma) in the Tapajós Domain	Miguel Jr. (2011); Assis (2015); Trevisan (2015); Alves et al. (2019)

Table 3.1 *(Cont.)*

Geologic domains	Geologic units	Ages (Ma)	Tectonic settings (T_{DM} ages reported in Ga)	References
Cuiú-Cuiú magmatic arc: Syn to late orogenic plutonic sequences (Cont.)	Undifferentiated granite Syenogranite, monzogranite, syenite, and quartz-monzonite	Unknown age	Calc-alkaline volcanic arc granites (no isotopic data available)	Assis et al. (2012)
	Volcaniclastic sequence (Serra Formosa Formation) Feldspathic-sandstone, feldspathic-wake, lithic-sandstone, and matrix supported sandy-polymictic conglomerate	Minimum age: 2009[1]	Back-arc foreland basin within an active continental margin (no isotopic data available)	Assis (2011); Miguel Jr. (2011)
Cuiú-Cuiú magmatic arc: metamorphosed early orogenic plutonic sequences	Cuiú-Cuiú complex Migmatitic orthogneiss and metagranitoid of dioritic, tonalitic and granodioritic composition	2045 ± 11[2]; 2028 ± 17; 2012 ± 11; 2008 ± 3.6[3]; 2014 ± 5[3]; 1992 ± 7[3]	Juvenile continental magmatic arc (2.32 < T_{DM} < 2.49; -3.36 < $\varepsilon_{Nd(t)}$ < -1.90)	Souza et al. (2005); Paes de Barros (2007); Trevisan (2015); Dezula (2016); Silva (2017); Alves (2019)
Neoarchean basement inliers	Gneisses and migmatites	2816 ± 7; 2689 ± 11[2,5]	Oceanic magmatic arc (No isotopic data available)	Souza et al. (2005); Paes de Barros (2007); Moreira (2019)

[1] Detrital zircon LA-ICP-MS U-Pb ages; [2] LA-ICP-MS U-Pb zircon crystallization ages; [3] SHRIMP U-Pb zircon crystallization ages; [4] Units that host gold deposits; [5] Single zircon Pb-Pb evaporation crystallization ages

The oldest basement rocks in the region would be Neoarchean inliers such as the Gavião migmatitic gneiss (2,816 ±7 Ma, Pb-Pb single-zircon evaporation; Paes de Barros, 2007) and the Paraíba biotite gneiss (2,689 ±11 Ma; LA-ICP-MS U-Pb in zircon; Moreira, 2019). These gneisses were metamorphosed during the Cuiú-Cuiú arc evolution in the Early Orosirian (Moreira, 2019). From 2.1 Ga onwards, the lithostratigraphic evolution of the AFMP is divided in three stages (Assis et al., 2017; Alves et al., 2019; Duarte et al., 2019):

(1) Early Orosirian (2100 to 1950 Ma) comprehends the syn to late orogenic stages of the Cuiú-Cuiú magmatic arc. This stage is represented by the Cuiú-Cuiú Complex (2.03-1.95 Ga; Santos et al., 2000), Pé Quente Suite (1.98-1.96 Ga; Miguel-Jr, 2011), and Nhandu Intrusive Suite (1.97-1.95 Ga; Paes de Barros, 2007; Barros et al., 2015) (Table 3.1). The Cuiú-Cuiú Complex comprises foliated granitoids, tonalite to granodiorite gneisses, and metavolcanic rocks (Pessoa et al., 1977; Quispe, 2016), that delineate a primitive calc-alkaline magmatic arc that matured during the Early Orosirian (Santos et al., 2000; Paes de Barros, 2007; Trevisan, 2015; Assis, 2015; Quispe, 2016; Alves et al., 2019). Some authors refer to the Cuiú-Cuiú Complex as "the basement" or as "part of the basement" (Pessoa et al., 1977, Santos et al., 2001, 2004; Souza et al., 2005; Assis, 2011, 2015) because most of the later arc-related units, such as the Pé Quente and Nhandu suites, intrude into the Cuiú-Cuiú Complex. However, the earliest crustal stage in the region (and, therefore, the earliest basement age) amasses the Neoarchean inliers in the region (e.g. Moreira, 2019) that correlate to the Xingu Complex in the Carajás province (2,859 ±2 Ma and 2,851 ± 4 Ma; Machado et al., 1991).

The Pé Quente and Nhandu suites rocks correspond to oxidised I-type calc-alkaline, medium- to high-K, metaluminous to peraluminous granitic magmas that interacted with juvenile crust (Paes de Barros, 2007; Assis, 2011) and that are part of a syn- to late orogenic stage of the Cuiú-Cuiú continental arc (Paes de Barros, 2007; Assis, 2011; Trevisan, 2015; Alves et al., 2019). Moreover, Trevisan (2015) described ore-related epizonal microgranites coeval to the Pé Quente and Nhandu suites (i.e., Luiz feldspar-porphyry; 1.97 Ga, SHRIMP U-Pb zircon age), which supports the possibility that there are ore forming events associated to this late orogenic stage of the Cuiú-Cuiú magmatic arc.

Assis (2011) previously defined the Pé Quente suite as the major host rock unit of the Pé Quente deposit. However, Alves et al. (2019) expanded it to encompass other coeval units, such as the Pezão monzogranite (1.98 Ga; Trevisan, 2015), Luiz granodiorite (1.96 Ga; Trevisan, 2015), and Luiz feldspar-porphyry (1.97 Ga; Trevisan, 2015). The Pé Quente suite is correlated to the Cumaru Intrusive Suite, São Jorge Velho granite and Vila Riozinho Formation (2.0-1.98 Ga) in the Tapajós domain. In the NE of the Mato Grosso State, the Pé Quente suite is known as the Vila Rica Intrusive Suite (1.99-1.97 Ga; Alves et al., 2010) with a volcanic counterpart known as the Jarinã Formation (Alves et al., 2010).

The Nhandu granite was previously dated between 1.88-1.87 Ga (Paes de Barros, 2007). However, Barros et al. (2015) replicated the geochronological assays for the type area of the Nhandu granite and obtained an earlier age, at around 1.95-1.96 Ga, which is closer to the Novo Mundo granite (1.97-1.96 Ga) described in Paes de Barros (2007). Therefore, both the Novo Mundo and Nhandu granites were assembled as the Nhandu Intrusive Suite (as in Barros et al., 2015; and Alves et al., 2019).

(2) Late Orosirian (1905 Ma to 1848 Ma) represents the postorogenic stage of the Cuiú-Cuiú magmatic arc that includes the Guarantã do Norte suite (1.90 Ga; Assis, 2015; Alves et al., 2019), Matupá Intrusive Suite (1.88-1.86 Ga; Moura, 1998; Silva, 2014), and Flor da Serra Intrusive Suite (unknown age; correlated to the Matupá Intrusive Suite) (Table 3.1). These magmatic suites constitute oxidised, calc-alkaline to alkaline, medium- to high-K, meta- to peraluminous intrusions with a wide range of compositions from tonalite to syenogranite (Moura et al., 2006; Paes de Barros, 2007; Assis, 2011; Leite, 2017). They represent the latest magmatic event that occurred in the Tapajós-Parima province regarding the Cuiú-Cuiú magmatic arc (Moreton and Martins, 2005; Alves et al., 2019). Earlier postorogenic magmatism seldom occurs between 1950 and 1905 Ma, and the only registry of this interval is the Aragão granite (1.93 Ga; Miguel Jr.).

The Guarantã do Norte suite was expanded by Alves et al. (2019) to encompass the X1 granodiorite (1904 Ma; Assis, 2015) and the Pé Quente tonalite (1901 Ma; Assis, 2015). The Matupá Intrusive Suite was also expanded to include the União granodiorite (1.86-1.85 Ga) and the 1889-1849 Ma granitoids that previously belonged to the Nhandu granite (Paes de Barros, 2007; Alves et al., 2019). The Flor da Serra is a mafic intrusive suite composed of diabase, gabbro and monzogabbro that is closely

related to the Matupá granitic facies, often with magma mingling between those granitic facies and portions of gabbroic compositions (Moreton and Martins, 2005).

(3) Statherian (1810 to 1727 Ma) represents the late orogenic to post-orogenic felsic magmatism and back-arc volcanic-sedimentary covers of the Juruena magmatic arc, which include the Colíder Group (1.81-1.77 Ga; Pimentel, 2001; Silva and Abram, 2008; Duarte et al., 2019) and Paranaíta Intrusive Suite (1.82-1.79 Ga; Santos et al., 2000; Duarte et al., 2019), and the later anorogenic magmatism of the Teles Pires Intrusive Suite (1.79-1.75 Ga; Santos et al., 2000; Pinho et al., 2003; Prado et al., 2013). This Statherian magmatic event is important because it is coeval to the sulfide Re-Os ages obtained to the disseminated gold-rich deposits reported by Assis et al. (2017). According to them, the metallogenetic epoch in the province occurred *circa* 1.78-1.77 Ga, related to the Paranaíta-Colíder magmatism (Assis, 2015; Assis et al., 2017; Duarte et al., 2019). In a global tectonics scenario, the Juruena magmatic arc marks the onset of the Columbia Supercontinent Cycle (1.8-1.7 Ga; Cordani et al., 2009), in which the Paraguá (or Rio Apa) proto-craton collided with the Tapajós crustal block (Scandolara et al., 2017). Therefore, the Paranaíta-Colíder magmatism in the Tapajós-Parima province represents a hinterland manifestation of the accretionary processes that built the Rondônia-Juruena province. The Paranaíta Intrusive Suite and the Colíder Group are the intrusive and extrusive counterparts, respectively, of the same magmatic suite. Therefore, anatomically, the Paranaíta Intrusive Suite occurs generally underneath the Colíder volcanic group.

The Colíder Group comprises acidic to intermediate volcanic rocks with a controversial origin: whether from continental arc magmatism (Duarte et al., 2012; Scandolara and Souza, 2016; Duarte et al., 2019) or anorogenic magmatism (Souza and Abram, 2008; Alves et al., 2019). The Colíder Group has anorogenic (A2-type) to calc-alkaline orogenic signature (Silva and Abram, 2008; Alves et al., 2019), is spatially arranged as a NW-trending volcanic arc and is somewhat coeval to the epithermal- and porphyry-style mineral systems in the easternmost segment of the AFMP (Duarte et al., 2012, 2019; Assis, 2015; Assis et a., 2017). Ultimately, the geochemical controversy surrounding the Colíder Group arises because of the crustal contamination of mature continental magmas by processes such as wall-rock assimilation and fractional crystallisation (AFC; DePaolo, 1981; Duarte et al., 2019). Therefore, the Colíder Group is herein assumed to be influenced by the continental arc magmatism of the late stage

subduction of the Juruena arc (as in Duarte et al., 2012, 2019; Assis et al. 2017; Scandolara et al., 2017).

The Paranaíta Intrusive Suite comprises I-type to A-type monzo- to syenogranites, porphyrytic and epizonal granites. They tend to crop out mostly in the northwesternmost portions of the AFMP and in the Tapajós domain (Coutinho, 2008; Duarte, 2015; Duarte et al., 2019). However, in our study area, the Paranaíta subvolcanics may be exposed where the Colíder pyroclastic sediments are eroded. Other individual intrusions are interpreted to be part of Paranaíta Intrusive Suite (as in Duarte et al., 2019), such as the Peixoto granite (1.79 – 1.76 Ga; Paes de Barros, 2007; Silva, 2014), X1 quartz-feldspar porphyry (1.78 Ma; Assis, 2015) and União do Norte porphyry (1.77 Ga; Miguel-Jr, 2011; Assis, 2011).

The Teles Pires Intrusive Suite corresponds to the regional anorogenic magmatism in the Alta Floresta and Tapajós domains. It intrudes in all the aforementioned units, including the Colíder Group. Several authors regard the Teles Pires Intrusive Suite as the plutonic counterpart of the Colíder Group (Souza and Abram, 2008; Assis, 2015; Assis et al., 2017; Alves et al., 2019). However, because the Teles Pires Intrusive Suite was primarily designated as an anorogenic, barren magmatism (Paes de Barros, 2007), it has been problematic to associate the Statherian metallogenetic event to it. Therefore, the introduction of the Paranaíta Intrusive Suite to incorporate those ore-related epizonal granites (as done in Duarte 2015; Duarte et al., 2019) was crucial to overcome this conundrum.

In the Juruena terrane (SW of AFMP), the Statherian epoch is characterised by an accretionary phase represented by the Juruena Complex, which is a supersuite correlated to the abovementioned units that includes the Vitória plutonic suite (1787-1775 Ma), São Pedro granite (1786 Ma), São Romão granite (1784 Ma), Vespor mafic suite (1776-1764 Ma), Apiacás granite (1784 Ma), Roosevelt group (1760-1740 Ma), Teodósia suite (1762-1749 Ma) and Igarapé das Lontras (1754 Ma) suite (Duarte et al., 2012; Scandolara and Souza, 2016).

The Statherian metallogenetic event gave rise to the intrusion-hosted Au-rich mineral systems related to the Colíder and Paranaíta suites, which are largely prone to occur at late stages of arc maturity (Richards et al., 2011, 2012). This was evidenced by Re-Os dating in molybdenite and pyrite from the mineralized zones of the Pé Quente (1792 ± 9 to 1784 ± 11 Ma), Luizão (1805 ± 21.5 and 1782 ± 8.9 Ma) and X1 (1787 ± 7

and 1785 ± 7 Ma) deposits (Assis et al., 2017). Moreover, at the Francisco deposit, sericite associated to the gold-related phyllic alteration exhibits $^{40}Ar/^{39}Ar$ sericite ages constrained between 1779 ± 6.5 and 1777 ± 6.3 Ma, in agreement with the sulfide Re-Os ages (Assis, 2015).

3.3 Geology of the investigated mineral deposits

For our study, we selected ore-related samples from an epithermal deposit (Francisco) and from intrusion-hosted gold deposits (Luizão, Pé Quente and X1) in the Alta Floresta mineral province. We also selected samples representative of the unmineralised host rocks of these deposits, and from barren granitoids of the A-type Teles Pires Intrusive Suite.

3.3.1 Luizão deposit

The Luizão deposit is hosted within the Novo Mundo granite, which is part of the Nhandu Intrusive Suite (Fig. 3.3; Paes de Barros, 2007; Barros et al., 2015; Alves et al., 2019). The Novo Mundo granite is mainly composed of leuco-biotite-syenogranite (foliated to equigranular) and lesser monzogranite, quartz-monzonite and monzonite (Fig. 3.4; Paes de Barros, 2007; Assis et al., 2017). It has Pb-Pb zircon age of 1970 ± 3 for the monzogranite, 1964 ± 1 Ma for the syenogranite, and 1956 ± 12 Ma for the monzonite (Paes de Barros, 2007). It has whole-rock T_{DM} ages spanning from 2.76 to 2.55 Ga and $\varepsilon_{Nd(t)}$ from -7.6 to -3.5, for the syenogranite and the monzonite, respectively (Paes de Barros, 2007). This suggests that the emplacement of the Novo Mundo granite occurred in a juvenile arc setting with Neoarchean to Paleoproterozoic sources and small crustal contribution (Assis, 2015; Assis et al., 2017).

The Novo Mundo granite is an I-type, magnetite-bearing, oxidized, calc-alkaline, medium- to high-potassium, and metaluminous to slightly peraluminous rock (Paes de Barros, 2007; Assis, 2015). The Novo Mundo granite is deeply altered in the Luizão deposit into (1) incipient sodic alteration with albite and quartz, (2) strong and pervasive potassic alteration with microcline ± magnetite (turning to hematite), (3) pervasive phyllic-like alteration with interstitial sericite and/or coarse-grained fibrous radial Fe-rich muscovite + Fe-Mg-rich chlorite + rutile + pyrite, and (4) propylitic alteration in pervasive style or in veinlets, with epidote + apatite + chlorite + Ca-Mg-rich carbonate (Paes de Barros, 2007; Assis et al., 2017). The mineralized zone occurs

within the phyllic alteration, and consists of gold included in pyrite (Ag 4-22%) or gold associated with Fe- or Mg-rich chlorite in breccias. Pyrite also contains inclusions of

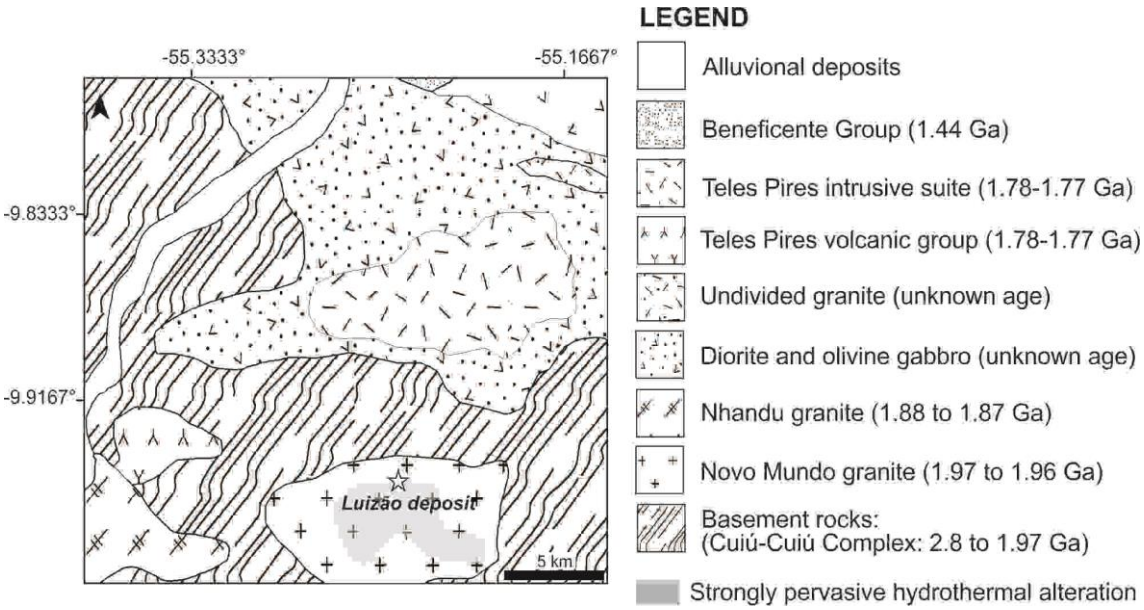

Figure 3.3 – Geological map of the Luizão deposit (Assis et al. 2017; Paes de Barros, 2007).

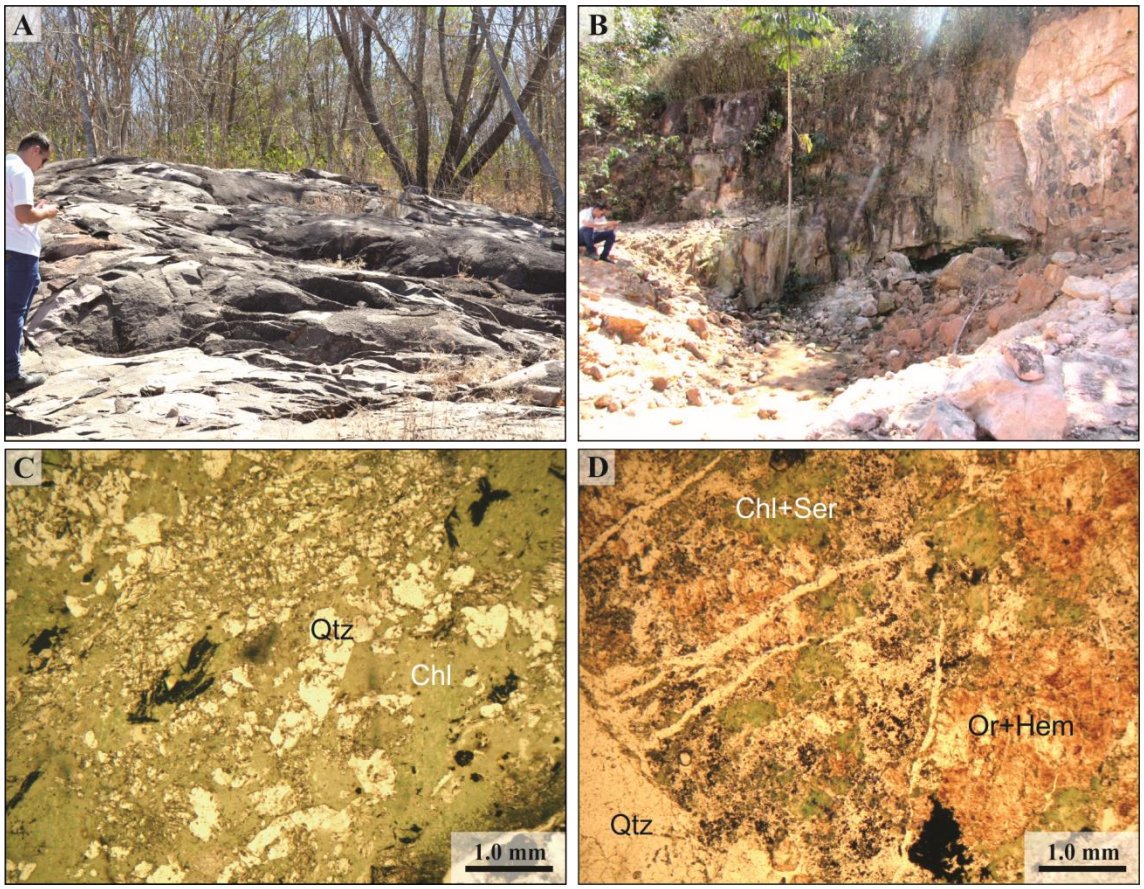

Figure 3.4 – Photographs and photomicrographs of outcrops, textures and hydrothermal alteration of the Luizão deposit. (a) Outcrop of the Novo Mundo granite, the unaltered host rock of the Luizão deposit. (b) Overview of the hydrothermal alteration zone of the Luizão deposit, with a person at the left side for scale. (c) Pervasive chloritic alteration forming anastomosing patterns. (d) Chloritic alteration overprinting potassic alteration, and being crosscut by quartz veinlets. (c, d) Images in transmitted plane-polarised light.

plagioclase, sericite, Fe-Mg-rich chlorite chalcopyrite, sphalerite, galena, monazite, thorite and Au-Ag telurides (Paes de Barros, 2007; Assis et al. 2017).

4.3.2 Pé Quente deposit

The Pé Quente gold deposit is hosted at two different intrusives suites (Fig. 3.5; Assis, 2015; Alves et al., 2019): the (1) Pé Quente suite, represented by an oxidized I-type biotite tonalite dated at 1979 ± 31 Ma (LA-ICP-MS U-Pb zircon crystallization age; Miguel Jr. 2011) that hosts a major portion of the deposit, and then a lesser portion of the deposit that is hosted in the (2) Guarantã do Norte suite, represented by a quartz monzonite dated at 1901 ± 6.8 Ma (SHRIMP U-Pb zircon crystallization age; Assis et al. 2017) that is cross-cut by aplite dikes of granodioritic and syenogranitic composition.

The Pé Quente suite and the Guarantã do Norte suite are two different expanded magmatic series that are part of different geodynamic settings of the Cuiú-Cuiú magmatic arc. Both have similar geochemical affinities with calc-alkaline, medium- to high-K, metaluminous to peraluminous granitic rocks, but the Pé Quente suite trends towards synorogenic granitic rocks that originated at the onset of a juvenile magmatic arc, whereas the Guarantã do Norte suite trends towards more fractionated, postorogenic magmatic sequences (Assis, 2011; Alves et al., 2019). They are crosscut by calc-alkaline plutons of tonalitic to monzogranitic composition, presumably related to the postorogenic sequences of the Matupá Intrusive Suite (1.87-1.86 Ga; Moura et al. 2006) and Paranaíta Intrusive Suite (1.79-1.78 Ga; Paes de Barros, 2007; Silva et al. 2014). The Pé Quente Intrusive Suite has $T_{DM(t)}$ from 2.51 to 2.41 Ga and $\varepsilon_{Nd(t)}$ from -5.13 to -2.88, which indicates Neoarchean to Siderian juvenile sources with crustal contribution (Assis, 2015).

Hydrothermal alteration at the Pé Quente gold deposit (Fig. 3.6), according to Assis (2011), consists of (1) pervasive sodic alteration with albite + quartz + coarse-grained pyrite, (2) widespread and pervasive potassic alteration with orthoclase and microcline ± hematite, that surrounds the mineralized area, (3) strong phyllic-like alteration with coarse-grained muscovite + quartz + pyrite ± chalcopyrite (potassic and phyllic alterations are well-developed in the deposit), (4) interstitial carbonate alteration with fine to coarse-grained calcite, (5) silicification and quartz infill commonly accompanied by breccias and comb-texture quartz veins, (6) subordinated Mg-rich

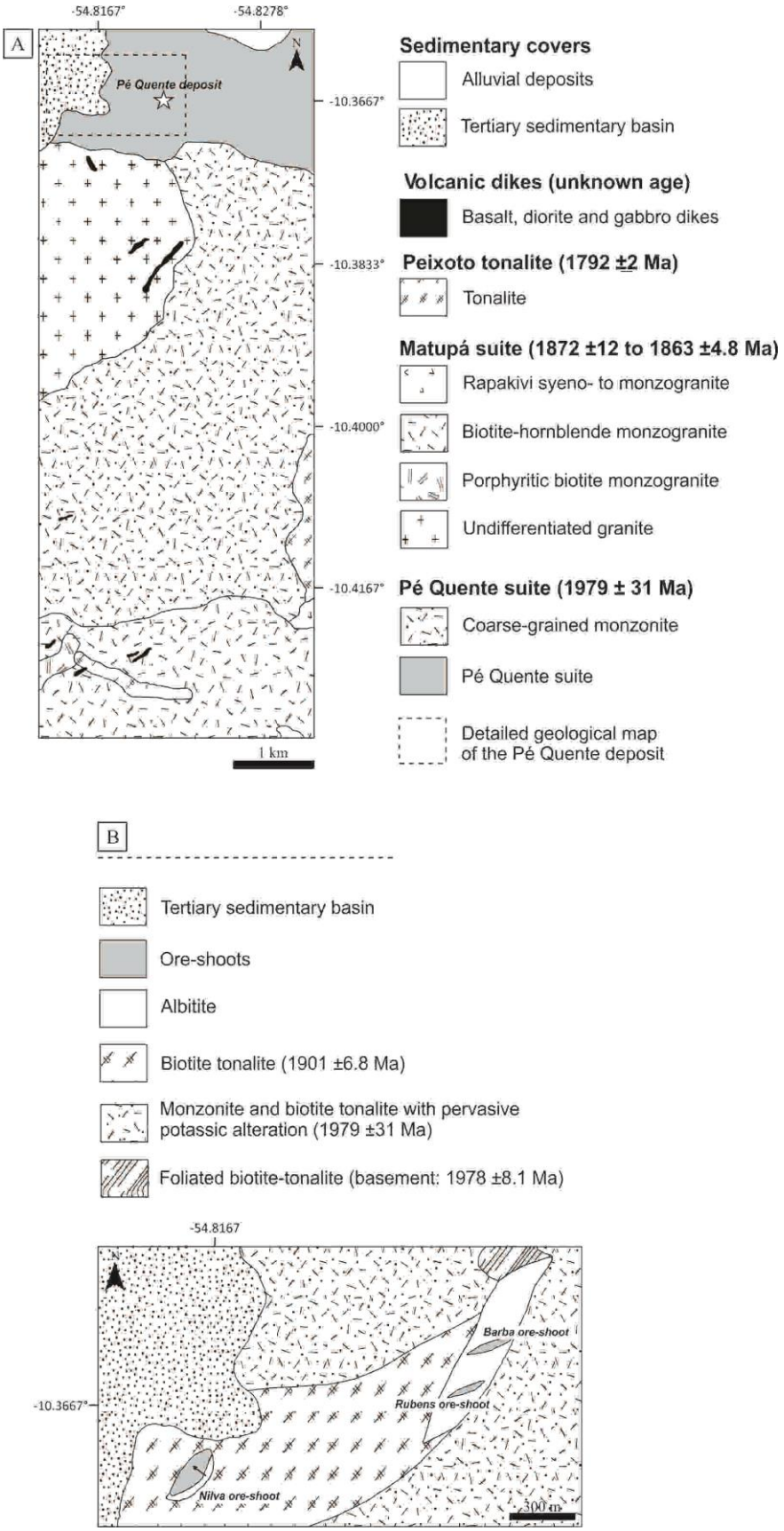

Figure 3.5: Geological map of the Pé Quente deposit (Assis, 2015; Assis et al. 2017), in two scales: (A) a regional map (Assis, 2011), and a (B) detail map (Stabile, 2012).

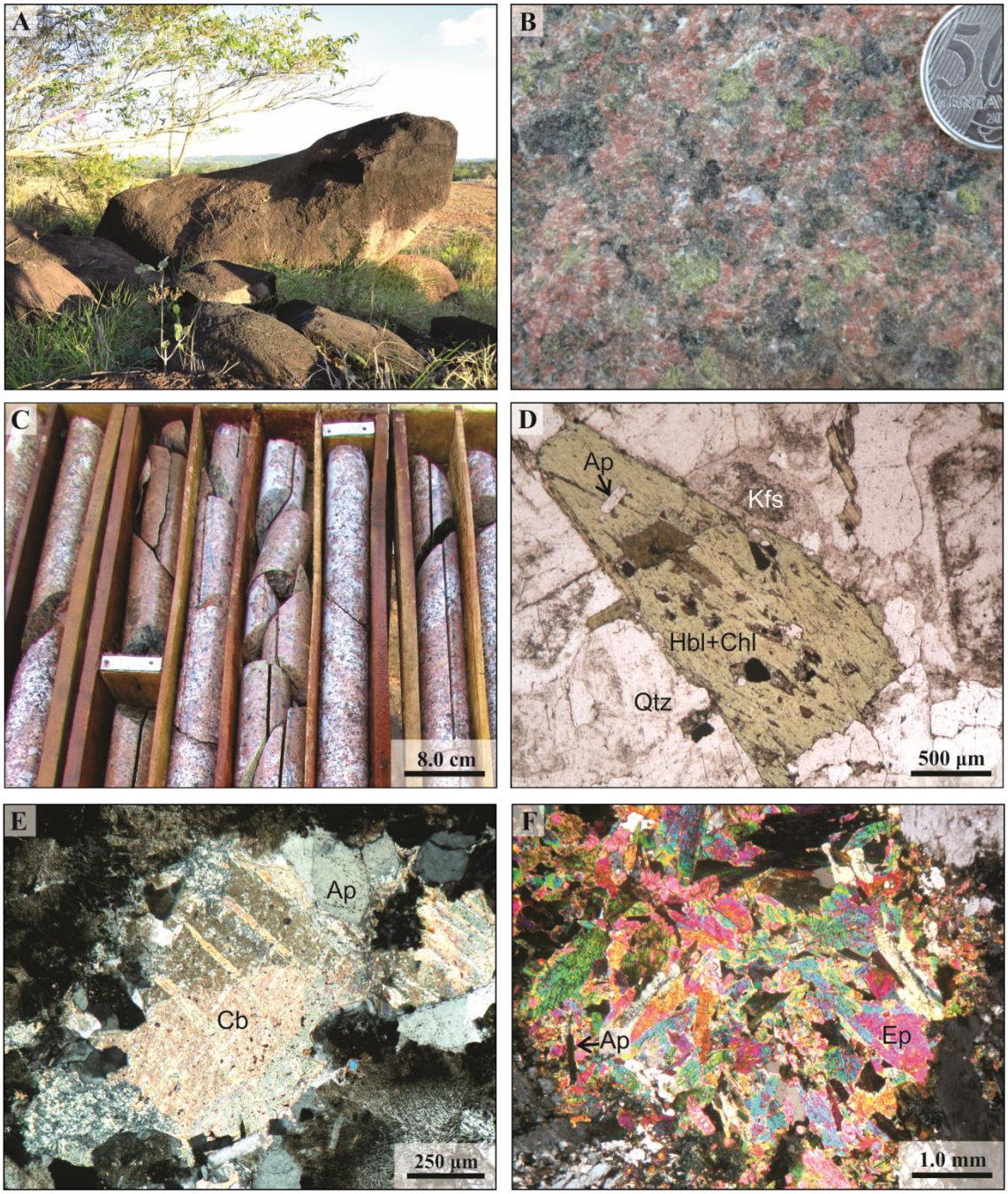

Figure 3.6 Photographs and photomicrographs of outcrops, textures and hydrothermal alteration of the Pé Quente deposit deposit. (a) Overview of a Pé Quente suite outcrop, within the hydrothermal zone. (b) Coarse-grained monzonite altered by potassic and propylitic alteration. Green epidote botches display spherulithic texture. (c) Drill core samples analysed for the unaltered host rock of the Pé Quente deposit. (d) Lamellar hornblende in unaltered monzonite of the Pé Quente suite. (e) Carbonate alteration in the Pé Quente suite. (f) Spirulithic growth as seen in (b), but under the microscope, showing radial clusters of propylitic alteration minerals, such as epidote, quartz, apatite and chlorite. Apatite is shown extinct. (d) Image in transmitted plane-polarised light, (e, f) images in transmitted cross-polarised light.

chlorite, (7) quartz + albite ± pyrite veinlets, (8) regional propylitic alteration with epidote + chlorite + tremolite + clinozoisite + apatite + rutile + pyrite ± titanite ± quartz ± calcite ± actinolite ± prehnite ± chalcopyrite mineral associations.

4.3.3 X1 deposit

The X1 deposit is hosted at two intrusions with distinct ages (Fig. 3.7): the (1) 1.90 Ga Guarantã granite, a medium to coarse-grained, equigranular to porphyritic biotite granodiorite (Fig. 3.8), and a (2) 1.78 Ga quartz-feldspar porphyry stock with tonalitic composition and cross-cut by mafic dykes (Fig. 3.7; Rodrigues, 2012; Assis, 2015). The Guarantã granite has a whole-rock T_{DM} age of 2.46 to 2.4 Ga and $\varepsilon_{Nd(t)}$ -1.7 to 1.39, while the quartz-feldspar porphyry has T_{DM} 2.12 to 2.18 Ga and $\varepsilon_{Nd(t)}$ -1.7 to 1.39, which indicates a Paleoproterozoic juvenile source with crustal contribution (Assis, 2015; Assis et al., 2017). At first, the Guarantã granite was thought to be part of the Matupá Intrusive Suite (~1.87 Ga; Rodrigues, 2012), but SHRIMP U-Pb zircon geochronology proved it to be older (at 1904 ± 4.6 Ma; Assis, 2015). Also, because there are xenoliths of the quartz-feldspar porphyry inside the granodiorite, these units were thought to be coeval (Rodrigues, 2012). However, given the imperative of geochronological data that points out that the quartz-feldspar porphyry is related to the Paranaíta Intrusive Suite (at 1.78 Ga), these xenoliths may indicate only a local process of magma mingling and assimilation.

Hydrothermal alteration in the X1 deposit occurs at the cupola of the 1.78 Ga porphyry stock and in the overprinting halo above it, in the surrounding 1.9 Ga biotite granodiorite (Rodrigues, 2012). Hydrothermal alteration consists of the following (Rodrigues, 2012; Assis et al., 2017): (1) strong pervasive potassic alteration with orthoclase ± hematite lying distally to the ore zones; (2) pervasive phyllic alteration zones with coarse-grained muscovite + quartz + pyrite either within the core of the granitic host or as alteration halos around quartz-rich veins, in both cases as 1- to 30-m-thick alteration zones; (3) pervasive propylitic alteration with chlorite + epidote + calcite ± apatite ± rutile ± hematite ± pyrite lying distally to the ore zones, (4) restricted pervasive chloritic alteration; (5) late-calcite-rich veinlets, with recognized bladed calcite.

The ore zone occurs in the phyllic alteration, associated with pyrite ± molybdenite ± chalcopyrite ± rutile ± hematite and quartz stockwork veins (Rodrigues,

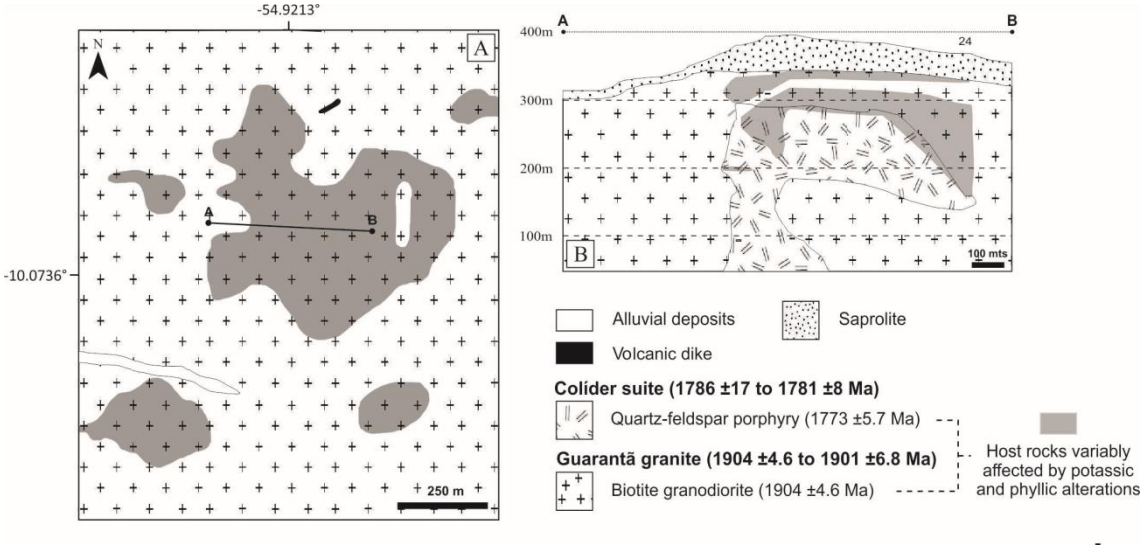

Figure 3.7 Geological map of the X1 deposit and interpreted A-B geological section (Ianhez, 2008; Rodrigues, 2012; Assis 2015; Assis et al., 2017).

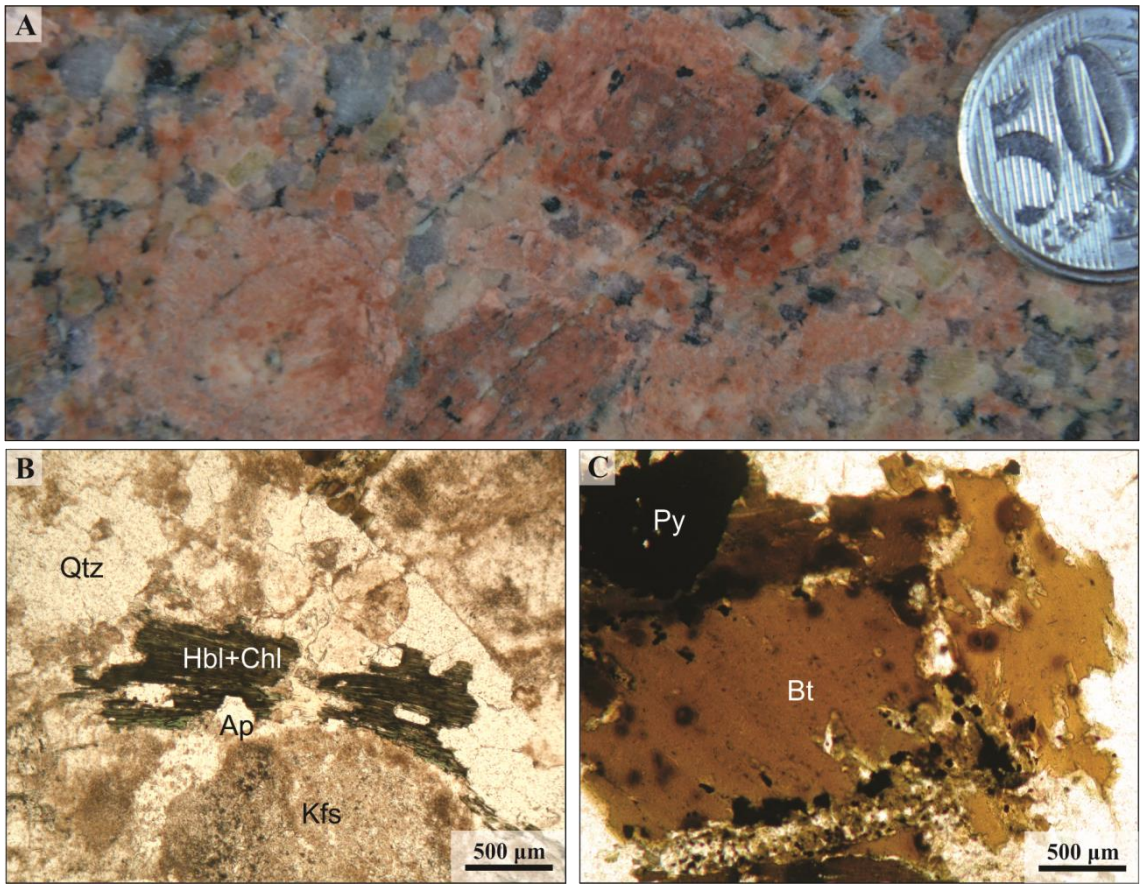

Figure 3.8 Photographs and photomicrographs of hand sample and textures of the X1 deposit. (a) Hornblende-biotite Guarantã granodiorite overprinted by chloritic and potassic alterations, with K-feldspar phenocrysts. (b) Fibrous chlorite-altered hornblende with inclusions of apatite. (c) Micaceous biotite with apatite inclusions in the Guarantã granodiorite. (b, c) Images in transmitted plane-polarised light.

2012; Assis, 2015). Gold (Ag 20-30 wt. %) occurs as small inclusions (<20-µm) in pyrite, associated with tsomoite (BiTe), hessite (Ag_2Te), galena, monazite, sphalerite and apatite (Rodrigues, 2012). Gold has an estimated grade of 0.5 to 10 g/t, and it

occurs disseminated in muscovite + quartz + pyrite alteration and in sulfide veinlets (Rodrigues, 2012).

4.3.4 Francisco deposit

Francisco is a polimetallic deposit (Au-Ag-Zn-Pb-Cu) with gold and ore minerals such as sphalerite + galena ± digenite ± chalcopyrite (Assis, 2011; Assis et al. 2012). The Francisco deposit is hosted at an epsiclastic sedimentary rock with volcanic contribution (Fig. 3.9), referred to as the *volcaniclastic unit* (Assis, 2011). Above the volcaniclastic unit, there is an arcosian arenite with graded bedding and flat laminae that does not have any contribution of volcanic sediments and that might be part of the mesoproterozoic Dardanelos formation (Assis et al. 2012). The volcaniclastic unit occurs right beneath the arcosian arenite, and it displays abundant iron oxides spread across the sediments. Iron oxides form aggregates of pristine, euhedral titanomagnetite (and martite) crystals, ranging in size from ~10 to ~40 mm. The volcaniclastic unit is divided into two sub-units (Assis et al. 2012): a feldspar-greywacke and a lithic arcosian volcaniclastic sandstone (Fig. 10a, b). Both subunits have graded bedding, centimeter-scale cross-beddings, and micrometer-scale magnetite-rich layers that intercalate with quartz-rich layers. Underneath it all, drill holes reveal a conglomerate of about 13 m in length that is classified as matrix-supported polymict sandy conglomerate (Assis et al. 2012). The volcaniclastic unit has a subvertical primary foliation (S_0), indicating at least one deformational event in the region. Given this context, the volcaniclastic unit is assumed to be part of the Colíder Group, as part of the Braço Norte Formation (Alves et al., 2019).

The volcaniclastic unit is intruded by the subvolcanic União do Norte porphyry (Fig. 3.10e, f; Assis, 2011; Assis et al. 2012) and underlaid by the União granodiorite. The União granodiorite is related to the Matupá Intrusive Suite, given its U-Pb zircon age at 1,853 ± 23 Ma and its I-type, calc-alkaline, high-K, and tonalitic to granodioritic composition (Fig. 3.10g, h; Miguel-Jr, 2011; Assis et al. 2012). The União do Norte porphyry is an epizonal stock of alkali-feldspar monzogranite, red-colored and isotropic, with porphyritic and micrographic texture, and a mineralogy that includes biotite, magnetite, fluorite, titanite, zircon, monazite and rutile. It is an A-type, high-K, Fe-rich, meta- to peraluminous granitoid, with U-Pb zircon age at 1,774 ± 4.5 Ma (Miguel-Jr, 2011; Assis et al., 2012; Alves et al., 2019). The União do Norte porphyry is related to

the Paranaíta Intrusive Suite and indicates a post-colisional, intraplate geodynamic setting (Duarte et al. 2019; Alves et al. 2019).

According to Assis (2011), hydrothermal alteration at the Francisco deposit consists of : (1) pervasive potassic alteration with orthoclase ± quartz ± hematite, (2) sericitic alteration, (3) argillic alteration with kaolinite, sericite ± hematite, (4) silicification, that might be intense and sulfide-bearing next to the ore zone and, distally, forms a silica cap with allunite, and (5) propylitic alteration that is disseminated or in veinlets that superposes previous alterations, with epidote + chlorite + actinolite ± magnetite (martite) ± pyrite ± carbonate ± quartz ± chalcopyrite. Barite veins also occur crosscutting the volcaniclastic unit (Fig. 3.10d).

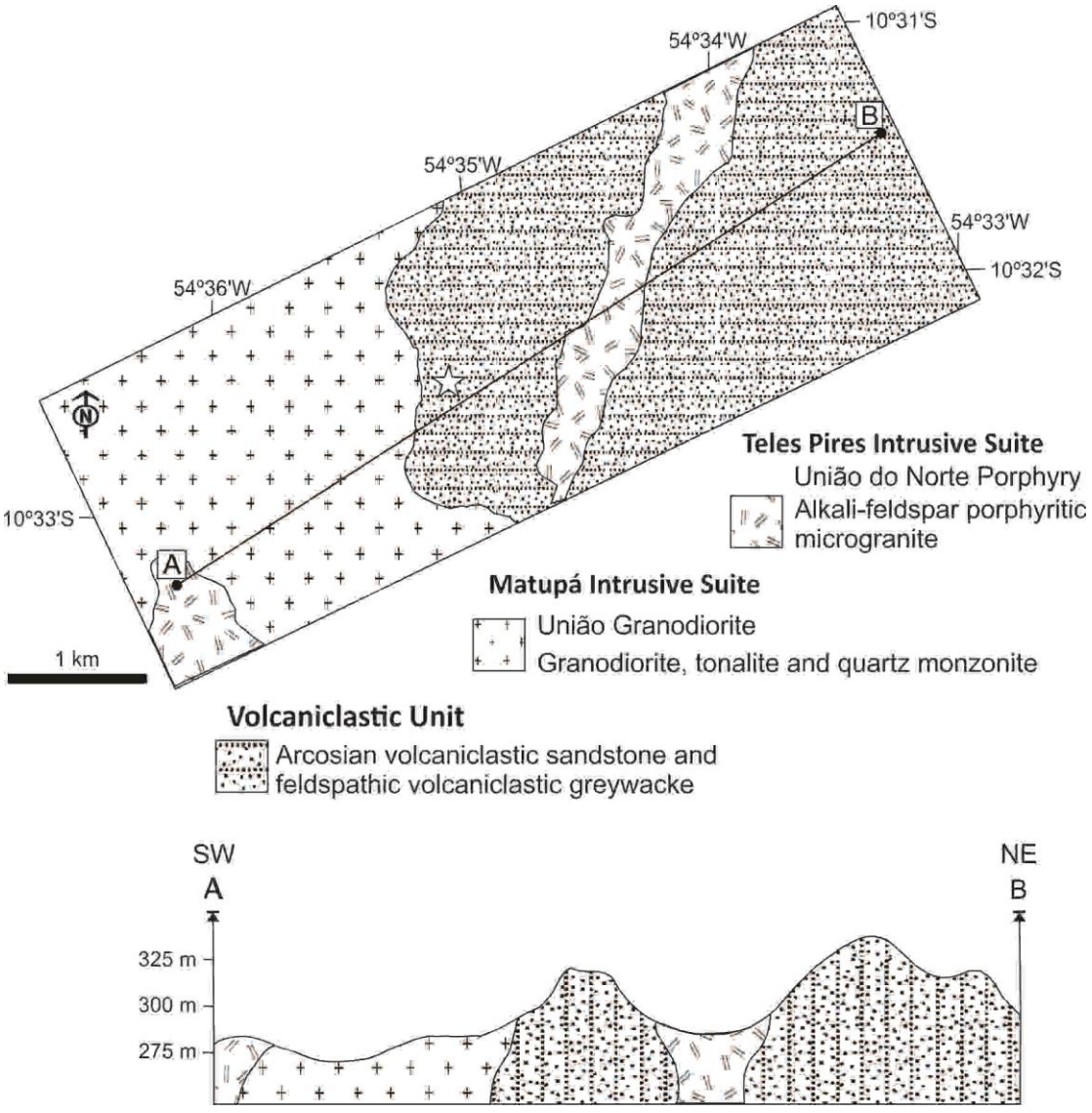

Figure 3.9 Geological map of the Francisco deposit and interpreted A-B geologic section (Assis, 2011; Assis, 2015; Assis et al., 2017).

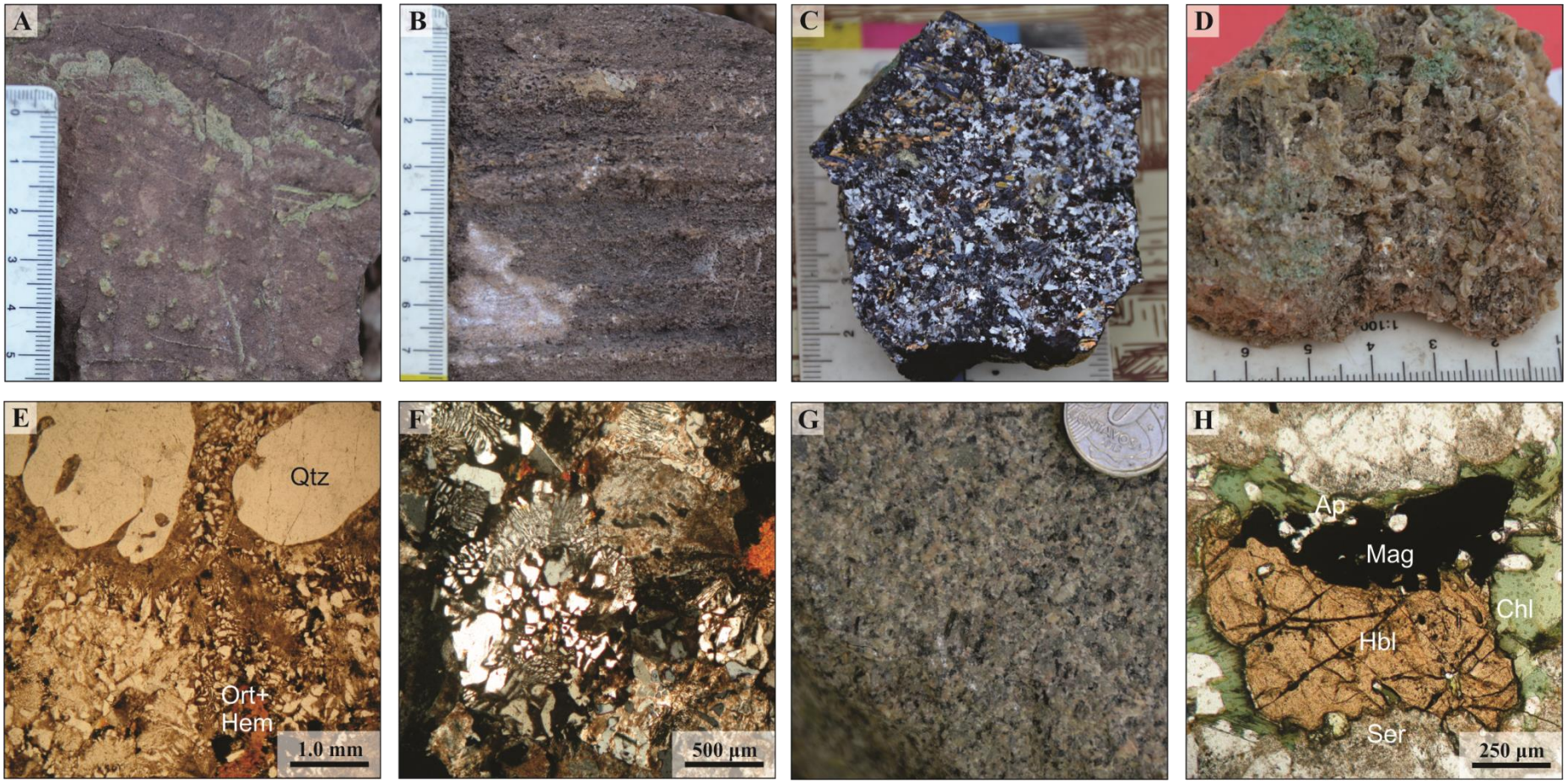

Figure 2.10 Photographs and photomicrographs of hand samples, ore minerals and textures of the Francisco deposit. (a) Arcosian volcaniclastic sandstone altered by propylitic alteration. (b) Unaltered arcosian volcaniclastic sandstone displaying plane-parallel lamination. (c) Galena from the Francisco deposit. (d) Barite sample with quartz and malachite, taken from a vein in the volcaniclastic unit. (e) União do Norte porphyry with porphyric texture and orthoclase + hematite in the matrix. (f) União do Norte porphyry displaying graphic texture. (g) Hand sample of the União granodiorite that occurs in the surroundings of the Francisco deposit as a host rock. (h) Hornblende and magnetite as part of the primary igneous assemblage of the União granodiorite. Chlorite occurs as a secondary mineral, altering hornblende. Apatite occurs as inclusions in magnetite. Images in (f, h) transmitted plane-polarised light, and (f) transmitted cross-polarised light.

The hydrothermal alteration zone is confined to the volcaniclastic unit, except for the propylitic alteration that regionally spreads to the intrusive rocks around it. The ore zone constitutes in sulfide-bearing quartz veins that have some centimetres in width, in textures such as stockwork, breccias, combs, spherulitic, and druses (face-controlled quartz textures; Assis, 2015). Phyllic alteration envelopes these veins and are relate to disseminated sulfides. These sulfides are represented by pyrite + sphalerite + galena + digenite + chacopyrite + hematite ± magnetite + bornite ± pyrrhotite ± monazite ± apatite ± greenockite (Assis, 2011; Assis et al. 2014). According to Assis et al. (2012, 2014), invisible gold (0.52-2,05 g/t) and silver (5,9-13,7 ppm) may be found included in pyrite, and massive galena and sphalerite may be aggregated in ore-rich zones (Fig. 3.10c). The mineralogy, boiling-associated textures and epizonal context, enables the Francisco deposit to be classified as an epithermal deposit of intermediate sulfidation (Assis et al., 2012).

4.3.5 Teles Pires Intrusive Suite

The Teles Pires intrusive suite comprises anorogenic plutonic batholiths and stocks associated to a post-colisional tectonic setting that occurs throughout both Alta Floresta and Tapajós mineral provinces. These plutonic bodies range from circular to ellipsoidal, elongated in the W-E to WNW-ESE direction (Moreton and Martins, 2005). They consist mostly of biotite syeno- to monzogranite, coloured from a brick-red/pink to a reddish-grey, that are isotropic, non-foliated, medium- to coarse-grained, equigranular to porphyritic. The Teles Pires intrusive suite is A-type, calc-alkaline, high-K and metaluminous. It has a U-Pb zircon age of 1,757 ± 16 Ma to 1,782 ± 17, whole-rock $T_{DM}(t)$ from 1.94 to 2.28 Ga and $\varepsilon_{Nd(t)}$ from -3.4 to + 3.0 (Santos et al., 2000). In our study, the Teles Pires Intrusive Suite was sampled and classified as a barren unit, since there are no descriptions of ore deposits hosted in this unit. Also, the anorogenic setting of the Teles Pires Intrusive Suite is incompatible with the types of mineral deposit that occur in the AFMP.

Figure 3.11 Photographs and photomicrographs of outcrops, hand samples and textural patterns of the Teles Pires granite. (a) Hornblende-biotite syonogranite with equigranular, isotropic and granular/rapakivi texture. (b) Outcrop showing Teles Pires granitic boulder. (c) Primary igneous assemblage altered by weathering and chlorite alteration (selectively in hornblende). (c) Image in transmitted plane-polarised light.

Chapter 4

Methods

4.1 Sample preparation

Most samples were collected in previous studies at the Alta Floresta mineral province (Assis, 2011; Assis, 2015). These samples were available as thin sections with thicknesses of 25-35-μm. Fieldwork was undertaken[4] to collect samples from the Luizão deposit, Francisco deposit and Teles Pires granite. For the Pé Quente and the X1 deposits, we examined and collected drill core samples granted by the Rio Novo Mining (currently merged into Aura Minerals). Collected samples were sub-divided into (a) hydrothermal zones: samples from intensely hydrothermally altered zones of the mineral deposit; (b) barren zones: samples from the unaltered or least altered host rocks; and (c) barren anorogenic Teles Pires Intrusive Suite. We collected 90 hand samples in the fieldwork and prepared 17 thin sections. Thin sections were made at a standard thickness (30-35-μm) at the Department of Petrology and Metallogeny of the São Paulo State University (Unesp) in Rio Claro, SP. Twelve representative thin sections were selected from the database. For the chemical analysis, thin sections were chosen only if they contained at least 5 grains of apatite or magnetite (Table 4.1). Each thin section contained about 5-11 apatite grains and 10-33 magnetite grains. Six thin sections were analysed for both apatite and magnetite grains, in which these minerals were mostly in close association with each other.

[4] Fieldwork occurred from 25 July 2018 to 29 July 2018. It had logistical support by the *Cooperativa dos Garimpeiros do Vale do Rio Peixoto* (Coogavape), localised in Peixoto de Azevedo (MT).

Table 4.1 Macroscopic and microscopic description of each sample.

Sample	Locality	Sampling / references	Sample description
B6	X1 deposit	Drill hole (this study)	Equigranular, isotropic, medium-grained biotite granodiorite. Acessory minerals include apatite and zircon. Weak propylitic alteration with chlorite-epidote-pyrite-sericite. Apatite occurs as 50- to 200-µm euhedral to subeuhedral crystals within or along biotite. Magnetite is scarce and fine-grained (<20-µm). Larger Fe-Ti oxides are mostly magnetite exsolved into ilmenite. Medium-grained pyrite is also present. No magnetite was analyzed by EMPA or LA-ICP-MS.
GT-2	Pé Quente host rock	Surface sample (this study)	Hornblende-biotite Guarantã tonalite. The rock is mostly fresh, with some sericitic and chloritic alteration. Chlorite-quartz veinlets with a few centimeters crosscut parts of the hand sample and thin section. Coarse-grained apatite (100-600-µm) occurs as euhedral hexagonal and elongated grains. Apatite is associated with hornblende, quartz, magnetite, and chlorite. It may occur included within or along biotite and hornblende rims. Magnetite occurs as euhedral to rounded crystals, 200-400-µm in size. Magnetite can be strongly altered to titanite ("sphenitization") along its rims. Magnetite also displays ghost-like vacant lamallaes whence ilmenite was chemically depleted. Titanite is anhedral, reddish-brown, and associated with chlorite and magnetite.
FD20-7	Pé Quente host rock	Drill hole (this study)	Guarantã biotite tonalite with incipient autometasomatism. Apatite crystals are euhedral to subeuhedral, 100-200-µm in size, and display hexagonal and rounded morphologies. Apatite occurs as inclusions within biotite, or along the borders and bays of biotite. Apatite is associated with zircon, chlorite, titanite and magnetite. Magnetite is subeuhedral to anheudral, about 200-300-µm in size. Smaller, rounded magnetite (~100-µm) is often associated with larger magnetite crystals. Magnetite is altered to titanite ("sphenitisation") in some cases, in an often cryptic texture. Titanite is abundant and occurs associated with magnetite along its rims. Titanite occurs as patches, fine disseminations, and irregular curvilinear stringers within magnetite.
RA73	Pé Quente host rock	Assis (2011)	Tonalite mildly altered by incipient autometasomatism, with localised replacement of hornblende by chlorite. Apatite is about 50-µm to 200-µm in size, and occurs included in plagioclase phenocrysts, within chlorite-altered hornblende, or along the intergranular boundaries. Apatite crystals are euhedral pristine prisms and hexagons. Few apatite crystals are subeuhedral and exhibit overgrowths. Magnetite is euhedral to subeuhedral, about 100-250-µm, and with varied shapes from cubic to subrounded forms. Magnetite is often pristine with small fractures, but it also has several inclusions (with <30-µm in size) of apatite, plagioclase, and quartz.

Table 4.1 (*Cont.)*

Sample	Locality	Sampling / references	Sample description
RA24	Pé Quente deposit	Assis (2011)	Biotite tonalite with sericitic and potassic alteration. Biotite is mostly altered to chlorite. Apatite occurs within or along chlorite. Apatite exhibit 50-200-µm in size, and a number of morphologies, such as prismatic and elongated. Subeuhedral apatite crystals display overgrowths and lobate borders. Apatite may have a distinct yellow color, instead of the common colorless aspect that it usually displays at transmitted light; and under CL, these apatite grains display a green luminescence. Apatite is usually associated with euhedral magnetite, and it may lie along magnetite crystals or within it as inclusions. Magnetite occurs as euhedral and rounded crystals that are usually clear and pristine, and that display sizes of 50- to 200-µm. Magnetite is constantly associated with chlorite, titanite and apatite.
RA69	Pé Quente deposit	Assis (2011)	Strongly altered Pé Quente tonalite overprinted with K-feldspar, phyllic and propylitic alteration. Apatite occurs associated with chlorite, sericite, carbonate, magnetite, and zircon. Apatite has variable morphologies and sizes (20-220-µm). Large apatite tabular crystals (>200-µm) are generally fractured, while smaller apatite is generally euhedral and forms clusters of hexagonal and elongated crystals, with a few overgrowths. Apatite may also occur in donut-shaped crystals, i.e. with holes in it (similar to the shapes described in Banfield and Eggleton, 1989). Magnetite is euhedral to subeuhedral, medium- to coarse-grained (100-200-µm), and is strongly altered. It displays abundant inclusions of apatite and zircon. Magnetite occurs with ghost-like curvilinear planes and ghost-like lamellae of Ilm(ss) still apparent along (111) planes.
SPQ1	Pé Quente deposit	Surface sample (this study)	Pervasive K-feldspar altered Pé Quente Suite overprinted by propylitic alteration (chlorite-epidote-quartz). Epidote is tabular and fibrous. Propylitic minerals may form clusters of elongated crystals. Apatite is associated with propylitic alteration minerals. Apatite has a number of morphologies, ranging from small hexagonal crystals (~50-µm) to large tabular and acicular crystals (~200-µm). Large tabular apatite generally displays corroded borders. Magnetite forms scarce clusters of small grains (<20-µm) that were not analyzed by EMPA and LA-ICP-MS.
BS07	Luizão deposit	This study	Inequigranular, anisotropic, medium-grained biotite syenogranite with pervasive propylitic alteration (chlorite-epidote-quartz-albite-carbonate-pyrite). Elongated medium-grained quartz. Apatite occurs in a number of morphologies ranging from small, anhedral, spherical crystals to large, fractured, tabular crystals. Magnetite was deemed too small (<20-µm) to be analyzed by EMPA and LA-ICP-MS.

Table 4.1 *(Cont.)*

Sample	Locality	Sampling / references	Sample description
PGD-01	Francisco host rock	Surface sample (this study)	Equigranular, isotropic, medium-grained hornblende-biotite granodiorite. Weak propylitic alteration with chlorite, epidote, sericite, titanite and barite. Abundant hornblende and biotite has been altered to chlorite. Apatite occurs as small, subeuhedral, and hexagonal crystals (50- to 100-µm) associated with magnetite or within chlorite-altered hornblende. Larger apatite crystals (>150-µm) are generally isolated and fractured. Magnetite occurs as medium to coarse crystals that may form large aggregates. Larger magnetite crystals may have apatite and quartz inclusions, and occur alongside subeuhedral to anhedral titanite. Titanite may occur as elongated crystals in clusters or filling fractures in magnetite.
VU20-4	Francisco host rock	Assis (2011)	Volcaniclastic lithic arkose that displays flat laminations of fine-grained quartz- feldspar intercalated with medium-grained quartz and feldspar grains. Iron oxide-rich beddings (1-1.5-cm thick) occur parallel to the lamination. Iron oxides consist of corroded magnetite mostly altered into hematite. Hematite retains the pseudomorphology of magnetite (i.e. martite). Iron oxides were evaluated by EMPA, whilst apatite was seldom found and thus was not analysed by EMPA or LA-ICP-MS.
PTO19	Francisco deposit	Assis (2011)	Chloritic alteration overprinting volcaniclastic lithic arkose. Sedimentary strata have less defined lamellae due to strongly pervasive and intergranular alteration. Chloritic alteration also includes epidote and sericite. Magnetite occurs as euhedral grains that are rounded or cubic, or as subeuhedral grains altered into chlorite and sericite. Magnetite may display internal fractures, corroded borders, and skeletal morphology, depending on the degree of alteration. Magnetite is generally <30-µm in size, and therefore, it was analyzed by EMPA and not by LA-ICP-MS. Apatite was not analyzed in neither, because it does not occur in this sample.
TP01	Teles Pires intrusive suite	Surface sample (this study)	Equigranular, isotropic hornblende-biotite syenogranite with apatite, zircon, titanite and magnetite as accessory phases. Chlorite and epidote occur as alteration products of hornblende and biotite. Reddish K-feldspar phenocryst mantled by plagioclase give the hand sample a rapakivi texture. Magnetite occurs as euhedral, cubic crystals of 150-250-µm in size, with apatite and plagioclase inclusions. Magnetite displays extensive exsolution of parallel- or sandwich- type lamellae. Apatite occurs very sparsely and is intergranular to other accessory minerals. Apatite occurs as euhedral crystals of 50-200-µm, with rounded and tabular shapes.

4.2 Petrographic analysis

Petrographic analysis aimed to identify and describe apatite and magnetite crystals, relate them to specific igneous and hydrothermal parageneses, and characterise mineral morphologies, associations and textures. Petrographic analysis relied on the following imaging methods:

Optical Microscopy. Transmitted and reflected light microscopies were performed in a ZEISS Axioskop 40 model coupled with a Canon PowerShot G5. Transmitted and reflected light were respectively used to identify and characterize apatite and magnetite. Samples of interest were marked with circles to be easily found in further steps.

Scanning Electron Microscopy (SEM). After optical microscopy, thin sections were carbon-coated for further analyses. SEM was performed with high contrast backscattered electron (BSE) imaging and fully integrated energy X-ray spectrometry (EDS). BSE allowed identifying textures, such as mineral zonation and exsolution patterns. EDS allowed for semi-quantitative chemical analyses of selected grains and recognition of mineral phases. SEM analyses were executed in a JEOL JSM-6010 LA, with an acceleration tension of 15 kV and a 10 mm focal distance. EDS was performed with a counting time of ~45 s.

Cathodoluminescence (CL) microscopy. Thin sections containing apatite were analysed through a hot cathode Lumic HC3-LM CL microscope (Fig. 4.1) with an acceleration tension of 7.7 kV and current at 0.2-0.4 mA. The electron bombardment of a hot cathode may affect the chemical composition of apatite through halogen diffusion. Therefore, CL imaging was performed after WDS measurements of the EMP and LA-ICP-MS analyses. Luminescence images were acquired in a coupled digital video-camera Kappa PS 40c-285 (DX) with an exposition time of about 100 ms.

Each of the abovementioned petrographic analyses were respectively performed at the Optical Microscopy, SEM and CL laboratories at the Department of Petrology and Metallogeny of Unesp, Rio Claro (SP).

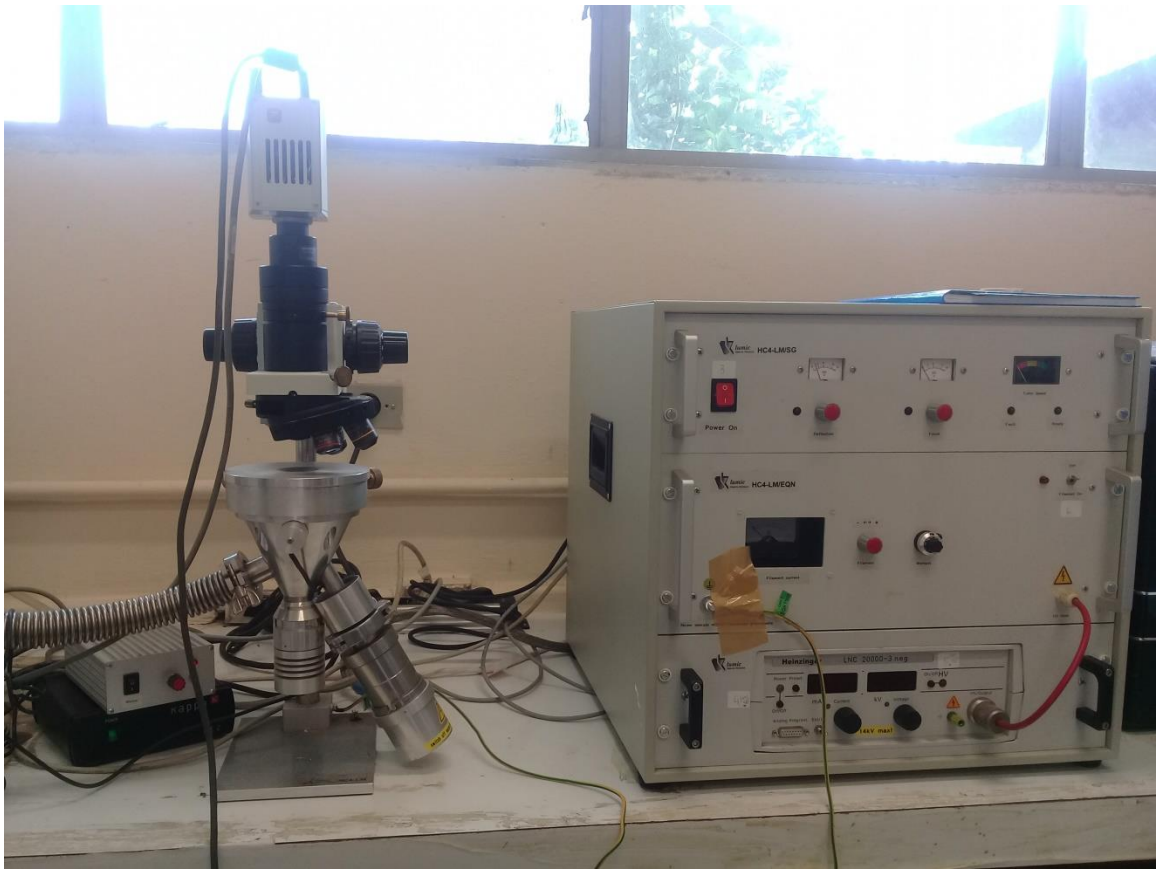

Figure 4.1 – Lumic HC3-LM cathodoluminescence microscope at Unesp, Rio Claro (SP).

4.3 Chemical analysis

4.3.1 EMPA

The electron microprobe analyses (EMPA) were conducted on a JEOL JXA-8230 electron microprobe (Figure 4.2) equipped with five wavelength dispersive X-ray spectrometers (WDS) and an energy dispersive X-ray spectrometer (EDS). The EMPA were performed in the EMPA laboratory at the Depart ment of Petrology and Metallogeny of Unesp, Rio Claro (SP). Samples were examined by BSE imaging for mineral inclusions or zonings. Grains with considerable amount of inclusions, fracturing, alteration, and chemical variation were excluded from further LA-ICP-MS analysis. A total of 129 apatite and 120 magnetite crystals were analysed by EMPA. Table 4.2 presents the detection limits (DL) for each element analysed by EMPA. EMPA compositions for apatite and magnetite are displayed in Appendices I and III, respectively.

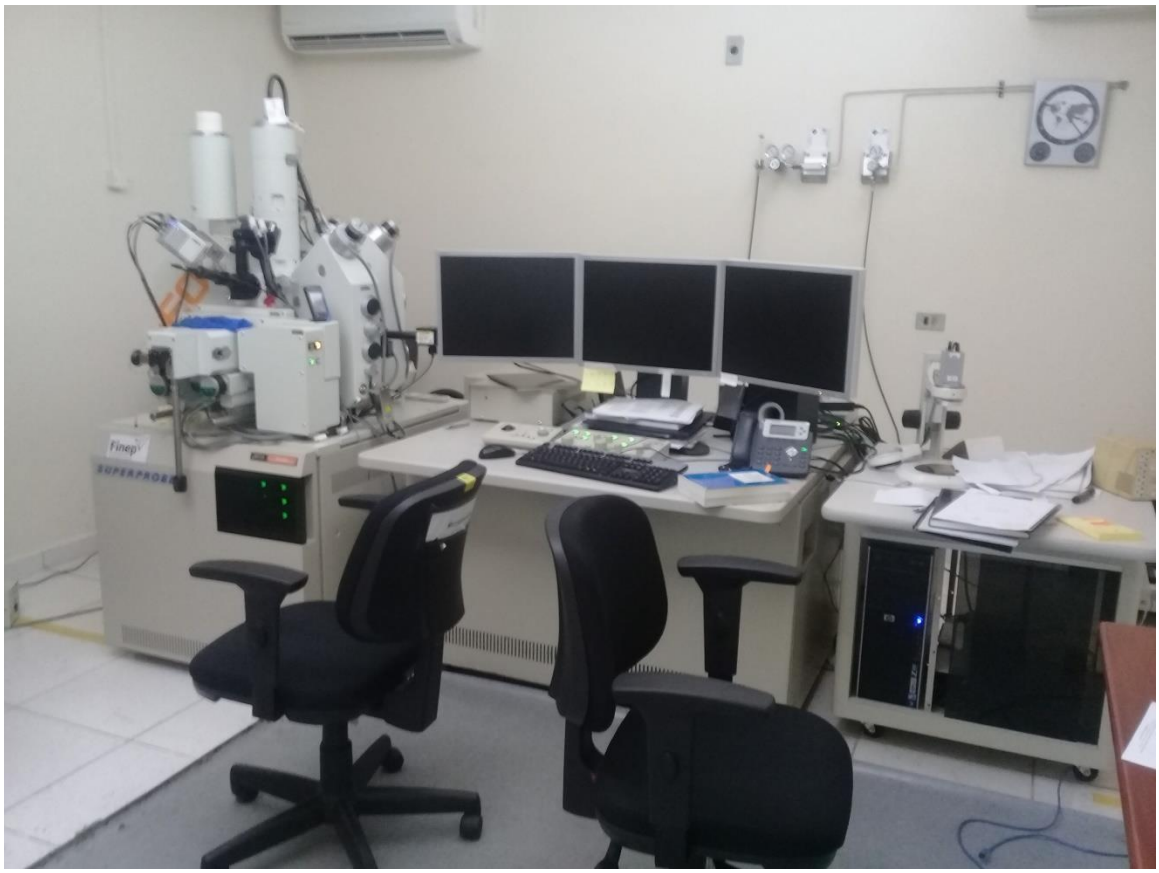

Figure 4.2 – JEOL JXA-8230 electron microprobe at Unesp, in Rio Claro (SP).

4.3.1.1 EPM operation conditions for apatite analyses

Apatite EMPA was performed using the wave dispersion mode with an acceleration voltage of 15 kV, a beam current of 10 nA, a peak counting time of 30 s, a background counting time of 15 s, and a wide beam diameter of 10- μm to avoid diffusion of volatile elements such as F, Cl and Na (Stormer et al., 1993). The following standards, X-rays lines and crystals were used: apatite, FKα, LDE1; albite, NaKα, TAP; orthoclase, SiKα, TAP; diopside, MgKα, TAP; apatite, PKα, PETL; sodalite, ClKα, PETL; wollastonite, CaKα, PETJ; ilmenite, FeKα, LIFH; rhodonite, MnKα, LIFH; apatite, CeLα, LIFH; apatite, LaLα, LIFH; apatite NdLα, LIFH.

Minimum detection limits are displayed in Table 4.2. The average precision (2s relative %) was 1 % for Ca, 1 % for P, 3 % for F, 73 % for Si, 25 % for Na, 15 % for Fe, 26 % for Cl, 31 % for Mn, 36 % for Mg, 14 % for Ce, 29 % for La, and 42 % for Nd. Several analyses for Si, Na, Mn, Mg, Ce, La and Nd have standard deviations that were

deemed too high (>30 %) to be reliable. These elements were then further analysed by LA-ICP-MS, which provided more reliable information.

Table 4.2 EMPA detection limits (DL), in ppm, for each element analysed in apatite and magnetite.

Apatite EMPA DL (in ppm)				Magnetite EMPA DL (in ppm)			
	Mean	Min	Max		Mean	Min	Max
F	660	633	704	Ca	158	140	204
Si	329	314	340	Al	153	144	195
Mg	115	108	120	Si	198	189	265
Na	142	136	146	Mg	136	123	161
Ca	331	305	351	Ca	248	234	260
P	294	265	331	K	199	165	210
Cl	66	63	69	Ti	268	213	281
Fe	217	211	229	Fe	478	375	506
Mn	213	203	229	Mn	314	264	332
Ce	605	587	622	Ni	369	319	407
La	532	495	560	Cr	308	245	330
Nd	552	481	642				

4.3.1.2 EMPA operation conditions for magnetite analyses

Magnetite EMPA was operated at an acceleration voltage of 15 kV, a beam current of 100 nA, and a beam diameter of 10-μm, which is wide enough to avoid overheating of magnetite, but sufficiently focused to avoid measuring visible inclusions or exsolution lamellae in magnetite. After the peak counting time of 20-40 s, the background counting was measured on both sides of the peak for 10 s in a flat region of the spectrum free of interfering element X-ray wavelengths. The following standards, X-rays lines and crystals were used: ilmenite, FeKα, LiFH; natural standard, CrKα, LiFH; synthetic standard, NiKα, LiFH; rhodonite, MnKα, LiFH; orthoclase, KKα, PET; ilmenite, TiKα, PETJ; wollastonite, CaKα, PETJ; orthoclase, SiKα, TAP; anorthite, AlKα, TAP; albite, NaKα, TAP; diopside, MgKα, TAP. The use of magnetite for Fe standard minimises the matrix correction.

Minimum detection limits are displayed in Table 4.2. The average precision (2s relative %) was 0.62 % for Fe, 4.5 % for Al, 13 % for Si, 19 % for Na, 27 % for Ca, 2 % for Ti, and 19 % for Mn. Average precisions for Mg (112 %), Cr (172 %), Ni (419 %)

and K (122 %) are deemed too high (>70 %) to be reliable. These elements were further analysed by LA-ICP-MS, which provided more reliable data.

4.3.2 LA-ICP-MS

Laser ablation inductively coupled plasma mass spectrometry (LA-ICP-MS) analysis were performed on a New Wave UP-213A/F laser ablation system coupled to a Thermo iCAP Q quadrupole ICP-MS. LA-ICP-MS analyses were carried out at the Chemistry and ICP Laboratory "NAP GeoAnalitica" in the Institute of Geosciences, University of São Paulo (USP). Calcium was chosen as the internal standard of apatite because (1) it is a major constituent in apatite, (2) it is homogeneously distributed in the ablation volume, and (3) its three isobaric (Ca_{42}, Ca_{43}, Ca_{44}) isotopes are in low abundance and do not interfere with each other. For similar reasons, Fe contents were used for internal standardisation in magnetite. Ca and Fe contents were previously determined by EMPA. Ablation spots were aimed right on (or close by) the same spots in which EMPA were previously performed. For cases in which this was not possible (e.g. sample BS-07), the internal standard adopted was the median element content (Ca or Fe) of the nearby analyses.

External standard calibrations for apatite and magnetite used silicate glasses NIST-610, BCR-2G and BHVO-2G as reference materials. The standards were repeated every 10 analysis of each analytical session. Before each analysis, a warm-up of 5 s was performed to avoid unstable laser energy. Data collection was recorded for a total of 120-170 s, including 30 s of background signal pre-ablation, 60 s during ablation, and a minimum of 30 s post-ablation to optimise ICP-MS sensitivity and avoid oxide formation. Detected limits were calculated by the following equation (Longerich et al., 1996):

$$Detection\ limit = \frac{3\ s\ background}{S}$$

where 3 s background is three times the standard deviation of the gas background signal before each ablation; and S is the sensitivity (counts s^{-1} per unit of concentration) normalised to the mass of sample ablated and determined from NIST glass per element and in each session.

Elements that were below the detection limits by both EMPA and LA-ICP-MS will not be discussed. Following on convention, element concentrations below the detection limits were considered to have half the value of the detection limits to enhance data availability for the discriminant analysis (Canil et al., 2016; Mao et al., 2016). LA-ICP-MS data for apatite and magnetite are displayed in Appendices II and IV, respectively. Data for LA-ICP-MS and EMPA were compared in Appendix V, and only the more reliable results for each were described.

Figure 4.3 – New Wave UP-213A/F laser ablation system (center-left) coupled to a Thermo iCAP Q quadrupole ICP-MS (left) at the Institute of Geosciences, University of São Paulo (USP).

4.3.2.1 LA-ICP-MS operation conditions for apatite analysis

Apatite grains were analysed with a laser spot diameter of 25-30-μm, a pulse rate of 2-5 Hz, and measured fluence ranging from 1.4 to 2.8 J.cm^{-2}. A total of 32 trace elements were analysed by LA-ICP-MS that included B, Sc, V, Ga, Ge, As, Rb, Sr, Y, Zr, Nb, Ba, La, Ce, Pr, Nd, Sm, Eu, Gd, Tb, Dy, Ho, Er, Tm, Yb, Lu, Hf, Ta, Pb, Th, and U.

Accuracy and precision were monitored over time by repeated analysis of the reference materials, with laser spot diameter of 25-30 μm. Precision (2σ) is between 5

and 10% for Ge, Dy and Yb; between 10 and 20% for Sr, Pr, Sm and Gd; between 20 and 30% for Mg and Y; between 30 and 46% for Mn, Ti, La and Nd, and <5% for the remaining elements. Although Fe and Ce had poor precisions (136 % and 89 % respectively), they were also evaluated by EMPA, which supplied complementary data. Table 4.4 displays the detection limits and experimental precision for the reference materials, and Table 4.4 exhibits these results for the entire apatite database.

4.3.2.2 LA-ICP-MS operation conditions for magnetite analysis

Magnetite grains were analysed with a laser spot diameter of 25-μm, a pulse rate of 2-5 Hz, and a measured fluence ranging from 1.4 to 2.8 Jcm^{-2}. We avoided inclusions or ilmenite exsolution lamallae during ablation. If there was nm-length sandwich-type zoning beneath the laser beam diameter as detected in the SEM, the laser beam was large enough to homogenise and integrate those chemical variations onto a wholesome titanomagnetite composition. A total of 19 trace elements were analysed by LA-ICP-MS that included Mg, Al, Si, Ca, Sc, Ti, V, Mn, Cr, Co, Ni, Cu, Zn, Ga, Nb, Mo, Sn, Ta, and W.

Accuracy and precision were monitored over time by repeated analysis of the reference materials, with laser spot diameter of 25-30-μm. Elements such as Na, Mg, Al, P, Ti, V, Mn and Zn had a poor median precision (<5%) and were only evaluated if the correspondent EMPA data was available. Precision was <5% for the remaining elements. Detection limits were typically <106 ppm for P; <45 ppm for Mg; <30 ppm for Na and K; <10 ppm for Ti, Zn and Cd, and <5 ppm for the remaining elements. Table 4.5 displays the detection limits and experimental precision for the reference materials, and Table 4.6 exhibits these results for the entire magnetite database.

Table 4.3 Apatite LA-ICP-MS quality control of external calibration using certified reference materials, with detection limits (DL) and standard errors (SE) for each analyte.

		NIST-610		BCR-2G		BHVO-2G				
Element	Isotope	Mean	SE	Mean	SE	Mean	SE	DL, min	DL, median	DL, max
B	11	359.4	102.5	9.7	3.7	9.4	4.0	2.3	6.1	257.2
Sc	45	441.8	28.7	30.4	2.5	31.4	2.7	0.3	0.6	18.9
V	51	442.5	27.4	398.2	30.9	328.0	27.1	0.3	0.6	18.9
Ga	69	438.0	31.6	32.5	2.2	25.6	2.5	0.1	0.3	10.9
Ge	70	427.0	30.4	5.8	1.2	4.9	1.1	0.9	2.1	42.4
As	75	317.0	43.9	0.0	1.0	2.5	1.4	1.0	2.6	65.5
Rb	85	431.6	33.6	44.0	4.7	10.2	1.4	0.2	0.4	15.5
Sr	88	499.6	33.5	326.7	25.5	390.1	37.8	0.0	0.2	7.4
Y	89	451.7	31.0	31.7	2.7	24.8	2.6	0.1	0.1	11.9
Zr	90	441.8	31.3	170.8	12.8	165.0	18.6	0.1	0.3	8.6
Nb	93	421.3	33.5	10.6	1.0	16.7	2.4	0.1	0.2	5.0
Ba	135	425.8	40.2	564.8	59.8	125.6	15.7	1.2	2.6	96.9
La	139	459.7	33.3	24.5	2.4	16.1	2.6	0.1	0.2	12.2
Ce	140	448.8	36.0	47.8	3.7	38.2	5.8	0.1	0.2	20.2
Pr	141	431.1	33.7	6.2	0.5	5.7	0.9	0.1	0.2	6.9
Nd	145	431.9	38.5	29.9	4.8	27.4	4.0	1.0	2.4	69.4
Sm	147	451.5	33.8	6.9	1.3	6.9	1.4	0.5	1.4	45.5
Eu	151	463.7	35.4	1.9	0.4	2.4	0.5	0.2	0.4	15.2
Gd	157	421.9	34.5	5.8	1.1	5.6	1.2	0.4	1.3	39.1
Tb	159	446.7	32.9	1.0	0.2	1.0	0.3	0.1	0.2	8.5
Dy	163	427.4	33.0	5.6	1.0	5.7	1.1	0.5	0.9	32.6
Ho	165	451.4	31.7	1.2	0.2	1.0	0.3	0.1	0.2	7.9
Er	166	429.0	31.9	3.0	0.6	2.4	0.5	0.2	0.6	23.8
Tm	169	422.1	30.1	0.5	0.1	0.4	0.1	0.1	0.2	6.3

Table 4.3 *(Cont.)*

		NIST-610		BCR-2G		BHVO-2G				
Element	Isotope	Mean	SE	Mean	SE	Mean	SE	DL, min	DL, median	DL, max
Yb	173	464.3	37.0	3.5	1.0	2.3	0.9	0.6	1.5	47.8
Lu	175	436.6	30.8	0.6	0.2	0.3	0.2	0.1	0.2	10.4
Hf	179	420.4	39.7	4.5	1.2	5.0	1.4	0.8	1.6	85.9
Ta	181	377.3	27.0	0.5	0.2	1.0	0.2	0.1	0.2	8.3
Pb	208	412.6	35.3	9.4	1.5	1.6	0.4	0.2	0.6	20.2
Th	232	451.4	33.4	5.4	0.7	1.3	0.2	0.1	0.1	4.8
U	238	456.9	30.2	1.5	0.2	0.5	0.1	0.1	0.1	2.1

Table 4.4 Detection limits (DL) and standard errors (SE) for each analyte in apatite LA-ICP-MS results.

Element	Isotope	DL, min	DL, median	DL, max	SE, min	SE, median	SE, max
B	11	2.28	6.08	257.18	1.28	3.59	116.03
Mg	24	0.645	1.72	54.3	3.01	27.435	18779
Sc	45	0.33	0.639	18.89	0.2	0.375	8.73
Ti	48	0.293	0.546	14.88	28.14	42.93	12458.6
V	51	0.324	0.642	18.91	0.25	0.745	63.1
Mn	55	0.938	1.89	39.89	16.08	39.225	731.42
Fe	57	29.68	64.26	1784.46	33.91	136.685	37381.8
Ga	69	0.112	0.33	10.93	0.1	0.19	16.54
Ge	70	0.921	2.09	42.41	1.2	5.4	23.52
As	75	0.955	2.55	65.5	1.27	2.66	112.75
Rb	85	0.208	0.428	15.46	0.13	0.3	22.15
Sr	88	0.0488	0.151	7.37	0.76	16.53	156.82
Y	89	0.0515	0.1255	11.91	2.64	29.79	252.49
Zr	90	0.079	0.287	8.56	0.11	0.365	27.3
Nb	93	0.0721	0.1585	5.01	0.032	0.091	105.25
Ba	135	1.15	2.63	96.9	0.94	2.405	141.7
La	139	0.0526	0.212	12.17	0.41	31.045	351.69
Ce	140	0.0927	0.227	20.19	0.38	89.46	767.44
Pr	141	0.0703	0.2035	6.88	0.18	11.01	85.88
Nd	145	1.01	2.445	69.38	1.49	46.23	306.94
Sm	147	0.534	1.44	45.54	0.85	12.475	72.85
Eu	151	0.156	0.418	15.22	0.28	1.69	12.51
Gd	157	0.446	1.25	39.14	0.78	11.55	72.54
Tb	159	0.092	0.206	8.53	0.19	1.545	8.01
Dy	163	0.476	0.9005	32.61	1.26	7.57	75.26
Ho	165	0.0717	0.2135	7.91	0.33	1.605	11.85
Er	166	0.234	0.621	23.76	0.85	4.49	33.35
Tm	169	0.0646	0.202	6.34	0.15	0.795	4.07
Yb	173	0.556	1.46	47.81	1.02	5.09	37.23
Lu	175	0.0735	0.225	10.39	0.22	0.675	4.19
Hf	179	0.751	1.62	85.88	0.45	0.905	26.57
Ta	181	0.0788	0.221	8.27	0.057	0.115	7.54
Pb	208	0.203	0.564	20.17	0.49	1.025	13.39
Th	232	0.0556	0.1005	4.84	0.14	0.995	32.85
U	238	0.0753	0.1033	2.08	0.14	0.76	9.97

Table 4.5 Magnetite LA-ICP-MS results or quality control of external calibration using certified reference materials, with detection limits (DL) and standard errors (SE) for each analyte.

		NIST-610		BCR-2G		BHVO-2G				
Element	Isotope	Mean	SE	Mean	SE	Mean	SE	DL, min	DL, median	DL, max
Li	7	524.1	196.3	10.7	4.1	5.5	2.1	0.7	1.2	3.1
Sc	45	470.6	164.7	36.1	12.7	32.1	9.6	0.5	0.9	1.7
V	51	473.8	172.7	491.8	185.7	333.4	107.9	0.5	0.8	1.8
Cr	52	436.3	160.6	18.5	7.8	300.4	98.4	3.4	5.7	12.5
Mn	55	465.4	167.5	1,766.1	661.3	1,253.4	379.3	1.1	2.1	4.4
Co	59	436.9	161.7	46.5	18.1	49.0	15.2	0.1	0.2	0.6
Ni	60	480.7	179.6	14.2	5.7	131.7	43.4	0.6	1.3	3.3
Cu	65	459.3	160.4	22.3	7.7	127.8	42.4	0.6	1.5	4.3
Zn	66	488.4	175.9	183.3	66.1	129.9	41.4	3.7	5.9	12.3
Ga	71	468.5	169.0	26.0	9.4	23.9	7.7	0.2	0.4	1.0
As	75	342.2	135.6	3.0	1.8	0.0	1.4	1.8	3.2	5.9
Se	77	126.1	83.5	0.0	12.0	16.8	12.3	9.7	19.3	55.2
Rb	85	461.1	159.8	59.5	19.8	10.5	3.3	0.3	0.6	1.5
Sr	88	532.1	184.8	382.2	128.0	384.7	120.3	0.1	0.2	0.4
Y	89	479.2	159.5	38.1	12.0	23.6	6.8	0.1	0.2	0.3
Zr	90	472.4	167.7	208.4	72.0	163.9	51.6	0.1	0.3	1.1
Nb	93	449.9	157.2	13.1	4.5	16.4	4.9	0.1	0.2	0.5
Mo	95	402.3	140.8	285.1	100.5	4.3	1.4	0.6	1.5	4.1
Cd	111	277.1	104.6	0.0	3.3	0.0	3.1	3.0	6.6	14.9
Sn	118	423.5	150.4	5.0	1.8	3.8	1.5	1.5	2.5	5.8

Table 4.6 Detection limits (DL) and standard errors (SE) for each analyte in magnetite LA-ICP-MS results.

Element	Isotope	DL, min	DL, median	DL, max	SE, min	SE, median	SE, max
Li	7	0.662	1.24	3.13	0.44	0.7	4.62
Na	23	14.37	25.37	48.04	11.02	372.88	15039.58
Mg	25	23.24	42.23	93.5	15.36	81.24	1770.51
Al	27	13.87	19.28	40.22	18.77	359.42	2196.84
P	31	46.77	106.8	269.14	33.32	104.45	27457.67
K	39	14.46	28.86	51.81	9.9	42.81	619.59
Sc	45	0.486	0.863	1.67	0.27	0.47	3.71
Ti	49	3.93	7.71	17.58	8.5	240.04	15064.38
V	51	0.546	0.78	1.75	40.22	223.18	751.45
Cr	52	3.42	5.74	12.51	2.61	22.66	575.31
Mn	55	1.06	2.08	4.41	34.91	217.09	2408.31
Co	59	0.116	0.233	0.614	1.25	3.42	18.34
Ni	60	0.577	1.34	3.3	0.84	4.37	48.02
Cu	65	0.649	1.52	4.3	0.51	0.88	73.93
Zn	66	3.73	5.9	12.3	18.52	150.08	1607.85
Ga	71	0.178	0.3905	0.95	0.97	4.58	33.13
As	75	1.79	3.24	5.89	0.84	1.34	2.04
Se	77	9.7	19.28	55.24	4.98	8.695	22.83
Rb	85	0.302	0.552	1.49	0.19	0.32	4.16
Sr	88	0.0871	0.211	0.415	0.11	0.88	15.82
Y	89	0.0771	0.1685	0.332	0.049	0.29	29.51
Zr	90	0.133	0.329	1.14	0.14	0.61	12.37
Nb	93	0.101	0.197	0.455	0.049	0.12	21.97
Mo	95	0.641	1.48	4.06	0.38	0.82	8.36
Cd	111	3.03	6.595	14.94	1.67	2.81	5.27
Sn	118	1.45	2.5	5.76	0.93	4.06	36.66
Cs	133	0.13	0.255	0.714	0.071	0.12	0.59
Ba	137	1.03	2.085	4.47	0.62	2.79	15.73
La	139	0.147	0.289	0.765	0.11	0.44	13.97
Ce	140	0.129	0.266	0.925	0.11	0.47	19.37
Pr	141	0.0828	0.258	0.492	0.071	0.17	2.4
Nd	143	0.783	2.115	4.3	0.63	1.31	13.53
Sm	147	0.927	1.88	3.51	0.45	0.94	4.63
Eu	151	0.172	0.5935	1.2	0.14	0.25	0.43
Gd	157	0.549	1.61	3.23	0.35	0.82	3.57
Tb	159	0.127	0.265	0.587	0.07	0.13	0.96
Dy	161	0.651	1.555	2.66	0.36	0.75	7.02
Ho	165	0.105	0.298	0.628	0.081	0.15	1.19
Er	166	0.347	0.868	1.81	0.24	0.44	2.88
Tm	169	0.145	0.3	0.682	0.07	0.14	1.01
Yb	172	0.702	1.42	2.59	0.32	0.67	4.29
Lu	175	0.14	0.3215	1.06	0.076	0.15	0.5

Element	Isotope	DL, min	DL, median	DL, max	SE, min	SE, median	SE, max
Hf	178	0.404	1.065	2.36	0.31	0.5	1.07
Ta	181	0.0952	0.294	0.781	0.072	0.13	0.66
W	182	0.712	1.57	4.1	0.41	0.73	33.05
Pb	206	0.945	1.63	3.9	0.3	1.11	201.74
Th	232	0.173	0.192	0.223	0.032	0.115	2.89
U	238	0.116	0.241	0.404	0.034	0.245	4.87

4.4 Statistical methods

4.4.1 R language

We performed all our statistical analysis using R. R is a high-level language and software environment for statistics, data analysis, data mining and graphics. There are several open-sourced integrated development environments (IDEs) available, from which we chose the RStudio. R users can create their own *packages*, specifically developed for statistical techniques and graphical interfaces. Those packages are archived and organised by the R packaging system, and made available for public sharing in systematic repositories, such as the Comprehensive R Archive Network (CRAN) and Github. For our statistical analysis, we used the packages *MASS*, *ggplot2*, *GCDkit* and *compositions*. For more information on statistical learning and R language structure, see Crawley (2007), James et al. (2013), and Janoušek et al. (2016).

4.4.2 Discriminant analysis

Discriminant analysis is a statistical method that creates a classification rule that best separates the data and best predicts whether a sample belongs to one group rather than the other. Discriminant analysis is used at any task that requires large datasets to be classified into smaller groups. It has application in many disciplines, such as geology, biology, medicine and finance. Each discipline refers to discrimination by synonyms such as “classification” (in the life sciences), “supervised learning” (in machine learning) and “pattern recognition” (in artificial intelligence). In mineral exploration, discriminant analysis is used to separate alteration zones, to reveal the link between a given indicator mineral and its genesis in a mineral system, and to estimate whether a given target is fertile. Examples of this applied technique include Canil et al. (2016), Mao et al. (2016), and Pisiak et al. (2017).

Linear Discriminant Analysis (LDA) explicitly maximizes the difference between classes within a multivariate dataset. If classes are as far apart as possible relative to their spread, it is possible to define a hyperplane between them that best separates the data. This particular hyperplane will be the one with the greatest ratio of the difference between the specific means and the standard deviations. A hyperplane reduces the dimensionality of a sample space to one dimension by projecting the data onto a line. The resulting linear discriminator works as a threshold function that obeys a classification rule. This rule decides in which class to put each sample.

The blind spot of LDA is that it does not directly shows which parameters are responsible for the discrimination result. Thus, LDA does not provide the weights of the variables that classify the samples. This blind spot, on the other hand, is covered by Principal Component Analysis (PCA). PCA is an unsupervised learning technique that explicitly shows which parameters are changing over each class. PCA finds which trace elements vary the most within the entire range of mineral compositions, and which the directions of maximum variance are. Even though LDA performs supervised learning and depends on an *a priori* classification that labels each sample to a class, PCA does not depend on such classification. PCA just states how each independent component varies within a Gaussian curve that treats the entire dataset as a whole. Therefore, LDA efficiently divides the sample space into classes, while PCA finds which parameters vary the most.

Chapter 5

Petrography of apatite and magnetite

5.1 Luizão deposit

In the Luizão deposit, 9 thin sections were analysed, from which only one had a considerable amount of apatite crystals (B-07 sample) — that is described as the Novo Mundo granitoid overprinted by propylitic and phyllic alteration (Table 4.1). Apatite was not found in the unaltered Novo Mundo granite, but in other studies (e.g., Paes de Barros, 2007), it was described as part of the primary igneous assemblage.

Apatite grains are subeuhedral, tabular, prismatic, often fractured, and with irregular rims that render it a "messy" texture (Fig. 5.1a, b). Apatite occurs mainly related to the phyllic alteration, associated with sericite, chlorite, quartz and pyrite assembled together as anastomosing chlorite-sericite patches (5.1a, b, c). Apatite that occurs within chlorite-sericite patches are often more euhedral and much larger (>100-µm, figs. 5.1a, b, b, d) than apatite that occurs as independent crystals (<80-µm, figs. 5.1e, f) in the quartz-feldspathic groundmass. A few apatite grains are pristine and exhibit overgrowths (Fig. 5.1e), while others are fractured and crosscut by propylitic-related micro-veinlets (Fig. 5.1f). Propylitic alteration overprints the phyllic alteration as micro-veinlets and as intergranular fillings of chlorite, epidote and carbonate.

Under CL, apatite from the Luizão deposit displays a distinct violet-purple luminescence, which is not seen elsewhere. Luminescence colours vary from pink to purple with changes in light deflection (5.2a, b). Violet-luminescent apatite is closely associated with the phyllic alteration and tends to be subeuhedral, tabular, prismatic, often fractured and with irregular borders (5.2a, b, c, d). Complex CL textural patterns occur especially in apatite grains associated with the propylitic alteration. These apatite grains tend to display bright violet-luminescent rims and dull purple-luminescent cores (Fig. 5.2e). Some apatite grains display ambiguous CL textural pattern, in which there are yellow-luminescent apatite at the rims and dark blue blotches at the crystal cores (Fig. 5.2f), with no evidences of violet-luminescent apatite.

Magnetite was not found in the Luizão deposit, except for <20-µm grains that were too small to be analysed on EPMA or LA-ICP-MS. Although these magnetite grains are too small, they exhibit alteration textures, as they are closely associated to the

chlorite-sericite alteration, often as cloudy-anheudral botches. Instead of magnetite, phyllic alteration assemblage contains pyrite.

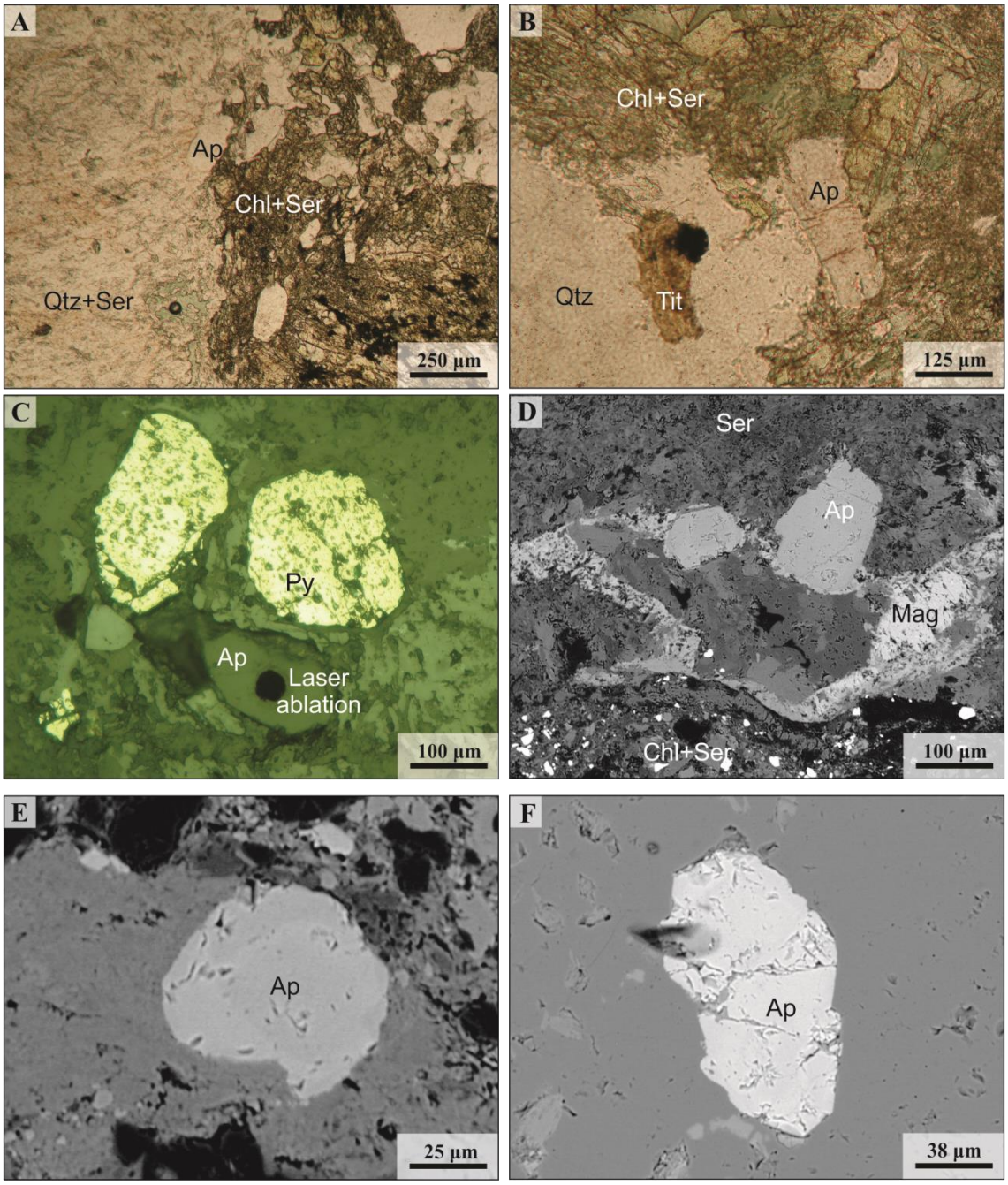

Figure 5.1 – Thin section microphotographs illustrating textures and morphologies of apatite in the Luizão deposit: (a) Hipidiomorphic apatite associated with chlorite-sericite-quartz-epidote alteration; (b) Euhedral, tabular apatite associated with chlorite-sericite-epidote, next to a magnetite altering to titanite; (c) Apatite closely associated with pyrite, chlorite, and sericite. (d) Apatite associated with chlorite-sericite-magnetite. (e) Subrounded apatite grains with quartz, plagioclase, chlorite and sericite. (f) Fractured apatite included within quartz vein. (a-b) Transmitted light, (c) reflected light and (d-f) BSE images.

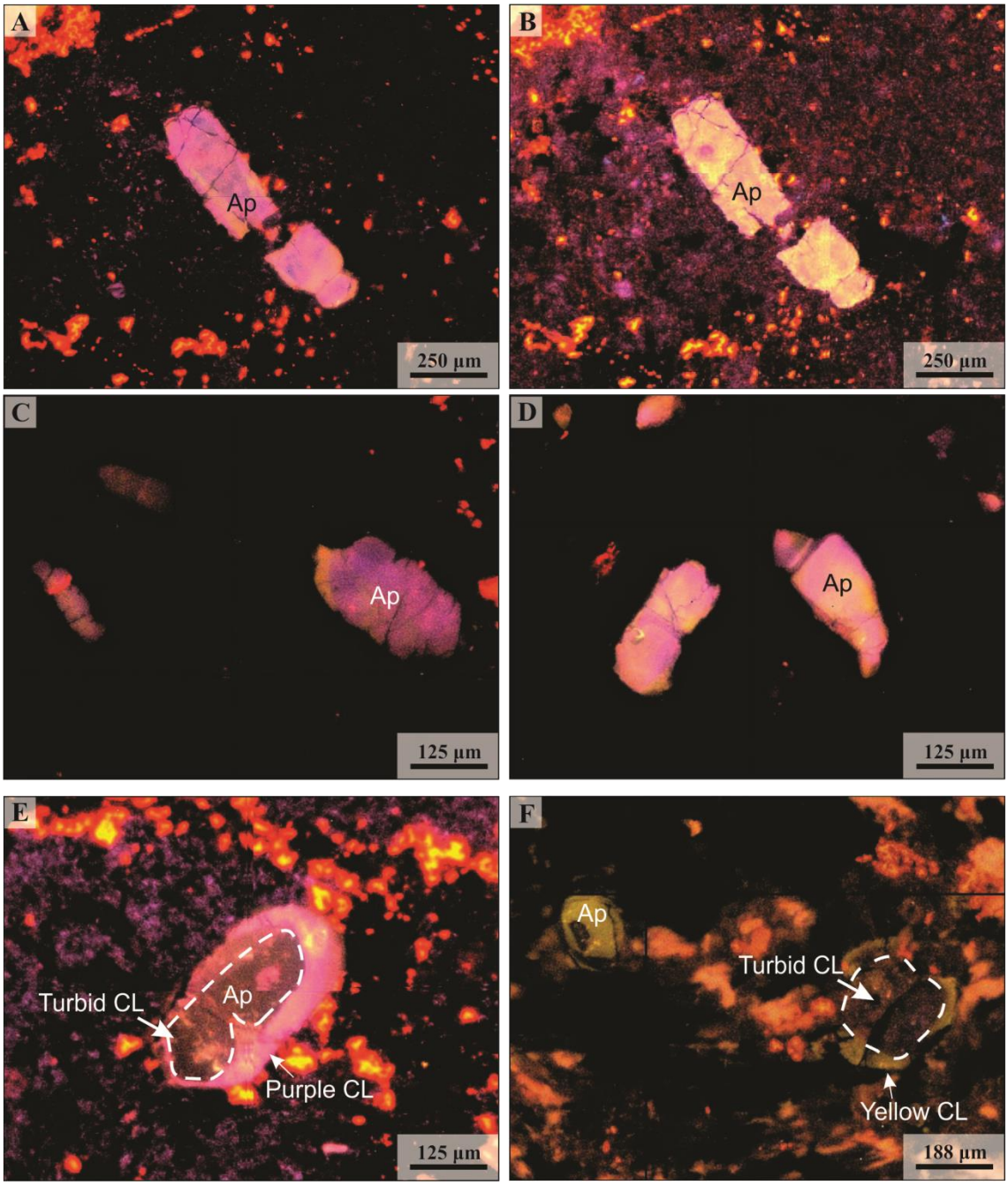

Figure 5.2 – Cathodoluminescence images of apatite in the Luizão deposit. (a-b) Apatite is fractured and displays bright, lavender-luminescent rims. Light deflection changes CL colours from a violet-purple in (a) to a lavender-magenta in (b). (c) Larger apatite grain has contrasting zones of purple-bluish and fuchsia luminescence. Purple-bluish zone is more clear and pristine than fuchsia zone. Smaller apatite grains are homogeneous. (d) Apatite with violet luminescence and rims that display concentric growth zones of purple-bluish luminescence. (e) Apatite displays wine-bluish core and bright violet-luminescent rims, and occurs amongst propylitic assemblage with red-luminescent carbonate. (f) Yellow-luminescent apatites with dull glow and bluish core, related to propylitic alteration and orange luminescent carbonate.

5.2 Pé Quente deposit

Three apatite types were recognized in the Pé Quente deposit, according to their morphology, texture, luminescence and mineral association.

Type 1. Apatite with barren host rocks. Apatite in the unaltered host tonalite of the Pé Quente deposit typically occurs as part of the primary igneous assemblage. Apatite grains are 100-200-µm, associated with magnetite, titanite and zircon, and occur as inclusions in hornblende (Fig. 5.3a, b, c). Hornblende is generally unaltered or slightly altered into chlorite by incipient alteration. Apatite may also occur as small inclusions (<50 um) within magnetite, plagioclase, K-feldspar and biotite. Apatite is typically euhedral to subeuhedral with a wide range of morphologies, such as prismatic, tabular, hexagonal, ovoid, C-shaped, and long tapering prismatic crystals. Apatite is homogeneous at transmitted light and BSE (Fig. 5.3c, d, e), and may display more complex textural patterns under CL (Figs. 5.3f, h). Type 1 apatite grains generally display a yellow-green-luminescence, though they may display turbid, brown-orange-luminescent crystal cores (Fig. 5.3f, g). Clear, bright yellow-luminescent apatite tends to occur at the rims and alongside fractures of turbid apatite grains. Smaller apatite tends to be entirely clear and yellow-luminescent. Bright yellow-luminescent apatite may be overgrown by pale-green-luminescent apatite at its rims (Fig. 5.3h).

Type 2. Apatite with phyllic alteration. Apatite that occurs with phyllic alteration is euhedral to subeuhedral, and 100-200-µm in size. Phyllic alteration is pervasive, extensive and contains sericite, quartz, chlorite, pyrite, and coarse-grained muscovite. Apatite occurs as prismatic, tabular and ovoid crystals that have irregular, corroded and etched borders (Fig. 5.4a, b, c). Some of these phyllic-related apatite grains are broken-down in smaller fragments (<20-µm) that are dispersed in the phyllic alteration (Fig. 5.4d); while others are anhedral to subeuhedral, with etched and irregular rims and corroded crystal cores (Fig. 5.4 c, e). Phyllic-related apatite can be tentatively distinguished from igneous-related apatite under CL. Phyllic-altered apatite tends to have a bright green luminescence, with blended patches of blue and grey luminescent crystal cores (Fig. 5.4c, d, e, f). Finer apatite grains are usually clear and brightly green-luminescent, whereas larger apatite grains display more complex CL textural patterns, with bluish-luminescent patches (Fig. 5.4c, d). Clear, brightly green-luminescent apatite occurs alongside rims and fractures as overgrowths in larger, turbid apatite grains. Green-luminescent apatites may display inner cores of grey to blue-luminescent

concentric zonings (Fig. 5.4e). A few apatite grains are completely turned blue to dark grey (Fig. 5.4f). These blue-luminescent apatites may also be discriminated by their dull glow and cloudy aspect.

Type 3. Apatite with propylitic alteration. Propylitic alteration occurs at the core of the mineral deposit, and as distal outer halos affecting the host rock. In the Pé Quente deposit, propylitic alteration overprints intensely K-feldspar altered rocks. It occurs as veinlets, or in interstitially pervasive style. Propylitic-related apatite may occur as (1) small tabular, hexagonal and ovoid crystals (Fig. 5.5a, b) and as (2) large elongated, acicular and tapering prismatic crystals (Fig. 5.5c, d, e). Apatite is part of the accessory phase with magnetite and zircon (Fig. 5.5b), and part of the propylitic assemblage with epidote, chlorite, carbonate and pyrite (Fig. 5.5e). Apatite may have been altered beforehand by potassic alteration, but the textural evidence for this would be the close association of apatite and magnetite (Fig. 5.5b; in sample RA69)[5]. Type 3 apatite is often pristine and displays a distinctly dull, grey luminescence (Fig. 5.5d, g, h). It may occur as torus-shaped crystals with a complete central hole in it (Figs. 5.5c, e, g) or with a partial central depression in a C-like shape and may be scalenohedral (Fig. 5.5c, h). In contrast to those long prismatic crystals, small apatite grains usually have subeuhedral morphologies, such as tabular, hexagonal and ovoid (Fig. 4.5g, h). Other propylitic-related minerals, such as epidote, quartz and chlorite, may also display acicular and elongated habits that amass together as clusters of radial crystals in spherulithic growth.

[5] Magnetite in sample RA69 is interpreted to be part of the potassic alteration (Section 7.2.5).

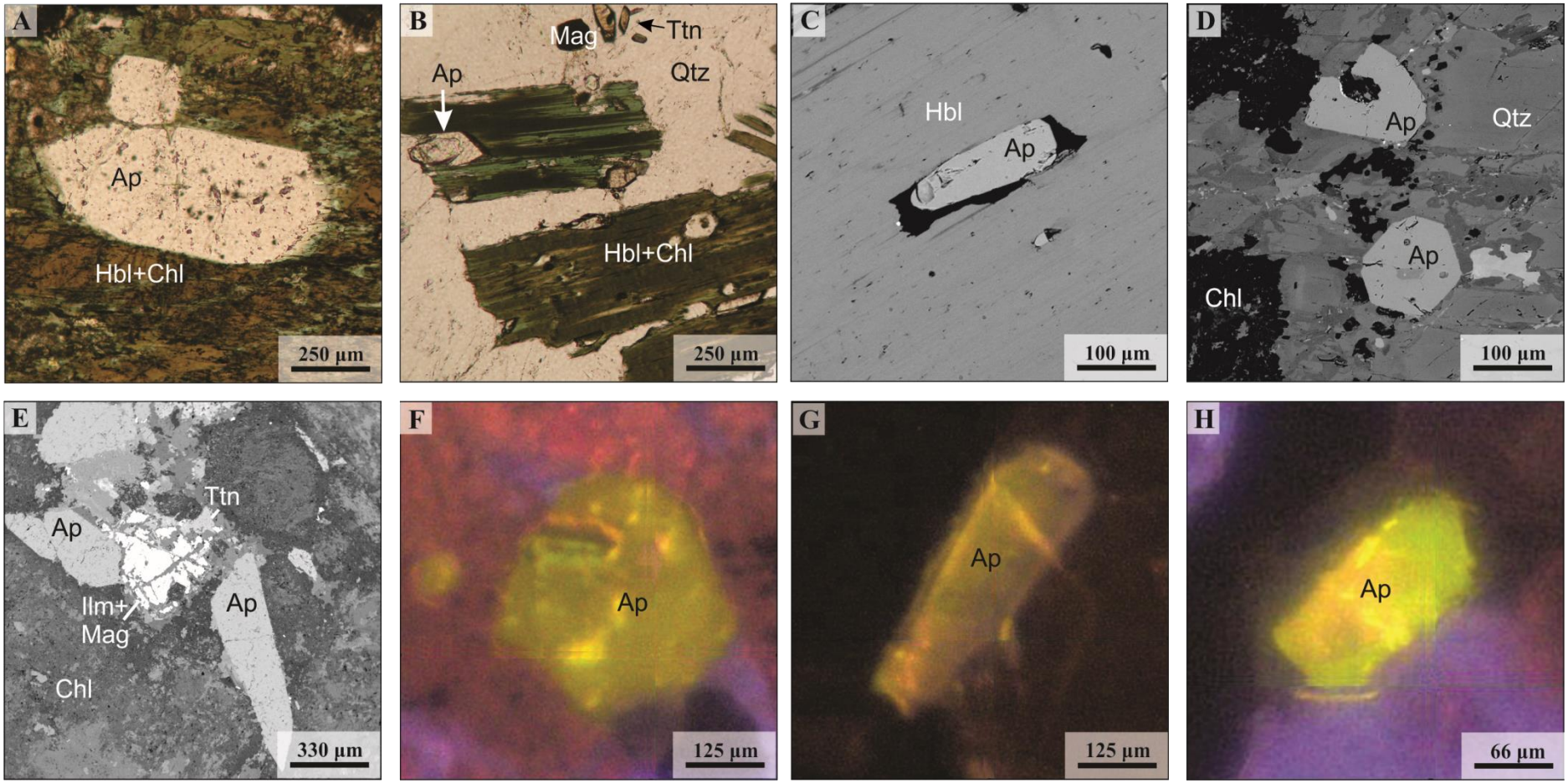

Figure 5.3 – Thin section microphotographs illustrating textures and morphologies apatite in barren rocks (type 1) in the Pé Quente deposit. (a) Euhedral and prismatic apatite crystals included within chlorite-altered hornblende. (b) Subeuhedral apatite crystals included within chlorite-altered hornblende. (c) Prismatic apatite included within hornblende. (d) Hexagonal apatite and "C"-shaped apatite. (e) Tapering long-prismatic apatite crystals amongst exsolved magnetite and titanite. (f) Euhedral hexagonal apatite with an overall dull yellow-brown luminescence and a few bright yellow-luminescent spots. (g) Prismatic yellow-brown-luminescent apatite with a dull glow replaced by a bright yellow luminescence at the rims and alongside fractures. (h) Yellow-green-luminescent apatite crystals showing clear green-luminescent zones and turbid yellow-luminescent zones. (a-b) Images in transmitted plane-polarised light, (c-e) BSE images, and (f-h) CL images.

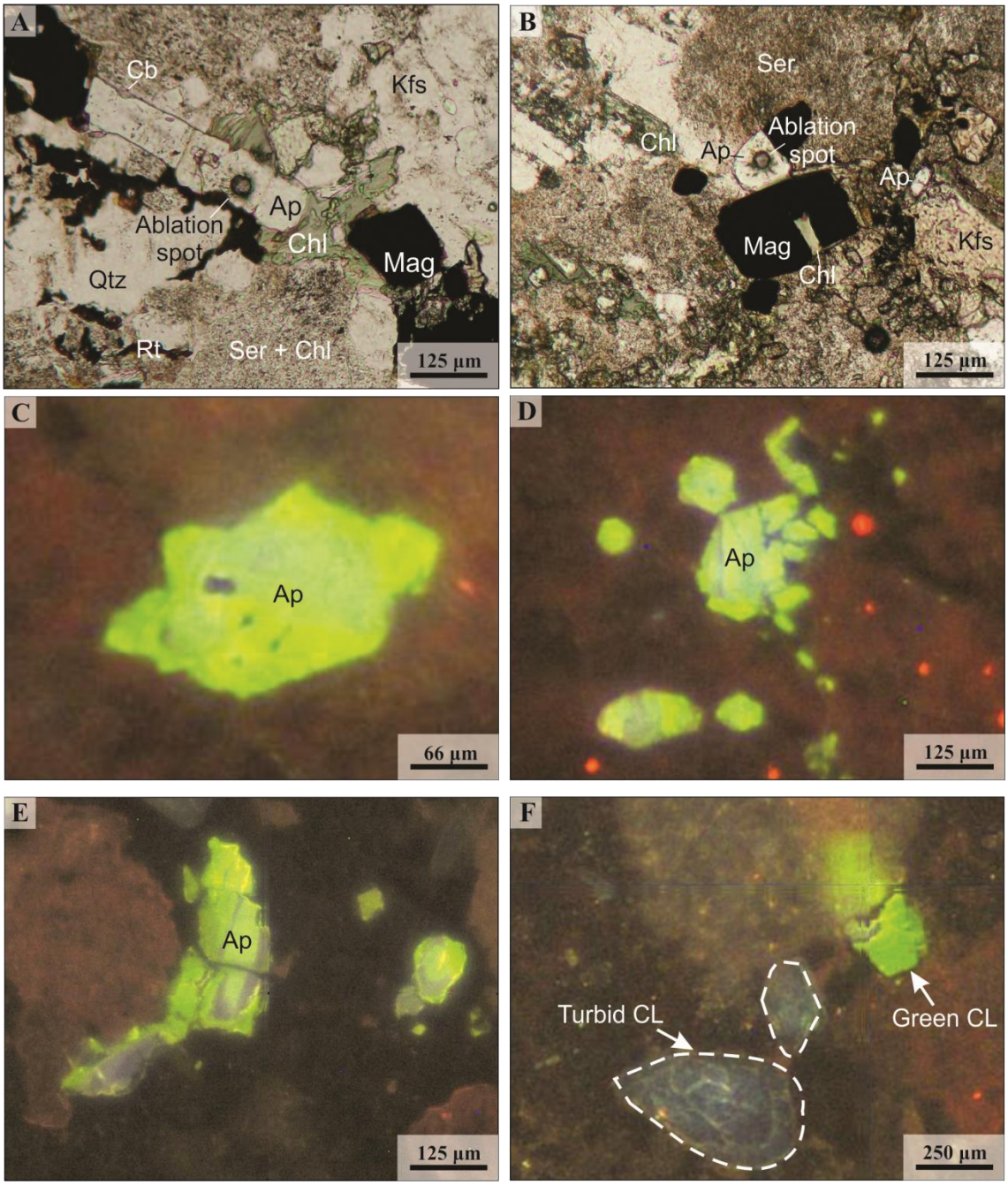

Figure 5.4 – Thin section microphotographs illustrating textures and morphologies of phyllic-altered apatite (type 2) in the Pé Quente deposit. (a) Long-tabular apatite associated with magnetite, rutile, Fe-bearing carbonate, and sericite-chlorite alteration. (b) Subeuhedral apatite associated with magnetite and phyllic alteration. (c) Green-luminescent apatite with dissolution features and pristine overgrowths at the crystal rims, while turbid grey-bluish-luminescent apatite occurs at the crystal core. (d) Broken-down green-luminescent apatite with grey-bluish-luminescent patches mainly at the crystal cores. (e) Dull green-luminescent apatite with a few bright green-luminescent overgrowths, and dull blue-luminescent concentric cores. (f) Fractured green-luminescent apatite with concentrically blue-luminescent apatite at the crystal core. A few apatite grains are completely blue-luminescent and turbid, with a dull glow. (a-b) Images in transmitted plane-polarised light and (c-f) CL images. LA: Laser ablation spot.

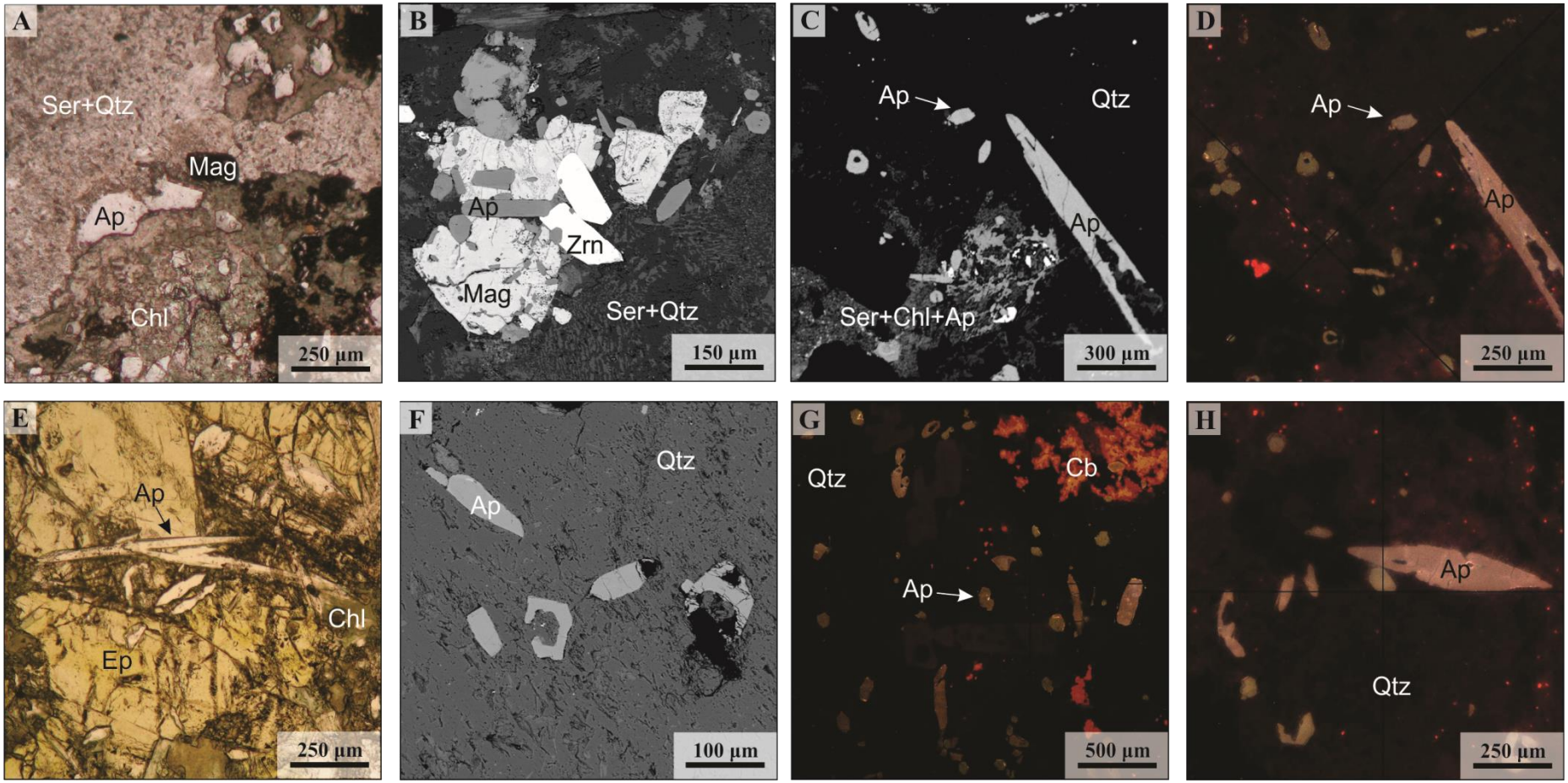

Figure 5.5 – Thin section microphotographs illustrating textures and morphologies of propylitic-altered apatite (type 3) in the Pé Quente deposit. (a) Apatite with irregular borders amongst carbonate, sericite, magnetite, quartz and chlorite-altered hornblende. (b) Euhedral prismatic apatite closely associated to magnetite and zircon. (c) Long tapering prismatic apatite, small prismatic apatite and torus-shaped apatite associated with propylitic assemblage. (d) Same image as (c), but under CL microscopy. Apatite displays a dull grey-luminescence and clear, homogeneous texture. (e) Acicular apatite crystals amongst propylitic assemblage. (f) Subeuhedral prismatic apatite and "C"-shaped apatite. (g) Subeuhedral, tabular grey-luminescent apatite and fine-grained, ovoid apatite amongst carbonate alteration. (h) Long grey-luminescent apatite with scalenohedral habit and smaller subeuhedral apatite grains. (a, e) Images in transmitted plane-polarised light, (b, c, f) BSE images, and (d, g, h) CL images.

Magnetite does not offer a CL response, but may be classified according to its morphology, texture and mineral assemblage when analysed at both reflected light microscopy and BSE imaging. Magnetite types in the Pé Quente deposit are threefold:

Type 1. Magnetite in barren host rocks. It is associated to the primary igneous assemblage, which contains hornblende, biotite, zircon and apatite (Fig. 5.6a, c, d). Magnetite is euhedral to subeuhedral and about 100-200-µm in size. It is often cubic, with inclusions of chlorite and apatite. Some grains display overgrowths, fractures and form clusters of smaller, rounded <50-um grains (Fig. 5.6b, e, f). Other grains are rhombohedric and pristine, which might indicate martitisation (pseudomorphic alteration into hematite).

Type 2. Magnetite in transitional zones. It occurs in the biotite tonalite that is affected by incipient chloritic alteration. Igneous primary assemblage is mostly unaltered, except for magnetite. Magnetite is 200-500-µm, subrounded, subeuhedral to anhedral, and displays skeletal texture, i.e. ghost-like vacant lamellae wherein ilmenite was chemically depleted (Fig. 5.7a, b, c). Magnetite is often exsolved into titanite and ilmenite, as trellis-type exsolution lamellae with an ülvospinel component (Fig. 5.7d). Titanite occurs as subeuhedral to anhedral crystals along skeletal magnetite rims.

Type 3. Magnetite with potassic alteration. Most magnetite grains are cubic, fractured, with 50-200-µm in size, and with several mineral inclusions of apatite, plagioclase and chlorite (Fig. 5.8b, d). It often displays sandwich-type exsolution lamellae (Fig. 5.8c). Larger magnetite grains generally occur surrounded by clusters of <50-µm magnetite blobs.

Type 4. Magnetite with phyllic alteration. It occurs as subeuhedral, cubic, hexagonal and subrounded grains, with 50- to 100- µm in size. It is generally associated with the primary igneous assemblage, particularly apatite. Type 3 magnetite is often pristine and with few inclusions, but it may also display a skeletal texture (Fig. 5.8a).

Types 1 and 2 magnetite occur in the same samples that type 1 apatite occurs. Type 4 magnetite occurs in the same phillically altered samples that type 2 apatite occurs. Potassically altered magnetite (type 3) occurs in the same sample (RA-69) that propylitically altered apatite (type 3) occurs, but each mineral seems to be selectively altered by different hydrothermal processes.

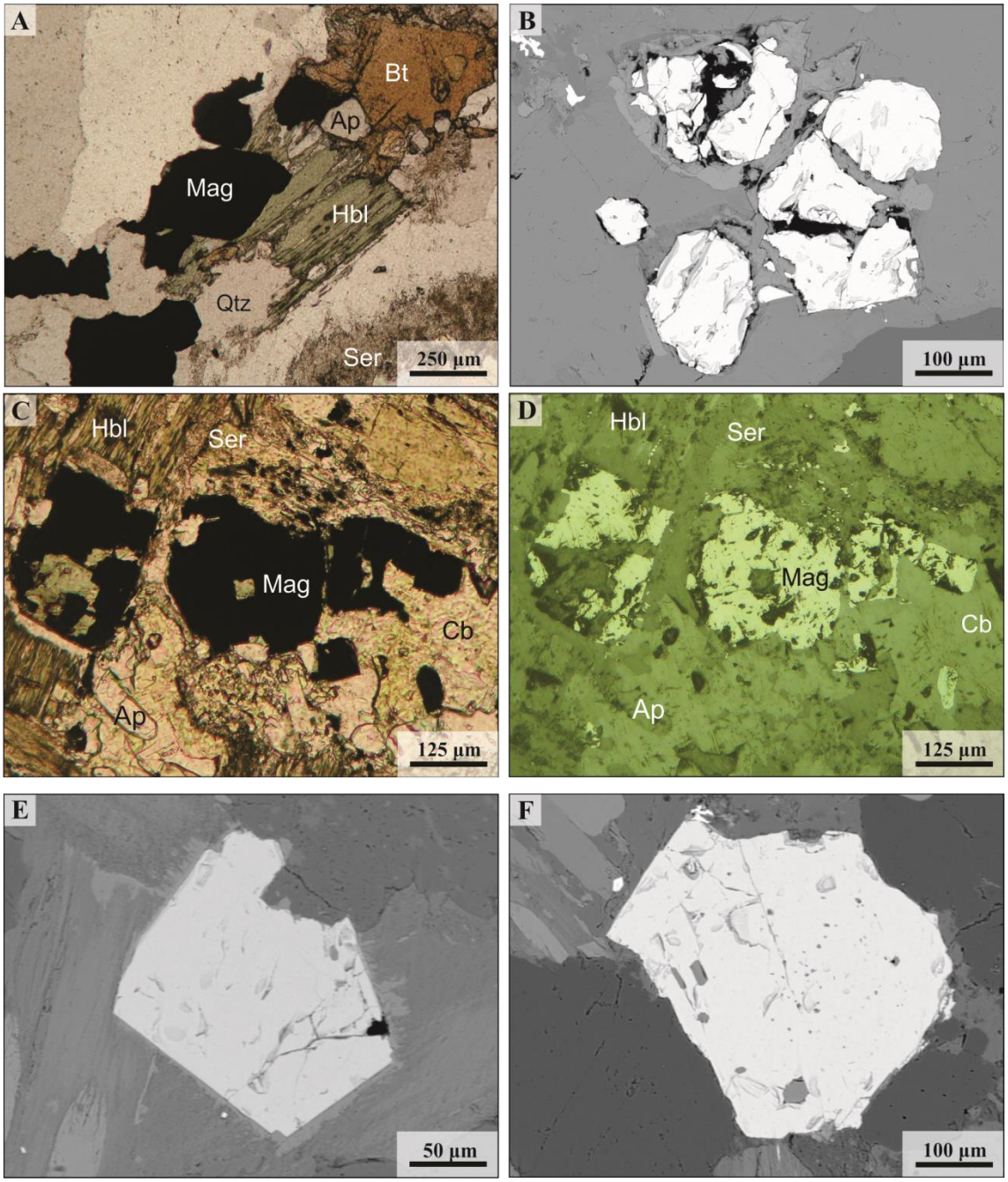

Figure 5.6 – Thin section microphotographs illustrating characteristics of magnetite (type 1) with the barren host rocks of the Pé Quente deposit. (a) Magnetite associated with hornblende, biotite, apatite and quartz. (b) Fractured subeuhedral magnetite grains. (c) Cubic magnetite associated with hornblende, biotite, apatite, chlorite and carbonate. (e, f) Euhedral magnetite grains with apatite inclusions. (a, c) Images in transmitted plane-polarised light, (b, e, f) BSE images and (d) image in reflected light.

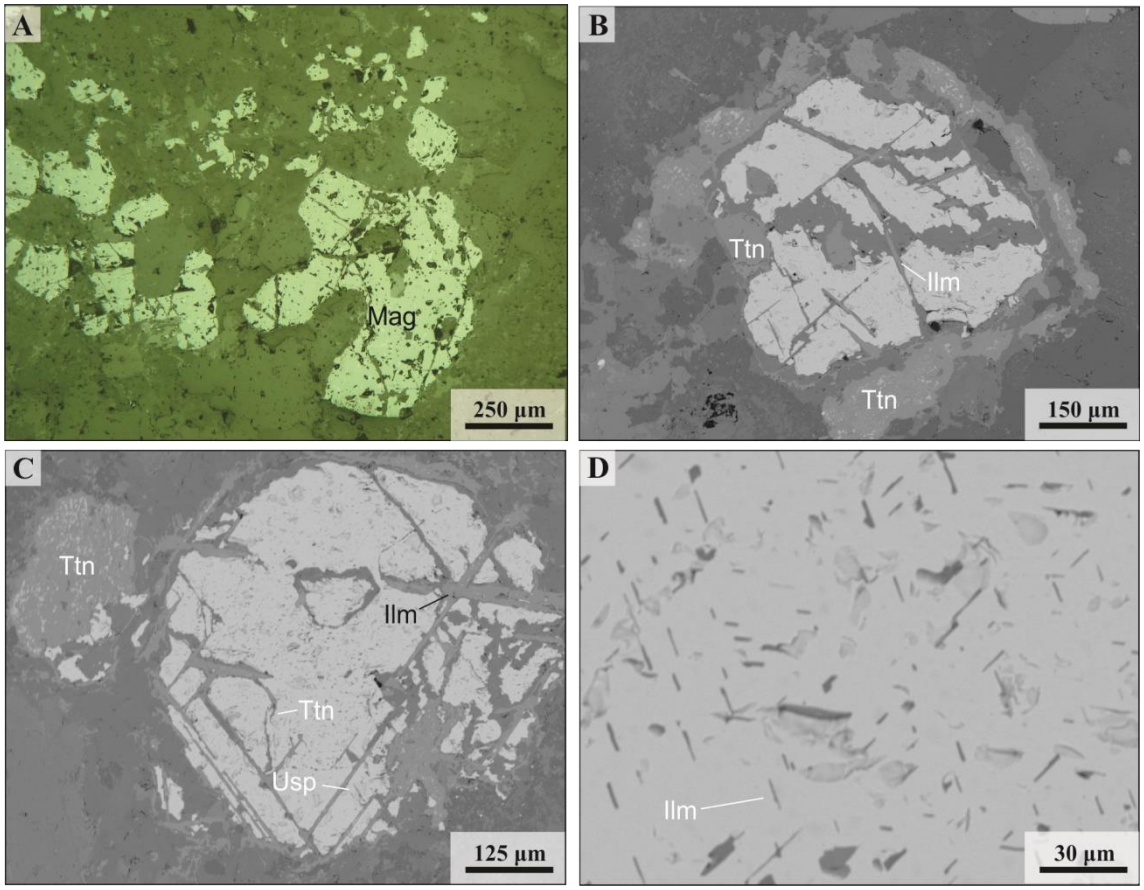

Figure 5.7 – Thin section microphotographs illustrating textures and morphologies of magnetite in transitional zones (type 2) in the Pé Quente deposit. (a) Skeletal magnetite in a cluster of subeuhedral magnetite grains. (b, c) Magnetite exsolved into ülvospinel + ilmenite + titanite. Ilmenite occurs as intergrowths and titanite occurs as irregular stringers and independent crystals. (d) Magnetite with finely disseminated ilmenite. (a) Image in reflected light and (b-d) BSE images.

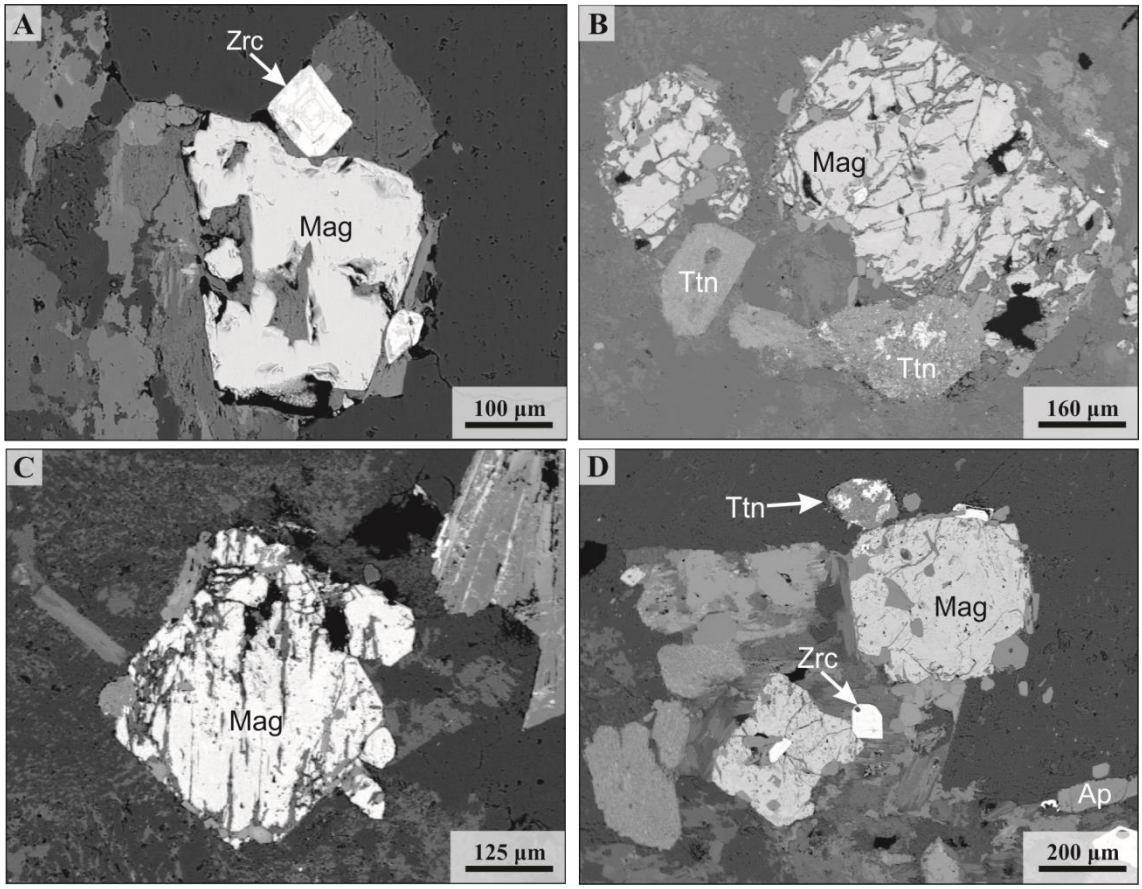

Figure 5.8 – Backscattered electron images of magnetite in hydrothermally altered rocks (type 3) of the Pé Quente deposit. (a) Skeletal magnetite alongside hopper-type zircon in phyllic-altered granitoid. (b) Magnetite grains with exsolved ilmenite and titanite as stringer inclusions, alongside independent, turbid titanite crystal. (c) Sandwich-type ilmenite exsolution lamellae in magnetite. (d) Poikilitic magnetite with inclusions of apatite and zircon, and disseminated titanite as irregular stringers.

5.3 X1 deposit

Several thin sections were made out of the drill core samples of the X1 deposit. Samples represented the Guarantã granite, the quartz-feldspar porphyry, and the hydrothermal zones. Apatite was only found in the phyllic alteration of the X1 deposit. Magnetite was found in small amounts of <30-µm grains that were not further analysed.

Apatite occurs in a phyllic alteration zone (sericite-pyrite-quartz) that regionally envelops the X1 deposit. Alteration intensity is weak, and phyllic alteration occurs interstitially in the biotite granodiorite. Apatite occurs mostly as large euhedral prismatic grains (>100-µm) associated with smaller subeuhedral crystals (30-70-µm) as ovoids and hexagonal prisms. It often occurs as inclusions within or alongside biote rims (Fig. 5.9a, e). Apatite may occur closely associated with cubic

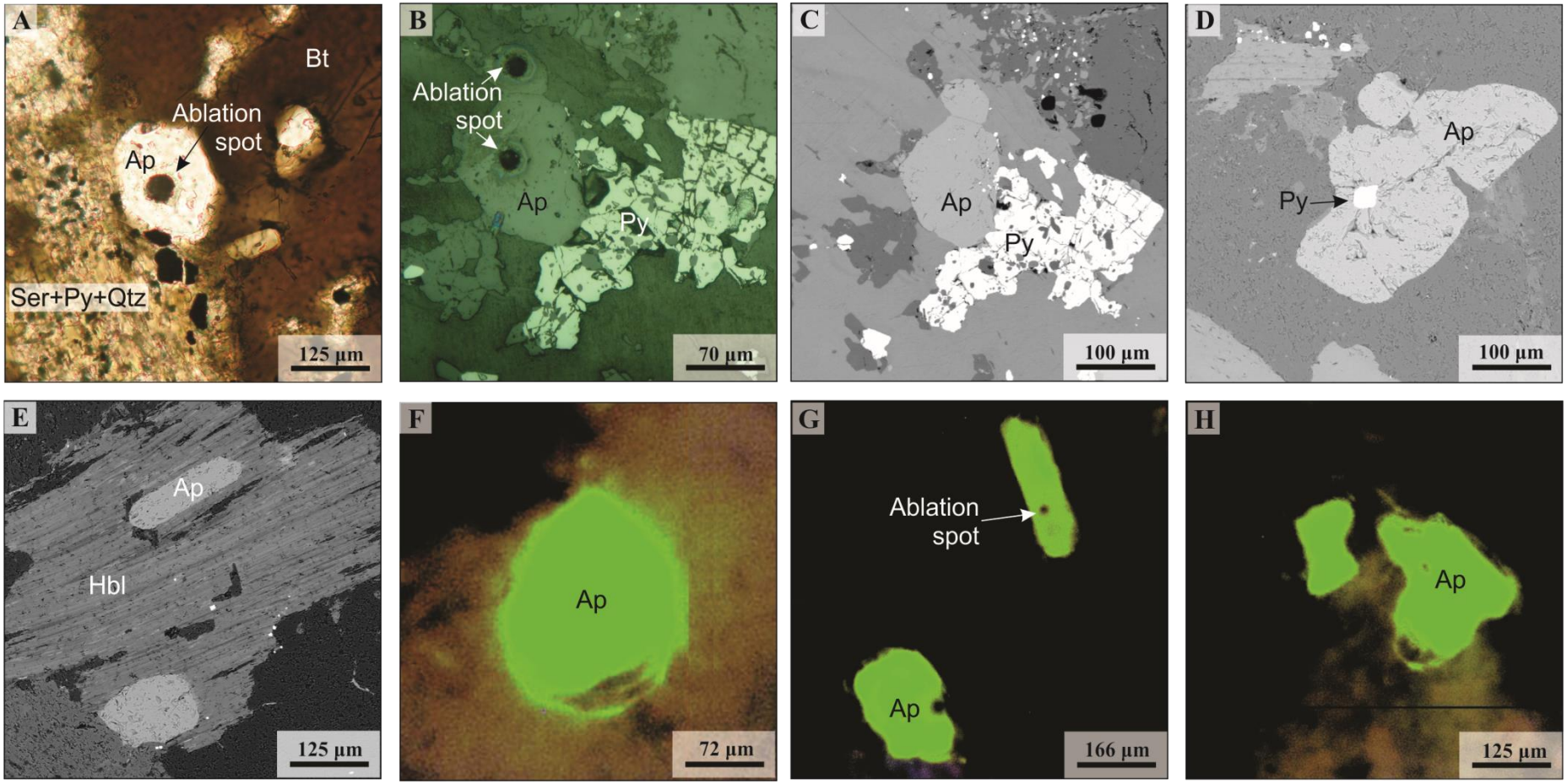

Figure 5.9 – Thin section microphotographs illustrating apatite characteristics in the phyllic alteration of the X1 deposit. (a) Apatite associated with biotite, pyrite and sericite. (b-c) Apatite grains closely associated to pyrite as inclusions in biotite. (d) Subeuhedral apatite with pyrite inclusion. (e) Prismatic and tabular apatite grains as inclusions within hornblende. (f ,g, h) Strongly saturated green-luminescent apatite as prismatic, overgrown and ovoid grains. (a) Image in transmitted plane-polarised light, (b) image in reflected light, (c-e) BSE images, and (f-h) CL images.

pyrite, or as inclusions within it (Fig. 5.9b, c, d). Apatite may be pristine, fractured, or crosscut by sericite veinlets. It occurs associated with the primary igneous assemblage (hornblende, biotite and zircon) and with the phyllic assemblage (quartz, sericite and pyrite). Under CL, apatite exhibits a bright green to yellow luminescence (Fig. 5.9f, g, h), similar to the barren host rocks of the Pé Quente deposit. However, apatite luminescence in the X1 deposit is strongly saturated — it emits a bright luminescent halo that smittens any complex CL textural pattern. This strongly saturated luminescence pattern distinguishes the X1 apatite from the Pé Quente apatite.

5.4 Francisco deposit

The Francisco deposit is an epithermal-style deposit, mainly hosted in a volcaniclastic sequence, and lesser in the União do Norte porphyry. The União granodiorite underlays the volcaniclastic unit, and also functions as a host rock, being distally affected by propylitic alteration (with chlorite, epidote, actinolite, chalcopyrite, pyrite, barite and quartz). The volcaniclastic unit was sampled at both its hydrothermal zone (chlorite-sericite-altered arcosian sandstone) and barren zone (unaltered arcosian sandstone). The União granodiorite was also sampled, as part of the barren plutonic host rock of the Francisco deposit. Given their different petrological characteristics, the volcaniclastic unit and the União do Norte granodiorite were separately analysed for apatite and magnetite.

5.5.1 União granodiorite

The União granodiorite is equigranular, isotropic, with granular texture, and slightly altered by propylitic alteration. It is composed of hornblende, biotite, apatite, magnetite and titanite as accessory phases (fig. 5.10a). Hornblende occurs as dark-greenish elongated crystals (200-500-µm) that may be strongly altered, with irregular borders that may contain embayements and corrosion features. Hornblende displays lobated borders, chlorite-altered rims and penetrating propylitic veinlets.

Apatite occurs similarly as in the barren zones of other deposits. It is euhedral to subeuhedral, between 50-200-µm in size, and with prismatic and hexagonal habits. Apatite occurs associated to hornblende, biotite and magnetite as part of the primary igneous assemblage (Fig. 5.10a). It may occur as inclusions within hornblende and magnetite, and with other accessory minerals, such as magnetite and zircon (Fig. 5.10b).

Long apatite grains (>100-µm) are generally broken-down and crosscut by veinlets of chlorite-epidote-carbonate. Under CL, apatite from the União granodiorite is green-luminescent, and turns yellow-luminescent with slight changes in light deflection, similarly to those from the barren host rocks of the Pé Quente deposit.

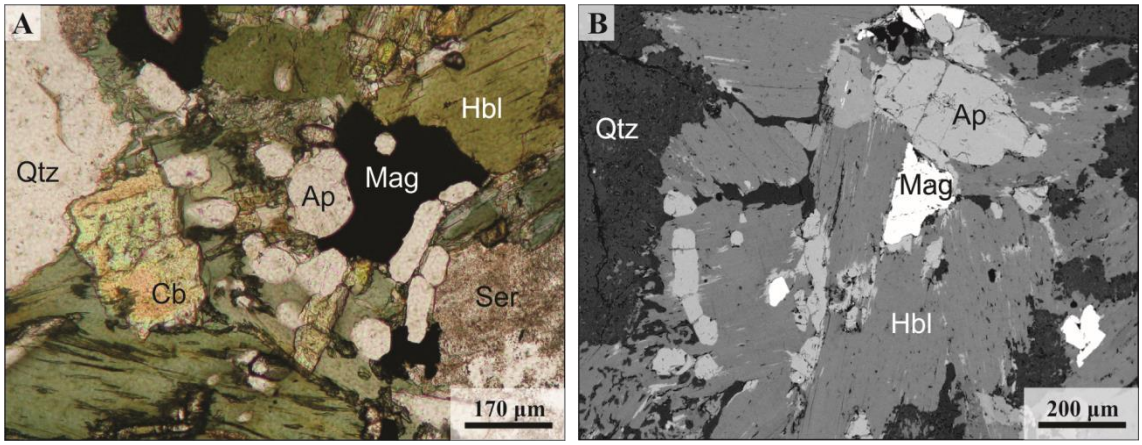

Figure 5.10 – Thin section microphotographs illustrating textures and morphologies of apatite from the barren plutonic host rock of the Francisco deposit (União granodiorite). (a) Euhedral apatite grains with primary igneous assemblage (quartz, hornblende and magnetite), carbonate and sericite. (b) Subeuhedral to anhedral apatite as inclusions within hornblende. (a) Image in transmitted plane-polarised light and (b) BSE image.

In the União granodiorite, magnetite occurs closely associated to hornblende, apatite, titanite and rutile, and displays signs of alteration (Fig. 5.11a, b). Magnetite is subeuhedral to anhedral, between 200-500-µm, and contains several inclusions of apatite (Fig. 5.11c, d). Anhedral magnetite forms clusters of grains within hornblende lamellae and along veinlets. Magnetite is deeply altered, with many grains having skeletal morphology, porkilitic texture, and forming clusters of crystal blobs. Titanite and rutile occur along magnetite rims, closely associated to propylitic minerals. Titanite, especially, seems to be related to incipient autometasomatism or propylitic alteration, given its subeuhedral to anhedral shape.

5.5.2 Volcaniclastic unit

The volcaniclastic sequence contains thin magnetite-rich layers (150-200-µm in length), intercalated with thicker arcosian-rich layers (Fig. 5.12a). Magnetite is a major constituent of the feldspar-greywacke and arcosian volcaniclastic sandstone, both of which comprise the volcaniclastic unit. Only the arcosian volcaniclastic sandstone was analysed for magnetite in this study. The arcosian volcaniclastic sandstone consists of fine-grained magnetite, quartz and feldspar clasts (all about <30-um).

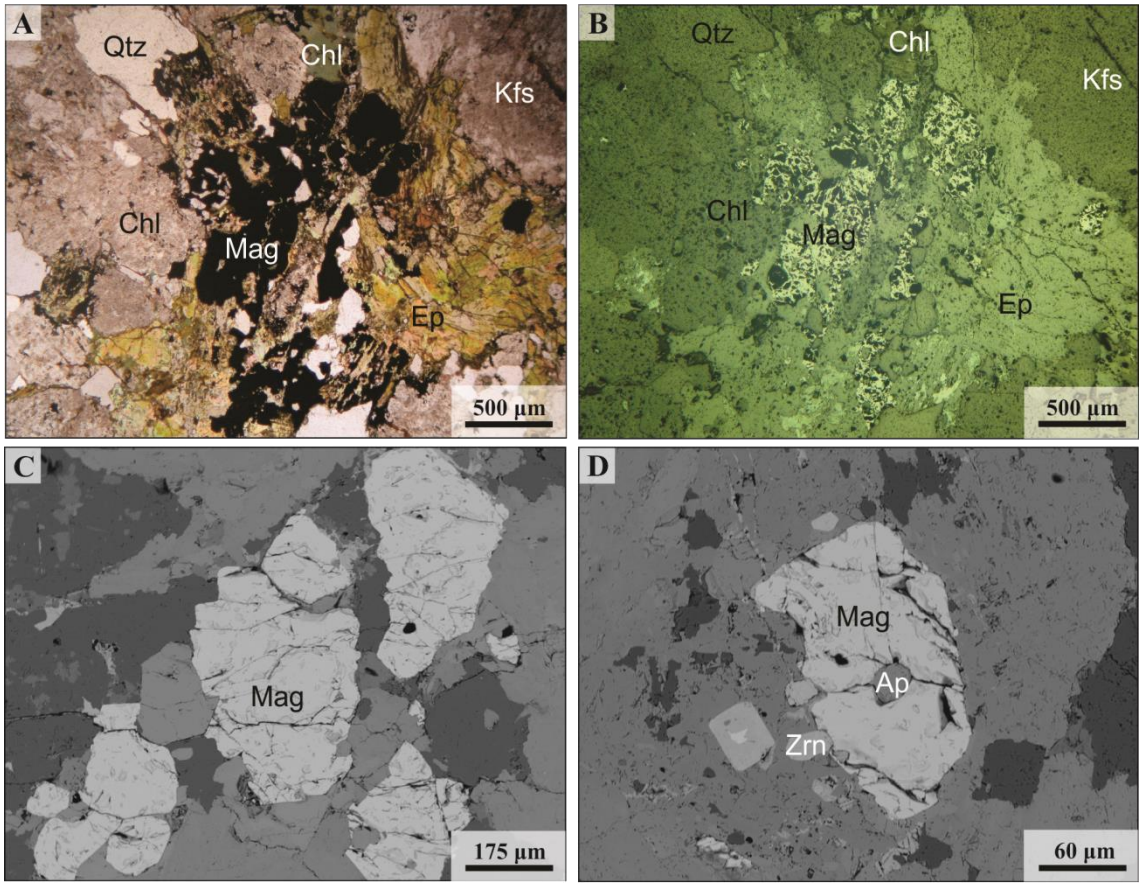

Figure 5.11 – Thin section microphotographs illustrating textures and morphologies of magnetite in the barren plutonic host rock of the Francisco deposit (União granodiorite). (a) Clustered anhedral magnetite included within hornblende, altered by carbonate-epidote-chlorite in veinlets or interstitially. (b) Same image spot as (a), but under reflected light. (c) Large, fractured, subeuhedral magnetite grains associated with apatite and hornblende. (d) Magnetite with inclusions of apatite, closely associated to zircon, and included within hornblende. (a) Image in transmitted plane-polarised light, (b) image in reflected light and (c, d) BSE images.

Apatite seldom occurs as a volcaniclastic grain, so it was not possible to analyse it neither at EPMA nor at the LA-ICP-MS. When apatite does occur, it consists of euhedral, blunt, prismatic grains (~15-µm) that occur alongside the borders of volcaniclastic magnetite, or as inclusions within it (Fig. 5.12b). Magnetite grains are too small (25-35-µm) to be analysed by LA-ICP-MS, but large enough to be analysed by EMP. Some magnetite grains are pseudomorphically altered into hematite (martitisation), so they will be treated here as iron oxides more broadly. Magnetite in the volcaniclastic sequence is discriminated in two types:

Type 1. Volcaniclastic iron oxide (barren zone, VU20-4 sample). Volcaniclastic iron oxides are strongly altered, subrounded to subangular, with corroded and embayed rims resembling alveoli. They contain multiple inclusions (primarily of apatite) in a sieve-like texture (Fig. 5.12c, d). They also contain ilmenite exsolutions (Fig. 5.12d), which denotes an igneous titanomagnetite origin. The majority of magnetite grains

occur along specific sediment layers (~0.2 mm in length) with subrounded lithic fragments, and subrounded to subangular quartz and feldspar grains.

Type 2. Volcaniclastic iron oxide type 2 (hydrothermal zone, PTO19 sample). Volcaniclastic lithic arkose is strongly altered by pervasive propylitic alteration. Iron oxides are subeuhedral and associated to the propylitic assemblage with chlorite, epidote and sericite. These iron oxide grains can be further sub-divided into: (2A) martite skeletal grains (Fig. 5.13a, b, c); (2B) pristine, cubic to rhombohedric iron oxide grains (Fig. 15.13d, e, f). Martitisation transforms magnetite (2A) into hematite (2B).

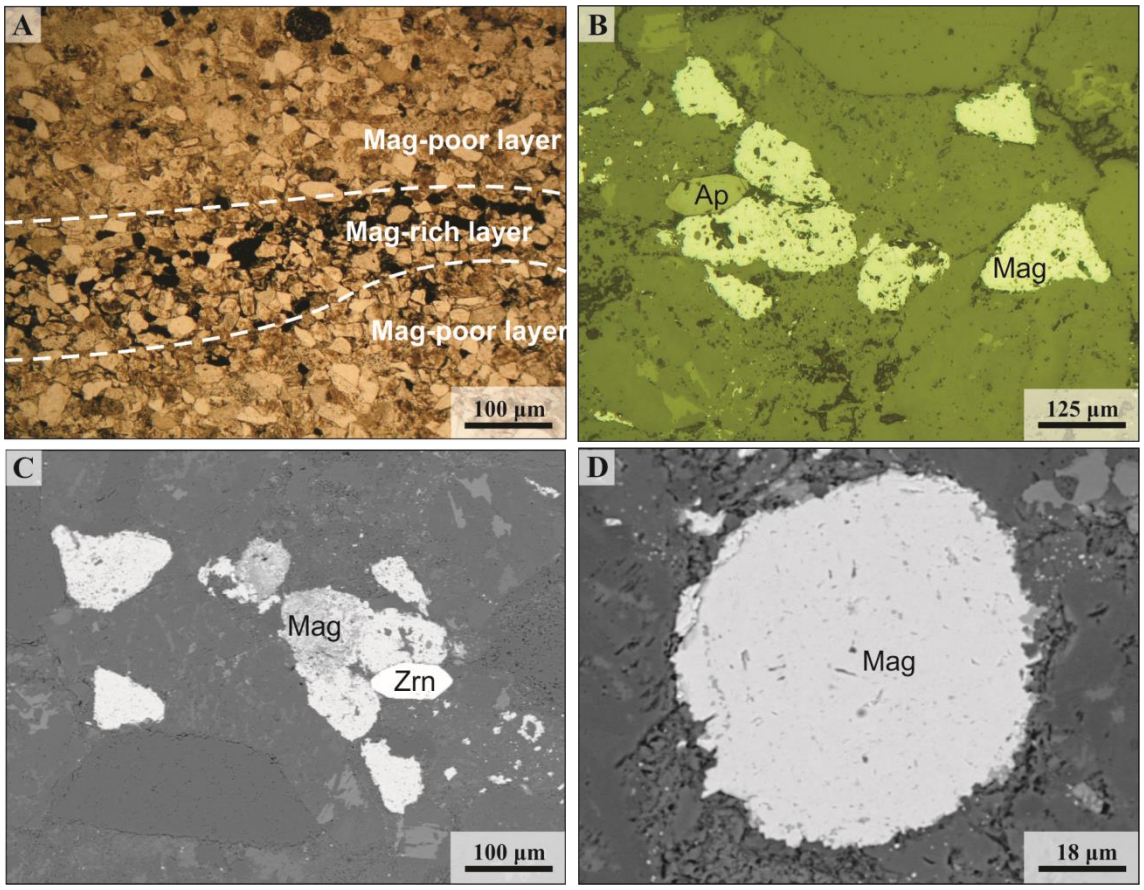

Figure 5.12 – Thin section microphotographs illustrating textures and morphologies of detrital magnetite grains in the barren zone of the volcaniclastic sequence of the Francisco deposit. (a) Arcosian sandstone displaying thin magnetite-rich layer between two thick arcosian-rich layers. (b) Subrounded magnetite grains are strongly altered, and bounded to apatite grain. (c) Silt-sized, subrounded to subangular magnetite occurs amongst lithic fragments, quartz and feldspar sand. Magnetite is filled with pores and microcrystalline inclusions, in a sieve-like texture. Apatite occurs within or along the borders of magnetite grains. (d) Rounded magnetite grain with irregular, auveolar-like rims. (a) Image in transmitted plane-polarised light, (b) image in reflected light and (c, d) BSE images.

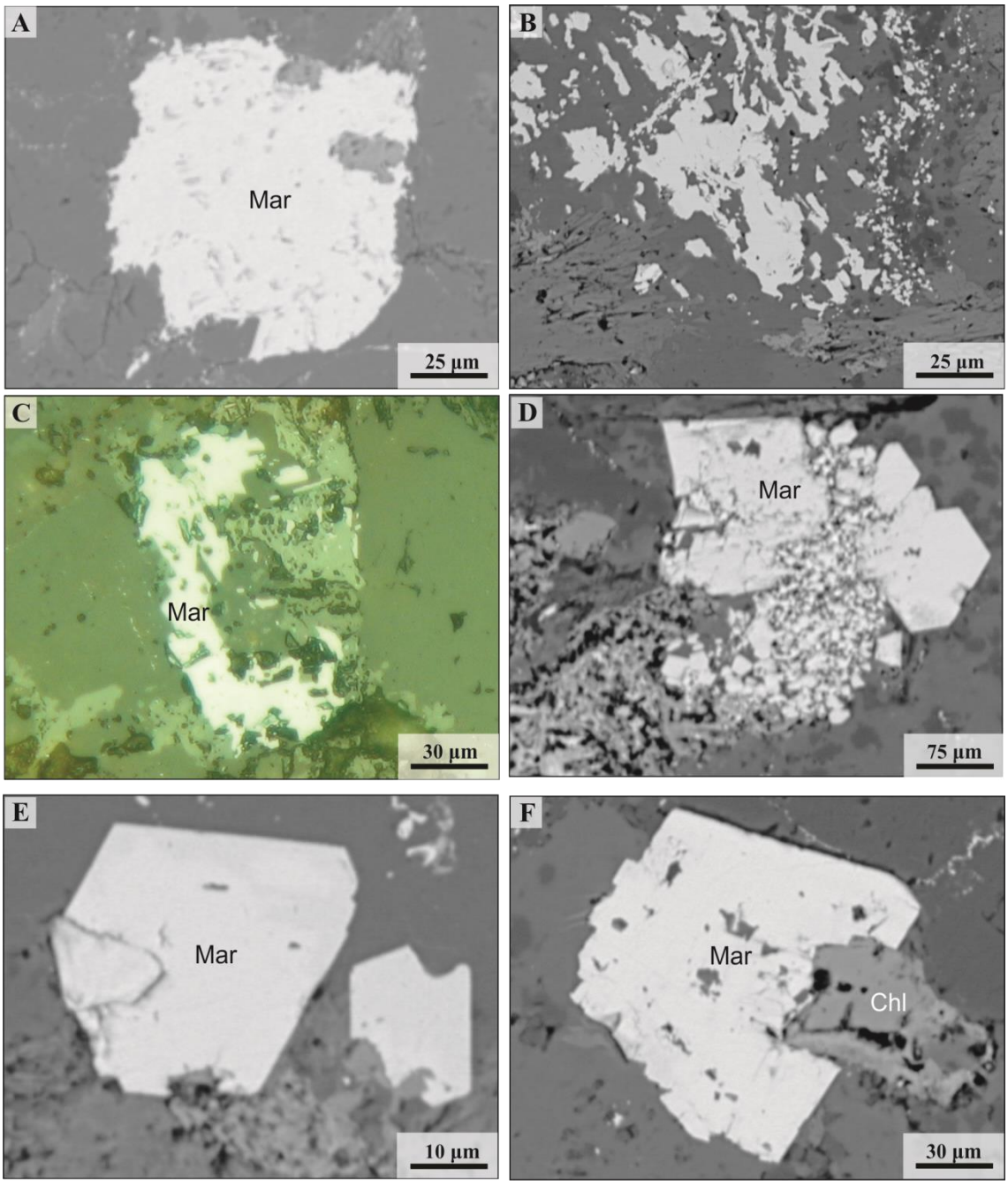

Figure 5.13 – Thin section microphotographs illustrating textures and morphologies of magnetite grains in the barren zone of the volcaniclastic sequence of the Francisco deposit. (a) Magnetite with irregular rims, altered into martite. (b, c) Skeletal martite. (d) Martite-hematite grains coalescing from anhedral magnetite. (e, f) Euhedral rhomboedric hematite grains. (a-d, f) BSE images and (e) image in reflected light.

5.5 Teles Pires Intrusive Suite

The Teles Pires Intrusive Suite is represented by an equigranular to porphyritic hornblende-biotite syenogranite. It is mostly unaltered, except for some surface weathering and incipient alteration that comprises chlorite, sericite and epidote. The hornblende-biotite syenogranite is predominantly pink and grey, and the association between K-feldspar phenocrysts and plagioclase gives it rapakivi and anti-rapakivi textures. Accessory minerals include apatite, zircon, titanite and magnetite.

Apatite occurs with the primary igneous assemblage, as 50-200-μm, tabular, prismatic and subrounded crystals that are generally associated with magnetite (Fig. 5.14a, b). Apatite may occur as inclusions within biotite and hornblende (Fig. 5.14c, d). Under CL, apatite is similarly yellow-luminescent as those from other barren host rocks. However, the luminescence is somewhat dimmed by the interference of weathering-related, red-luminescent hematite (Fig. 5.14e, f).

Magnetite is euhedral, with about 150-200-μm, and often contains apatite inclusions. Compared to other units, Teles Pires magnetite has the most pronounced exsolution lamellae (Fig. 5.15a). Exsolution lamellae occur as parallel-type lamellae (Fig. 5.15e, f) and trellis-type lamellae (Fig. 5.15c, d). Skeletal magnetite is also present (Fig. 5.15b). Ilmenite commonly occurs along microfractures inside magnetite, as a product of exsolution (Fig. 5.15g, h). Titanite occurs along magnetite rims as subeuhedral to aneuhedral crystals, often associated with ilmenite.

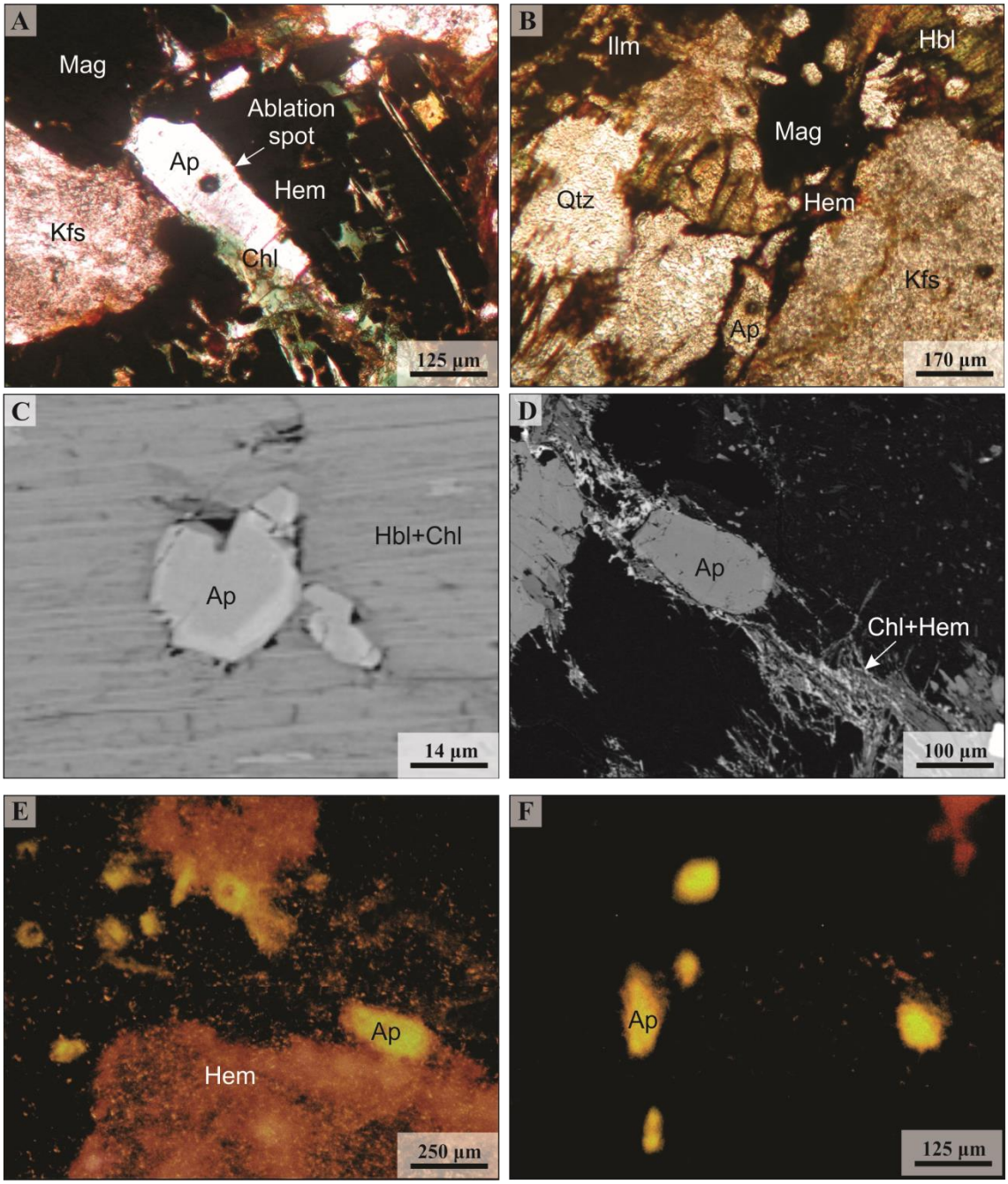

Figure 5.14 – Thin section microphotographs illustrating textures and morphologies of apatite in the Teles Pires Intrusive Suite. (a, b) Prismatic apatite associated with magnetite, hornblende and hematite-altered chlorite. (c) Overgrown apatite included within hornblende. (d) Subeuhedral, prismatic apatite. (e, f) Yellow-luminescent prismatic apatite grains with red-luminescent hematite at its rims, as a weathering product that dims the resolution of the CL image. (a) Image in transmitted cross-polarised light, (b) image in transmitted plane-polarised light, (c, d) BSE images and (e, f) CL images.

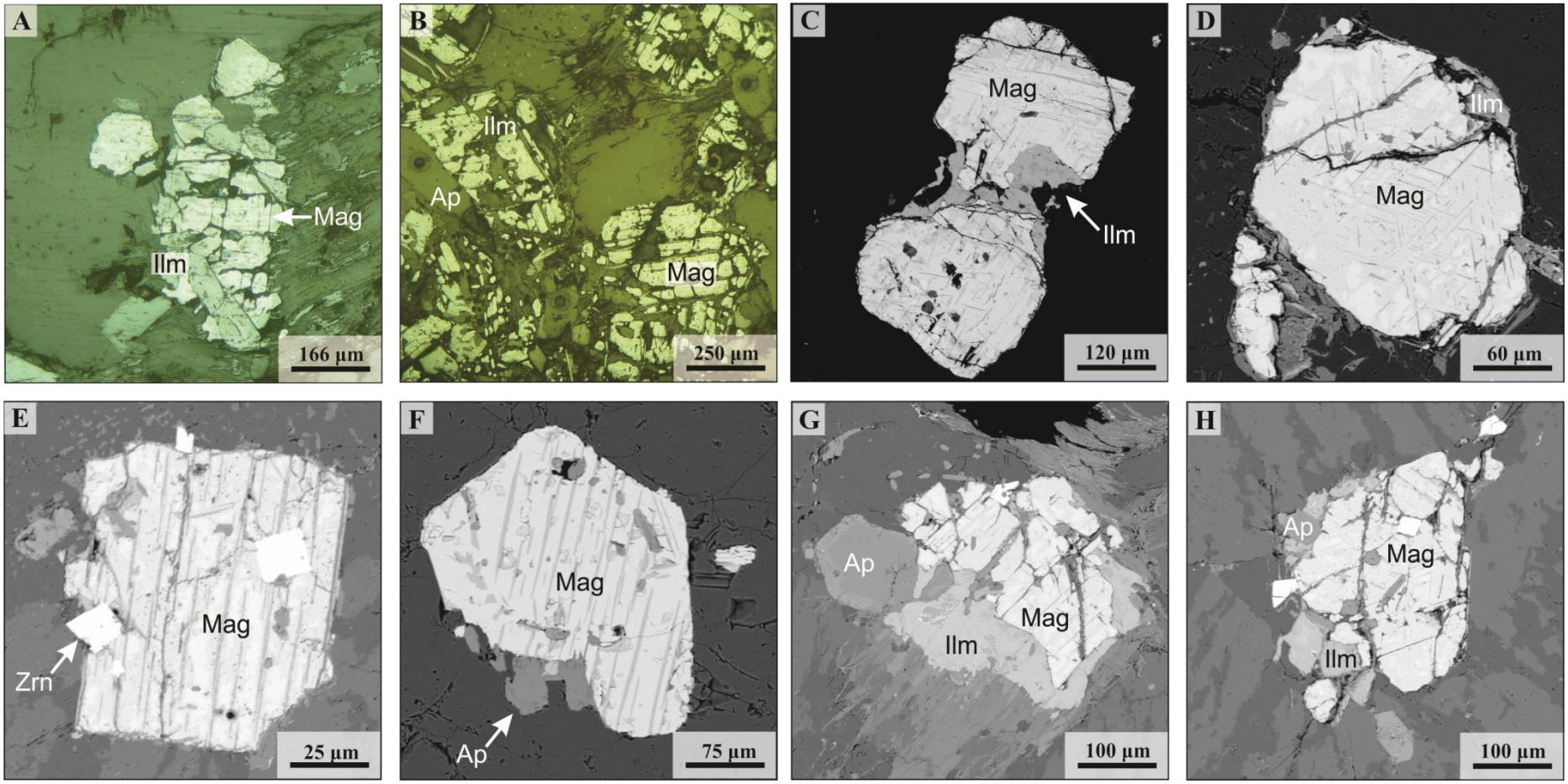

Figure 5.15 – Thin section microphotographs illustrating characteristics of apatite in the Teles Pires Intrusive Suite. (a) Exsolved magnetite grain with thick ilmenite laths. (b) Large skeletal magnetite grains in clusters. (c) Magnetite grains with exsolution lamellae, bounded together by ilmenite. (d) Fractured magnetite with trellis-type exsolution lamellae. Ilmenite occurs at magnetite rims. (e) Sandwich-type exsolution lamellae in magnetite with zircon inclusions. (f) Magnetite with inclusions of apatite and sandwich-type exsolution lamellae. (g, h) Skeletal magnetite associated with ilmenite, hornblende, and apatite that occur as inclusions or bordering magnetite rims. Larger apatite grain displays overgrowth texture. (a, b) Images in reflected light, and (c-h) BSE images.

Chapter 6

Compositional variability of apatite and magnetite

6.1 Apatite chemistry

6.1.1 Calcium and phosphorus

Calcium and phosphorus are major components of apatite and do not vary much among samples. However, because they are major components, their overall concentrations reflect on the amount of trace elements that is partitioned into apatite. Calcium contents range from 37.25 to 40.21 wt. % (Fig. 6.1a). The highest Ca contents occur in apatite from the Teles Pires Intrusive Suite (median 39.09 wt. %), from the hydrothermal zone of the Luizão deposit (median 39.31 wt. %), and from the barren host rocks of the Francisco (median 39.96 wt. %) and Pé Quente (median 39.67 wt. %) deposits. Apatite that occurs at the phyllic alteration zone of the Pé Quente deposit (type 2) also has higher Ca content (median 39.43 wt. %). The lowest Ca contents – and the broadest ranges thereof – occur in the hydrothermal zone of the X1 deposit (median 37.75 wt. %) and in the propylitic alteration zone of the Pé Quente deposit (type 3; median 38.63 wt. %).

Phosphorus contents range from 17.06 to 18.47 wt. % (Fig. 6.1b). The P contents are highest in apatite from the barren host rocks of the Francisco (median 18.07 wt. %) and Pé Quente deposits (median 18.02 wt. %), and in apatite from the phyllic alteration of the Pé Quente deposit (median 18.09 wt. %). On the other hand, P contents are lower in apatite from the Teles Pires Intrusive Suite (median 17.84 wt. %) and from the hydrothermal zones of the Luizão (median 17.75 wt. %), X1 (median 17.82 wt. %) and Pé Quente deposits (particularly in type 3 apatite, with a median of 17.69 wt. %).

6.1.2 Fluorine and chlorine

Fluorine contents range from 2.44 to 4.50 wt. % (Fig. 6.1c). They have a relatively high detection limit (between 633-704 ppm) and a good average precision (3 % standard deviation) at EPMA. Concentrations of F are higher in apatites from the Teles Pires Intrusive Suite (median 3.95 wt. %) and from the hydrothermal zones of the Luizão (median 3.89 wt. %), X1 (median 3.84 wt. %) and Pé Quente deposits (medians 3.86 wt. % at type 2; 2.69 wt. % at type 3), and lower in apatites from the barren host

rocks of the Francisco (median 3.67 wt. %) and Pé Quente deposits (median 2.92 wt. %).

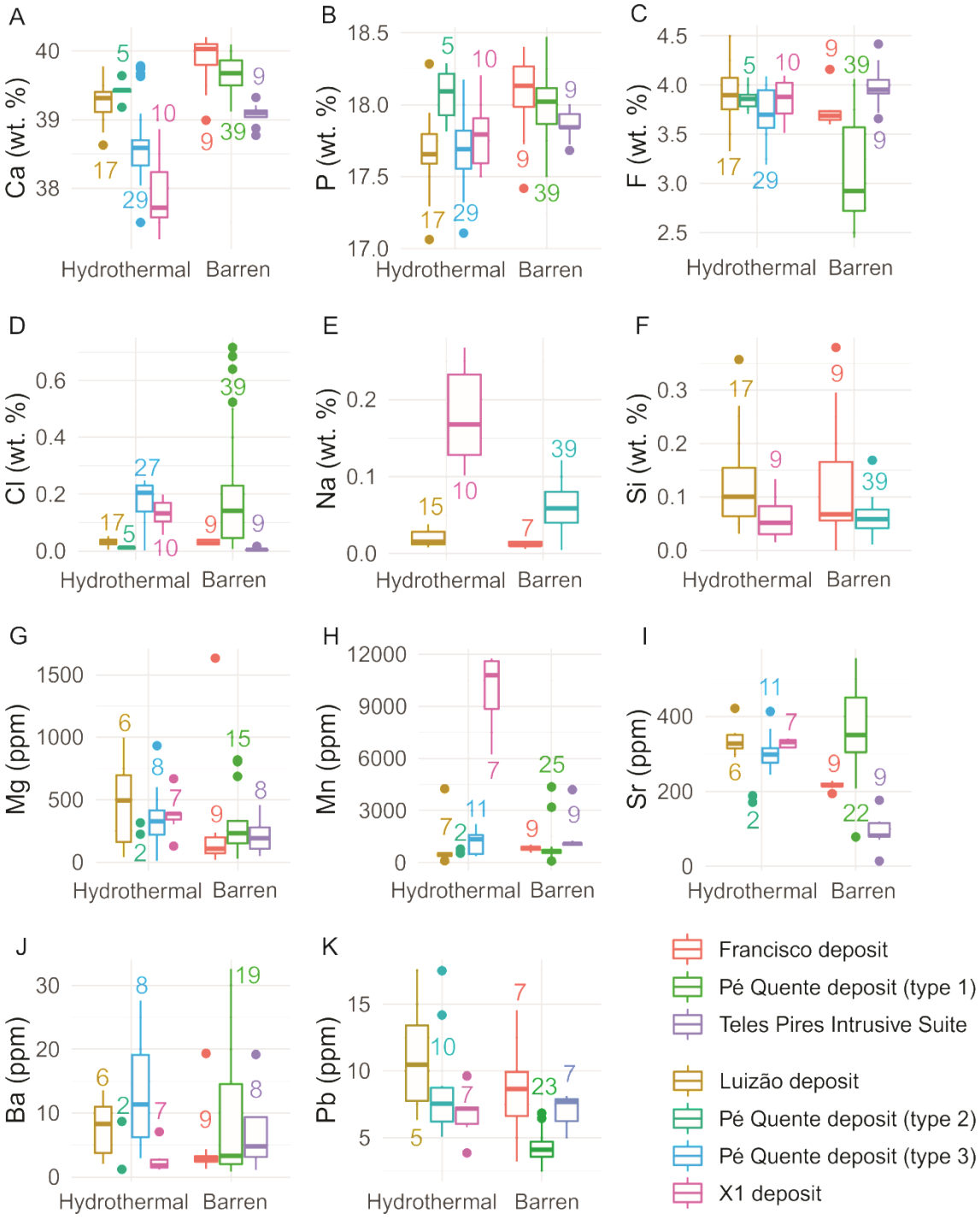

Figure 6.1. Box and whisker plots for important major, minor and trace elements in apatite. Major and minor elements are shown in weight percentage (wt. %), while trace elements are in parts per million (ppm). The box corresponds to the interquartile range (between 25th-75th percentile), and the whiskers correspond to the 5th to 25th percentiles (lower whisker) and 75th to 95 percentiles (upper whisker). The line inside the box is the median value. The closed circles are the <5th and >95th percentiles. The numbers above or beneath the whiskers correspond the number of samples (n).

Chlorine concentrations have interquartiles between 0.02-0.20 wt. % (Fig. 6.1d), with the lowest values occurring in the Luizão (median 313 ppm) and Francisco

(median 272 ppm) deposits, and in the Teles Pires Intrusive Suite whither most analyses were below the detection limits (<66 ppm). In the the Pé Quente deposit, Cl contents remained roughly similar in the barren and propylitic zones, with medians of 0.14 wt. % and 0.2 wt. % respectively — which are considerably higher than in the aforementioned units and in the phyllic zone of the Pé Quente deposit that displays a median of 129 ppm. Together with the Pé Quente deposit, the X1 deposit also displays a high F concentration (median 0.11 wt. %). Assuming that either F-, Cl-, or OH- occupy the anion site located along the c-axis, about half of the apatites from the barren host rock of the Pé Quente deposit reach a hydroxylapatite composition (> 51 mol wt. % OH, at the lower quartile of F compositions), because of F-OH exchange.

6.1.3 Sodium and silicon

Sodium concentrations range from <142 ppm to 0.26 wt. % (interquartiles 167-924 ppm, median 467 ppm) (Fig. 6.1e). The Na contents are considerably higher in the hydrothermal zone of the X1 deposit (median 1,623 ppm) than in the Luizão deposit (median 155 ppm). In barren host rocks, Pé Quente apatite has slightly more Na concentrations (median 588 ppm) than Francisco (median 129 ppm) apatite.

Silicon, on the other hand, is one of the few elements that tend to accommodate in the P site (together with As). The Si contents range from below the detection limits (<314 ppm) to 0.37 wt. %, with interquartiles between 419-953 ppm and a median of 659 ppm (Fig. 6.1f). The lowest Si concentrations occur in the hydrothermal zone of the X1 deposit (median 414 ppm), whereas the highest Si concentrations occur in hydrothermal zone of the Luizão (median 1,004 ppm) and in the barren host rock of the Francisco deposit (median 820 ppm). Neither the Teles Pires granite nor the hydrothermal zone of the Pé Quente deposit were analysed for Na and Si.

6.1.4 Magnesium, manganese, strontium, barium and lead

Alkaline earth metals, transition metals and heavy metals tend to accommodate into the Ca sites. Magnesium concentrations have interquartiles between 142 and 1,633 ppm, with a median of 330 ppm (Fig. 6.1g). Apatites from the hydrothermal zone of the Luizão deposit and from the barren host rock of the Pé Quente deposit have the highest Mg concentrations (medians 690 ppm and 686 ppm, respectively). Apatite from the hydrothermal zone of the Luizão deposit has a broader Mg concentration range than

apatite from the barren host rock of the Pé Quente deposit. On the other hand, lower Mg concentrations prevail in apatites from the hydrothermal zones of the Pé Quente[6] (median 349 ppm) and X1 deposits (median 391 ppm), and from the barren plutonic rocks of the Francisco deposit (median 107 ppm) and the Teles Pires granite (median 248 ppm).

Manganese concentrations (interquartiles 548-1,206 ppm, median 742 ppm) have their largest distribution ranges in apatite from hydrothermal zones (Fig. 6.1h). The Mn contents in the X1 deposit have a median of 1.05 wt. %. This is far greater than elsewhere, given that the overall median of Mn in other deposits is 732 ppm. The Mn concentrations are comparatively lower in all other units: in the Teles Pires Intrusive Suite (median 1,110 ppm), in the hydrothermal zones of the Pé Quente (median 668 ppm) and Luizão deposits (median 447 ppm), and in the barren host rocks of the Pé Quente (median 682 ppm) and Francisco deposits (median 837 ppm).

Strontium contents (interquartiles 215-368 ppm, median 310 ppm) are detectable in all apatite analyses (Fig. 6.1i). Apatite from the barren host rocks of the Pé Quente deposit has greater Sr contents (median 360 ppm) than in the hydrothermal zone of the same deposit (median 294 ppm). The Sr contents are also higher in the hydrothermal zones of the Luizão (median 345 ppm) and X1 (median 334 ppm) deposits, and lower in the barren plutonic host rock of the Francisco deposit (median 296 ppm). Apatite related to the anorogenic Teles Pires Intrusive Suite has the least amounts of Sr (median 82 ppm).

Barium contents (interquartiles 2-22 ppm, median 6 ppm) are too low and do not display any significant correlation to any unit (Fig. 6.1j). X1 and Francisco apatites have the least amount of Ba (generally below the detection limits). Lead contents (interquartiles 4-13) are slightly higher in the hydrothermal zone of the Pé Quente deposit (average 25 ppm) than in the barren host rock of that same deposit (average 4 ppm) (Fig. 6.1k). Phyllic-related apatite of the Pé Quente deposit displays the highest Pb contents (of 20 ppm and 80 ppm), but that are considered outliers and were not represented graphically. Otherwise, Pb contents are too low in other deposits.

[6] By "apatites from the hydrothermal zone of the Pé Quente deposit", we mean both types 2 and 3 apatites, from the phyllic and propylitic alterations. These two apatite types are encompassed together in the text from then on due to the low sample size (n=2) of LA-ICP-MS analyses of the phyllic-related apatite.

6.1.5 Titanium and Iron

Even though the results for titanium and iron concentrations in either EPMA or LA-ICP-MS analysis have low precision, they display distribution patterns that match those of other elements, which might indicate that, despite the low precision, the results are accurate. Overall, Ti contents have a median of 804 ppm, interquartiles between 781-861 ppm (Fig. 6.2a), and the standard errors median of 42 % (Table 4.4). Apatite related to the barren host rocks of the Francisco and Pé Quente deposits can be discriminated by its slightly higher Ti contents. The median of Ti contents in apatites from the Francisco deposit is 805 ppm, and in the barren host rock of the Pé Quente deposit, it is 829 ppm. The Ti concentrations are slightly lower in apatites from the Teles Pires granite (median 782 ppm), and from the hydrothermal zones of the X1 deposit (median 780 ppm) and Pé Quente deposit (median 797 ppm). In the hydrothermal zone of Luizão deposit, Ti contents are high (median 815 ppm). These distribution patterns concur with the results from other elements that have better precision.

The Fe contents have a median of 1,126 ppm and interquartiles between 565 and 2,323 ppm (Fig. 6.2b). The Fe contents have low precision on LA-ICP-MS analysis (standard error median of 136 %) and better precision on EPMA (standard deviation median of 18 %). High Fe contents occur in apatites from the Teles Pires granite (median 1,290 ppm) and from the fertile zones of the Luizão deposit (median 1,817 ppm), Pé Quente deposit (median 1,128 ppm) and X1 deposit (median 2,305 ppm). The Fe contents in the barren host rocks are generally lower, such as in the Francisco deposit (median 601 ppm) and in the Pé Quente deposit (median 647 ppm).

6.1.6 Rare earth elements and Y

The REE and Y tend to be incorporated in the Ca cation. The REE can be split into light REE (LREE) and heavy REE (HREE), and each group presents different distribution patterns than the other. We consider LREE as La, Ce, Pr, Nd and Sm (Fig. 6.2c). Europium plays an intermediate REE role, and displays a distinguished pattern (Fig. 6.2d). The HREE encompass Gd, Tb, Dy, Ho, Er, Yb and Lu (Fig. 6.2e). Yttrium, which is not a REE, displays a signature strongly similar to HREE (Fig. 6.2f), and thus, it may be analysed with REE (shortened as REE+Y or REY).

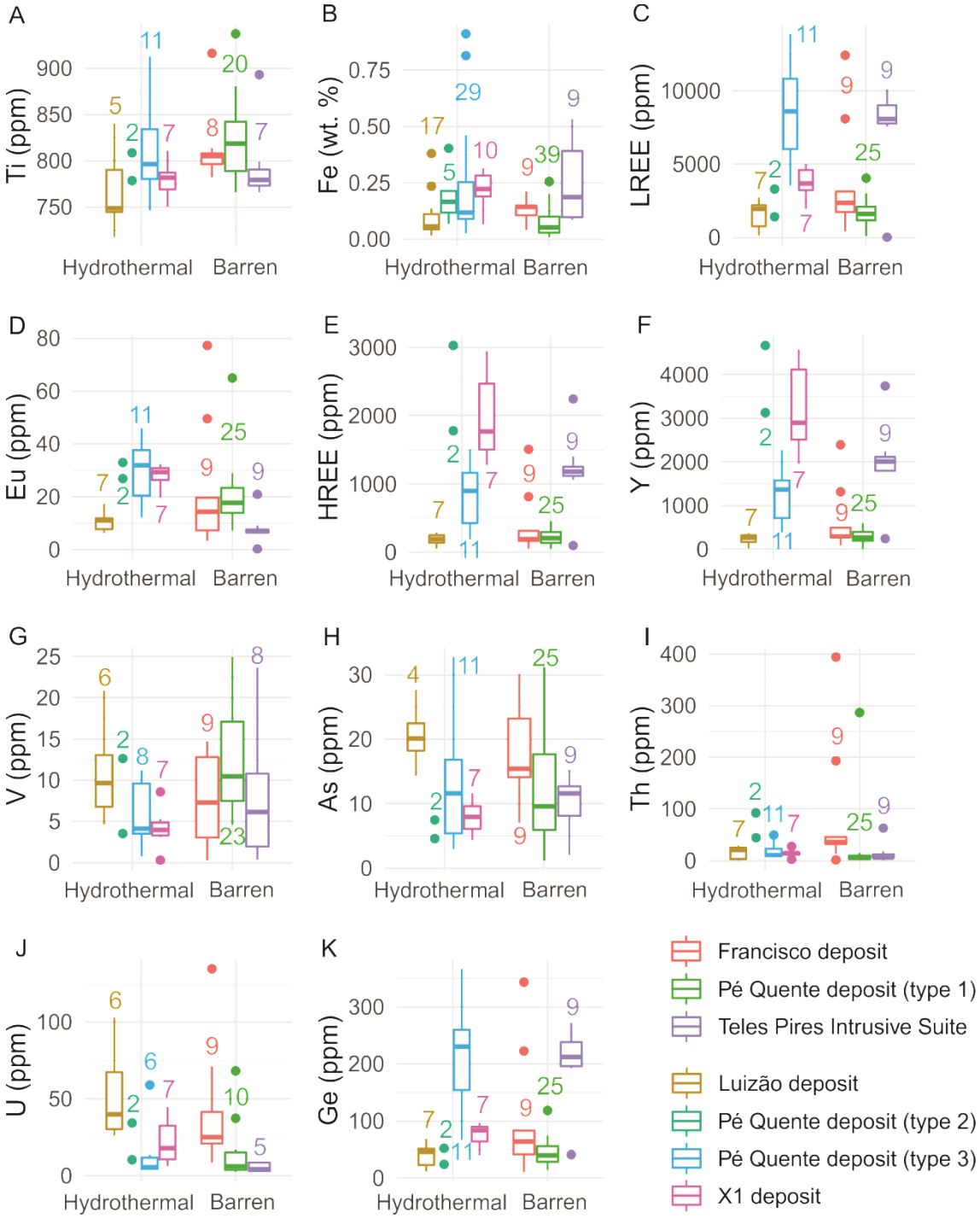

Figure 6.2 Box and whisker plots for trace elements in apatite. The box corresponds to the interquartile range (between 25th-75th percentile), and the whiskers correspond to the 5th to 25th percentiles (lower whisker) and 75th to 95 percentiles (upper whisker). The line inside the box is the median value. The closed circles are the <5th and >95th percentiles. The numbers above or beneath the whiskers correspond the number of samples (n).

The sum of LREE has a median of 2,218 ppm and an interquartile range of 1,395 ppm to 5,388 ppm (Fig. 6.2c). The largest LREE contents occur in apatite from the Teles Pires Intrusive Suite (median 8,082 ppm) and from the hydrothermal zones of the Pé Quente (median 6,841 ppm) and X1 (median 3,584 ppm) deposits. The lowest LREE

contents are displayed in apatite from the hydrothermal zone of the Luizão deposit (median 1,641 ppm) and from the barren host rocks of the Francisco (median 2,360 ppm) and Pé Quente (median 1,607 ppm) deposits.

The sum of HREE has a median of 297 ppm and an interquartile ranging between 183-1,155 ppm (Fig. 6.2e). The HREE display the same distribution pattern as the LREE, but at lower overall concentrations. Therefore, HREE concentrations are higher at the Teles Pires granite (median 1,181 ppm) and at the hydrothermal zones of the Pé Quente (median 986 ppm) and X1 (1,693 ppm) deposits; and lower at the Luizão deposit, and at the barren host rocks of the Francisco (191 ppm) and Pé Quente (206 ppm) deposits. The REE concentrations are illustrated in Figure 6.3. The REE distribution patterns display a descending slope from the heaviest to the lightest element, with the LREE and HREE separated by a chasm of Eu depletion (a "seagull"-shaped distribution pattern). REE concentrations are generally higher in apatites from the Teles Pires Intrusive Suite and from the hydrothermal zones, except for those from the Luizão deposit (Fig. 6.3).

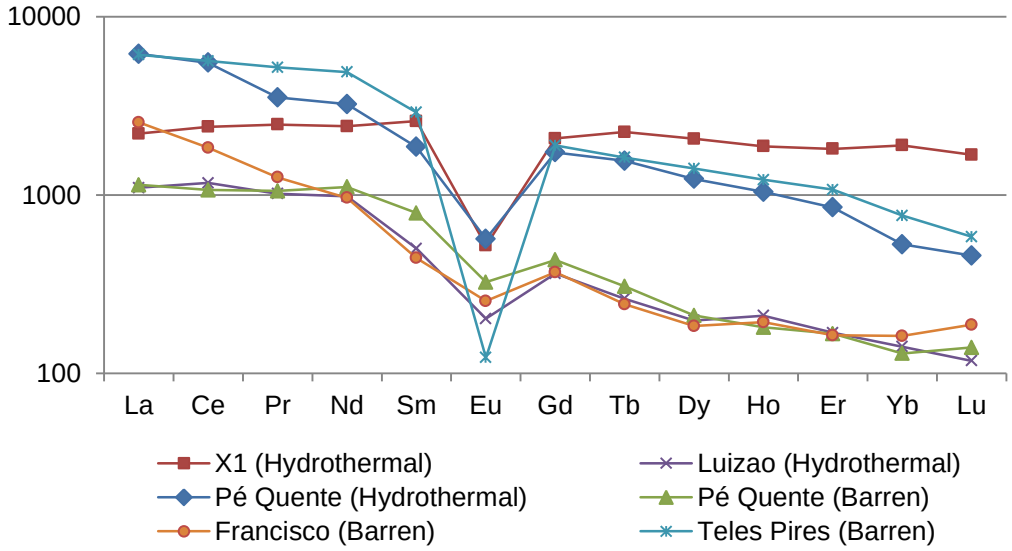

Figure 6.3 Chondrite-normalised REE plots for median apatite compositions.

Some other specific ratios may deepen our perspective on how these concentrations are distributed. The $(La/Sm)_N$ ratio, for instance, may indicate the slope of the distribution pattern of LREE. Apatite from the hydrothermal zone of the Pé Quente deposit has a broader $(La/Sm)_N$ distribution range (from 0.01 to 6.92) than apatite from the Teles Pires Intrusive Suite (from 1.13 to 2.72) and from the hydrothermal zone of the X1 deposit (from 0.27 to 0.91), which has a more constrained

distribution ranges (Fig. 6.4a). On the other hand, the $(La/Sm)_N$ ratios in the barren plutonic unit of the Francisco deposit are also comparatively broader in their range (3.13 to 7.93). The $(La/Sm)_N$ ratios of the X1 deposit have low and narrow ranges.

6.1.7 Eu and Ce anomalies

Apatites from the hydrothermal zones of the Pé Quente and X1 deposits, despite their different $(La/Sm)_N$ ratios, have similar Eu contents (Fig. 6.2d, 6.4a, 6.4b). The median of these Eu contents are respectively of 32 and 30 ppm for the Pé Quente and X1 deposits (Fig. 6.2d). Likewise, apatite from the Luizão deposit and from the barren host rocks of the Pé Quente and Francisco deposits similarly have lower Eu contents, with medians between 11-17 ppm. Lastly, apatites from the Teles Pires Intrusive Suite have the lowest amounts of Eu. This general trend of Eu depletion compared to other REE is known as a negative Eu anomaly. Both Eu and Ce contents may display these anomalies, which are important to evaluate specific properties of the magmatic-hydrothermal system (Fig. 6.4b).

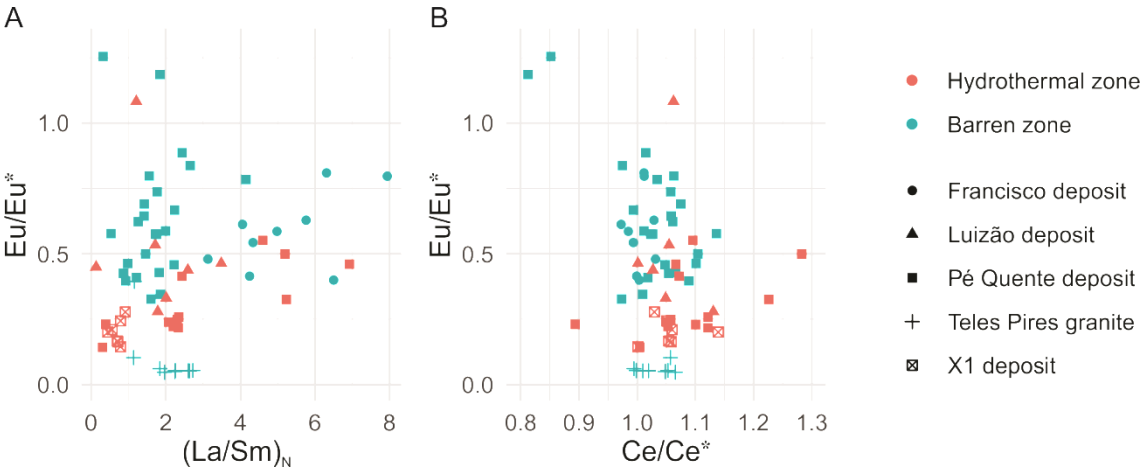

Figure 6.4 – (a) Eu/Eu* vs. $(La/Sm)_N$ plot for apatites. (b) Eu/Eu* vs. Ce/Ce* plot for apatites.

The Eu and Ce anomalies were calculated as: $Eu/Eu^* = Eu_{CN}*(Sm_{CN}+Gd_{CN})^{0.5}$ and $Ce/Ce^*=Ce_{CN}*(LA_{CN}*Pr_{CN})^{0.5}$ (CN=chondrite normalisation values from McDonough and Sun, 1995). Positive anomalies are those in which Ce/Ce* or Eu/Eu* are >1.0 and negative anomalies are those in which these ratios are below 1. Strong negative Eu anomalies occur when Eu/Eu* is closest to zero, as it is the case in the Teles Pires and X1 deposits (with Eu/Eu* medians of 0.05 and 0.20, respectively). Apatite from the hydrothermal zone of the Pé Quente deposit also has a strong negative Eu anomaly (median of 0.25), but that is relatively widespread, ranging from Eu/Eu*

0.14 to 2.87 (Fig. 6.4b). Apatite from the Luizão deposit and from the barren host rocks of the Pé Quente and Francisco deposits has weaker negative Eu anomalies, with medians of 0.58, 0.45 and 0.58 respectively, and that are also widespread in their concentration ranges. On the other hand, Ce contents did not display any significant anomaly, with medians between Ce/Ce*=1.00-1.06, which is a negligible positive Ce anomaly.

6.1.8 Vanadium and Arsenium

Both vanadium and arsenium are redox sensitive elements, due to their multiple valence states. Incorporation of V^{5+} and As^{5+} into apatite structure requires a high oxygen fugacity. Therefore, high amounts of V and As are correlated to a high oxygen fugacity (oxidising environment), whereas low amounts of these elements are usually related to low oxygen fugacity (reducing environment).

The V contents (interquartile 4-17 ppm, median 9 ppm) do not have enough variation to be efficient discriminators among groups (Fig. 6.2g). Nevertheless, some observations can be drawn from As concentrations (interquartile 7-19 ppm, median 11 ppm) (Fig. 6.2h). Arsenic, alongside Si, is one of the few elements that substitutes into the P site of apatite. Concentrations of As are significantly higher in the Luizão deposit (median 36 ppm). Luizão apatite also displays a broader range of As concentrations (interquartiles between 20-154 ppm). Elsewhere, As contents are significantly lower and with a narrower concentration range, with medians at around 8-15 ppm and with a maximum upper quartile of 17 ppm.

6.1.9 Thorium and Uranium

Thorium concentrations range from 0.2 to 393 ppm, and have a median of 10 ppm (Fig. 6.2i). They are higher in the barren host rocks of the Francisco deposit (median 25 ppm) and in the hydrothermal zone of the Luizão deposit (median 40 ppm). They are lower in the X1 deposit (median 18 ppm) and in the Teles Pires Intrusive Suite (median 4 ppm). The Th concentrations are slightly higher in the hydrothermal zone of the Pé Quente deposit (median 8 ppm) than in the barren host rock of the same deposit (median 6 ppm).

Uranium concentrations range from below the detection limits (<0.1 ppm) to 134 ppm, with a median of 15 ppm (Fig. 6.2j). The U contents are higher in the Luizão

(median 39 ppm) and Francisco (median 25 ppm) deposits, intermediate in the X1 deposit (median 17 ppm), and lower in the Teles Pires granite (median 4 ppm) and in the Pé Quente deposit (either in the barren host rock, with a median of 6 ppm, and in the hydrothermal zone with a median of 8 ppm).

6.1.10 Boron, Scandium, Galium, Germanium, Rubidium, Zircon, Niobium, Hafnium and Tantalum

These elements are often below the detection limits in most analyses and usually do not surpass 50 ppm. However, they can offer scrutable information. Boron, for instance, is detected only in the Teles Pires granite (ranging from 2 to 19 ppm), in the Luizão deposit (2-227 ppm), in grey-luminescent apatite from the Pé Quente deposit (7-58 ppm; sample SPQ-1), and in apatite from barren host rocks of the Pé Quente deposit (2-71 ppm). On the other hand, Sn contents have lower detection limits and concentrations (with a median of 0.88 ppm), and are only detected sporadically. Galium contents are mostly below the detection limits, except for the Luizão deposit where apatites display outliers with Ga contents of 22 ppm, 151 ppm and 185 ppm. Otherwise, Ga contents are too low and display a median of 0.5 ppm. Niobium and zircon contents are also mostly below the detection limits.

Germanium concentrations may be an efficient discriminator. The Ge contents range from 10 to 368 ppm, and display a median of 63 ppm and interquartiles between 39-167 ppm (Fig. 6.2k). Higher Ge contents occur in apatites from the Teles Pires granite (median 212 ppm) and from the hydrothermal zones of the X1 deposit (median 85 ppm) and Pé Quente deposit (median 168 ppm), while lower Ge contents occur in the Luizão deposit (median 47 ppm) and in the barren zone of the Pé Quente (median 39 ppm) and Francisco (median 63 ppm) deposits. Other elements, such as Rb, Hf and Ta do not clearly exhibit any distribution patterns, since most of them are below the detection limits.

6.2 Magnetite chemistry

6.2.1 Iron and titanium

Iron is the major constituent of magnetite, and it varies considerably from 60.73 to 72.08 wt. % (Fig. 6.5a). The median of Fe contents is 71.06 wt. %, which indicates that the lower range of Fe contents are represented by just a few magnetite grains, i.e. only sample RA69, from the K-feldspar alteration zone of the Pé Quente deposit (type 3 magnetite), that has particularly low Fe contents (median 61.78 wt. %). Otherwise, the phyllic alteration zone of the Pé Quente deposit (type 4 magnetite) yields higher Fe concentrations (median 70.97 wt. %) similar to the barren zone of the same deposit (types 1 and 2; median 71.20 wt. %), the plutonic host rock of the Francisco deposit (median 71.66 wt. %) and the barren Teles Pires granite (median 69.26 wt. %). The Fe contents in the granite-related magnetite are generally higher than in the volcaniclastic unit (Fig. 6.5a, 6.6a). Moreover, iron oxide grains from the volcaniclastic unit display higher Fe contents in the hydrothermal zone (median 67 wt. %) than in the barren zone (median 64.77 wt. %) (Fig. 6.6a). Therefore, volcaniclastic iron oxide displays an inverse behaviour than that of granite-related magnetite, which has lower Fe contents in the hydrothermal zone.

Titanium concentrations vary from 11 ppm to 4.64 wt. % in the granitic rocks (Fig. 6.5b). Magnetite with the lesser Fe contents has the highest Ti contents, and vice-versa. This proportionally inverse behaviour occurs mainly because of magnetite solid solution in titanomagnetite(ss) that replaces Ti for Fe. Exsolved phases of ilmenite are only seen at the Teles Pires intrusive suite, as trellis- and sandwich-type exsolution lamellae. These Ti contents are assumed to be in solid solution with titanomagnetite. Possible nanoinclusions and contaminations will be further evaluated in Section 7.2.6. The Ti contents are higher and have a wider compositional range in the hydrothermal zone of the Pé Quente deposit (median 4.27 wt. %). This wider range is the result of two different samples, RA69 and RA24 (representing type 3 and type 4 magnetites, from the potassic and phyllic alteration zones, respectively) having two roughly different Ti concentrations (medians 4.45 wt. % for the former and 950 ppm for the latter). This distribution pattern is also seen for Fe and other cations. Titanium and most other trace elements partition differently in hydrothermal and magmatic conditions. The Ti contents are much lower in the barren zone of the Pé Quente deposit (types 1 and 2, with medians of 0.1 wt. % and 0.21 wt. %, respectively), in the host granodiorite of the

Francisco deposit (median 122 ppm) and in the Teles Pires Intrusive Suite (median 3,055 ppm).

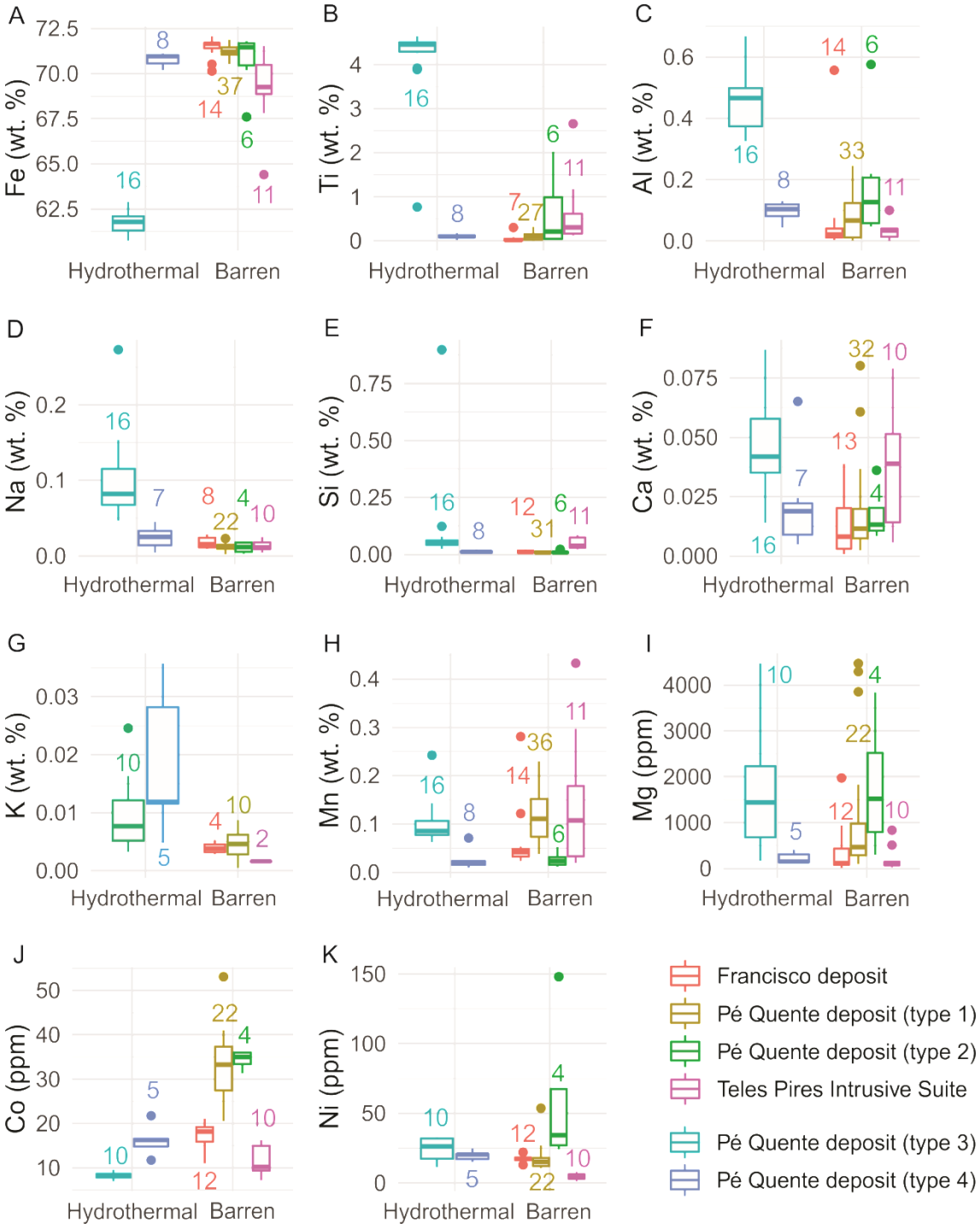

Figure 6.5 – Box and whisker plots for major, minor and trace elements in magnetite from plutonic units. Some elements are shown in weight percentage (wt. %), while others are shown in parts per million (ppm). The box corresponds to the interquartile range (between 25th-75th percentile), and the whiskers correspond to the 5th to 25th percentiles (lower whisker) and 75th to 95 percentiles (upper whisker). The line inside the box is the median value. The closed circles are the <5th and >95th percentiles. The numbers above or beneath the whiskers correspond the number of samples (n).

In the volcaniclastic unit of the Francisco deposit, Ti contents follow an opposite trend than in the intrusion-hosted deposits (Fig. 6.6b). Volcaniclastic magnetite from the barren zone has higher Ti concentrations (median 2.69 wt %) than those from the hydrothermal zones (median 0.14 wt %). Since volcaniclastic iron oxides were too small to be ablated by LA-ICP-MS, they were only analysed by EMPA, which allowed for only a limited quantity of trace elements to be investigated.

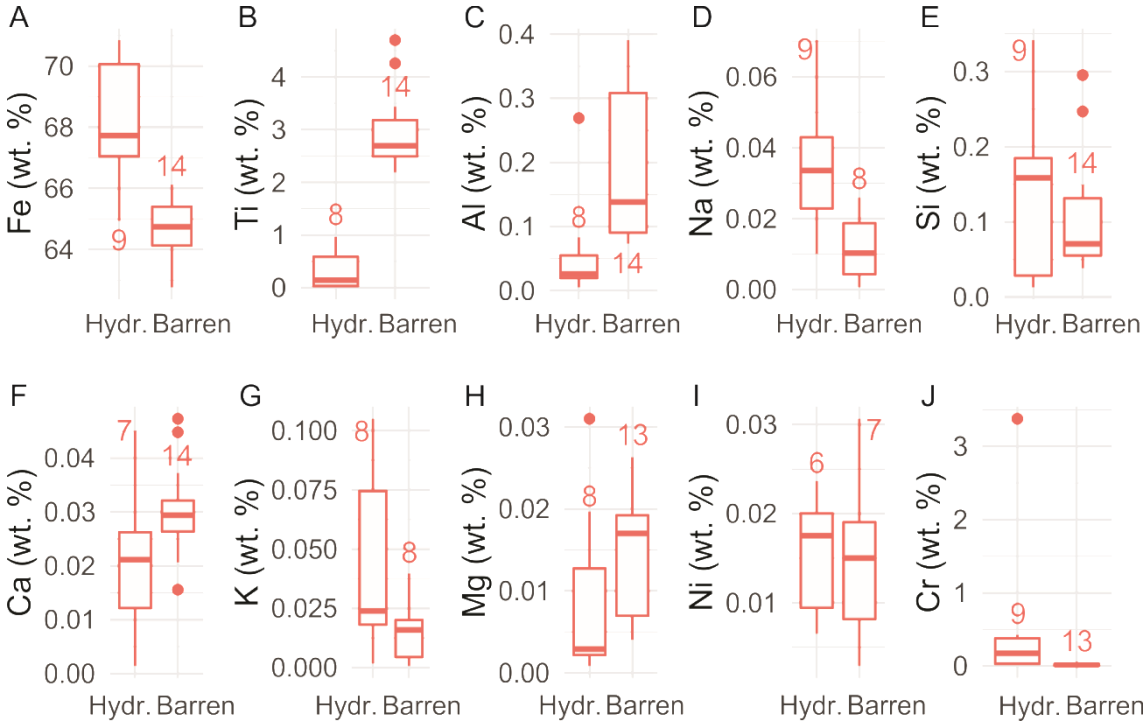

Figure 6.6 – Box and whisker plots for major and minor elements in iron oxides from the barren and hydrothermal zones of the volcaniclastic sequence of the Francisco deposit. All elements are shown in weight percentage. The box corresponds to the interquartile range (between 25th-75th percentile), and the whiskers correspond to the 5th to 25th percentiles (lower whisker) and 75th to 95 percentiles (upper whisker). The line inside the box is the median value. The closed circles are the <5th and >95th percentiles. The numbers above or beneath the whiskers correspond the number of samples (n).

6.2.2 Aluminium

Aluminium concentrations have a median of 762 ppm and interquartiles between 200-1,784 ppm in magnetite related to granitic rocks (Fig. 6.5c). The highest Al contents occur in magnetite from the hydrothermal zone of the Pé Quente deposit[7]

[7] Types 3 and 4 magnetites are often reffered to in the text as “magnetite from the hydrothermal zone of the Pé Quente deposit” due to the low sample size of each individual type (that may be as low as n=10 and n=5, respectively.) However, the distinction between them is regularly emphasised because type 4 magnetite has a composition much more similar to those of the barren host rocks (types 1 and 2) than those of the potassic alteration zone (type 3). Likewise, types 1 and 2 magnetite are often not distinguished in the text because of their similar composition, and are mutually reffered to as “magnetite from the barren host rocks of the Pé Quente deposit”.

(median 3,685 ppm). Elsewhere, Al contents are much lower, such as in the Teles Pires granite (median 347 ppm), in the barren zones of the Pé Quente (median 761 ppm), and in the plutonic host rock of the Francisco deposit (median 215 ppm). In the volcaniclastic unit, Al contents are considerably higher in the barren zone (median 1,382 ppm) than in the hydrothermal zone (median 259 ppm) (Fig. 6.6c).

6.2.3 Sodium, silicon, calcium and potassium

Sodium contents are consistently higher in magnetite from the hydrothermal zone, especially within potassic alteration (type 3; median 820 ppm). This is valid for both the intrusion-hosted Pé Quente deposit and the volcaniclastic-hosted Francisco deposit (Fig. 6.5d, 6.6d). The Na contents are higher in the hydrothermal zone of the volcaniclastic unit (median 336 ppm) and lower in the barren zone (median 143 ppm). Similarly, Na contents are considerably higher in the hydrothermal zone of the Pé Quente deposit (median 688 ppm) than in its barren zone (median 124 ppm). Other barren zones display low Na contents with a median of 111 ppm in the Teles Pires granite, and a median of 153 ppm in the plutonic host rock of the Francisco deposit. Overall, in magnetite from granitic rocks, Na contents have a median of 161 and interquartiles between 20-399 ppm.

Silicon contents have interquartiles between 78-312 ppm and a median of 130 ppm in granite-related magnetite (Fig. 6.5e). These Si contents in the hydrothermal zone of the Pé Quente deposit have the highest values, with a median of 383 ppm. The Si contents are lower in magnetite from the barren zone of the Pé Quente deposit (median 81 ppm), from the plutonic host rock of the Francisco deposit (median 102 ppm), and from the barren Teles Pires granite (median 37 ppm). For the volcaniclastic iron oxides of the Francisco deposit, Si concentrations are higher in the hydrothermal zone (median of 1,586 ppm) and lower in the barren zone (median of 708 ppm) (Fig. 6.6e).

Calcium concentrations have interquartiles between 88-373 ppm and a median of 156 ppm in magnetites from granitic rocks. These Ca concentrations are considerably higher in the hydrothermal zone of the Pé Quente deposit (median 353 ppm) than in the barren zone (median 115 ppm) (Fig. 6.5f). They are also higher in the Teles Pires Intrusive Suite (median 388 ppm), but lower in the plutonic host rock of the Francisco deposit (81 ppm). In the volcaniclastic unit of the Francisco deposit, Ca contents are

higher in the barren zone (median 294 ppm) and lower in the hydrothermal zone (median 211 ppm) (Fig. 6.6f).

Potassium concentrations (interquartiles 82-262 ppm and median 130 ppm in the plutonic units) are higher in the hydrothermal zones of the Pé Quente deposit (median 195 ppm) than in the barren zone (median 138 ppm) (Fig. 6.5g). The lowest K concentrations occur in the Teles Pires granite (median 95 ppm) and in the plutonic host rock of the Francisco deposit (median 108 ppm). In the hydrothermal zone of the volcaniclastic unit of the Francisco deposit, K contents are higher (median 234 ppm) than in the barren zone (median 158 ppm) (Fig. 6.6g).

6.2.4 Manganese, magnesium, cobalt, nickel, gallium and chromium

Manganese contents have interquartiles between 407-1,231 ppm, and a median of 770 ppm in the plutonic units. They are higher in the Teles Pires Intrusive Suite (median 1,075 ppm) and in the hydrothermal zone of the Pé Quente deposit (median 949 ppm) (Fig. 6.5h). The barren zone of the latter deposit has intermediate Mn concentrations (median 772 ppm), and the plutonic host rock of the Francisco deposit has the lowest Mn contents (median 420 ppm). In the volcaniclastic unit of the Francisco deposit, magnetite grains from the barren (median 517 ppm) and hydrothermal zones (median 552 ppm) have similar concentrations of Mn.

Magnesium contents have interquartiles between 132-951 ppm, and a median of 398 ppm in the plutonic units. They are higher in the hydrothermal zones of the Pé Quente deposit (median 660 ppm) than in the barren zones (520 ppm) (Fig. 6.5i). The lowest Mg contents occur in magnetite from the Teles Pires granite (median 92 ppm) and from the plutonic host rock of the Francisco deposit (median 115 ppm). In the volcaniclastic unit of the Francisco deposit, Mg contents are higher in the barren arcosian sandstone (median 170 ppm) than in the propylitic-altered zone (median 28 ppm) (Fig. 6.6h).

Cobalt occurs very strictly, in minor concentrations (interquartiles 10-31 ppm and median 18 ppm in the plutonic units). Cobalt concentrations are slightly higher in the barren zones of the Pé Quente (median 33 ppm) and Francisco deposit (median 18 ppm), and lower in the hydrothermal zone of the Pé Quente deposit (median 8 ppm) and Teles Pires granite (median 10 ppm) (Fig. 8j). As a rule of thumb, potassic-related magnetite (type 3) has a higher trace element concentration than phyllic-related

magnetite (type 4) for all elements, except Co, Ni, Ga, Cr and Se. Since the volcaniclastic iron oxide grains were below the size of the laser ablation (<35-µm), Co contents were not analysed there. Other elements that were not captured by EMPA, such as Ga, Zn, Pb, Sn, Ba, Se, and Zr, were displayed only for the granitoid-related magnetite in which LA-ICP-MS data were available.

Figure 6.7 – Box and whisker plots for trace elements in magnetite from plutonic units. All elements are shown in parts per million (ppm). The box corresponds to the interquartile range (between 25th-75th percentile), and the whiskers correspond to the 5th to 25th percentiles (lower whisker) and 75th to 95 percentiles (upper whisker). The line inside the box is the median value. The closed circles are the <5th and >95th percentiles. The numbers above or beneath the whiskers correspond the number of samples (n).

Nickel concentrations display interquartiles between 11-21 ppm and a median of 16 ppm for the plutonic units (Fig. 6.5k). Nickel concentrations are higher in the hydrothermal zone of the Pé Quente deposit (median 23 ppm), intermediate in the barren zones of the Pé Quente deposit (15 ppm) and Francisco deposit (17 ppm), and substantially lower in the Teles Pires granite (median 4 ppm). Moreover, Ni contents are

roughly equivalent in the volcaniclastic iron oxide grains of both zones of the Francisco deposit (Fig. 9I) (Fig. 6.6i).

Galium concentrations (interquartiles 9-36 ppm, median of 21 ppm) are highest and have the widest ranges in magnetites from the Teles Pires granite (median 29 ppm) and in the barren zone of the Pé Quente deposit (median 30 ppm) (Fig. 6.7a). Other units have very narrow ranges of Ga concentrations. The hydrothermal zone of the Pé Quente deposit has slightly lower Ga contents (median 21 ppm), but the lowest contents occur in the barren host granodiorite of the Francisco deposit (median 6 ppm).

Chromium concentrations (with median 81 ppm and interquartiles between 47-150 ppm in granitic rocks) are highest in the barren host granodiorite of the Francisco deposit (median 161 ppm) (Fig. 6.7b). In the Pé Quente deposit, Cr contents are higher in the barren zone (median 103 ppm) than in the hydrothermal zone (median 74 ppm). Magnetite Cr concentrations are considerably higher in the hydrothermal zone of the volcaniclastic unit of the Francisco deposit (median 1,733 ppm) than in the barren zone (median 122 ppm) (Fig. 6.6j). The lowest Cr contents occur in the Teles Pires granite (median 19 ppm).

6.2.5 Zinc, lead, tin, barium, selenium and zirconium

Zinc concentrations (interquartiles 406-1,405 ppm, median 712 ppm) are higher in the hydrothermal zone of the Pé Quente deposit (median 4,524 ppm) and lower in the barren zone (median 538 ppm) (Fig. 6.7c). Other barren granitoids also have low Zn concentrations, such as in the Teles Pires granite (median 924 ppm) and in the plutonic host rock of the Francisco deposit (median 445 ppm).

Lead concentrations (interquartiles 1-118 ppm, median 2 ppm) are higher in the Teles Pires granite (median 206 ppm), and lower in the hydrothermal zone of the Pé Quente deposit (median 166 ppm) (Fig. 6.7d). However, Pb concentrations are almost absent in the barren zones of the Pé Quente deposit and in the plutonic host rock of the Francisco deposit.

Tin concentrations (interquartiles 5-31 ppm, median 13 ppm) are likewise minimal in the barren zones of the Francisco and Pé Quente deposits (with medians lower than 10 ppm) (Fig. 6.7e). However, Sn concentrations are higher in the hydrothermal zone of the Pé Quente deposit (median 28 ppm) and highest in the Teles Pires granite (109 ppm). Barium contents (interquartiles 4-19 ppm, median 9 ppm)

display similar distribution patterns as Pb and Sn, with minimal contents in the barren zones of theFrancisco and Pé Quente deposits, and higher contents in the hydrothermal zone of the Pé Quente deposit (median 24 ppm) and in the Teles Pires granite (11 ppm) (Fig. 6.7f).

Selenium contents (interquartiles 8-13 ppm, median 10 ppm) are more balanced between the evaluated units, such as in the Teles Pires granite (median 9 ppm), in the hydrothermal zone of the Pé Quente deposit (median 15 ppm), and in the barren zones of the Francisco (median 10 ppm) and Pé Quente deposit (median 9 ppm). Zirconium contents (interquartiles 1-12 ppm, median 2 ppm), on the other hand, are highest in the Teles Pires granite (median 6 ppm) and in the hydrothermal zone of the Pé Quente deposit (median 29 ppm), but barely detectable in the barren zones of the Francisco and Pé Quente deposit. Other elements, such as Zr, Y, Nb, Mo, La, Ce, Pr, Nd, Sm, Gd, Dy, Er, Yb, Th, and U, have medians below 5 ppm, except for the Teles Pires granite in which they display medians between ~10-20 ppm. All other elements are not detectable or have negligible contents, such as As, Cu, Eu, Tb, Tm, Lu, Hf, Ta and W. Sample RA73 (barren Pé Quente) is the one exception in which W has a higher median of 11 ppm.

Chapter 7

Discussions

7.1 Apatite

7.1.1 Discriminant analysis

PCA is a multivariate statistical method that identifies the best discriminant elements in apatite and which of these elements cluster together towards specific magmatic-hydrothermal reactions. Principal component data were analysed as a compositional dataset (Aitchison, 1982; Van den Boogaart and Tolosana-Delgado, 2013). Principal component arrow lengths are dependent on whether the variables are near-constant (short arrows) or highly variable (long arrows). In the covariance biplot (Fig 7.1), the longest arrows are F and Mn, which coordinate most of the Principal Components 1 and 2 respectively (Fig. 7.2). They are the most abundant elements in apatite. Since arrow lengths correspond to the sheer amount of element variation in

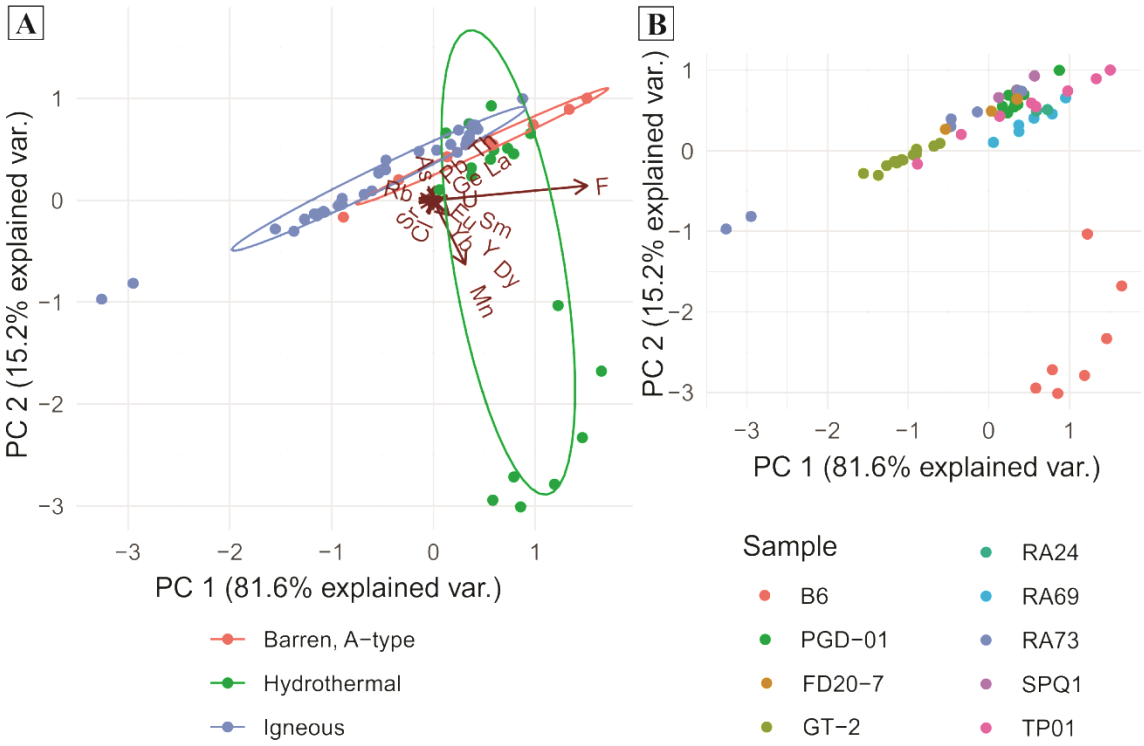

Figure 7.1 – Principal component multiplots of (a) classification scores and element loadings with Mahalanobis distances outlining clusters of data, and (b) sample scores of apatite in deposits from this study, plotted on the first and second principal component axes (PC1 and PC2) that account for 81.6% and 15.2% of the total explained variance, respectively. Teles Pires granite (TP01). X1 deposit (B6). Luizão deposit (BS-07). Francisco deposit (PGD0-1). Pé Quente: barren (GT-2, RA73, FD20-7) and hydrothermal (RA24, RA69, SPQ-1).

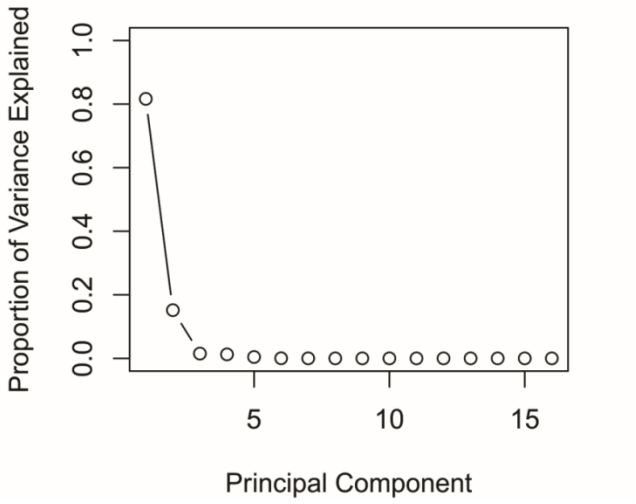

Figure 7.2 – Scree plot with the principal components of apatite analysis and the proportion of variation that each principal component explains.

apatite, the most useful information out of the covariate biplot is the angular difference (rotation) between the elemental variables.

Principal components are roughly merged in three separate clusters: (1) Mn, Sm, Eu, Dy, Yb and Y; (2) F, La, Pb, Th, U and Ge; and (3) Cl, Sr and As. Firstly, apatites from the hydrothermal zone of the X1 deposit (sample B6) are dispersed along Mn, Sm, Eu, Dy, Yb and Y arrows, which have less than 45º between each other (Fig. 7.1a). Secondly, at about 90º anticlockwise from these arrows, propylitic- and phyllic-related apatites from the Pé Quente deposit are coordinated by elements such as La, Pb, Th, and Ge (Fig. 7.1a). These elements also coordinate apatite compositions from the Teles Pires granite and from the plutonic host rock of the Francisco deposit. Element F has the longest arrow and is positioned mid-way between the (1) and (2) elemental clusters (at ~45º) (Fig. 7.1a). It is interpreted as a common feature between these clusters. F has a similar rotation to U, but it explains the variation of PC1 to a much higher degree than the latter. Thirdly, elements Cl, Sr and As are important discriminants for magmatic fractionation. Cl and Sr are magmatic discriminators that are opposed orthogonally and diametrically to elements related to other clusters that represent hydrothermal processes (Fig. 6.1a). Element As is slightly offset, and coordinates apatites from the barren zone of the Pé Quente deposit (RA73) (Fig. 7.1b). The As-bearing apatites from the Luizão deposit were kept out of the PCA since they did not have Cl and F contents evaluated by EPMA. But if Cl and F were excluded from the PCA, Luizão apatites would be coordinated alongside the As arrow. Ultimately, each of these elemental clusters corresponds to a different magmatic-hydrothermal process: (1) Mn, Sm, Eu, Dy, Yb and

Y are mostly related to the phyllic alteration (type 2 apatite), (2) F, La, Pb, Th, U and Ge are mostly related to the potassic alteration overprinted by propylitic alteration (type 3 apatite), and (3) Cl, Sr and As are mostly related to magmatic fractionation (type 1 apatite).

These apatite elemental concentrations were applied to the discriminant functions of Mao et al. (2016) that were trained with a more robust dataset (Figure 7.3). Mao et al. (2016) gathered apatite grains from various mineral deposit types, and from different host rocks and tectonic settings. They classified each apatite as a hydrothermal or igneous grain depending on whether it was from a hydrothermal vein or whether it was distal from the mineralization, as part of the barren zone. After classification, they applied a linear discriminant analysis (LDA) to discriminate each mineral deposit type. Such stepped discriminant diagrams are dimensions of the same discriminant analysis (Figs. 7.4, 7.5, 7.6, 7.7), and should be conjointly analysed (Fig. 7.3).

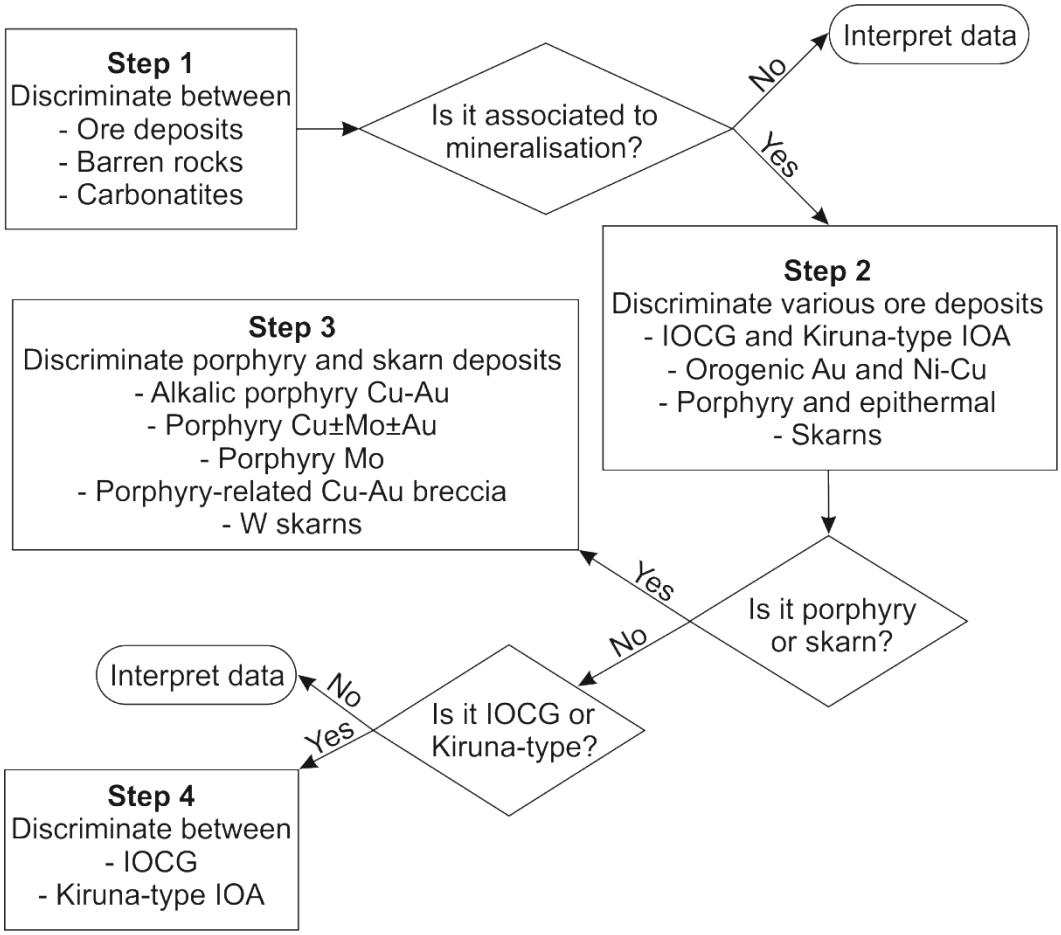

Figure 7.3 – Flow chart describing procedural steps for linear discriminant analysis of apatite concentrations, as undertaken by Mao et al. (2016). Step 1 is further displayed in Figure 7.4; Step 2 is displayed in Figure 7.5; Step 3 is shown in Fig. 7.6; and Step 4 is not shown.

Predictably, anorogenic Teles Pires apatite consistently plots in the field of barren rocks (Fig. 7.4). However, most apatites from the phyllic and propylitic alterations of the Pé Quente deposit (SPQ-1, RA69, RA24) also fall under the barren field (Fig. 7.4). Such samples were nevertheless proceeded to further steps (Figs. 7.5, 7.6, 7.7), given that their geological descriptions (Table 4.1) concur with the concept of "hydrothermal apatite" in Mao et al. (2016). Moreover, apatite grains from the barren Pé Quente zone are actually spread out in the ore deposits field (RA73, FD20-7, and GT-2). These igneous apatites were then excluded from further steps, except for GT-2 sample that contains a slightly higher degree of propylitic alteration as determined *a posteriori* (it is also associated with type 2 "transitional" magnetite, Section 5.2; Table 4.1). Hence, this first step renders paradoxical results that warn us that phyllic- and propylitic-related apatites were not initially conceptualised in these discriminant functions. But this step also indicates that apatites from barren host rocks actually retain the geochemical signature of the magma source linked to mineralisation.

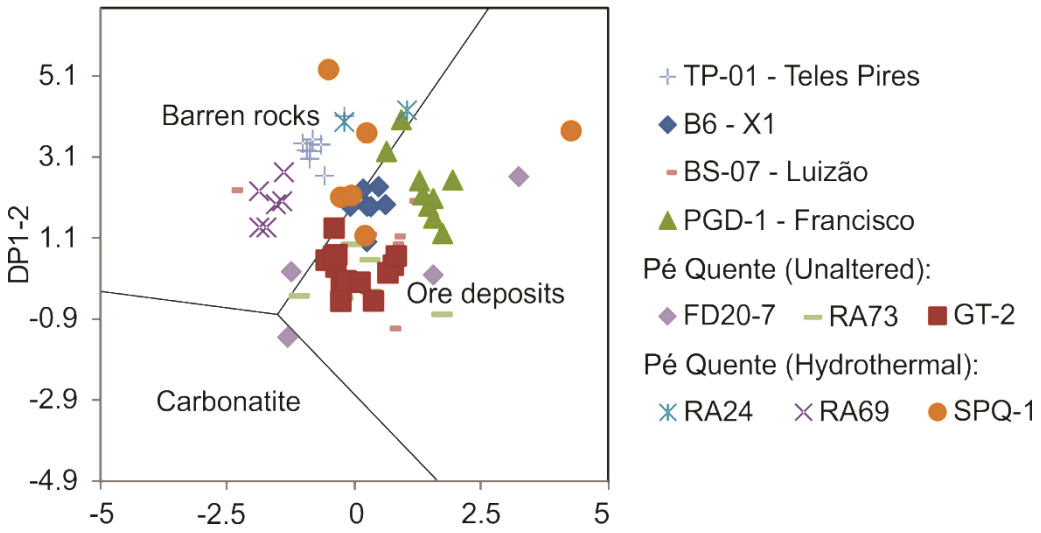

Figure 7.4 – Discrimination diagrams (Step 1) for apatites from carbonatites, barren rocks, and hydrothermal ore deposits (Mao et al., 2016). Samples correspond to: Teles Pires granite (TP01). X1 deposit (B6). Luizão deposit (BS-07). Francisco deposit (PGD0-1). Pé Quente: barren (GT-2, RA73, FD20-7) and hydrothermal (RA24, RA69, SPQ-1).

To further evaluate hydrothermal zones, Mao et al. (2016) developed discriminant functions for several types of ore deposits (Fig. 7.3). We plotted hydrothermal-related apatites (from strongly to weakly altered zones; GT-2, RA24, RA69, SPQ-1) in these discriminant functions (Fig. 7.5) and left out igneous apatites from barren zones (TP-01, FD20-7, RA73). Apatite from the X1 deposit consistently

falls under the porphyry Cu-Mo-Au and epithermal Au-Ag fields, whereas apatites from the Luizão deposit falls under the fields of orogenic Au and Ni-Cu deposits. A few apatites related to the potassic and propylitic alteration from the Pé Quente deposit tend to plot in the IOCG and Kiruna-type deposit fields (specifically sample RA69, most likely because of high temperature K silicate alteration), while others tend to plot in the porphyry fields (samples RA24 and SPQ-1). Most other apatites from slightly altered propylitic halos fall between the skarn, porphyry and epithermal fields.

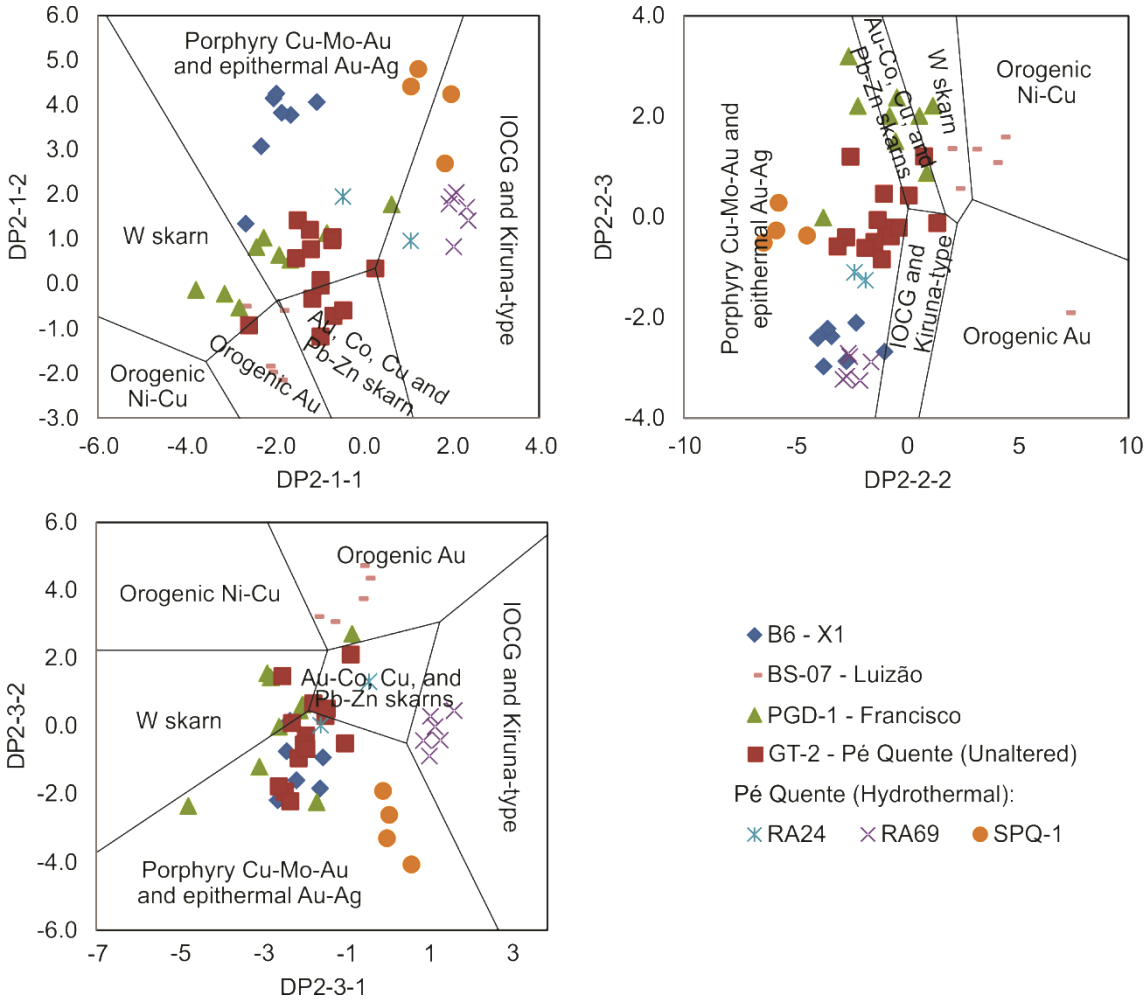

Figure 7.5 – Discrimination diagrams (Step 2) for apatites from different ore deposits (Mao et al., 2016). Samples correspond to: X1 (B6), Luizão (BS-07), Francisco (PGD-1), and Pé Quente (GT-2, RA69, RA24, SPQ-1) deposits.

To better discriminate between porphyry and skarn types, Mao et al. (2016) developed a further third step (Fig. 7.6), and a fourth step to discriminate IOCG and Kiruna-type deposit. Apatite from the X1 deposit consistently falls under the porphyry Cu-Mo-Au field, while Pé Quente apatite falls either at the porphyry Mo and Cu-Mo-Au fields (RA24 and RA69), or at the IOCG and Kiruna-type fields (SPQ-1) (Fig. 7.5,

Table 7.1 – Coefficients for Discriminant Functions of Mao et al. (2016).

Variables	Mg	V	Mn	Sr	Y	La	Ce	Eu	Dy	Yb	Pb	Th	U	Constant
DP1-1			-0.064	- 1.559	2.608	0.363	- 1.76	0.624	- 3.641	0.708	-1.178	0.416	0.962	7.588
DP1-2			0.207	- 1.034	15.10	4.995	- 5.80	0.174	- 8.771	- 4.32	2.022	-0.67	0.020	-10.4
DP2-1-1			-2.275	- 1.429	1.503		3.246	-1.087	0.192	0.763		- 0.05	-1.538	- 3.65
DP2-1-2			1.320	1.5758	14.62		-0.005	1.604	- 17.50	3.250		- 0.24	-1.155	- 20.2
DP2-1-3			0.009	- 1.040	1.641		1.176	-0.117	4.351	- 3.32		- 1.50	-0.085	- 12.2
DP2-2-2	1.882		-1.871	- 0.803	-12.2		-0.691	-2.014	14.83	- 3.94		-0.73	2.512	24.19
DP2-2-3	-0.30		-0.078	-1.591			-0.612	-0.291	0.722	2.686		1.465	0.423	17.26
DP2-3-1	1.034		-3.068		4.044		3.3680	-3.127	-0.23	-0.77	-0.10	-1.22	-0.223	-4.26
DP2-3-2	1.888		-1.838		- 4.81		-0.321	-3.421	10.66	- 5.66	1.705	-1.04	1.803	14.23
DP3-1	0.871		-4.155	-3.064	7.341		-1.704	-1.805		- 7.31	-0.28	0.694	1.698	21.06
DP3-2	-1.47		2.5504	- 2.981	- 5.39		0.559	-2.898		3.780	2.108	-0.410	-0.137	8.534
DP3-3	0.161		-1.172	-4.364	2.634		0.845	3.377		-3.184	1.619	1.956	-0.621	4.471
DP4-1		-5.37	1.02	1.000			- 0.044	3.169		-5.412	-0.33	0.108		5.384

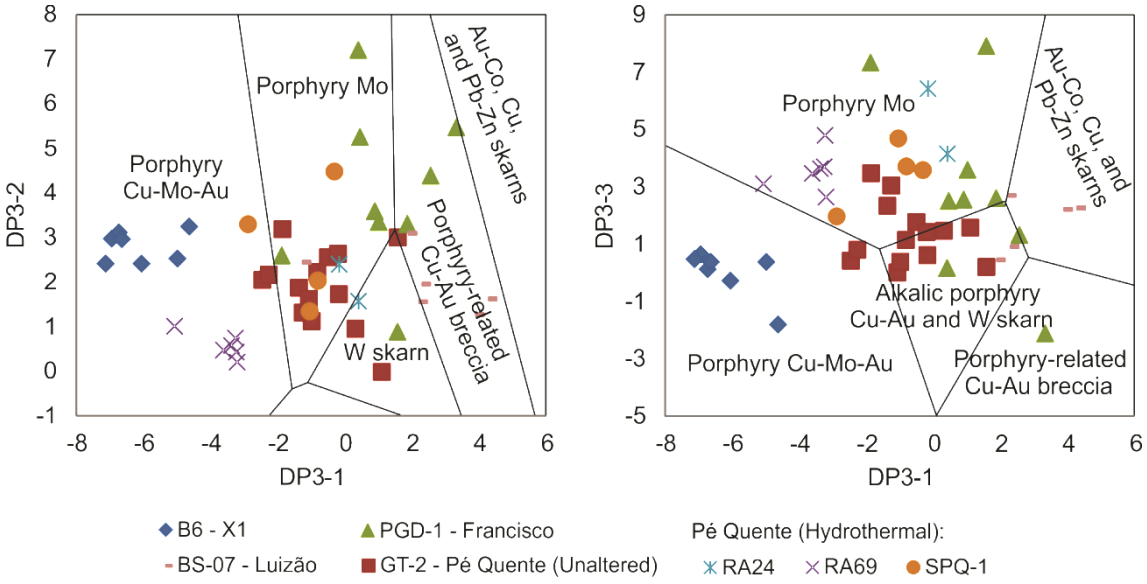

Figure 7.6 – Discrimination diagrams (Step 3) for apatites from different porphyry and skarn deposits (Mao et al., 2016). Samples correspond to: X1 (B6), Luizão (BS-07), Francisco (PGD-1), and Pé Quente (GT-2, RA69, RA24, SPQ-1) deposits.

7.6). Slightly propylitic-altered apatites (GT-2 and PGD-1) are spread along the W skarn, porphyry Mo and alkalic porphyry Cu-Au fields. Apatite from the Luizão deposit falls almost randomly in Figure 7.6, probably because such diagrams do not discriminate for orogenic Au deposits (Fig. 7.5). On the fourth step, Pé Quente apatites do not display relevant plot patterns, since they are probably neither IOCG nor Kiruna-type deposits.

7.1.2 Texture and luminescence

Magmatic processes primarily influence growth zonation in apatite (concentric, oscillatory and sector zonations, as in Zirner et al., 2015). Hydrothermal processes, on the other hand, will tend to cause dissolution-reprecipitation textures (Zirner et al., 2015; Broom-Fendley et al., 2016). It is difficult to draw the line between which apatite is hydrothermal or magmatic regarding only its morphology and texture. The relationship between textures and hydrothermal processes will be gathered and more broadly discussed in Sections 7.3 and 7.5.

Yellow-green-luminescent apatite often occurs with orange-brown cores or rims, and is typical of the accessory phase of the barren granitoids (Fig. 5.3f-h, 5.14e-f). The yellow luminescence in apatite occurs due to Mn^{2+} uptake in the Ca(II) site, and is typical of igneous-related apatite (Kempe and Götze, 2002; Götze, 2012; Bouzari et al., 2016). Even though dissolution-reprecipitation textures are intensified in pervasive

hydrothermal zones, they are likewise present to a lesser degree in igneous-related apatite. Other luminescence patterns in hydrothermal apatite are somewhat different from those described in the literature. Table 7.2 shows a summary of the apatite luminescence/chemical properties in our work and in Bouzari et al. (2016).

Table 7.2 – Comparison of CL analysis of apatite in this work with Bouzari et al. (2016).

Source	CL	Alteration type	Element concentrations
This work	Yellow-green	Unaltered	Mn-, REE-poor; except for TP01 (REE-rich)
	Green or purple	Phyllic alteration	Mn-, HREE-, Y-rich, LREE-intermediate
	Gray	Propylitic alteration (± potassic)	Mn-intermediate, Ge-rich, LREE-rich
Bouzari et al. (2016)	Yellow-green	Unaltered	REE+Y-, Mn-, Cl-, Na-rich
	Green	K-feldspar alteration	REE+Y-, Mn-, Cl-, Na-intermediate
	Gray	Phyllic alteration	REE+Y-, Mn-, Cl-, Na-poor

In Bouzari et al. (2016), green-luminescent apatite occurs with the K-feldspar alteration and is hypothesised to depend on the depletion of the Mn/Fe ratio. In our work, strongly saturated green-luminescent apatite occurs with the phyllic alteration (Fig. 5.4) and is actually enriched in Mn (enlargement of Mn/Fe ratio instead of depletion). There is also enrichment in Fe in green-luminescent apatite from our work, but to a lesser degree than Mn enrichment. Phyllic alteration, according to Bouzari et al., (2016), would cause acidic fluids to turn apatite luminescence to grey. In our work, grey-luminescent apatite occurs in K-feldspar altered rocks that are overprinted by propylitic alteration. It is associated with both potassically altered magnetite (sample RA69) and with the propylitic assemblage (sample SPQ-1). Thus, grey-luminescent apatite has been altered by potassic alteration and selectively replaced by propylitic alteration; the extent of each is unknown. Grey-luminescent sectors often occur as patchy textures within yellow- and green-luminescent apatite (Fig. 5.4d-f, 5.9f-h). Complete apatite recrystallization due to propylitic alteration processes create homogeneous, grey-luminescent, and prismatic to needle-like apatite grains in the Pé Quente deposit (Fig. 5.5).

The incorporation of Fe^{2+} or As^{5+} is thought to quench apatite luminescence into a dull glow (Perseil et al., 2000; Götze, 2012), whereas REE activation may tint apatite in blue and violet CL colours (Kempe and Götze, 2002). However, violet-luminescent apatite from the Luizão deposit displayed very low REE concentrations and distinctly higher As concentrations, while dull gray-luminescent apatite displayed high REE concentrations. Therefore, As is thought to activate violet CL colours in apatite from the Luizão deposit, and high LREE are thought to induce the quenching of propylitic-related apatite from the Pé Quente deposit. But there are many other factors at play in CL besides elemental concentrations. In fact, any material science technology that relies on defected lattice site structures, such as CL, will render imperfect results (Pagel et al., 2000; Nasdala et al., 2013).

7.1.3 Sr, REY and halogens in apatite as indicators of magmatic fractionation

Strontium occupies almost exclusively the Ca(II) site in apatite (Rakovan and Hughes, 2000) (Fig. 2.2), and it follows an opposite trend relative to other trace elements in apatite (Prowatke and Klemme, 2006). It is compatible in apatite (D>1) and is incorporated early during apatite crystallisation, while other trace elements are incompatible (D<1) until later crystallisation stages (Watson and Green, 1981). Strontium is steadily incorporated into plagioclase and is depleted in the melt and apatite at more evolved stages of magmatic fractionation (Prowatke and Klemme, 2006). Furthermore, Sr contents in apatite mimic those reported in whole rocks (Belousova et al., 2001; Bruand et al., 2014; 2016; 2017; Mao et al., 2016), being higher in mafic magmas and gradually lower towards felsic magmas (Belousova et al., 2001; Piccoli and Candela, 2002).

Depletion in Sr occurs in hydrothermal apatites, while enrichment in Sr occurs in magmatic apatites from the Pé Quente and Luizão deposits. The distribution of Sr in apatite is also correlated with the temporal evolution of magmatic activity in the region. For instance, the highest Sr concentrations prevail in the oldest intrusions (Pé Quente and Nhandu intrusive suites; 1.98-1.96 Ga), while the lesser Sr concentrations prevail in the youngest intrusions. Apatite from the postorogenic Matupá Intrusive Suite (União granodiorite; ~1.85 Ga) has intermediate Sr concentrations, and apatite from the anorogenic Teles Pires granite (1.77-1.76 Ga) has the lowest Sr concentrations (Fig.

6.1i). This Sr trend might occur due to the decreasing availability of Sr in the crust during magmatic fractionation.

High Sr/Y is a typical property of adakites (together with high mg# and high silica) that are often formed via slab-melting of a basaltic subducted crust interacting with felsic melts (Defand and Drummond, 1990; Moyen, 2009). Since Sr and REE+Y contents in apatite are direct indicators of magmatic fractionation, Sr/Y ratio in apatite can be used to identify adakite-like rocks (Fig. 7.7) (Pan et al., 2016; Zafar et al., 2019). High Sr/Y ratios are seen in the host rocks of the Pé Quente and Francisco deposits, and in the phyllic alteration zone of the Luizão deposit.

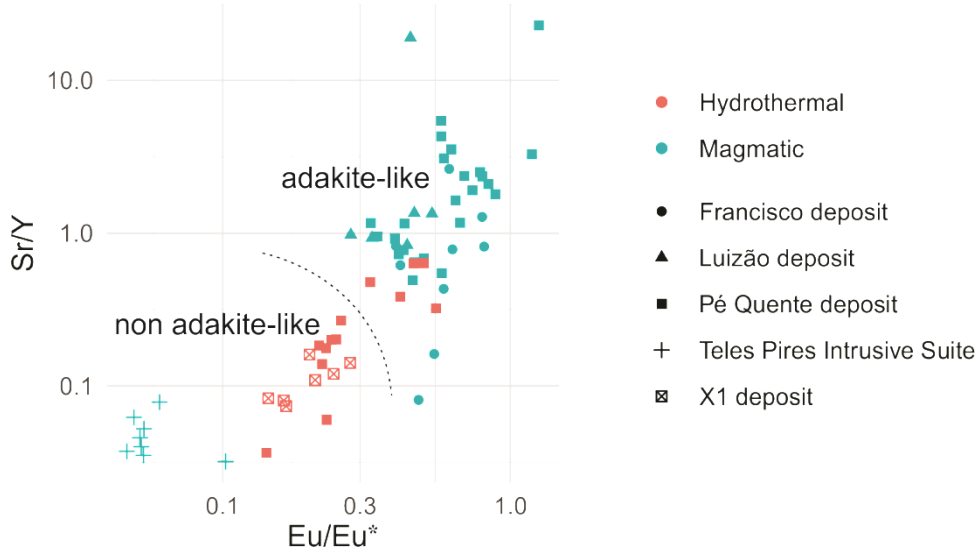

Figure 7.7 – Eu/Eu* vs. Sr/Y plot for apatites. Fields based on Pan et al. (2016).

The Luizão deposit also displays distinctly As-enriched apatites that might indicate either that: (1) metassomatic fluids have been channelled through metasedimentary rocks, or that (2) mantle-derived intrusions have been contaminated by crustal material (Guo et al., 2019). However, since As is controlled by crystallographic mechanisms and kinetic processes because of its varied oxidation states (Liu et al., 2017), As contents are mostly disregarded as efficient discriminators. Even though apatite from the Luizão deposit occurs in a hydrothermal zone, it still retains a relatively unchanged magmatic composition: (1) isolated and fractured prismatic crystals (Fig. 5.1, 5.2), (2) high Sr and low Y contents (Fig. 6.1i, 6.2e-f), and (3) high La/Yb (Fig. 6.3) – which indicate deep melting of a balsatic source according to Moyen (2009). Thus, apatite from the Luizão deposit does not reflect the chemistry of the phyllic alteration that surrounds it, and was considered an inherited igneous apatite (Fig. 7.7).

Most hydrothermal apatites from the Pé Quente deposit have low Sr/Y ratios (Fig. 7.7). The Sr/Y patterns in igneous-related apatite accurately match the high whole-rock Sr/Y ratios described by Assis (2015) for the Pé Quente and Luizão deposits. However, because Sr is mobile in ore zones (Olade and Fletcher, 1976), it is considered an unreliable magmatic indicator in altered samples (Moyen, 2009). But Sr/Y vs. Eu/Eu* in apatite (Fig. 7.7) continuously follow the magmatic-hydrothermal trend, thereby making them promising tools in further efforts for vectoring the outer propylitic and phyllic halos.

At the PCA (Fig. 7.1), Sr and REE are orthogonally opposed to each other, and that suggests a negative correlation between them. The REE are likewise sensible to magmatic and hydrothermal processes (Hoskin et al., 2000; Belousova et al., 2002; Chu et al., 2009). In Zirner et al. (2015), less evolved igneous rocks had REE incorporated into apatite by the following coupled substitution (Fig. 7.8a):

$$Ca^{2+} + P^{5+} = REY^{3+} + Si^{4+}$$

Whereas hydrothermally altered rocks were affected by the following (Zirner et al., 2015) (Fig. 7.8b):

$$2\ Ca^{2+} = REY^{3+} + Na^{+}$$

Both these reactions are displayed in Figure 7.8a-b with other common substitutions in the Ca(II) site (Fig. 7.8c).

Halogens are important in apatite, often reaching the percentile-range of total composition. Both halogens, F and Cl, are diametrically opposed to each other at the PCA of Figure 7.1. Most samples do not fall consistently in a linear trend in a Cl vs. F diagram (Fig 7.9a). Chlorine can be further used as an indicator of magmatic fractionation, in which higher Cl concentrations are roughly correlated with higher rock basicity (Xie et al., 2019) (Fig. 7.9b). As shown in Fig. 7.9a**,** most apatites are constrained within the same range of F concentrations (ranging between 3.25-4.50 wt. %), but igneous apatites have low Cl contents (0.0-0.1 wt. %) while hydrothermal apatites have slightly higher Cl contents (0.1-0.25 wt. %). The highest Cl contents occur in adakite-like Pé Quente apatites that also display the lowest F contents (<3.25 wt. %) (Fig. 7.9a).

The REE are lowest in igneous apatite (Figure 7.8b,c, 7.9c-e), except for apatites from the Teles Pires granite in which high LREE and HREE concentrations are akin to those found in hydrothermal zones (Fig. 7.9c-e). Since REE partition coefficients are enhanced by melt polymerisation (Prowatke and Klemme, 2006), these high REE

contents might be due to the fact that hydrothermal alteration in the AFMP occurs only at late orogenic stages (as suggested by Assis et al., 2017). Notwithstanding, Eu/Eu* ratios are suggested to discriminate between hydrothermal- and anorogenic-related apatites (Fig. 7.7, 7.9b), given that hydrothermal apatites retain considerably higher Eu contents than anorogenic-related apatites (Fig. 6.3). Moreover, low Eu concentrations also occur in apatite from the Luizão and Francisco deposits (Fig. 7.7b, 7.9e). This negative Eu anomaly might be due to the relict magmatic nature of apatite as a result of early partitioning of Eu to feldspar during magmatic fractionation.

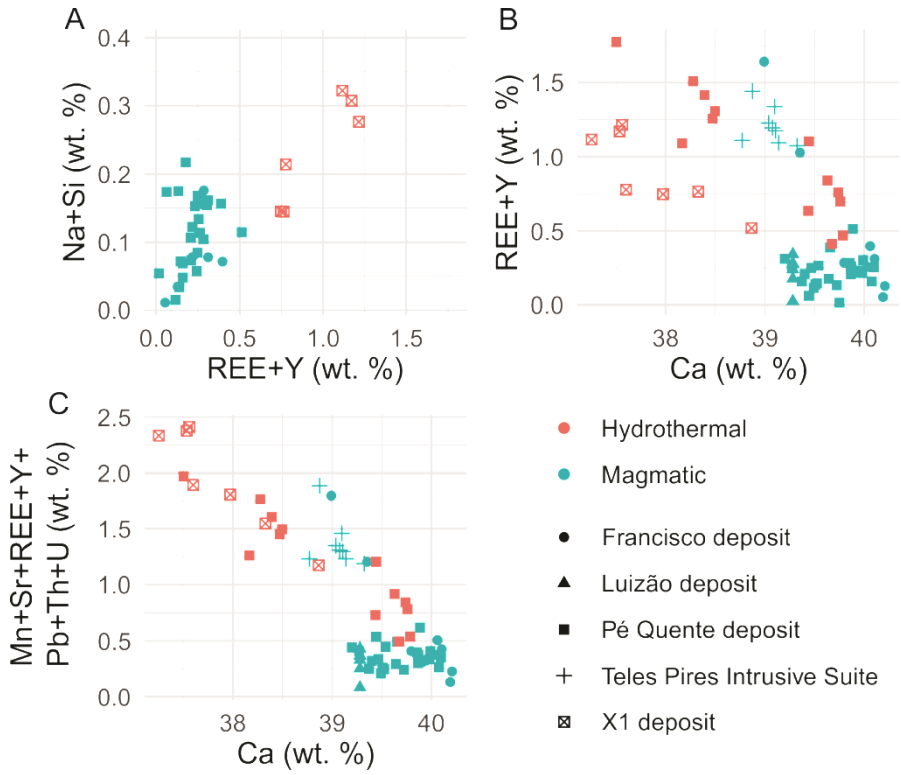

Figure 7.8 – Scatterplots for apatite compositions. (a) Na+Si vs. REE+Y. (b) REE+Y vs. Ca. (c) Mn+Sr+REE+Y+Pb+Th+U vs. Ca.

Apatite from the X1 deposit is distinct for its relatively constant LREE and HREE concentrations (Fig. 6.3, 7.9c-e). This REE pattern is similar to whole-rock REE compositions of ilmenite-series I-type granites (Sha and Chappell, 1999; Ishihara, 2004; Ishihara et al., 2007); an analogy sustained by the presence of mottled ilmenite-magnetite in the X1 sample (Fig 7.10). Other redox proxies, such as high Mn concentrations and association with pyrite, also indicate that apatite was crystallised under reducing conditions (Miles et al., 2014). Moreover, X1 apatites also display distinctly high Mn and Yb concentrations, which are similar to apatites from porphyry Cu-Au deposits (particularly to the Kemess South deposit, Mao et al., 2016). Apatites from porphyry Cu-Au deposits are distinguished for their higher Yb concentrations

(>100 ppm) and moderate Mn concentrations (0.1-0.3 wt. %), which is the case of X1 apatites (Mao et al., 2016).

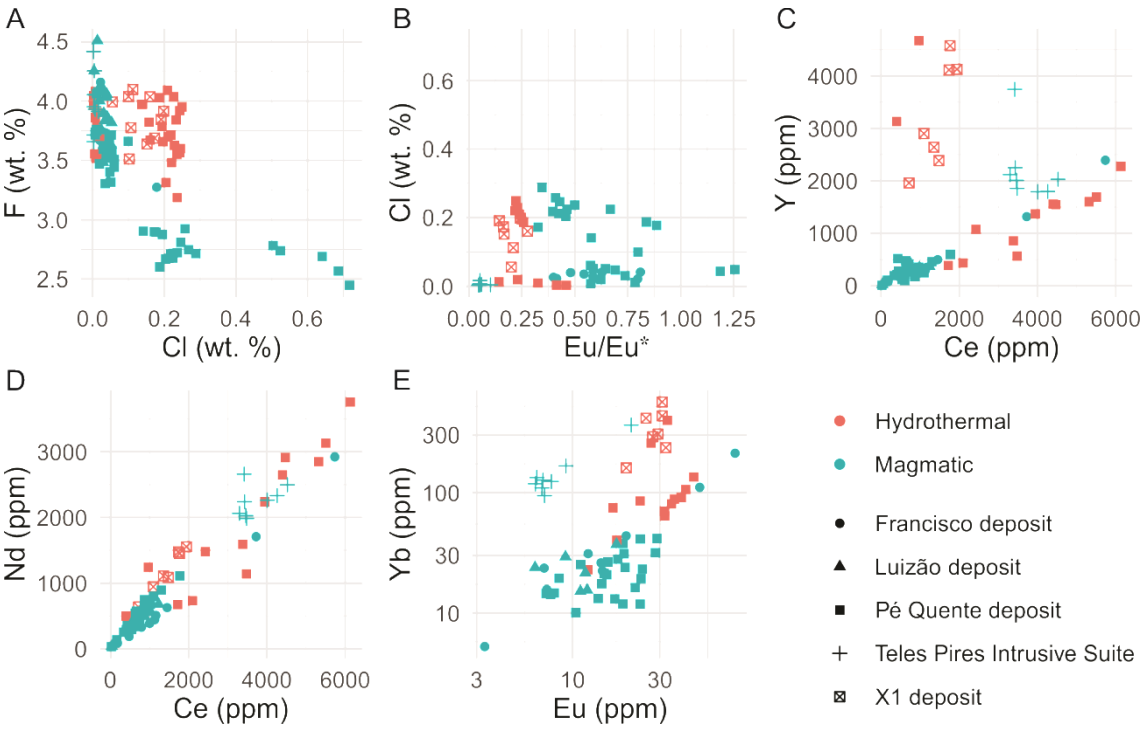

Figure 7.9 – Scatterplots for apatite compositions. (a) Cl vs. F. (b) Eu/Eu* vs. Cl. (c) Ce vs. Y. (d) Ce vs. Nd. (e) Eu vs. Yb.

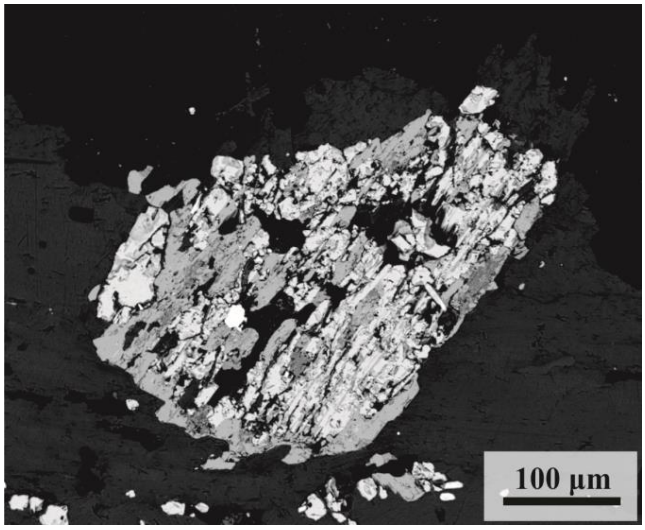

Figure 7.10 – Ilmenite-magnetite intergrowths with mottled texture in the phyllic alteration of the X1 deposit (sample B6). Brighter intergrowths are magnetite; darker mineral intergrowths are ilmenite.

7.1.4 Mn contents in apatite as a proxy for redox conditions in magmatic-hydrothermal systems

Manganese has four ionic valences (Mn^{2+}, Mn^{3+}, Mn^{4+} and Mn^{5+}), each of which depends on specific oxidation states of the magma to be incorporated into apatite (Pan and Fleet, 2002; Sha and Chappel, 1999). Thus, Mn is a redox-sensitive element that can be used as a proxy to estimate the redox conditions of magmas during the crystallisation of apatite.

$$Mn^{2+} \rightarrow Ca^{2+} \quad (1)$$

$$Mn^{3+} + Mn^{2+} \rightarrow 2.5Ca^{2+} \quad (2)$$

Since apatite incorporates Mn^{2+} more readily than Mn^{3+}, oxidising environments tend to have a low Mn^{2+}/Mn^{3+} (low overall Mn), while reducing environments tend to have a high Mn^{2+}/Mn^{3+} ratio (resulting in a high overall Mn). Apart from the redox conditions, there are several factors that can influence Mn concentrations in apatite, such as temperature, composition and competition. For instance, Mn may be uptaken by the following coupled substitutions:

$$Mn^{5+} + Mn^{2+} \rightarrow Ca^{2+} + P^{5+} \quad (3)$$

$$Mn^{3+} + Si^{4+} \rightarrow Ca^{2+} + P^{5+} \quad (4)$$

$$Mn^{3+} + Ge^{4+} \rightarrow Ca^{2+} + P^{5+} \quad (5)$$

Reaction (3) implies that overall Mn concentrations in apatite would increase. But as Hughes et al. (2004) showed, Mn^{5+} encompasses only 2.6% of total Mn contents in synthetic apatite, which makes Reaction (3) unlikely. Reaction (4) implies that an equivalent Si uptake would also increase Si concentrations. As there was no concomitant increase in Si concentrations in Mn-rich apatites (e.g. X1 deposit), this hypothesis was discarded. However, Reaction (5) might have taken place to some extent, especially in Pé Quente and Teles Pires apatites where it would have made up a quarter to a fifth of total reactions (Pé Quente medians: 668 ppm Mn, 168 ppm Ge; Teles Pires medians: 1,110 ppm Mn, and 212 ppm Ge).

To ascertain that temperature did not influence Mn partitioning in apatite, we can calculate apatite saturation temperatures (AST) (Piccoli and Candela, 1994) by compiling whole-rock SiO_2 and P_2O_5 concentrations from previous studies (Moreton and Martins, 2005; Paes de Barros, 2007; Assis, 2011; Rodrigues, 2012). Apatite saturation temperatures are estimated between 802-985ºC, and do not vary much between geological units (Table 7.3). These temperatures are higher than the saturation

Table 7.3 – Apatite saturation temperatures calculated with whole-rock SiO_2 and P_2O_5 from compiled literature for the evaluated geological units.

Metallogenic context	Geological units	SiO_2	P_2O_5	T (ºC)	Details
Luizão deposit[(1)]	Novo Mundo granite	74.55	0.03	839	Syenogranite (N=16, average)
		75.46	0.03	847	Monzogranite (N=3, average)
		63.38	0.09	821	Monzonite (N=3, average)
Pé Quente deposit[(2)]	Pé Quente suite	58.7	0.13	802	RA.40.B
		59.96	0.14	826	RA.40.C
		68.07	0.15	927	RA.40
		67.71	0.17	937	RA.41.A
	Coarse-grained monzonite	61.62	0.23	904	RA-16
		58.78	0.29	897	RA-27
		60.51	0.21	879	RA-120
		59.73	0.21	869	RA-122
	Pé Quente Tonalite	69.29	0.09	887	RA-22
		67.15	0.13	902	RA-72
		69.87	0.1	903	RA-73
		68.16	0.11	895	RA-107
Francisco deposit[(3)]	União granodiorite	55.07	0.31	855	FR-03
		62.32	0.25	922	FR-07
		67.15	0.15	907	FR-08
		60.5	0.28	914	FR-113G
		57.94	0.36	914	PTO 50
		57.37	0.36	907	PTO 53.B
		54.33	0.32	848	PTO 77.A
		65.79	0.17	917	VU-09
X1 deposit[(4)]	Guarantã granodiorite	73.51	0.03	829	SEX 1-51
		72.55	0.04	844	
		72.65	0.05	865	
		73.63	0.03	830	
		73.61	0.04	854	
Teles Pires Intrusive Suite[(5)]		74.53	0.02	806	GM-04
		71.32	0.15	960	GM-07
		72.89	0.05	867	GM-10
		70.62	0.2	985	PV-195
		75.6	0.02	816	CC-183

References: (1) Paes de Barros (2007); (2) Assis (2011); (3) Assis (2008); (4) Rodrigues (2012); and (5) Moreton and Martins (2005).

temperatures of other Mn-bearing minerals, such as hornblende, biotite and magnetite. Apatite also regularly occurs as inclusions within those Mn-bearing minerals (and not

the opposite), evidencing an earlier crystallisation for apatite. Thus, we can discard the hypothesis that temperature, composition or competition might have influenced Mn uptake in apatite. Other elements, such as As, Fe, Eu and Ce, can also occur in diverse valence states and be considered redox-sensitive elements. However, these elements are not yet properly systematised as proxies of redox conditions in natural apatite.

Therefore, the uptake mechanism of Mn in apatite is mostly reliable on the redox conditions of the magmatic-hydrothermal system, as shown by Miles et al. (2014), which correlated Mn concentrations in apatite with oxygen fugacities estimated by Ce/Ce* in zircon and Fe^{3+}/Fe^{2+} in biotite in the zoned Criffell granitic pluton, in southern Scotland. Apatites from the reduced inner zones of the Criffell pluton have progressively increasing Mn concentrations relative to the oxidised outer zones. Miles et al. (2014) obtained the experimentally calibrated expression:

$$\log fO_2 = -0.0022(\pm 0.0003)\mathrm{Mn(ppm)} - 9.75(\pm 0.46)$$

We applied this expression to our data and obtained coherent results, as shown in Tables 7.4 and 7.5.

Table 7.4 – Hydrothermal apatite $\log fO_2$ values based on model by Miles et al. (2014).

Hydrothermal apatite				
	X1	Pé Quente		
Summary statistics	B6	SPQ1	RA69	RA-24
Minimum	-35.67	-10.93	-14.68	-11.26
Q1	-35.31	-10.91	-13.27	-11.24
Median	-33.51	-10.74	-13.22	-11.22
Q3	-29.21	-10.63	-12.35	-11.20
Maximum	-23.43	-10.53	-11.19	-11.19
Mean	-31.67	-10.75	-12.45	-11.22
Range	12.24	0.40	3.50	0.07

The $\log fO_2$ values were considerably lower for hydrothermal apatite than for magmatic apatite. Magmatic apatite ranges between -7.92 and -9.62 $\log fO_2$, whereas hydrothermal apatite ranges between -10.53 and -35.66 $\log fO_2$. Apatites from the Luizão deposit, even though they are immersed in chlorite-sericite alteration, once more display an inherited magmatic signature, with higher fO_2 than other apatites from hydrothermal zones. The most unaltered samples, TP01 and FD20-7 (Teles Pires Intrusive Suite and Pé Quente tonalite), display the highest $\log fO_2$, at between -7.92 and -7.63. On the other hand, hydrothermal apatite in the Pé Quente deposit ranges from -

10.53 to -14.68 logfO_2, and in the X1 deposit, it ranges from -23.42 to -35.66 logfO_2. These logfO_2 values suggest strongly reducing conditions for the hydrothermal reactions, especially in the X1 deposit that also displays consonant mineralogical evidence, in which overgrown apatite occurs with inclusions of pyrite and associated with it. The strongly negative values together with the wide range of their distributions are certainly not quantitatively correct for hydrothermal environments, especially because the expression of Miles et al. (2004) was not calibrated for such systems. However, the logfO_2 values can still be used semi-quantitatively for broad comparisons between samples, especially with those of magmatic origin.

Table 7.5 – Igneous apatite logfO_2 values based on model by Miles et al. (2014).

Magmatic apatite						
	Pé Quente			Luizão	Francisco	Teles Pires
Summary statistics	GT-2	RA73	FD20-7	BS07	PGD-1	TP01
Minimum	-8.64	-9.54	-7.90	-9.62	-8.54	-7.64
Q1	-8.32	-8.86	-7.87	-9.28	-8.14	-7.52
Median	-8.22	-8.61	-7.84	-8.80	-7.91	-7.36
Q3	-8.16	-8.56	-7.78	-8.66	-7.72	-7.28
Maximum	-8.11	-8.42	-7.72	-8.50	-7.44	-7.93
Mean	-8.28	-8.79	-7.82	-8.96	-7.89	-7.36
Range	0.54	1.12	0.18	1.12	1.10	0.71

7.2 Magnetite

7.2.1 Discriminant analysis

Principal component analysis was performed on compositional data so we could enhance our understanding on the distribution and efficiency of discriminant elements in magnetite from granitic intrusions. Discriminant elements were selected through a precursory statistical analysis utilising box-and-whiskers plots from Chapter 6.2 (Figs. 6.6 and 6.8). The selected elements were: Ti, Al, Zn, Pb, Mn, Sn, Ga, Co, V, Ni, U, and Th. Multivariate diagrams with PCA are shown in Figure 7.11.

Titanium corresponds to a long arrow that coordinates the Principal Component 1 that corresponds to 98.5 % of the explained variation in the samples (Fig. 7.12). This highly explanatory potential is mostly due to the fact that concentrations of Ti are comparatively much higher than the concentrations of other trace elements. If Fe was added to the diagram, it would also coordinate most of the variance. The Fe arrows would be pointing to an orthogonal direction from Ti (at around a 180º difference), because they are inversely correlated. However, Fe would not be properly discriminant because it is a major element in magnetite, and thus, it is susceptible to all kinds of processes indiscriminately.

Elements Ga and Co are the most orthogonal to Ti. While Ti corresponds to the most variable element during hydrothermal alteration, Ga and Co remain immobile. A few elements point directly towards Ti, such as Pb, Ca and Zr, with arrows at angles close to 0º. Elements Pb^{4+} and Zn^{4+} can justifiably substitute Ti^{4+}, which might indicate collinearity or one-dimensional substitution where these elements might somewhat compete for the same vacant site under the same conditions. Other elements that are clustered together at less than 90º degrees of Ti are Ni, Al and Zn. Moreover, Mn and V have an angle of about 120º difference from Ti. These elements are not sensible to hydrothermal alteration *per se.* Instead, since they have multiple valence states, they are specifically sensible to changes in redox conditions. Hydrothermal alteration tends to incorporate Ti, Ca, Pb, Zn, Al and Ni in magnetite, while Ga and Co remain mostly constant. Igneous magnetite from ore-related host rocks will mobilise redox-sensitive elements such as Mn and V, whereas anorogenic-related magnetite from barren zones will mobilise mostly Sn. Hence, Sn plays an important role in discriminating magnetites from anorogenic and ore-related granites.

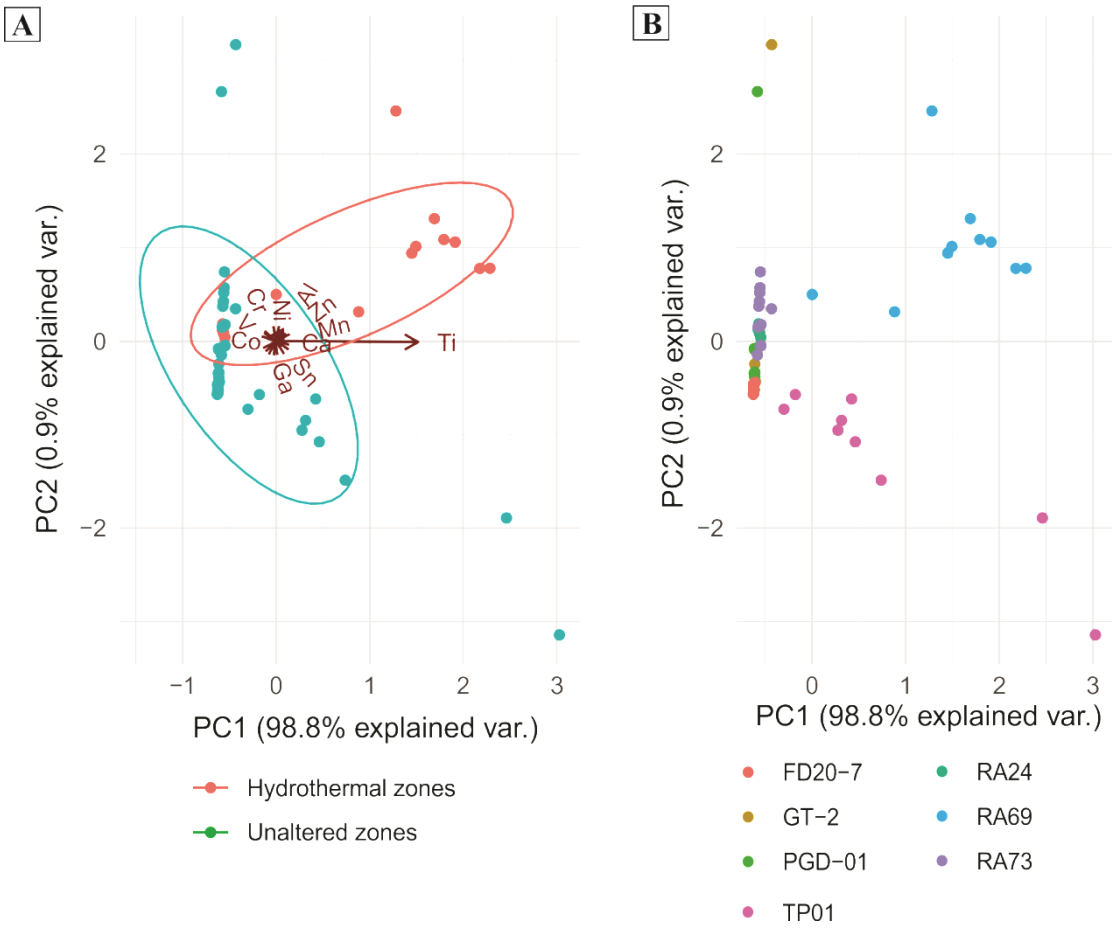

Figure 7.11 – Principal component multiplots of magnetite from granitic intrusions with (a) classification scores and element loadings (with Mahalanobis distances outlining clusters of data), and (b) scores for each sample in this study, plotted on the first and second principal component axes (PC1 and PC2) that account for 98.8% and 0.9% of the total explained variance, respectively. Samples correspond to: Teles Pires granite (TP01), Francisco deposit (PGD0-1), Pé Quente: barren (GT-2, RA73, FD20-7) and hydrothermal (RA24, RA69).

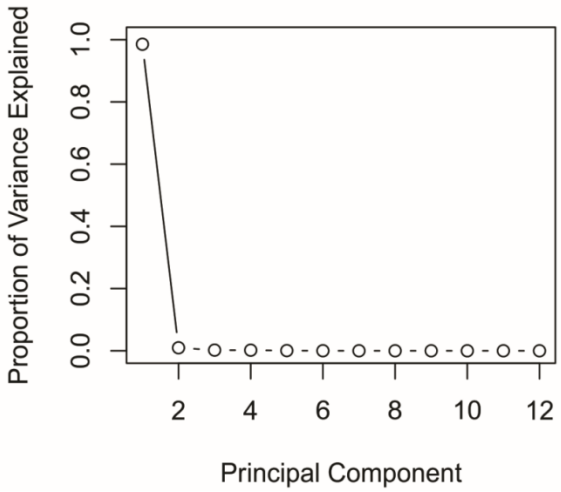

Figure 7.12 – Scree plot with the principal components for magnetite analysis and the proportion of variation that each principal component explains.

7.2.2 Titaniferous magnetite: igneous or hydrothermal?

Titanium is the most variable of all trace elements, ranging from 22 ppm to 4.7 wt. %, and one of the best discriminators (Dare et al., 2014; Canil et al., 2016). Partitioning of Ti into magnetite can be described by the reaction (Sievwright et al., 2017):

$$Ti^{4+}O_{2melt} + Fe^{2+}Fe^{3+}{}_2O_4 = Fe^{2+}{}_2 + Ti^{4+}O_4 + Fe^{3+}O_{1.5melt} + ¼O_2$$

The collinearity of Ti^{4+} with other group 4 elements, such as Zr^{4+} and Pb^{4+}, suggests that these elements undergo a similar reaction. Otherwise, in non-stoichiometric reactions, elements such as V, Mn, Al, Zn and Ca might behave as compensating cations. The Fe-Ti oxide solid solution induces an inverse correlation between Fe and Ti (Fig. 7.13), which is sensible to numerous igneous and hydrothermal processes (Buddington and Lindsley, 1964). Hydrothermal porphyry magnetite consistently tends to contain less than 1 wt.% Ti, while igneous porphyry magnetite tends to contain more than 1 wt.% Ti (Dupuis and Beaudoin, 2011; Dare et al., 2014; Nadoll et al., 2014; Canil et al., 2016; Pisiak et al., 2017). However, as shown by Sievwright (2017), hydrothermal replacement magnetite might still contain >1 wt. % Ti, suggesting a complex transition in the magmatic-hydrothermal system.

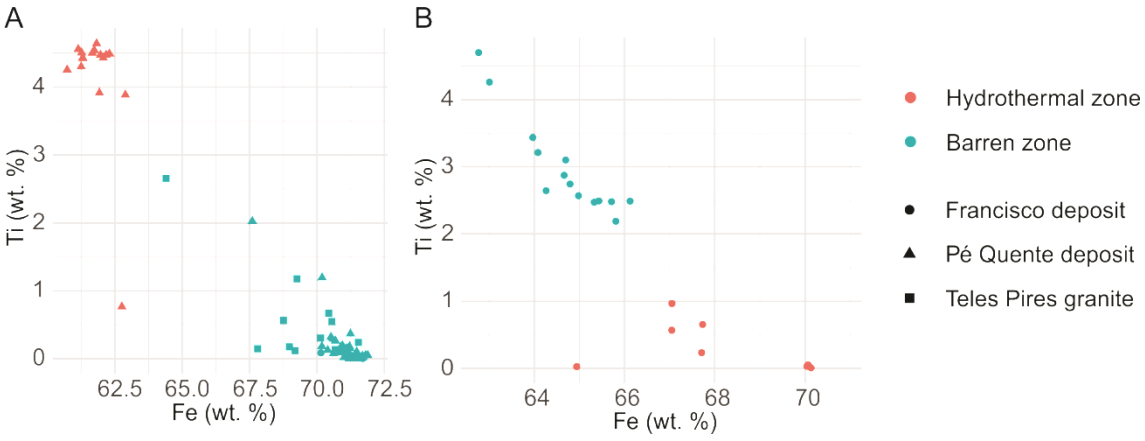

Figure 7.13 – Fe vs. Ti plots for magnetite analysis for (a) plutonic units and (b) volcaniclastic units.

Since Ti is not soluble enough to be transported by low temperature solutions (Van Baalan, 1993), it can be used to estimate the intensity of hydrothermal alteration. Presumably, igneous magnetite has >1 wt. % Ti because magmatic fractionation tends to produce titanomagnetite instead of pure magnetite (Huang et al., 2019a, Duan et al., 2019). Notwithstanding, Sievwright (2017) considered that hydrothermal magnetite might also have high Ti concentrations (>1 wt. %) if it occurs within high temperature potassic alteration, which is more proximal to the mineralised centre. Therefore, many

samples previously classified as igneous magnetites by their petrographic characteristics were actually overprinted by hydrothermal replacement (Putnis, 2009; Sievwright, 2018). Hydrothermal replacement magnetite is a transitional phase that is neither hydrothermal nor igneous, but hybrid. It displays a partly altered texture due to deuteric and/or potassic alteration, but it retains some of its igneous composition. In such instances, hydrothermal solutions change the crystal texture and composition within the same magnetite latticework that was formed during magmatic crystallisation.

7.2.3 Igneous titanomagnetite in the Teles Pires Intrusive Suite

The Teles Pires Intrusive Suite is an A-type granitic suite that assuredly has no direct relationship to the mineralisation or hydrothermal alteration. Therefore, it was the only geological unit that was sampled as a strictly barren igneous suite. The Teles Pires magmatism represents an anorogenic tectonic setting that is lithostratigraphically positioned after the 1.78 Ga metallogenenic event in the AFMP (Duarte et al., 2019; Assis et al., 2017).

The Teles Pires titanomagnetite is the only one that consistently displays igneous characteristics. Texturally, it displays trellis- and sandwich-type exsolution lamellae that are typical of Fe-Ti oxides formed at slow cooling rates during magmatic fractionation (Buddington and Lindsley, 1964; Mercer et al. 2015). Titaniferous magnetite also exsolve into ilmenite lamellae. Compositionally, it displays relatively high Ti concentrations (> 1 wt. % Ti) that are typical of igneous magnetite. It can also be distinguished from other magnetites for presenting high Sn concentrations, which are common in anorogenic and peraluminous granites (Imeokparia, 1985). Additionally, LA-ICP-MS data for Ti concentrations in the Teles Pires Intrusive Suite are more precise than EMP data, given that the larger ablation spots homogenise Fe-Ti compositions.

7.2.4 Hydrothermal magnetite in the volcaniclastic unit

Textures and compositions of magnetite have been extensively studied in porphyry, skarn, IOCG and IOA deposits (e.g. Liang et al. 2009; Hu et al., 2015; Duan et al., 2019; Huang et al., 2019a, b, c), but magnetite in epithermal deposits still lacks proper characterisation. Considering that porphyry and epithermal deposits are contiguous magmatic-hydrothermal systems (Sillitoe, 1989; Hedenquist and

Lowerstern, 1994; Gammons and William Jones, 1997; Heinrich, 2005; Taylor, 2007, Wilkinson, 2013), we reconstructed the history of volcaniclastic magnetite based on the thermodynamic characteristics of these transitional systems. Data from explosive volcanic eruptions also support the inference that porphyry- and epithermal-magnetite are partially related, since their trace element distributions depend on the depth and temperature of magmatic-hydrothermal processes (Ovalle et al., 2018). Moreover, most studies concerning trace elements in magnetite have not analysed mineral textures to conceptualise magnetite within a paragenetic sequence (e.g. Dupuis and Beaudoin, 2011; Dare et al., 2014). In these studies, magnetite was considered magmatic if within barren zones and hydrothermal if next to ore-bearing veins or disseminated ore. However, igneous magnetite may also be variably affected by hydrothermal alteration depending on extraneous controlling factors such as host rock composition, fluid salinity, oxygen fugacity, and temperature (Huang et al., 2019a, b).

In the Francisco volcaniclastic sequence, iron oxides from the barren zone (VC type 1)[8] have high-Ti concentrations, whereas iron oxides from the hydrothermal zone (VC type 2) have less than 1 wt. % Ti. If strictly based on this, magnetite from the barren zone would be considered of igneous origin. For instance, Nadoll et al. (2014) argued that only ten per cent of hydrothermal magnetites had more than 1 wt. % Ti, while thirty per cent of igneous magnetites had more than 1 wt. % Ti. However, magnetites from barren zones are strongly altered despite having high Ti concentrations (2.19-4.70 wt. % Ti). They display micro-vesicular texture and do not show evidences of typical igneous textures such as exsolution lamellae. These evidences corroborate that volcaniclastic magnetite has a hydrothermal replacement signature (as described in Section 7.2.2). Therefore, even though volcaniclastic magnetite occurs in an unaltered sedimentary rock, it is exhalative in origin (Assis, 2011; Assis et al., 2012).

Volcaniclastic iron oxides from hydrothermally altered zones (VC type 2) exhibit pristine, skeletal and cataclastic grains (Fig. 7.14). Magnetite underwent intense martitisation (hematite transformation), to the point that some rhombohedric hematite is distinguished among the grains. Martite-hematite contains <70 wt. % Fe, while pure magnetite contains 72.4 wt. % Fe (Deer et al., 1996). Furthermore, dissolution-recrystallisation processes are evidenced by the outline of partially reacted magnetite and skeletal magnetite, which usually contains higher Ti concentrations (~0.56 wt. %

[8] See Section 5.5.2 for typology.

Ti, Fig. 7.14) than recrystallised pristine martite-hematite grains (~0.03 wt. % Ti, Fig. 7.14). That kind of hydrothermal replacement of magnetite by hematite has been previously noticed in the Francisco deposit (in Assis, 2011; Assis et al., 2012) and is characteristic of epithermal deposits (Zhao et al., 2018). Martitisation is driven by interface coupled-dissolution reprecipitation via leaching of Fe^{2+} at low temperatures (100-220ºC) and at mildly acidic pH ranges (pH=~7.5 to ~4.5) (Ohmoto, 2003; Zhao et al., 2018). Martite-hematite grains are also smaller (~25-50-µm) than magnetite from barren zones (50-100-µm), which is explained by the ~33% decrease in volume predicted by the following non-redox reactions (Zhao et al., 2018):

$$Fe_3O_{4(mt)} + 2H^+ = Fe_2O_{3(hm)} + Fe^{2+} + H_2O \text{ (acidic conditions)}$$

$$Fe_3O_{4(mt)} + H_2O = Fe_2O_{3(hm)} + Fe^{2+} + 2OH^- \text{ (basic conditions)}$$

Volcaniclastic iron oxides from both the barren and hydrothermal zones underwent hydrothermal replacement, but only those in hydrothermal zones (VC type 2; martite-hematite related to chlorite-sericite alteration) were further overprinted by martitisation (Fig. 7.15). In barren zones, magnetite was most likely hydrothermally replaced while still in the magma chamber before being sedimented, for its texture and composition reflects higher temperature magmatic-hydrothermal reactions (Fig. 7.15) (Ovalle et al., 2018).

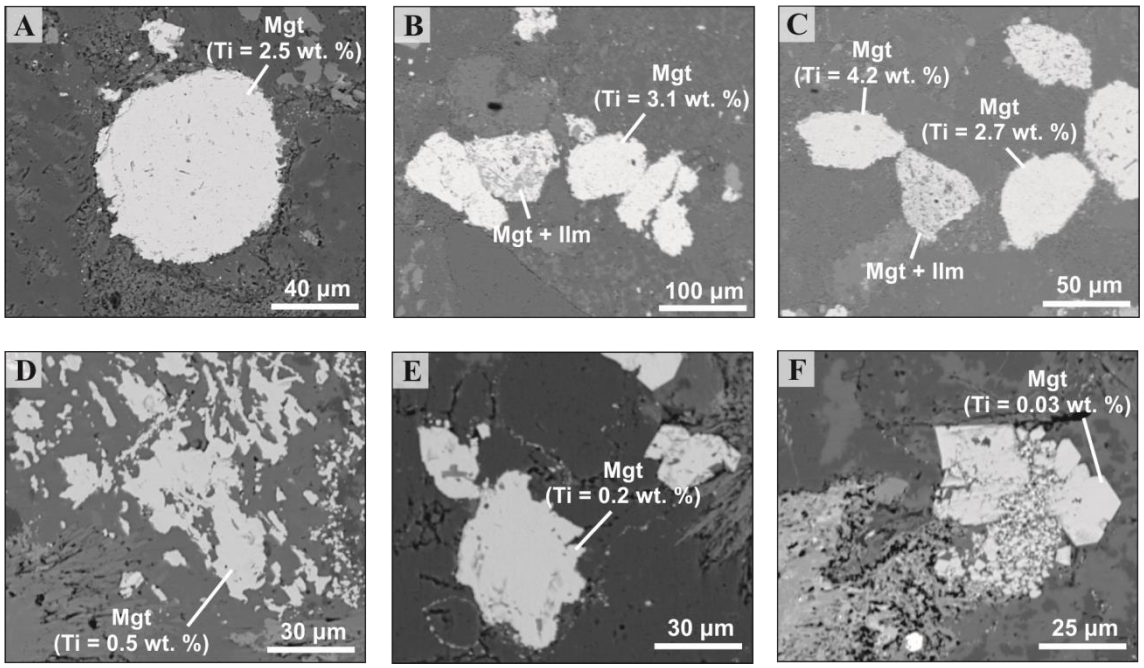

Figure 7.14 – Textures and compositions of volcaniclastic iron oxide grains (a-c) type 1, in barren zone of the Francisco deposit (VU20-4 sample); and (d-f) type 2, in hydrothermal zone (PTO19 sample). Figures are similar to those from Figures 4.12 and 4.13. (a-c) Type 1 grains have high Ti contents, while (d-f) type 2 grains have low Ti contents. Both grain types are affected by martitisation, but type 2 volcaniclastic iron oxide is more intensely affected by it.

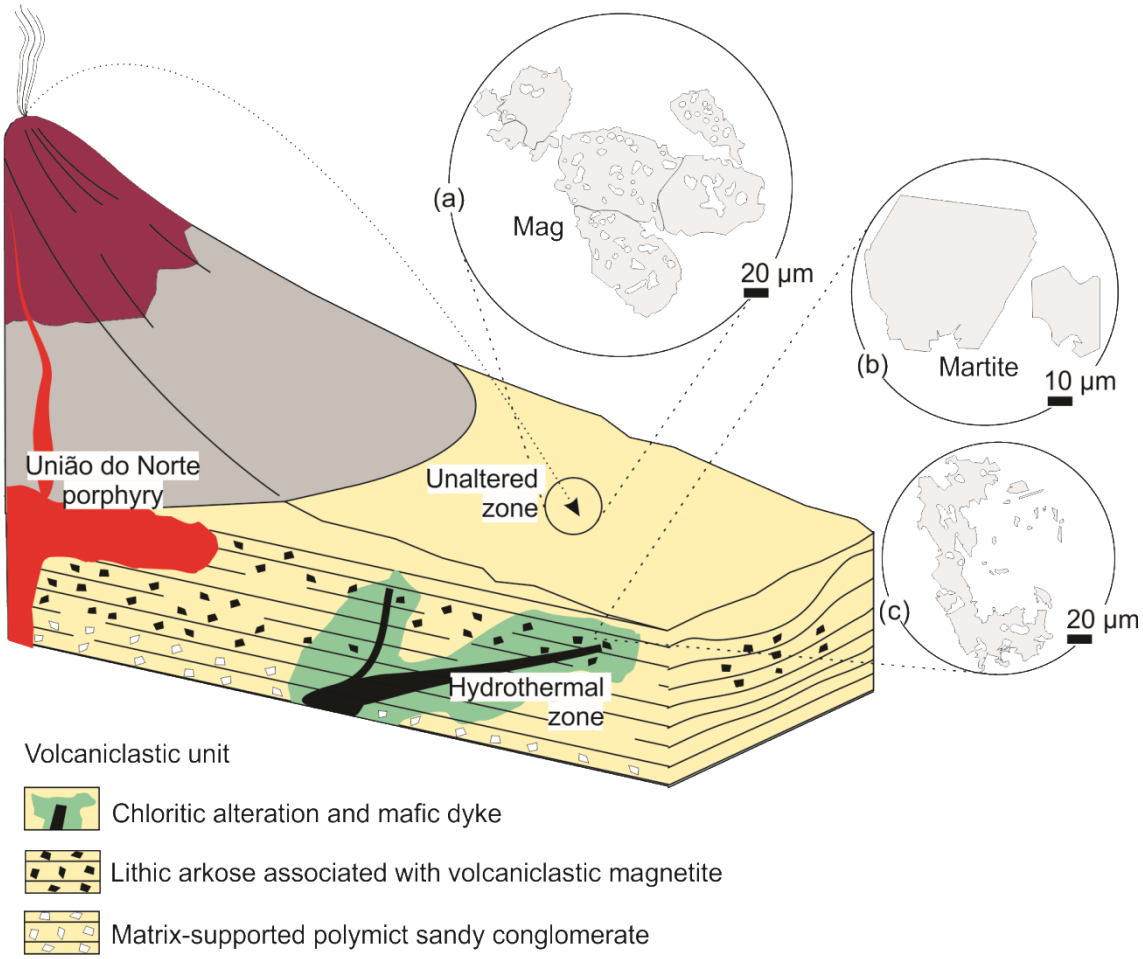

Figure 7.15 – Schematic illustration of the multiple magnetite generations in the Francisco deposit, associated to the (a) barren zone, and the (b-c) hydrothermal zone. (a) Type 1 volcaniclastic iron oxide: strongly altered and corroded magnetite. (b-c) Type 2 volcaniclastic iron oxide: (b) skeletal magnetite and (c) martite-hematite.

Volcaniclastic iron oxides from hydrothermal zones have increasing amounts of Fe, Na, Si, K and Cr. In barren zones, they have increasing amounts of Ti, Al, Ca and Mg concentrations, which might indicate nanoinclusions of diopside and aluminosilicates (as in Deditius et al., 2018). Nickel is the only element that was kept rather constant at both samples (as predicted by Wijbrans et al. 2015). Both types of iron oxides can be discriminated in Figure 7.16a, c (Dupuis and Beaudoin, 2011; Dare et al., 2014), mostly for their Ti concentrations.

Volcaniclastic iron oxides from barren zones plot in the field of magmatic Fe-Ti-V deposits (Fig. 7.16a). These iron oxides have a magmatic signature most likely due to their exhalative origin at higher temperatures. Martite-hematite is dispersed throughout many fields of lower temperature hydrothermal deposits (Fig. 7.16a). At the y-axis (Ca+Al+Mn, Fig. 7.16a), iron oxides are mostly dispersed and incoherent, indicating

that those elements are not efficient discriminators. Martitisation act mostly by increasing Fe concentrations in magnetite. Otherwise, only Na concentrations increases (most likely due to brine fluids) while no other trace elements are incorporated.

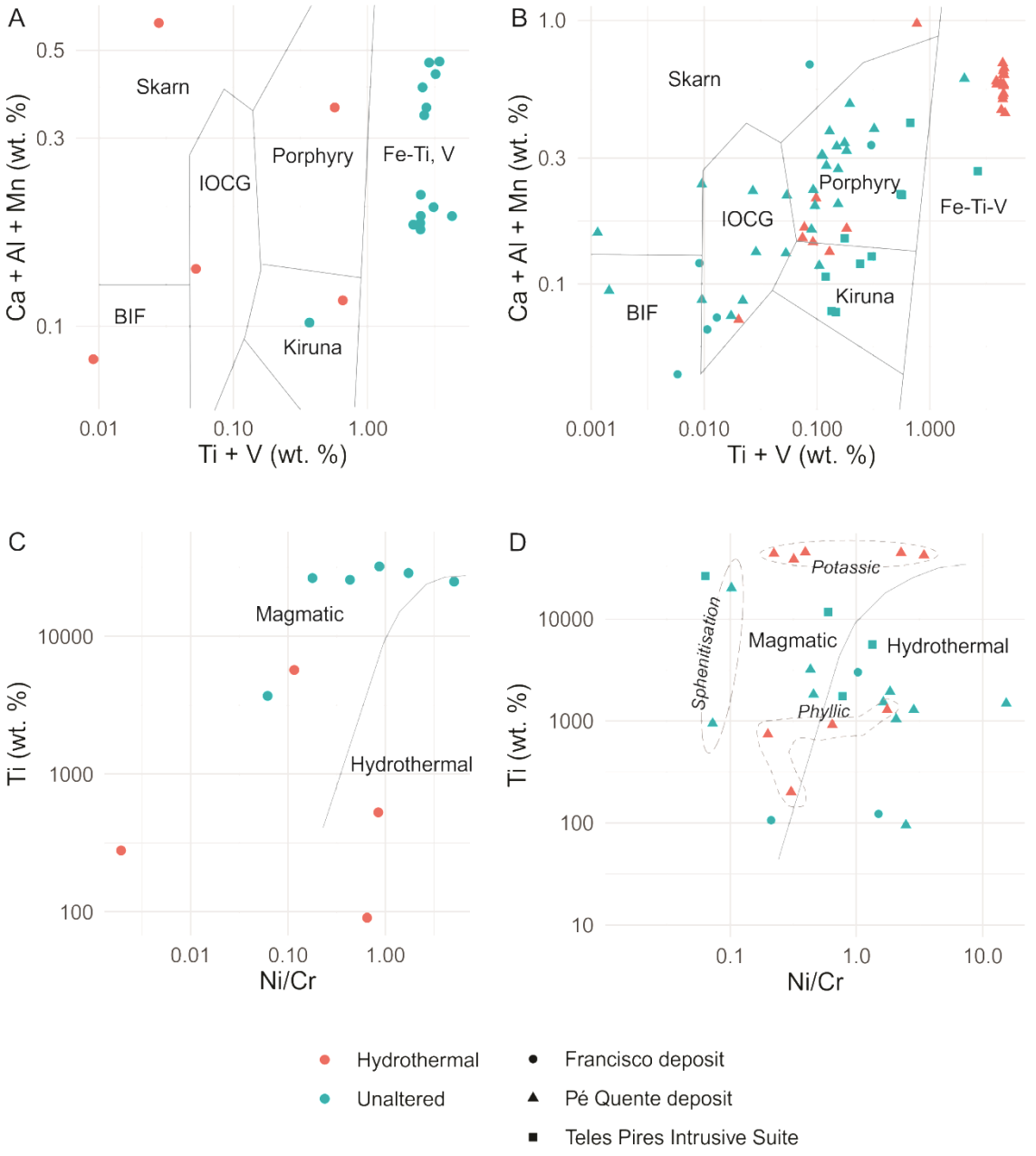

Figure 7.16 – Discriminant diagrams for magnetite compositions. Diagrams for volcaniclastic iron oxide grains are plotted in (a) and (c), while magnetite grains from granitic intrusions are plotted in (b) and (d). (a-b) Ti+V vs. Ca+Al+Mn plots based on Dupuis and Beaudoin (2011). (c-d) Ni/Cr vs. Ti plots based on Dare et al. (2014).

7.2.5 Hydrothermal magnetite in intrusion-hosted gold deposits

In the plutonic host rocks, the pattern of Ti distribution in magnetite is even more complex (Fig. 7.16b, d). Magnetite falls under the magmatic and hydrothermal fields of Dare et al. (2014) (Fig. b) and under a myriad of hydrothermal deposit fields in Dupuis and Beaudoin (2011) (Fig. 7.16b). Discriminant diagrams may be used to deduce one or several of the following: (1) magnetite crystallised under a wide range of temperatures conditions, (2) high concentrations of certain elements might be due to their abundance in hydrothermal solutions, and (3) hydrothermal fluids strongly interacted with the host rocks (Nadoll et al., 2014; Ovalle et al., 2018). Nevertheless, field compartmentalisation in these diagrams should not be taken at face value.

Every magnetite in the Pé Quente deposits displays some degree of hydrothermal alteration. This might be inferred either texturally or compositionally. Even in the barren zones, magnetite is altered, most likely due to distal propylitic alteration or deuteric (post-magmatic) processes. This affects the intrusive host rocks of both the Pé Quente and the Francisco deposit. Therefore, magnetite in the Pé Quente deposit generally displays low Ti concentrations as part of this hydrothermal signature. But there are two exceptions: (1) a potassically altered sample, and (2) a sphenitised sample.

Potassically altered sample (RA69): It is related to potassic alteration and overprinted by propylitic alteration. Texturally, it was considered a Type 3 magnetite in Section 5.2 because of its hydrothermal texture. However, it contains high Ti concentrations typical of igneous magnetite, and plots in the magmatic Fe-Ti-V deposit field (Fig. 7.16b). This pattern is replicated in the Dare et al. (2014) diagram (Fig. 7.16d) in which it is assumed to have an igneous signature. However, its texture and paragenesis suggests that it is a hydrothermal replacement magnetite[9] akin to samples observed in the volcaniclastic iron oxides of the Francisco deposit (type 1; sample VU-20-4; Fig. 7.16a, c). Probably, potassic alteration retains Ti and other trace elements in magnetite structure because it occurs at higher temperatures (~600ºC) than other alterations, thereby simulating an igneous signature.

Sphenitised sample (GT-2): Skeletal magnetite associated with hydrothermal titanite. It occurs in the barren zone of the Pé Quente deposit, but displays strong

[9] As defined in Section 7.2.2.

textural evidences of alteration (Fig. 5.7). Its close association with hydrothermal titanite might indicate sphenitisation, i.e. alteration into titanite. Sphenitisation occurs by the introduction of Ca- and Si-rich hydrothermal fluids at late stage magmatic processes, or by the breakdown of magnetite for the formation of Fe-rich alteration minerals such as sulphide, chlorite and amphibole (Haggerty, 1976; Weisse et al., 1985). Sphenitised magnetite displays symplectic intergrowths of titanite and ilmenite, and stringer-like exsolutions that might indicate titanite replacement. Thus, this is considered a hydrothermal replacement magnetite, with a distinct alteration texture (Fig. 5.7) and intermediate Ti composition (Fig. 7.16d). It has lower Al, Ca, Pb, Zn, and higher Co, Ga and Ni. In Section 5.2, it was classified as a Type 2 magnetite within a transitional zone – a term coined for the slightly altered propylitic halo that occurs between the barren and hydrothermal zones.

Phyllic-related magnetite (type 4; sample RA-24) has low Ti compositions similar to those from barren zones of the Pé Quente deposit (Fig. 7.16d). Otherwise, magnetite is generally absent from other phyllic alteration zones, such as in the Luizão and X1 deposits, where pyrite occurs instead. Similarly, Sievwright (2017) has not found magnetite in phyllic alteration to compose his LDA diagrams. Magnetite is either bypassed or replaced by pyrite during phyllic alteration. This is especially relevant since mineralisation in the AFMP occurs within the phyllic alteration (Assis, 2011; Assis et al., 2014). These evidences corroborate with the model that argues that magnetite fractionation ("magnetite crisis") triggers sulphide saturation and mineralisation in arc-related deposits (Sun et al., 2004; Jenner et al., 2010, Sun et al. 2013).

In the LDA of Pisiak et al. (2017) (Fig. 7.17), magnetite consistently falls in the hydrothermal field, which is consistent with the reasoning that most magnetite was indeed altered by deuteric and propylitic alteration. The LDA does not separate the anorogenic Teles Pires samples from the hydrothermal magnetites (Fig 7.17). Nevertheless, it was not trained to do so. Sphenitised magnetite (GT-2) falls between the fields of hydrothermal and ore-related igneous magnetite (Fig. 7.17), which is consistent with the previously discussed knowledge about the sample. Moreover, magnetite in the barren zone displays some degree of martitisation as well, but to a lesser degree than that described in the volcaniclastic unit. This widespread martitisation indicates that propylitic alteration in the province occurs as pervasive, wide halos.

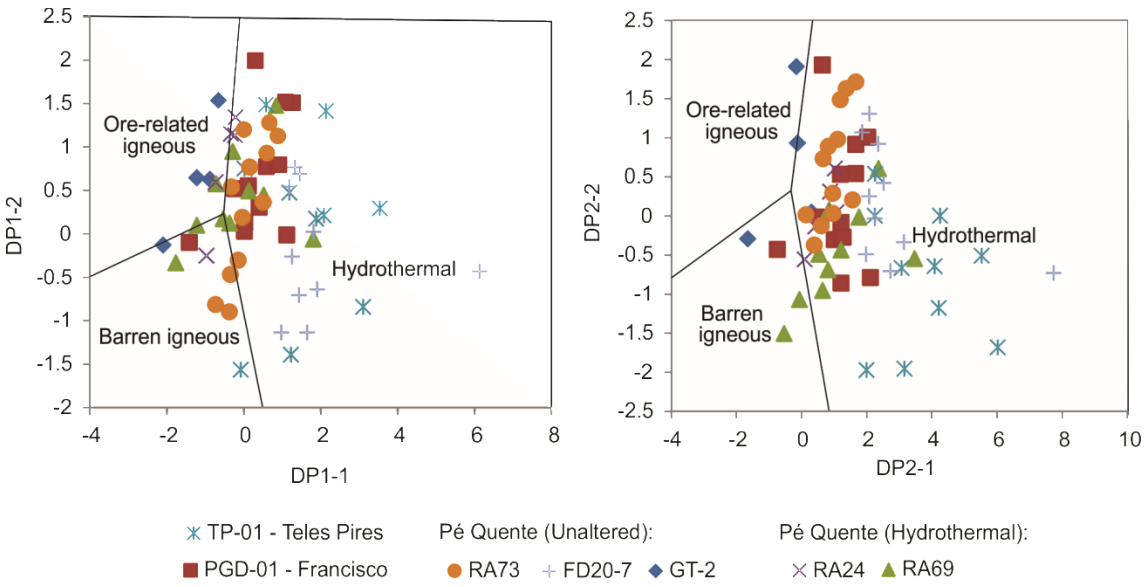

Figure 7.17 – Discrimination diagrams for magnetites as an indicator mineral for porphyry deposits (Pisiak et al., 2017). Samples correspond to: Pé Quente: transitional (GT-2), barren (RA73, FD20-7) and hydrothermal (RA69, RA24). Francisco deposit (PGD0-1). Teles Pires granite (TP01).

7.2.6 Contamination and inclusions

Before assuming that magnetite from sample RA69 was hydrothermally replaced, we shall test our plutonic samples for inclusions and contamination. A common contamination process is sphenitisation, which occurs in many samples, given the abundant observations of hydrothermal titanite associated with magnetite. This process has been previously noticed in the Alta Floresta mineral province where it seems widespread (Moura et al., 2006), and was interpreted as a deuteric process, i.e. related to incipient autometassomatism at late stage magmatic fractionation. To examine for titanite ($CaSiTiO_2$) replacement, we verify whether samples correlate Ca vs. Si and Ca vs. Ti contents in a proportion of 1:1, thus discriminating between titanite and ülvospinel (Figure 7.18a, b). Other common inclusions that ought to be verified are zircon (Zr:Si, Fig. 7.18c), apatite (Ca:P, Fig. 7.18d), and K-silicates (K-feldspar and biotite, K:Si, Fig. 7.18e).

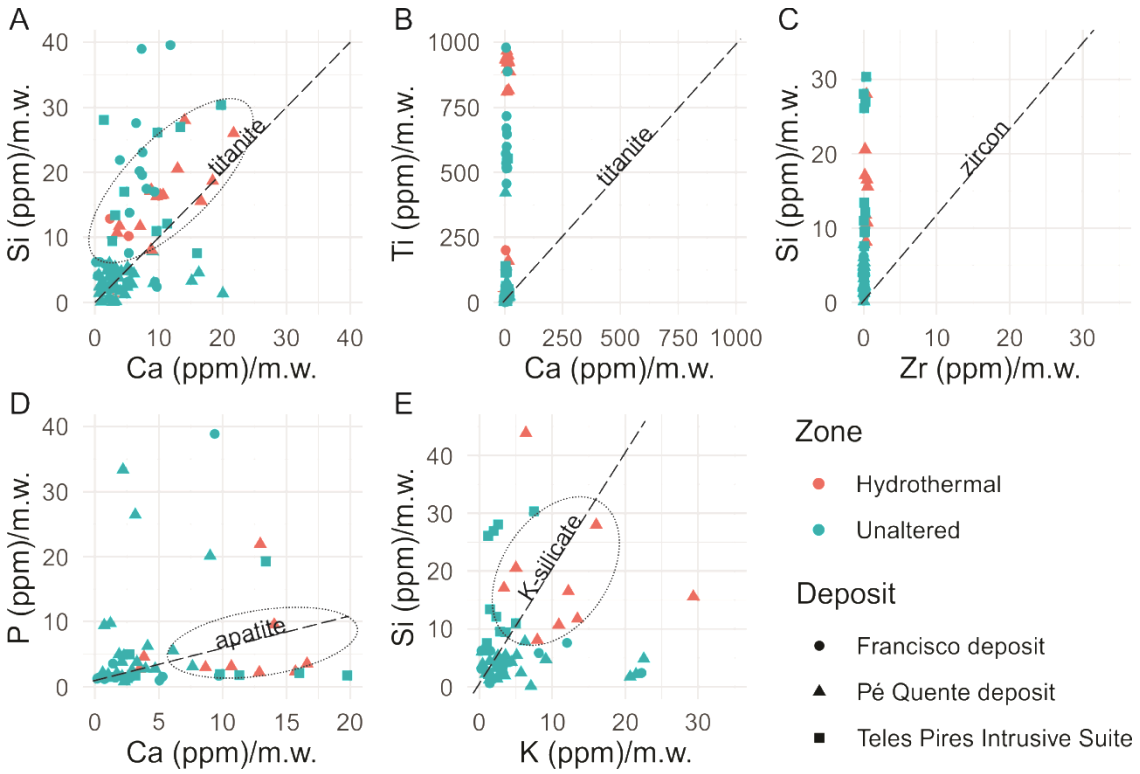

Figure 7.18 – Scatterplots for magnetite compositions divided by molar weight (m.w.) to make evident contaminations and inclusions in magnetite. (a) Ca vs. Si in which titanite contamination trend towards 1:1. Some degree of sphenitisation occurs at the hydrothermal zone of the Pé Quente deposit. (b) Ti vs. Ca in which titanite contamination would trend towards 1:1. In this instance, most of Ti concentrations in magnetite are not due to sphenitisation. (c) Zr vs. Si in which zircon contamination would trend towards 1:1. (d) Ca vs. P in which apatite contamination would trend towards 5:3. (e) K vs. Si in which K-silicates (K-feldspar and biotite) would trend towards 1:2.

Contaminations of apatite, K-silicate and titanite are suggested (Fig. 7.18a,d,e), so we rejected the few samples that had >1000 ppm of these selected elements. Most other possible contaminations were interpreted as nanoinclusions, which are typical in magnetite (Deditius et al., 2018). Titanite contamination abounds in magnetite from hydrothermal zones, but most Ti contents are not coordinated by sphenitisation and are probably remnants of Ti-rich igneous magnetite as inclusions (in both samples RA69 and RA24). By linear regression of EPM data of Si and Ca, we obtained a small p-value of 9.844e-07, which means that the null hypothesis H_0 (that Ca contents are not correlated to Si contents) do not adequately explain the observations (Fig. 7.18a). However, the coefficient of determination (R^2=0.252) is not robust enough. This would occur due to imprecision in EMP data, but other assumption could be furthered. For instance, a regression line that is 2:1 for Si:Ca shows a general trend towards higher Si contents that might correspond to diopside or quartz nanoinclusions (as in Deditius et al., 2018). Nevertheless, titanite replacement would not be enough to incorporate the

entire Ti contents hold by those samples, since titanite contamination would only correspond to a maximum of 0.1 wt. % Ti variation.

Incorporation of trace elements in magnetite must be understood with a caveat. Magnetite tends to incorporate elevated concentrations of extraneous nanoparticles, as hinted at by the numerous inclusions filtered out from the ablation signal spectrum during data processing. Many studies, such as Pisiak et al. (2017) and Deditius et al. (2018), demonstrate how patterns of trace elements in magnetite may be unknowingly considering the compositions of both magnetite and its nanoinclusions. Magnetite has a complicated structure due to a few factors: (1) titanomagnetite(ss) series may require the incorporation of trace elements to compensate for the charge of Ti^{4+}; (2) random arrangements of Fe^{2+}, Fe^{3+} and Ti^{4+} contribute in generating vacancies, local environments, and non-stoichiometric structures in magnetite, and (3) exsolution processes during hydrothermal alteration (Murad and Cashion, 2004).

7.2.7 Defining a relative proxy for redox conditions using magnetite

Oxybarometry via magnetite is one of the most common methods for estimating oxygen fugacity in magmatic rocks. The "two-oxide method" developed by Buddington and Lindsley (1964) is based on equilibria between magnetite-ülvospinel and ilmenite-hematite, from which solid solutions between Fe^{2+} and Fe^{3+} are used to estimate fO_2. For this method to work properly it requires that (1) magmatic magnetite and ilmenite are closely associated, i.e. are part of the same mineral assemblage, and that (2) the Fe-Ti oxides are unaltered; which is not the case with most of our samples.

There are other methods to estimate oxygen fugacity in hydrothermally altered rocks using Fe-Ti oxides. A recent example is Arató and Audétat (2017a, b, c), which is an oxybarometer based on vanadium partitioning in Fe-Ti oxides. Vanadium partitioning is strongly dependent on the redox state of the magmas due to varied valence states such as V^{3+}, V^{4+} and V^{5+}. Other trace elements in spinel with similar characteristics are Nb, Ta and Mo (Sievwright et al., 2017); but these have not been yet calibrated as oxybarometers. Nevertheless, the fastidious accuracy of this vanadium-based oxybarometer may be rather burdensome. For instance, to satisfy the calibration expression for this method, the partition coefficient $D(V)_{mgt/melt}$ is required (Arató and Audétat, 2017a). Even though we obtained V_{mgt} through LA-ICP-MS analysis, the V_{melt} data is unavailable — which would only be obtained by analysing melt inclusions. Melt

inclusions represent glassy microparticles of the melt that remained as inclusions within magnetite and that reflect V_{melt} composition during magnetite crystallisation. However, melt inclusions are particularly difficult to find and analyse. Other hindrances, such as lattice diffusion, may alter the original composition of melt inclusions and should also be acknowledged. However, we can use relative redox ratios to uphold our model.

We can determine relative redox ratios between Fe-Ti oxides and silicate melts by correlating our natural data to experimental fO_2 data such as that of Wijbrans et al. (2015) and Sievwright et al. (2017). Thenceforth, even though V_{melt} compositions are unavailable for the abovementioned oxybarometer, we can create a relative redox ratio by selecting an element that has not changed its composition from mineral to melt because of redox conditions, i.e. an element with a constant of about D(X)=1. Sievwright et al. (2017) obtained partition coefficient data for intermediate silicic magmas that suggested that D(Ga) remained relatively constant (between 0.51-1.37), even with changes in temperature and fO_2. Gallium only is strongly partitioned into spinel at temperatures above 1,250ºC (Sievwright et al., 2017). Such constant element can be used as the denominator of V_{mgt}, as a relative redox V/Ga ratio, to adjust the redox values for any abrupt changes in melt composition. Therefore, we correlated V and Ga partitioning data obtained in Sievwright et al. (2017), as exhibited in Table 7.6.

Table 7.6 – Summary of experimental partition coefficients for magnetite. Data from Sievwright et al. (2017).

Experiment	log fO2	V	Ga	D(V)	D(Ga)	V(mgt)/Ga(mgt)
RSM-11	-8.02	157 ± 14.7	55.2 ± 5.3	8.08	0.775	29.6729
RSM-11	-8.02	137 ± 18.2	54.1 ± 3.31	10.5	1.15	23.10897
RSM-21	-7.02	249 ± 25.5	83 ± 5.56	1.61	0.511	9.457547
RSM-21	-7.02	279 ± 37.9	65.3 ± 7.69	2.56	0.933	11.70772
RSM-9	-7.31	321 ± 25.8	54.7 ± 7.12	0.654	1.13	3.387097
RSM-19	-8.38	174 ± 27.8	50.6 ± 2.15	10.5	0.773	47.5051
RSM-4	-7.36	270 ± 8.34	60 ± 2.25	0.546	0.777	3.154506
RSM-19	-8.38	166 ± 10.6	64.8 ± 2.64	14.3	1.01	37.29573
RSM-4	-7.36	277 ± 21.2	55.7 ± 2.17	0.521	1.17	2.201835
RSM-15	-7.68	201 ± 17.2	48 ± 1.95	4.9	0.919	22.31293
RSM-17	-5.66	233 ± 15.6	38.4 ± 2.62	0.689	1.18	3.554084
RSM-15	-7.68	183 ± 12.8	57.4 ± 2.77	7.5	1.12	21.28682
RSM-17	-5.66	261 ± 7.76	47.1 ± 2.03	0.584	1.37	2.375776
RSM-12	-7.68	245 ± 10.8	48.2 ± 2.54	1.9	0.892	10.83721
RSM-12	-7.68	272 ± 27.8	57.4 ± 3.1	1.79	1.35	7.407895
RSM-18	-5.98	289 ± 25	67.4 ± 18.9	0.441	0.605	3.159204
RSM-18	-5.98	290 ± 37.5	70.8 ± 3.48	0.442	0.94	1.921922

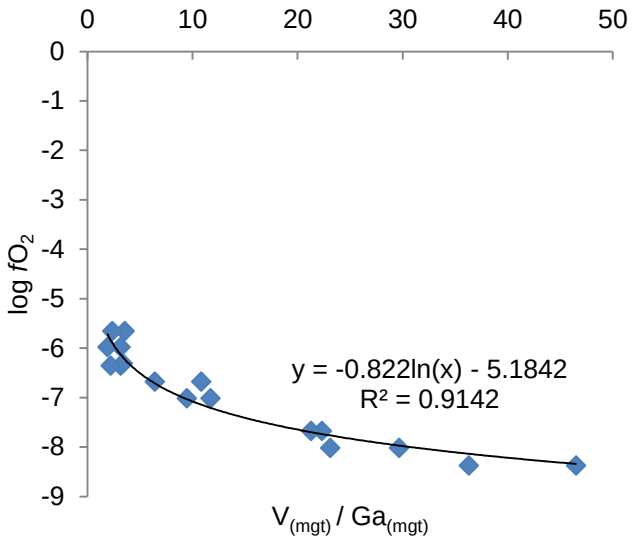

Figure 7.19 – Plot of data displayed in Table 7.6, with calibrated expression.

We calibrated the following expression (Fig. 7.19):

$\log fO_2 = -0.022 * \ln(V_{mgt}/Ga_{mgt}) - 5.1842$

Where $R^2 = 0.9142$.

Applying this expression to our data, we obtained the results displayed in Table 7.7. Magnetite $\log fO_2$ values range between -10.29 and -7.65. The lesser $\log fO_2$ values occur at the Teles Pires Intrusive Suite, with a median of -7.51, which are similar to those obtained in apatite (median -7.36). In the barren Pé Quente tonalite, $\log fO_2$ values in magnetite are conspicuously similar to those obtained in apatite (FD20-7 sample; median of -7.85 in magnetite compared to -7.84 in apatite). In an unaltered sample of the Pé Quente tonalite (RA73), apatite has slightly higher $\log fO_2$ (median -8.61) than magnetite (median -7.96). In samples from transitional zones (GT-2 and PGD-01), magnetite displays the lowest $\log fO_2$, ranging from -8.90 and -10.29. Precisely these low fO_2 magnetite samples also displayed textural and compositional evidences of sphenitisation. In all other samples, $\log fO_2$ values were kept high at -7.65 to -8.51.

Apatite $\log fO_2$ values tend to register the redox conditions during hydrothermal reactions better than magnetite. In fact, in most hydrothermal zones, magnetite is replaced by pyrite. Furthermore, we can conclude that apatite is an efficient redox proxy for hydrothermal reactions, whereas magnetite better registers petrogenetic processes. However, magnetite is still susceptible to sphenitisation during incipient alteration at late-stage magmatic fractionation.

Table 7.7 – Comparative results for fO_2 values in apatite and magnetite.

		Hydrothermal				Magmatic					
		X1	Pé Quente						Luizão	Francisco	Teles Pires
		B6	SPQ1	RA69	RA-24	GT-2	RA73	FD20-7	BS07	PGD-1	TP01
logfO_2 Apatite	Minimum	-35.67	-10.93	-14.68	-11.26	-8.64	-9.54	-7.90	-9.62	-8.54	-7.64
	Q1	-35.31	-10.91	-13.27	-11.24	-8.32	-8.86	-7.87	-9.28	-8.14	-7.52
	Median	-33.51	-10.74	-13.22	-11.22	-8.22	-8.61	-7.84	-8.80	-7.91	-7.36
	Q3	-29.21	-10.63	-12.35	-11.20	-8.16	-8.56	-7.78	-8.66	-7.72	-7.28
	Maximum	-23.43	-10.53	-11.19	-11.19	-8.11	-8.42	-7.72	-8.50	-7.44	-7.93
	Range	12.24	0.40	3.50	0.07	0.54	1.12	0.18	1.12	1.10	0.71
	Minimum			-8.41	-8.12	-10.30	-9.02	-8.51		-9.70	-8.16
logfO_2 Magnetite	Q1			-8.33	-8.04	-10.24	-8.13	-8.24		-9.56	-7.91
	Median			-8.20	-7.80	-10.17	-7.96	-7.85		-9.47	-7.51
	Q3			-7.83	-7.64	-9.96	-7.76	-7.78		-9.41	-7.09
	Maximum			-7.52	-7.44	-9.49	-7.55	-7.68		-8.93	-7.65
	Range			0.90	0.68	0.80	1.47	0.83		0.77	1.51

7.3 Implications for petrogenesis and metallogenesis in intrusion-hosted gold deposits

7.3.1 Barren zones

Type 1 apatite from the Pé Quente deposit is related to the primary igneous assemblage and retains its igneous texture and composition, even though some intergranular propylitic alteration might slightly envelop the sample, usually through selective replacement of hornblende rims by chlorite. Igneous apatite lacks any particular trace element enrichment, except for its higher F concentrations (>3 wt. %) that acts structurally as a minor element. Therefore, igneous apatite tends to belong to the fluorapatite subgroup (Piccoli and Candela, 2002; Hughes and Rakovan, 2015). Under CL, it displays minor textural alteration patterns, usually as intergrowths of yellow- and green-luminescent-apatite in which yellow-luminescent apatite might have a somewhat turbid, dull glow (Fig. 5.3f, g), and green-luminescent apatite has a brighter glow, pristine and homogeneous texture, and tends to occur as overgrowths at the crystal rims (Fig. 7.20, 5.3h). Yellow-luminescent apatite is also present in the Teles Pires granite; however, weathering-related hematite therein impairs any deeper textural analysis (Fig. 7.20; 5.14e, f). These evidences suggest that yellow-luminescent apatite might register magmatic fractionation processes, while green-luminescent apatite might correspond to a posterior, possibly hydrothermal process at the final crystallisation stages of apatite.

Type 1 magnetite, on the other hand, does not retain its igneous titanomagnetite composition. It is depleted in Ti, and thus, displays a hydrothermal signature despite its association with Type 1 apatite and primary accessory phases (Fig. 7.20). Magnetite is classified as Type 2 if it has undergone selective replacement during deuteric (post-magmatic) alteration or propylitic alteration, which is indicated by skeletal texture, inclusions, overgrowths, and clustering of small rounded magnetite grains (as in sample GT-2; Fig. 7.20). However, the widespread pseudomorphic alteration in magnetite (sphenitisation and martitisation) throughout the province may indicate that propylitic alteration occurs in wide halos surrounding the deposits (supergene alteration). At these transitional zones, the sphenitisation process may be shown by the lowering Ti concentrations in magnetite and its association with hydrothermal titanite. Type 2 magnetite thus has lower Ti concentrations (0.5-3.5 wt. %) than igneous titanomagnetite

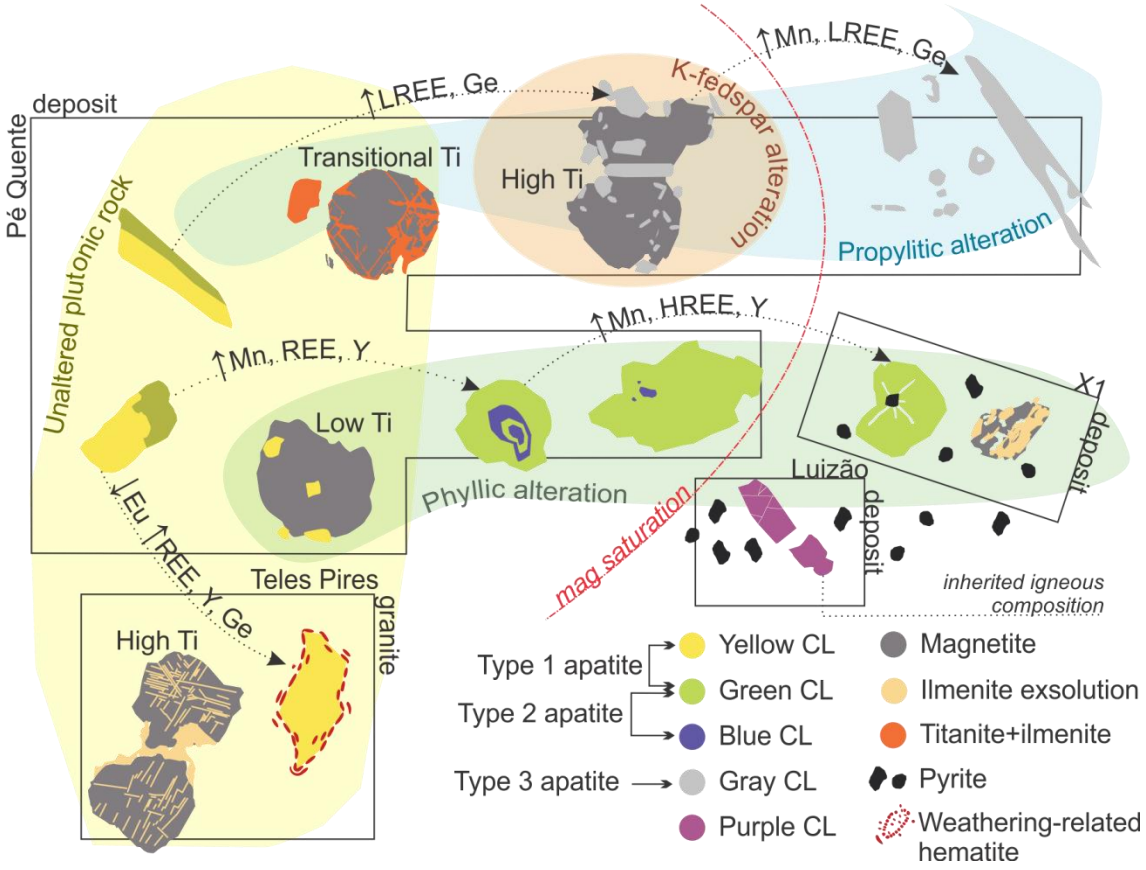

Figure 7.20 – Synoptic schema of the proposed paragenesis for apatite and magnetite in the intrusion-hosted gold deposits.

(Type 3) and higher Ti concentrations than hydrothermal magnetites (Type 1) thereby typifying a transitional composition. Therefore, both are characterised as hydrothermal magnetites. Type 1 magnetite is considered completely hydrothermal and does not retain any Ti composition, while Type 2 magnetite is referred to as transitional, since it retains some of its titanomagnetite composition (Fig. 7.20) and occurs associated with Type 1 apatite.

7.3.2 Phyllic alteration

Type 2 apatite from the Pé Quente depositis is typically hydrothermal and related to the phyllic alteration. It displays post-growth and partial alteration textures. This indicates the presence of dissolution and reprecipitation processes (Fig. 7.20) exemplified by complex CL textural patterns such as: (1) turbid yellow-green remnants at the apatite cores; (2) turbid blue/dark-grey apatite cores and pristine green-luminescent apatite rims with dissolution at the former and reprecipitation at the later;

(3) concentric zoning of green-luminescent apatite and blue-gray-luminescent apatite, indicating successive waves of hydrothermal solutions affecting mineral replacement (Fig. 7.20). Type 2 apatite is enriched in Mn, Fe, Y, HREE, and has intermediate LREE concentrations. It is associated to Type 4 magnetite (Fig. 7.20).

In the phyllic alteration of the X1 deposit, green-luminescent apatite displays a strongly saturated glow. It is distinct for its high Mn, Na and Fe contents, and for its balanced LREE and HREE concentrations (LREE≈HREE). Mn-rich apatite records the fluctuating oxygen fugacity that occurs during pyrite precipitation. Sulphide remains undersaturated throughout magmatic fractionation and only precipitates after magnetite crystallisation (Sun et al., 2004; Jenner et al., 2010), when there is a sudden decrease in fO_2 and pH due to sulphate reduction (Pokrovski and Dubrovinsky, 2011). Apatite only precipitates after sulphide, most likely because P concentrations are more soluble in peraluminous melts. Peraluminosity is hinted at by the presence of ilmenite-magnetite intergrowths at the X1 deposit (aluminium saturation index ASI=molar $Al_2O_3/CaO+Na_2O+K_2O>1$; Rodrigues, 2012.) The balanced REE concentrations in apatite are also similar to those of peraluminuous melts (Ishihara et al., 2008). Those physicochemical conditions give apatite from X1 deposit a metallogenic signature similar to those from Cu-Au porphyry deposits (Mao et al., 2016). Nonetheless, in the phyllic alteration of the Luizão deposit, apatite is inherited from the igneous assemblage, and is unique for its purple CL (Fig. 7.20).

7.3.3 K-feldspar alteration and propylitic alteration

Type 3 apatite occurs in the propylitic alteration that overprints the K-feldspar alteration of the Pé Quente deposit. It is associated with both the propylitic alteration (at sample SPQ-1) and the potassic alteration (at sample RA69). Texturally, it is distinguished by its homogeneous texture, dull gray luminescence, and needle- and donut-like morphologies (Fig. 7.20). Compositionally, it is distinguished by its high Cl, LREE and Ge concentrations. Type 3 apatite occurs assembled with Type 3 magnetite as part of the potassic alteration (RA69). Potassically altered magnetite is distinct for its higher Ti concentrations (>4 wt. % Ti) akin to igneous titanomagnetite. This might indicate that magnetite composition is only modified at lower temperature alterations (<600ºC). Since Ti coordinates much of the chemical variance in magnetite (Fig. 7.11,

7.13) it may also overrule the influence of other trace elements, such as Al, Ca, Pb and Zn, rendering them less successful as discriminators.

7.4 Advantages of apatite over magnetite and other indicator minerals

Indicator minerals, such as apatite, magnetite, zircon, chlorite, biotite and amphibole, have been developed as pathfinders for Cu ± Mo ± Au porphyry deposits (Wilkinson et al., 2015; Mao et al., 2016; Pisiak et al., 2017; Duan and Jiang, 2018; Xie et al., 2018; Nathwani et al., 2020; Xing et al., 2020). Apatite and magnetite are particularly interesting because they crystallise before hydrous mafic minerals and feldspars, and thus may record the crystallisation conditions of the primary magma in which they were formed. Hydrous mafic minerals, such as biotite and amphibole, may indicate petrogenetic conditions, such as temperature, oxygen fugacity, pressure and host magma composition, at more evolved stages of magmatic fractionation (Abdel-Fattah and Abdel-Rahman, 1994; LaTourrette et al., 1995; Tiepolo et al., 2007; Chakrabarty et al., 2008; Jennings et al., 2011). Apatite and magnetite saturation occur at about the same point at ~58% SiO_2 (Hoskin et al., 2000; Sun et al., 2004), which explains why both minerals are paragenetically associated.

Early crystallising apatite plays an important role in accessing magma conditions that would be important for ore fertility (Richards, 2011; Clemens and Stevens, 2012). Halogens in apatite (F and Cl) are especially important for magmatic volatiles (Dong, 2005). Apatite incorporates other trace elements such as F, Cl, Sr, REE, Y, Si, Na, Ge, Pb, U and Th, which can be used as discriminator elements for several physicochemical processes.

Magnetite also crystallises as early as apatite during magmatic fractionation, but it has a lesser range of efficient discriminant elements, which renders magnetite more unreliable as an indicator mineral. Its structure accommodates Ti, Al, Mg, V, Cr, Mn, Co, Ni, Zn and Ga. However, magnetite composition is more susceptible to factors such as fluid interaction, temperature, oxygen and sulphur fugacity, silica and sulphide activity, and host rock buffering (Nadoll et al., 2014). Magnetite is prone to incorporate trace elements even at <100ºC (Sidhu et al., 1978), which means that it is constantly being modified by hydrothermal processes. Furthermore, magnetite has a complex fabric with exsolutions, nanoinclusions and pseudomorphic alterations, which impair

accurate qualitative analysis of trace element concentrations (Nadoll et al., 2014; Deditius et al., 2018).

Zircon hosts trace elements such as REE, U, Th, Hf and Mo, and may likewise serve as an efficient indicator mineral (Hoskin and Schaltegger, 2003; Lu et al., 2016). It is formed in the early stages of magmatic fractionation, with a saturation point at 66% SiO_2, which is more evolved than apatite and magnetite (Hoskin et al., 2000; Hoskin and Schaltegger, 2003; Lu et al., 2016). Other indicator minerals may be used as pathfinders within propylitic alteration halos. Chlorite, for instance, is closely associated to the propylitic assemblage, and may accommodate several trace elements, such as Ti, V, Mg, Ni, and Sr, that may be used for vectoring the distance from porphyry centres (Wilkinson et al., 2015).

Apatite and magnetite are generally absent from the centre of mineral deposits, and may not be used as vectoring tools within the mineralised cores. Apatite was absent from the sodic alteration of the Pé Quente deposit, and magnetite was absent at both the X1 and Luizão deposit, where pyrite occurs instead. In the potassic alteration of the X1 deposit, both apatite and magnetite were absent. Even magnetite that occurs closer to the deposit centre within the potassic alteration actually does not exhibit a specific hydrothermal signature, being compositionally indistinguishable from igneous magnetite. Nevertheless, both apatite and magnetite are consistently found in the barren granitic host rocks and in the propylitic alteration zone that surrounds the mineral deposits, and thus, may be used at initial exploration efforts for targeting areas of interest and as fertility tools for intrusion-hosted mineral deposits (Mao et al., 2016; Nadoll et al., 2014; Pisiak et al., 2017; Duan and Jiang, 2018).

7.5 The classification of igneous and hydrothermal indicator minerals: suggestions for further developments

Boundaries between igneous and hydrothermal minerals are mostly not clear in the discriminant diagrams. Phyllic-related X1 apatite is distinguished because of its chemical composition (high Mn, HREE and Y concentrations) that indicates distinctly reducing crystallisation conditions. However, other types of hydrothermal apatites, ore-related igneous apatite and anorogenic-related apatite need more refinement to be efficiently discriminated from each other, as they do not easily match the constrained discriminant functions available in the literature (i.e. Mao et al., 2016; Bouzari et al.,

2016; Duan et al., 2018). Likewise, even though magnetites from barren and hydrothermal zones may be efficiently discriminated mainly because of Ti compositions, the overall composition of those samples when compared to literature data indicate that magnetites from barren zones are akin to Ti-poor hydrothermal magnetite. On the other hand, magnetites from hydrothermal zones have Ti-rich magmatic signatures similar to igneous titaniferous magnetites (on the terms of Nadoll et al., 2014, and Dare et al., 2014). Nonetheless, that igneous signature in magnetite is only reminiscent of a partial hydrothermal replacement reaction that did not particularly affect Ti concentrations.

Indeed, most magnetite grains analysed from the Pé Quente deposit are hydrothermal. Even magnetite that occurs in barren and only slightly altered granitic rocks displays strong alteration features, such as sphenitisation. Sphenitisation seems to occur at the later stages of magmatic fractionation as part of an incipient autometassomatism (deuteric) process that might render a hydrothermal signature to the indicator minerals as well. Volcaniclastic magnetite grains are also susceptible to the overprinting of multiple alteration processes. For instance, martitisation at the propylitic alteration halo of the Francisco deposit discloses Ti distributions that were predicted under such physicochemical conditions (such as low Ti; Nadoll et al., 2014). The only magnetite grains that display (1) high-Ti magmatic composition and (2) magmatic texture (such as exsolution lamallae) are those from the Teles Pires granite, which might be considered igneous titanomagnetites.

The ubiquity of mineral replacement reactions via hydrothermal solutions in magmatic rocks has been previously argued in Putnis and Putnis (2007), Putnis (2009) and Plümper and Putnis (2009). According to them, most granitoids have naturally undergone extensive, large-scale subsolidus re-equilibration that modified primary magmatic minerals due to deuteric and hydrothermal processes. Therefore, even feldspar phenocrysts that are often associated to typically igneous textures might have actually been affected by fluid-rock interaction (Plümper and Putnis, 2009; Parsons et al., 2015). Even though there is a conceptual difference between deuteric and externally derived fluids (Sederholm, 1929), there are a few pragmatic thresholds on how to distinguish between igneous- and hydrothermal-related processes through deterministic classification methods.

Most discriminant diagrams that aim to distinguish between barren and ore-related granitic rocks may be unable to correctly classify their indicator minerals *a priori*. This conundrum hinders on how discriminant diagrams may be extrapolated. Since extrapolation is the *raison d'être* of a robust machine learning algorithm for ore exploration, it is suggested that this conundrum may be solved through flexible methods that are independent of *a priori* classes, such as support vector machines and unsupervised statistical learning methods, such as PCA. Hence, even though LDA data is easily interpretable, they fail under scrutiny because of the blurred line between the *a priori* classification methods of igneous and hydrothermal indicator minerals.

Chapter 8

Concluding remarks

Textures and compositions of apatite and magnetite are sensible to melt and fluid variations, which makes them valuable petrogenetic and metallogenic proxies for the physicochemical conditions that triggered ore formation.

The following conclusions were reached for apatite:

(1) Apatite displays CL textural patterns that may be prognostic of specific alteration zones within the mineral deposit, especially the Pé Quentes deposit: (a) barren host rocks contain yellow-green-luminescent apatite (Type 1); (b) phyllic alteration contains green-luminescent apatite (Type 2) that is either brightly saturated and homogeneous, attesting recrystallisation, or dissolved and corroded, with dark blue and grey patches, indicating partial alteration; (c) propylitic alteration overprints potassic alteration and contains grey-luminescent apatite (Type 3) with homogeneous texture, dull glow, and ovoid, acicular and donut-like morphologies; and (d) inherited igneous apatite displays purple luminescence within phyllic alteration of the Luizão deposit. However, extrapolation of these patterns to other deposits is only tentative, since individual deposits imprint intrinsically different textural patterns into apatite.

(2) There is a general decrease in Sr contents and increase in Mn, REE, Y and Ge in apatite with hydrothermal alteration. These elements vary depending on the alteration type and on intrinsic conditions of each deposit. Propylitic-related apatite has higher LREE and Ge, while phyllic-related apatite has higher HREE and Y. Anorogenic-related apatite may be distinguished by its strong negative Eu anomaly.

(3) Mn-in-apatite oxybarometer in phyllic alteration indicates strongly reducing conditions during sulphide precipitation ($\log fO_2$ median -33). Apatite in the X1 deposit has high Mn and Yb contents similar to porphyry Cu-Au deposits.

And the following conclusions were reached for magnetite:

(1) Since Ti coordinates most of trace element variance in magnetite, it can be used as a single discriminator for magmatic-hydrothermal conditions. High-Ti magnetite is found in barren igneous rocks (Teles Pires granite) and in the high temperature potassic alteration wherein Ti from titanomagnetite remained immobile. Low-Ti magnetite occurs in the phyllic alteration and throughout the wide propylitic alteration halo.

(2) Magnetite is susceptible to several processes that might hinder its trace element evaluation, such as exsolution, nanoinclusions, sphenitisation and pseudomorphic alteration (martitisation).

(3) Most intrusion-related magnetite is altered by hydrothermal replacement (sphenitisation and martitisation) regardless of whether it occurs in barren zones or in hydrothermal zones, which indicates that propylitic alteration is widespread in the country rocks surrounding the deposits.

(4) V/Ga relative redox ratio in magnetite coincides with Mn-in-apatite oxybarometer in barren zones, but is susceptible to propylitic alteration.

(5) In the Francisco deposit, volcaniclastic magnetite displays high Ti as a signature of its exhalative origin. Volcaniclastic magnetite within the propylitic alteration is altered into low-Ti martite.

Overall, apatite is a promising indicator mineral because it consistently reflects a wide variety of magmatic-hydrothermal processes. Magnetite is less promising, though; at least in the Alta Floresta mineral province where granitoids have undergone widespread post-magmatic and propylitic alteration that selectively altered magnetite. Both apatite and magnetite have potentials and limitations in their use as indicator minerals. Herein, we suggest that *a priori* classification methods (that is, classifying beforehand whether a mineral is hydrothermal or igneous) might render biased results, given the ambiguous nature of fluid-induced trace element exchange at the transition between magmatic and hydrothermal conditions.

References

Abdel-Rahman, A. F. M. 1994. Nature of biotites from alkaline, calc-alkaline, and peraluminous magmas. *Journal of petrology*, *35*(2), 525-541.

Almeida F.F.M., Hasui Y., Brito Neves B.B., Fuck R.A. 1981. Brazilian structural provinces: an introduction. *Earth Science Reviews.* 17, 1-29.

Alves, C.L. 2019. Áreas de relevante interesse mineral - Projeto evolução crustal e metalogenia da Província Mineral Juruena-Teles Pires. Cleber Ladeira Alves, Gilmar José Rizzotto, Francisco Sene Rios, Gabriel Freitas Gonçalves. Goiânia: CPRM, 226 p. : il., 1 mapa. (Informe de recursos minerais. Série Províncias Minerais do Brasil; 22).

Aitchison, J. 1982. The statistical analysis of compositional data. *Journal of the Royal Statistical Society: Series B (Methodological)*, *44*(2), 139-160.

Aitchison, J., & Egozcue, J. J. 2005. Compositional data analysis: where are we and where should we be heading? *Mathematical Geology*, *37*(7), 829-850.

Arató, R., & Audétat, A. 2017a. Experimental calibration of a new oxybarometer for silicic magmas based on vanadium partitioning between magnetite and silicate melt. *Geochimica et Cosmochimica Acta*, *209*, 284-295.

Arató, R., & Audétat, A. 2017b. FeTiMM–A new oxybarometer for mafic to felsic magmas. *Geochemical Perspectives Letters*, *5*, 19-23.

Arató, R., & Audétat, A. 2017c. Vanadium magnetite–melt oxybarometry of natural, silicic magmas: a comparison of various oxybarometers and thermometers. *Contributions to Mineralogy and Petrology*, *172*(7), 52.

Assis R.R. 2008. Contexto geológico e associação paragenética das mineralizações auríferas de União do Norte, região de Peixoto de Azevedo, Província de Alta Floresta (MT). Instituto de Geociências, Universidade Estadual de Campinas; Trabalho de Conclusão de Curso; 81p.

Assis R.R. 2011. Depósitos auríferos associados ao magmatismo granítico do setor leste da Província de Alta Floresta (MT), Craton Amazônico: tipologia das mineralizações, modelos genéticos e implicações prospectivas. Dissertação de mestrado, Universidade Estadual de Campinas, Campinas, Brasil.

Assis R.R. 2015. Depósitos auríferos associados ao magmatismo félsico da Província de Alta Floresta (MT), Cráton Amazônico : litogeoquímica, idade das mineralizações e fonte dos fluidos. Tese de doutorado, Universidade Estadual de Campinas, Campinas, Brasil.

Assis, R. R., Xavier, R. P., de Barros, A. J. P., Barbuena, D., & Júnior, E. M. 2012. Contexto geológico e litogeoquímica das unidades plutônicas-vulcânicas da região de União do Norte, setor leste da Província Aurífera de Alta Floresta (MT): Geological setting and geochemistry of the plutonic-volcanic units from the União do Norte region, eastern portion of the Alta Floresta Gold Province (MT). *Revista Brasileira de Geociências*, *42*(1), 130-161.

Assis, R. R., Xavier, R. P., Paes de Barros, A. J., Barbuena, D., Trevisan, V. G., Ramos, G. S., & Santos, T. J. S. 2014. Depósitos de Au e Au+ metais de base associados a sistemas graníticos paleoproterozóicos do setor leste da Província de Alta Floresta (MT), Cráton Amazônico. In: *Metalogenia das Províncias Tectônicas Brasileiras: Belo Horizonte, Companhia de Pesquisa de Recursos Minerais (CPRM)*.

Assis, R. R., Xavier, R. P., & Creaser, R. A. 2017. Linking the Timing of Disseminated Granite-Hosted Gold-Rich Deposits to Paleoproterozoic Felsic Magmatism at Alta Floresta Gold Province, Amazon Craton, Brazil: Insights from Pyrite and Molybdenite Re-Os Geochronology. *Economic Geology*, *112*(8), 1937-1957.

Augustithis, S. S. 1995. Atlas of the textural patterns of ore minerals and metallogenic processes. Berlin. New York. Walter de Gruyter. 669p.

Averill, S. A. 2011. Viable indicator minerals in surficial sediments for two major base metal deposit types: Ni-Cu-PGE and porphyry Cu.

Ballhaus, C., Berry, R. F., & Green, D. H. 1990. Oxygen fugacity controls in the Earth's upper mantle. *Nature*, 348(6300), 437-440.

Banfield, J. F., & Eggleton, R. A. 1989. Apatite replacement and rare earth mobilization, fractionation, and fixation during weathering. *Clays and Clay Minerals*, *37*(2), 113-127.

Barros, M. A. S., Barros, A. J. P., Santos, J. O. S., & Rocha, M. L. B. P. 2015. Extension of the Tapajós domains to the Alta Floresta gold province: Evidence from U-Pb SHRIMP ages of the Nhandu intrusive suite at 1962 and 1967 Ma. *Proceedings of the 14◦ Simpósio de Geologia da Amazônia, Belém, Pará, Brazil*, *400*.

Belousova, E. A., Walters, S., Griffin, W. L., & O'reilly, S. Y. 2001. Trace-element signatures of apatites in granitoids from the Mt Isa Inlier, northwestern Queensland. *Australian Journal of Earth Sciences*, *48*(4), 603-619.

Belousova, E. A., Griffin, W. L., O'Reilly, S. Y., & Fisher, N. I. 2002. Apatite as an indicator mineral for mineral exploration: trace-element compositions and their relationship to host rock type. *Journal of Geochemical Exploration*, *76*(1), 45-69.

Betkowski, W. B., Rakovan, J., & Harlov, D. E. 2017. Geochemical and textural characterization of phosphate accessory phases in the vein assemblage and metasomatically altered Llallagua tin porphyry. *Mineralogy and Petrology*, *111*(4), 547-568.

Bettencourt, J. S., Juliani, C., Xavier, R. P., Monteiro, L. V., Neto, A. C. B., Klein, E. L., & Pereira, V. P. 2017. Metallogenetic systems associated with granitoid magmatism in the Amazonian Craton: An overview of the present level of understanding and exploration significance. *Journal of South American Earth Sciences*, *68*, 22-49.

Bispo-Santos, F., D'Agrella-Filho, M. S., Pacca, I. I., Janikian, L., Trindade, R. I., Elming, S. A., Silva, J.A., Barros, M.A.S., Pinho, F. E. 2008. Columbia revisited: Paleomagnetic results from the 1790 Ma colider volcanics (SW Amazonian Craton, Brazil). *Precambrian Research*, *164*(1-2), 40-49.

Boutroy, E., Dare, S. A., Beaudoin, G., Barnes, S. J., & Lightfoot, P. C. 2014. Magnetite composition in Ni-Cu-PGE deposits worldwide: application to mineral exploration. *Journal of Geochemical Exploration*, *145*, 64-81.

Bouzari, F., Hart, C. J., Bissig, T., & Barker, S. 2016. Hydrothermal alteration revealed by apatite luminescence and chemistry: a potential indicator mineral for exploring covered porphyry copper deposits. *Economic Geology*, *111*(6), 1397-1410.

Broman, C., Nyström, J. O., Henríquez, F., & Elfman, M. 1999. Fluid inclusions in magnetite-apatite ore from a cooling magmatic system at El Laco, Chile. *Gff*, *121*(3), 253-267.

Broom-Fendley, S., Styles, M. T., Appleton, J. D., Gunn, G., & Wall, F. (2016). Evidence for dissolution-reprecipitation of apatite and preferential LREE mobility in carbonatite-derived late-stage hydrothermal processes. *American Mineralogist*, *101*(3), 596-611.

Bruand, E., Storey, C., & Fowler, M. 2014. Accessory mineral chemistry of high Ba–Sr granites from northern Scotland: constraints on petrogenesis and records of whole-rock signature. *Journal of Petrology*, *55*(8), 1619-1651.

Bruand, E., Storey, C., & Fowler, M. 2016. An apatite for progress: Inclusions in zircon and titanite constrain petrogenesis and provenance. *Geology*, *44*(2), 91-94.

Bruand, E., Fowler, M., Storey, C., & Darling, J. 2017. Apatite trace element and isotope applications to petrogenesis and provenance. *American Mineralogist*, *102*(1), 75-84.

Buddington, A. F., & Lindsley, D. H. 1964. Iron-titanium oxide minerals and synthetic equivalents. *Journal of petrology*, *5*(2), 310-357.

Burns, R. G., & Burns, R. G. 1993. *Mineralogical applications of crystal field theory* (Vol. 5). Cambridge university press.

Canil, D., Grondahl, C., Lacourse, T., & Pisiak, L. K. 2016. Trace elements in magnetite from porphyry Cu–Mo–Au deposits in British Columbia, Canada. *Ore Geology Reviews*, *72*, 1116-1128.

Cao, M., Li, G., Qin, K., Seitmuratova, E. Y., & Liu, Y. 2012. Major and trace element characteristics of apatites in granitoids from Central Kazakhstan: implications for petrogenesis and mineralization. *Resource Geology*, *62*(1), 63-83.

Cawood, P. A., Strachan, R. A., Pisarevsky, S. A., Gladkochub, D. P., & Murphy, J. B. 2017. Linking collisional and accretionary orogens during Rodinia assembly and breakup: Implications for models of supercontinent cycles. *Earth and Planetary Science Letters*, *449*, 118-127.

Chakrabarty, A., Sen, A. K., & Ghosh, T. K. 2009. Amphibole—a key indicator mineral for petrogenesis of the Purulia carbonatite, West Bengal, India. *Mineralogy and Petrology*, *95*(1-2), 105-112.

Cherniak, D. J. 2005. Uranium and manganese diffusion in apatite. *Chemical Geology*, 219(1-4), 297-308.

Chu, M. F., Wang, K. L., Griffin, W. L., Chung, S. L., O'Reilly, S. Y., Pearson, N. J., & Iizuka, Y. 2009. Apatite composition: tracing petrogenetic processes in Transhimalayan granitoids. *Journal of Petrology*, *50*(10), 1829-1855.

Clemens, J. D., & Stevens, G. 2012. What controls chemical variation in granitic magmas?. *Lithos*, *134*, 317-329.

Comodi, P., Liu, Y., Stoppa, F., & Woolley, A. R. 1999. A multi-method analysis of Si-, S-and REE-rich apatite from a new find of kalsilite-bearing leucitite (Abruzzi, Italy). *Mineralogical Magazine*, *63*(5), 661-661.

Cook, N., Ciobanu, C. L., George, L., Zhu, Z. Y., Wade, B., & Ehrig, K. 2016. Trace element analysis of minerals in magmatic-hydrothermal ores by laser ablation inductively-coupled plasma mass spectrometry: Approaches and opportunities. *Minerals*, *6*(4), 111.

Cooke, D. R., Agnew, P., Hollings, P., Baker, M., Chang, Z., Wilkinson, J. J., & Fox, N. 2017. Porphyry indicator minerals (PIMS) and porphyry vectoring and fertility tools (PVFTS)–indicators of mineralization styles and recorders of hypogene geochemical dispersion halos. Decennial Mineral Exploration Conferences.

Cooke D.R., Hollings P., Wilkinson J.J. and Tosdal R.M. 2014. Geochemistry of Porphyry Deposits. In: Holland H.D. and Turekian K.K. (eds.) Treatise on Geochemistry, Second Edition, vol. 13, pp. 357-381. Oxford: Elsevier.

Cooke, D. R., Wilkinson, J. J., Baker, M., Agnew, P., Phillips, J., Chang, Z., & Zhang, L. 2020. Using mineral chemistry to aid exploration: A case study from the Resolution porphyry Cu-Mo deposit, Arizona. *Economic Geology*, *115*(4), 813-840.

Corbett, G. 2009. Anatomy of porphyry-related Au-Cu-Ag-Mo mineralised systems: Some exploration implications. In: *Australian Institute of Geoscientists North Queensland Exploration Conference* (pp. 1-13).

Cordani, U. G., & Teixeira, W. 2007. Proterozoic accretionary belts in the Amazonian Craton. *Geological Society of America Memoirs*, *200*, 297-320.

Cordani, U. G., Teixeira, W., D'Agrella-Filho, M. S., & Trindade, R. I. 2009. The position of the Amazonian Craton in supercontinents. *Gondwana Research*, *15*(3-4), 396-407.

Cornell, R. M., & Schwertmann, U. 2003. The iron oxides: structure, properties, reactions, occurrences and uses. John Wiley & Sons.

Crawley, M. J. (2012). *The R book*. John Wiley & Sons.

Dall'Agnol R, Costi HT, da S. Leite AA, de Magalhães MS, Teixeira NP 1999. Rapakivi granites from Brazil and adjacent areas. *Precambrian Research* 95:9–39

Dare, S. A., Barnes, S. J., Beaudoin, G., Méric, J., Boutroy, E., & Potvin-Doucet, C. 2014. Trace elements in magnetite as petrogenetic indicators. *Mineralium Deposita*, *49*(7), 785-797.

Deditius, A. P., Reich, M., Simon, A. C., Suvorova, A., Knipping, J., Roberts, M. P. & Saunders, M. 2018. Nanogeochemistry of hydrothermal magnetite. *Contributions to Mineralogy and Petrology*, *173*(6), 47.

Deer, W. A., Howie, R. A., Wise, W. S., & Zussman, J. 2004. Rock-forming minerals. Volume 4B: Framework silicates: silica minerals, feldspathoids and the zeolites. *Rock-forming minerals. Volume 4B: Framework silicates: silica minerals, feldspathoids and the zeolites.*, (Ed. 2).

Defant, M. J., & Drummond, M. S. 1990. Derivation of some modern arc magmas by melting of young subducted lithosphere. *Nature*, *347*(6294), 662-665.

Dempster, T. J., Jolivet, M., Tubrett, M. N., & Braithwaite, C. J. R. 2003. Magmatic zoning in apatite: a monitor of porosity and permeability change in granites. *Contributions to Mineralogy and Petrology*, 145(5), 568-577.

Ding, T., Ma, D., Lu, J., & Zhang, R. 2015. Apatite in granitoids related to polymetallic mineral deposits in southeastern Hunan Province, Shi–Hang zone, China: Implications for petrogenesis and metallogenesis. *Ore Geology Reviews*, *69*, 104-117.

Dong, P. 2005. Halogen-element (F, Cl, and Br) behavior in apatite, scapolite, and sodalite: An experimental investigation with field applications: Unpublished Ph. D (Doctoral dissertation, thesis, Saskatoon, Saskatchewan, University of Saskatchewan).

Duan, D. F., & Jiang, S. Y. 2018. Using apatite to discriminate synchronous ore-associated and barren granitoid rocks: A case study from the Edong metallogenic district, South China. *Lithos*, *310*, 369-380.

Duan, C., Li, Y., Mao, J., Hou, K., Wang, C., Yang, B. & Li, W. 2019. Ore formation at the Washan iron oxide–apatite deposit in the Ningwu Ore District, eastern

China: Insights from in situ LA-ICP-MS magnetite trace element geochemistry. *Ore Geology Reviews*, *112*, 103064.

Duarte, T. B., Xavier, R.P., & Rodrigues, J.B. 2019. A review of the geodynamic setting of the Volcanic Domain in the Juruena Magmatic Arc, southwestern Amazon Craton, Brazil, based on geochemical, U-Pb and Sm-Nd data. *Journal of the Geological Survey of Brazil*, *2*(1), 37-73.

Dupuis, C., & Beaudoin, G. 2011. Discriminant diagrams for iron oxide trace element fingerprinting of mineral deposit types. *Mineralium Deposita*, *46*(4), 319-335.

Gammons, C. H., & William-Jones, A. E. 1997. Chemical mobility of gold in the porphyry-epithermal environment. *Economic Geology*, *92*(1), 45-59.

Ghiorso, M. S., & Evans, B. W. 2008. Thermodynamics of rhombohedral oxide solid solutions and a revision of the Fe-Ti two-oxide geothermometer and oxygen-barometer. *American Journal of Science*, 308(9), 957-1039.

Golonka, J., & Bocharova, N. Y. 2000. Hot spot activity and the break-up of Pangea. *Palaeogeography, Palaeoclimatology, Palaeoecology*, *161*(1-2), 49-69.

Götze, J. 2012. Application of cathodoluminescence microscopy and spectroscopy in geosciences. *Microscopy and Microanalysis*, *18*(6), 1270-1284.

Goldenfeld, N. 1987. Theory of spherulitic crystallization. *Journal of crystal growth*, *84*(4), 601-608.

Gratz, R., & Heinrich, W. 1997. Monazite-xenotime thermobarometry: Experimental calibration of the miscibility gap in the binary system CePO4-YPO4. *American Mineralogist*, 82(7-8), 772-780.

Groves, D. I., Bierlein, F. P., Meinert, L. D., & Hitzman, M. W. 2010. Iron oxide copper-gold (IOCG) deposits through Earth history: Implications for origin, lithospheric setting, and distinction from other epigenetic iron oxide deposits. *Economic Geology*, 105(3), 641-654.

Groves, D. I., Goldfarb, R. J., Gebre-Mariam, M., Hagemann, S. G., & Robert, F. 1998. Orogenic gold deposits: a proposed classification in the context of their crustal distribution and relationship to other gold deposit types. *Ore geology reviews*, *13*(1-5), 7-27.

Guo, Q., Planer-Friedrich, B., Liu, M., Yan, K., & Wu, G. 2019. Magmatic fluid input explaining the geochemical anomaly of very high arsenic in some southern Tibetan geothermal waters. *Chemical Geology*, *513*, 32-43.

Ferrero, S., & Angel, R. J. 2018. Micropetrology: Are inclusions grains of truth?. *Journal of Petrology*, 59(9), 1671-1700.

Haggerty, S. E. 1976. Opaque mineral oxides in terrestrial igneous rocks. In: *Reviews in mineralogy--oxide minerals*. Vol. 3. Edited by D. Rumble 111. Southern Printing Company, Blacksburg, VA, pp. 101-300.

Heinrich, C. A. 2005. The physical and chemical evolution of low-salinity magmatic fluids at the porphyry to epithermal transition: a thermodynamic study. *Mineralium Deposita*, *39*(8), 864-889.

Heinrich, W., Rehs, G., & Franz, G. 1997. Monazite–xenotime miscibility gap thermometry. I. An empirical calibration. *Journal of Metamorphic Geology*, 15(1), 3-16.

Hoskin, P. W. O., & Black, L. P. 2000. Metamorphic zircon formation by solid-state recrystallization of protolith igneous zircon. *Journal of metamorphic Geology*, *18*(4), 423-439.

Hu, H., Lentz, D., Li, J. W., McCarron, T., Zhao, X. F., & Hall, D. 2015. Reequilibration processes in magnetite from iron skarn deposits. *Economic Geology*, *110*(1), 1-8.

Huang, X. W., & Beaudoin, G. 2019. Textures and Chemical Compositions of Magnetite from Iron Oxide Copper-Gold (IOCG) and Kiruna-Type Iron Oxide-Apatite (IOA) Deposits and Their Implications for Ore Genesis and Magnetite Classification Schemes. *Economic Geology*, *114*(5), 953-979.

Huang, X. W., Sappin, A. A., Boutroy, É., Beaudoin, G., & Makvandi, S. 2019. Trace Element Composition of Igneous and Hydrothermal Magnetite from Porphyry Deposits: Relationship to Deposit Subtypes and Magmatic Affinity. *Economic Geology*, *114*(5), 917-952.

Hughes, J. M., & Rakovan, J. F. (2015). Structurally robust, chemically diverse: apatite and apatite supergroup minerals. *Elements*, 11(3), 165-170.

Ishihara, S. 1977. The magnetite-series and ilmenite-series granitic rocks. Mining geology, 27(145), 293-305.

Ishihara, S. 2004. The redox state of granitoids relative to tectonic setting and earth history: the magnetite–ilmenite series 30 years later. *Earth and Environmental Science Transactions of the Royal Society of Edinburgh*, *95*(1-2), 23-33.

Ishihara, S., Sawata, H., Arpornsuwan, S., Busaracome, P., & Bungbrakearti, N. 1979. The magnetite-series and ilmenite-series granitoids and their bearing on tin mineralization, particularly of the Malay Peninsula region. *Geological Society of Malaysia*, Bulletin, 11, pp. 103-110.

Ishihara, S., Hua, R., Hoshino, M., & Murakami, H. 2008. REE abundance and REE minerals in granitic rocks in the Nanling range, Jiangxi Province, southern China, and generation of the REE-rich weathered crust deposits. *Resource Geology*, *58*(4), 355-372.

James, G., Witten, D., Hastie, T., & Tibshirani, R. 2013. *An introduction to statistical learning with applications in R*. New York: Springer.

Jami, M., Dunlop, A. C., & Cohen, D. R. 2007. Fluid inclusion and stable isotope study of the Esfordi apatite-magnetite deposit, Central Iran. *Economic geology*, *102*(6), 1111-1128.

Janoušek, V., Moyen, J. F., Martin, H., Erban, V., & Farrow, C. 2017. *Geochemical modelling of igneous processes–principles and recipes in R language*. Springer, Berlin, doi, 10, 978-3.

Jenner, F. E., O'Neill, H. S. C., Arculus, R. J., & Mavrogenes, J. A. 2010. The magnetite crisis in the evolution of arc-related magmas and the initial concentration of Au, Ag and Cu. *Journal of Petrology*, *51*(12), 2445-2464.

Jennings, E. S., Marschall, H. R., Hawkesworth, C. J., & Storey, C. D. 2011. Characterization of magma from inclusions in zircon: Apatite and biotite work well, feldspar less so. *Geology*, *39*(9), 863-867.

Jonsson, E., Troll, V. R., Högdahl, K., Harris, C., Weis, F., Nilsson, K. P., & Skelton, A. (2013). Magmatic origin of giant 'Kiruna-type'apatite-iron-oxide ores in Central Sweden. *Nature Scientific Reports*, 3, 1644.

Kempe, U., & Götze, J. 2002. Cathodoluminescence (CL) behaviour and crystal chemistry of apatite from rare-metal deposits. *Mineralogical Magazine*, *66*(1), 151-172.

Knipping, J. L., Bilenker, L. D., Simon, A. C., Reich, M., Barra, F., Deditius, A. P., & Munizaga, R. 2015. Trace elements in magnetite from massive iron oxide-apatite

deposits indicate a combined formation by igneous and magmatic-hydrothermal processes. *Geochimica et Cosmochimica Acta*, 171, 15-38.

Knipping, J. L., Bilenker, L. D., Simon, A. C., Reich, M., Barra, F., Deditius, A. P., & Munizaga, R. 2015. Giant Kiruna-type deposits form by efficient flotation of magmatic magnetite suspensions. *Geology*, 43(7), 591-594.

Lang, J., & Baker, T. 2001. Intrusion-related gold systems: the present level of understanding. *Mineralium Deposita*, *36*, 477-489.

LaTourrette, T., Hervig, R. L., & Holloway, J. R. 1995. Trace element partitioning between amphibole, phlogopite, and basanite melt. *Earth and Planetary Science Letters*, *135*(1-4), 13-30.

Liang, H. Y., Sun, W., Su, W. C., & Zartman, R. E. 2009. Porphyry copper-gold mineralization at Yulong, China, promoted by decreasing redox potential during magnetite alteration. *Economic Geology*, *104*(4), 587-596.

Liu, W., Mei, Y., Etschmann, B., Brugger, J., Pearce, M., Ryan, C. G., & Boesenberg, U. 2017. Arsenic in hydrothermal apatite: Oxidation state, mechanism of uptake, and comparison between experiments and nature. *Geochimica et Cosmochimica Acta*, *196*, 144-159.

Longerich, H. P., Jackson, S. E., & Günther, D. 1997. Inter-laboratory note. Laser ablation inductively coupled plasma mass spectrometric transient signal data acquisition and analyte concentration calculation. *Journal of analytical atomic spectrometry*, *11*(9), 899-904.

Lu, Y., Loucks, R., Fiorentini, M., McCuaig, T., Evans, N. J., Yang, Z. M., & Kobussen, A. 2017. Zircon compositions as a pathfinder for porphyry Cu±Mo±Au deposits. *Society of Economic Geologists. Special Publications Series*, *19*, 329-347.

Hart, C. J. R., & Goldfarb, R. J. 2005. Distinguishing intrusion-related from orogenic gold systems. In *New Zealand Minerals Conference Proceedings* (Vol. 2005, pp. 125-133).

Hedenquist, J. W., & Lowenstern, J. B. 1994. The role of magmas in the formation of hydrothermal ore deposits. *Nature*, *370*(6490), 519-527.

Hoffman, P. F. 1999. The break-up of Rodinia, birth of Gondwana, true polar wander and the snowball Earth. *Journal of African Earth .l*and magnetite classification schemes. *Economic Geology*, *114*(5), 953-979.

Hoskin, P. W., Kinny, P. D., Wyborn, D., & Chappell, B. W. 2000. Identifying accessory mineral saturation during differentiation in granitoid magmas: an integrated approach. *Journal of Petrology*, *41*(9), 1365-1396.

Huang, X. W., Boutroy, É., Makvandi, S., Beaudoin, G., Corriveau, L., & De Toni, A. F. 2019. Trace element composition of iron oxides from IOCG and IOA deposits: relationship to hydrothermal alteration and deposit subtypes. *Mineralium Deposita*, *54*(4), 525-552.

Huang, X. W., Sappin, A. A., Boutroy, É., Beaudoin, G., & Makvandi, S. 2019. Trace Element Composition of Igneous and Hydrothermal Magnetite from Porphyry Deposits: Relationship to Deposit Subtypes and Magmatic Affinity. *Economic Geology*, *114*(5), 917-952.

Hughes, J. M., & Rakovan, J. 2002. The crystal structure of apatite, Ca5 (PO4) 3 (F, OH, Cl). *Reviews in Mineralogy and Geochemistry*, *48*(1), 1-12.

Hughes, J. M., & Rakovan, J. F. 2015. Structurally robust, chemically diverse: apatite and apatite supergroup minerals. *Elements*, *11*(3), 165-170.

Kroonenberg, S. B., & de Roever, E. W. 2011. Geological evolution of the Amazonian Craton. In: *Amazonia: Landscape and Species Evolution: A look into the past* Hoorn, C., & Wesselingh, F. (Eds.). (2011). *Amazonia: landscape and species evolution: a look into the past*. John Wiley & Sons.Mao, M., Rukhlov, A. S., Rowins, S. M., Spence, J., & Coogan, L. A. 2017. Apatite trace element compositions: a robust new tool for mineral exploration. *Economic Geology*, *111*(5), 1187-1222.

Krneta, S., Ciobanu, C. L., Cook, N. J., Ehrig, K., & Kontonikas-Charos, A. 2016. Apatite at Olympic Dam, South Australia: A petrogenetic tool. *Lithos*, 262, 470-485.

Mao, M., Rukhlov, A. S., Rowins, S. M., Spence, J., & Coogan, L. A. 2016. Apatite trace element compositions: a robust new tool for mineral exploration. *Economic Geology*, *111*(5), 1187-1222.

McClenaghan, M. B. 2005. Indicator mineral methods in mineral exploration. *Geochemistry: Exploration, Environment, Analysis*, *5*(3), 233-245.

McClenaghan, M. B. 2011. Overview of common processing methods for recovery of indicator minerals from sediment and bedrock in mineral exploration.

McDonough, W. F., & Sun, S. S. 1995. The composition of the Earth. *Chemical geology*, *120*(3-4), 223-253.

Mercer, C. N., Reed, M. H., & Mercer, C. M. 2015. Time scales of porphyry Cu deposit formation: Insights from titanium diffusion in quartz. *Economic Geology*, *110*(3), 587-602.

Miguel-Jr, E. 2011. Controle Estrutural das mineralizações auríferas e idades U-Pb das rochas encaixantes ao longo do Lineamento Peru-Trairão: Província Aurífera de Alta Floresta, Mato Grosso. Dissertação de mestrado, Universidade Estadual de Campinas, Campinas, Brazil.

Miles, A. J., Graham, C. M., Hawkesworth, C. J., Gillespie, M. R., Hinton, R. W., & Bromiley, G. D. 2014. Apatite: A new redox proxy for silicic magmas?. *Geochimica et Cosmochimica Acta*, *132*, 101-119.

Mollo, S., Putirka, K., Iezzi, G., & Scarlato, P. 2013. The control of cooling rate on titanomagnetite composition: implications for a geospeedometry model applicable to alkaline rocks from Mt. Etna volcano. *Contributions to Mineralogy and Petrology*, *165*(3), 457-475.

Moreton L.C. & Martins E.G. 2005. *Geologia e Recursos Minerais de Alta Floresta. Vila Guarita*. Escala 1:250.000. Brasília, CPRM, 68 p.

Moura, M.A. 1998. O Maciço Granítico Matupá e o Depósito de Ouro Serrinha (MT): Petrologia, Alteração Hidrotermal e Metalogenia. Tese de Doutorado, IG/UnB, 238p.

Moura, M. A., Botelho, N. F., Olivo, G. R., & Kyser, T. K. 2006. Granite-related Paleoproterozoic, Serrinha gold deposit, Southern Amazonia, Brazil: hydrothermal alteration, fluid inclusion and stable isotope constraints on genesis and evolution. *Economic Geology*, *101*(3), 585-605.

Moyen, J. F. 2009. High Sr/Y and La/Yb ratios: the meaning of the "adakitic signature". *Lithos*, *112*(3-4), 556-574.

Murad, E., & Cashion, J. 2004. Iron oxides. In: *Mössbauer spectroscopy of environmental materials and their industrial utilization* (pp. 159-188). Springer, Boston, MA.

Nadoll, P., Angerer, T., Mauk, J. L., French, D., & Walshe, J. 2014. The chemistry of hydrothermal magnetite: a review. *Ore geology reviews*, *61*, 1-32.

Nadoll, P., & Koenig, A. E. 2011. LA-ICP-MS of magnetite: methods and reference materials. *Journal of Analytical Atomic Spectrometry*, 26(9), 1872-1877.

Nadoll, P., Mauk, J. L., Hayes, T. S., Koenig, A. E., & Box, S. E. 2012. Geochemistry of magnetite from hydrothermal ore deposits and host rocks of the Mesoproterozoic Belt Supergroup, United States. *Economic Geology*, *107*(6), 1275-1292.

Nathwani, C. L., Loader, M. A., Wilkinson, J. J., Buret, Y., Sievwright, R. H., & Hollings, P. 2020. Multi-stage arc magma evolution recorded by apatite in volcanic rocks. *Geology*, *48*(4), 323-327.

Ohmoto, H. 2003. Nonredox transformations of magnetite-hematite in hydrothermal systems. *Economic Geology*, *98*(1), 157-161.

Ohmoto, H., & Goldhaber, M. B. 1997. Sulfur and carbon isotopes. In: *Geochemistry of Hydrothermal Ore Deposits*, 3rd edition Éds: HL Barnes.

Olade, M. A., & Fletcher, W. K. 1976. Trace element geochemistry of the Highland Valley and Guichon Creek Batholith in relation to porphyry copper mineralization. *Economic Geology*, *71*(4), 733-748.

Ovalle, J. T., La Cruz, N. L., Reich, M., Barra, F., Simon, A. C., Konecke, B. A., & Morata, D. 2018. Formation of massive iron deposits linked to explosive volcanic eruptions. *Nature Scientific Reports*, *8*(1), 1-11.

Nasdala, L., Götze, J., & Hanchar, J. M. 2013. Luminescence spectroscopy and imaging: analytical advances and perspectives in the Earth sciences and related disciplines.

Paes de Barros, A.J. 2007. Granitos da região de Peixoto de Azevedo – Novo Mundo e mineralizações auríferas relacionadas – Província Aurífera Alta Floresta (MT). Tese de Doutorado, IG/UNICAMP, 154p.

Pagel, M., Barbin, V., Blanc, P., & Ohnenstetter, D. 2000. Cathodoluminescence in geosciences: an introduction. In *Cathodoluminescence in Geosciences* (pp. 1-21). Springer, Berlin, Heidelberg.

Pan, Y., & Fleet, M. E. 2002. Compositions of the apatite-group minerals: substitution mechanisms and controlling factors. *Reviews in Mineralogy and Geochemistry*, *48*(1), 13-49.

Pan, L. C., Hu, R. Z., Wang, X. S., Bi, X. W., Zhu, J. J., & Li, C. 2016. Apatite trace element and halogen compositions as petrogenetic-metallogenic indicators: Examples from four granite plutons in the Sanjiang region, SW China. *Lithos*, *254*, 118-130.

Parsons, I., Fitz Gerald, J. D., & Lee, M. R. 2015. Routine characterization and interpretation of complex alkali feldspar intergrowths. *American Mineralogist*, *100*(5-6), 1277-1303.

Pawlowsky-Glahn, V., & Egozcue, J. J. 2002. BLU estimators and compositional data. *Mathematical Geology*, *34*(3), 259-274.

Perseil, E. A., Blanc, P., & Ohnenstetter, D. 2000. As-bearing fluorapatite in manganiferous deposits from St. Marcel–Praborna, Val d'Aosta, Italy. *The Canadian Mineralogist*, *38*(1), 101-117.

Piccoli, P. M., & Candela, P. A. 2002. Apatite in igneous systems. *Reviews in Mineralogy and Geochemistry*, *48*(1), 255-292.

Piccoli, P., & Candela, P. 1994. Apatite in felsic rocks; a model for the estimation of initial halogen concentrations in the Bishop Tuff (Long Valley) and Tuolumne Intrusive Suite (Sierra Nevada Batholith) magmas. *American Journal of Science*, *294*(1), 92-135.

Pimentel, M., 2001. Resultados geocronológicos do Projeto Promin Alta Floresta. ´ Internal Report. Brasılia, UnB.

Pinho, M.A.S.B., Chemale-Jr, F., Van Schmus, W.R., Pinho, F.E.C., 2003. U–Pb and Sm–Nd evidence for 1.76–1.77Ga magmatism in the Moriru region, Mato Grosso, Brazil: implications for province boundaries in the SWAmazon Craton. Precambrian Res. 126, 1–25.

Pirajno, F. 2008. *Hydrothermal processes and mineral systems*. Springer Science & Business Media.

Pisarevsky, S. A., Elming, S. Å., Pesonen, L. J., & Li, Z. X. 2014. Mesoproterozoic paleogeography: supercontinent and beyond. *Precambrian Research*, *244*, 207-225.

Pisiak, L. K., Canil, D., Lacourse, T., Plouffe, A., & Ferbey, T. 2017. Magnetite as an indicator mineral in the exploration of porphyry deposits: a case study in till near the Mount Polley Cu-Au deposit, British Columbia, Canada. *Economic Geology*, *112*(4), 919-940.

Plümper, O., & Putnis, A. 2009. The complex hydrothermal history of granitic rocks: multiple feldspar replacement reactions under subsolidus conditions. *Journal of Petrology*, *50*(5), 967-987.

Pokrovski, G. S., & Dubrovinsky, L. S. 2011. The S3–ion is stable in geological fluids at elevated temperatures and pressures. *Science*, *331*(6020), 1052-1054.

Pouchou, J. L., & Pichoir, F. 1985. PAP Φ(ρZ) procedure for improved quantitative microanalysis. Pp. 104À106 in: Microbeam Analysis (JT Armstrong, editor).

Prado, E. S., Barros, M. A. S., Pinho, F. E. C., & Pierosan, R. 2013. Granito Terra Nova–petrologia e geocronologia: um granito tipo-A da Província Aurífera Alta Floresta–Cráton Amazônico. *Brazilian Journal of Geology*, *43*(1), 101-116.

Prowatke, S., & Klemme, S. 2006. Trace element partitioning between apatite and silicate melts. *Geochimica et Cosmochimica Acta*, *70*(17), 4513-4527.

Putnis, A. 2009. Mineral replacement reactions. *Reviews in mineralogy and geochemistry*, *70*(1), 87-124.

Putnis, A., & Putnis, C. V. 2007. The mechanism of reequilibration of solids in the presence of a fluid phase. *Journal of Solid State Chemistry*, *180*(5), 1783-1787.

Rakovan, J. F., & Hughes, J. M. 2000. Strontium in the apatite structure: strontian fluorapatite and belovite-(Ce). *The Canadian Mineralogist*, *38*(4), 839-845.

Richards, J. P. 2011. High Sr/Y arc magmas and porphyry Cu±Mo±Au deposits: just add water. *Economic Geology*, *106*(7), 1075-1081.

Rizzotto, G. J., & Hartmann, L. A. 2012. Geological and geochemical evolution of the Trincheira Complex, a Mesoproterozoic ophiolite in the southwestern Amazon craton, Brazil. *Lithos*, *148*, 277-295.

Rodrigues R.M. 2012. *Caracterização geológica e metalogenética do Depósito X1 – Província Aurífera de Alta Floresta, Região de Matupá (MT)*. Instituto de Geociências, Dissertação de Mestrado, 70p. Universidade Estadual de Campinas, Campinas, São Paulo.

Rogers, J. J., & Santosh, M. 2002. Configuration of Columbia, a Mesoproterozoic supercontinent. *Gondwana Research*, *5*(1), 5-22.

Rakovan, J., & Reeder, R. J. 1994. Differential incorporation of trace elements and dissymmetrization in apatite: The role of surface structure during growth. *American Mineralogist*, 79(9-10), 892-903.

Santos J.O.S., Hartmann L.A., Faria M.S.G., Riker S.R., Souza M.M., Almeida M.E., McNaughton N.J. 2007. A compartimentação do Cráton Amazonas em

províncias: avanços ocorridos no período 2000-2007. *In:* SBG-NO, Simp. Geol. Amaz., 9, Belém, CD-Rom.

Santos J.O.S., Groves D.I., Hartmann A., Moura M.A., McNaughton N.J. 2001. Gold deposits of the Tapajós and Alta Floresta domains, Tapajós-Parima orogenic belt, Amazon Craton, Brazil. Mineralium Deposita, 36:278-299.

Santos, J. O. S., Hartmann, L. A., Gaudette, H. E., Groves, D. I., Mcnaughton, N. J., & Fletcher, I. R. 2000. A new understanding of the provinces of the Amazon Craton based on integration of field mapping and U-Pb and Sm-Nd geochronology. *Gondwana Research*, *3*(4), 453-488.

Scandolara, J. E., Correa, R. T., Fuck, R. A., Souza, V. S., Rodrigues, J. B., Ribeiro, P. S. E., & Lacerda Filho, J. V. 2017. Paleo-Mesoproterozoic arc-accretion along the southwestern margin of the Amazonian craton: The Juruena accretionary orogen and possible implications for Columbia supercontinent. *Journal of South American Earth Sciences*, *73*, 223-247.

Sederholm, J. J. 1929. The use of the term" deuteric". *Economic Geology*, *24*(8), 869-871.

Sha, L. K., & Chappell, B. W. 1999. Apatite chemical composition, determined by electron microprobe and laser-ablation inductively coupled plasma mass spectrometry, as a probe into granite petrogenesis. *Geochimica et Cosmochimica Acta*, *63*(22), 3861-3881.

Shannon, R. D. 1976. Revised effective ionic radii and systematic studies of interatomic distances in halides and chalcogenides. *Acta crystallographica section A: crystal physics, diffraction, theoretical and general crystallography*, 32(5), 751-767.

Shau, Y. H., Torii, M., Horng, C. S., & Peacor, D. R. 2000. Subsolidus evolution and alteration of titanomagnetite in ocean ridge basalts from Deep Sea Drilling Project/Ocean Drilling Program Hole 504B9 Leg 83: Implications for the timing of magnetization. *Journal of Geophysical Research: Solid Earth*, *105*(B10), 23635-23649.

Shishin, D., Jak, E., & Decterov, S. A. 2015. Thermodynamic assessment and database for the Cu–Fe–O–S system. *Calphad*, 50, 144-160.

Sidhu, P. S., Gilkes, R. J., & Posner, A. M. 1978. The synthesis and some properties of Co, Ni, Zn, Cu, Mn and Cd substituted magnetites. *Journal of Inorganic and Nuclear Chemistry*, *40*(3), 429-435.

Sievwright, R. H. 2017. Developing magnetite chemistry as an exploration tool for porphyry copper deposits. PhD thesis. Department of Earth Science and Engineering. Imperial College London. 344 p.

Sievwright, R. H., Wilkinson, J. J., O'Neill, H. S. C., & Berry, A. J. 2017. Thermodynamic controls on element partitioning between titanomagnetite and andesitic–dacitic silicate melts. *Contributions to Mineralogy and Petrology*, *172*(8), 62.

Silva M.G. & Abram M.B. 2008. *Projeto metalogenia da Província Aurífera Juruena-Teles Pires, Mato Grosso*. Goiânia, Serviço Geológico Brasileiro, CPRM, 212p.

Silva, F. R. D., Barros, M. A. S. A., Pierosan, R., Pinho, F. E. C., Rocha, M. L. B. P., Vasconcelos, B. R., & Rocha, J. 2014. Geochemistry and geochronology U-Pb Shrimp of granites from Peixoto de Azevedo: Alta Floresta Gold Province. *Brazilian Journal of Geology*, *44*(3), 433-455.

Sillitoe, R. H. 1989. Gold deposits in western Pacific island arcs: the magmatic connection. *Econ. Geol. Monograph*, *6*, 274-291.

Sillitoe, R. H. 2010. Porphyry copper systems. *Economic geology*, *105*(1), 3-41.

Simon, A. C., Pettke, T., Candela, P. A., Piccoli, P. M., & Heinrich, C. A. 2004. Magnetite solubility and iron transport in magmatic-hydrothermal environments. *Geochimica et Cosmochimica Acta*, 68(23), 4905-4914.

Sossi, P. A., Prytulak, J., & O'Neill, H. S. C. 2018. Experimental calibration of vanadium partitioning and stable isotope fractionation between hydrous granitic melt and magnetite at 800ºC and 0.5 GPa. *Contributions to Mineralogy and Petrology*, 173(4), 27.

Stormer, J. C., Pierson, M. L., & Tacker, R. C. 1993. Variation of F and Cl X-ray intensity due to anisotropic diffusion in apatite during electron microprobe analysis. *American Mineralogist*, *78*(5-6), 641-648.

Sun, W., Arculus, R. J., Kamenetsky, V. S., & Binns, R. A. 2004. Release of gold-bearing fluids in convergent margin magmas prompted by magnetite crystallization. *Nature*, *431*(7011), 975-978.

Tassinari, C. C., & Macambira, M. J. 1999. Geochronological provinces of the Amazonian Craton. *Episodes-Newsmagazine of the International Union of Geological Sciences*, *22*(3), 174-182.

Taylor, B. E. 2007. Epithermal gold deposits. Mineral deposits of Canada: a synthesis of major deposit-types, district metallogeny, the evolution of geological provinces, and exploration methods: Geological Association of Canada, Mineral Deposits Division, Special Publication, 5, 113-139.

Thompson, J. F. H., Sillitoe, R. H., Baker, T., Lang, J. R., & Mortensen, J. K. 1999. Intrusion-related gold deposits associated with tungsten-tin provinces. *Mineralium Deposita*, *34*(4), 323-334.

Thompson, A. J. B., Thompson, J. F. H., & Dunne, K. P. E. 1996. *Atlas of alteration: a field and petrographic guide to hydrothermal alteration minerals.* Geological Association of Canada. Mineral Deposits Division, 119.

Tiepolo, M., Oberti, R., Zanetti, A., Vannucci, R., & Foley, S. F. 2007. Trace-element partitioning between amphibole and silicate melt. *Reviews in mineralogy and geochemistry*, *67*(1), 417-452.

Van Baalen, M. R. 1993. Titanium mobility in metamorphic systems: a review. *Chemical Geology*, *110*(1-3), 233-249.

Van den Boogaart, K. G., & Tolosana-Delgado, R. 2013. *Analyzing compositional data with R*. Heidelberg: Springer.

Watson, E. B. 1980. Apatite and phosphorus in mantle source regions: an experimental study of apatite/melt equilibria at pressures to 25 kbar. *Earth and Planetary Science Letters*, 51(2), 322-335.

Watson, E. B., & Green, T. H. 1981. Apatite/liquid partition coefficients for the rare earth elements and strontium. *Earth and Planetary Science Letters*, *56*, 405-421.

Webster, J. D., & Piccoli, P. M. 2015. Magmatic apatite: A powerful, yet deceptive, mineral. *Elements*, 11(3), 177-182.

Weisse, P. A., Haggerty, S. E., & Brown, L. L. 1985. Paleomagnetism and magnetic mineralogy of the Nahant gabbro and tonalite, eastern Massachusetts. *Canadian Journal of Earth Sciences*, *22*(10), 1425-1435.

Whalen, J. B., & Chappell, B. W. 1988. Opaque mineralogy and mafic mineral chemistry of I-and S-type granites of the Lachlan fold belt, southeast Australia. *American Mineralogist*, *73*(3-4), 281-297.

Wijbrans, C. H., Klemme, S., Berndt, J., & Vollmer, C. 2015. Experimental determination of trace element partition coefficients between spinel and silicate

melt: the influence of chemical composition and oxygen fugacity. *Contributions to Mineralogy and Petrology*, *169*(4), 45.

Wilkinson, J. J. 2013. Triggers for the formation of porphyry ore deposits in magmatic arcs. *Nature Geoscience*, *6*(11), 917-925.

Wilkinson, J. J., Chang, Z., Cooke, D. R., Baker, M. J., Wilkinson, C. C., Inglis, S., & Gemmell, J. B. 2015. The chlorite proximitor: A new tool for detecting porphyry ore deposits. *Journal of Geochemical Exploration*, *152*, 10-27.

Xavier R.P. Assis R.R., Miguel-Jr E., Santos T.J.S., Paes de Barros A.J. 2011. Gold ± copper and gold-base metal deposits associated with granitic systems in the eastern sector of the Alta Floresta Province. In: 12° Simpósio de Geologia da Amazônia, Boa Vista, Roraima. CD-ROM.

Xie, F., Tang, J., Chen, Y., & Lang, X. 2018. Apatite and zircon geochemistry of Jurassic porphyries in the Xiongcun district, southern Gangdese porphyry copper belt: Implications for petrogenesis and mineralization. *Ore Geology Reviews*, *96*, 98-114.

Xing, K., Shu, Q., Lentz, D. R., & Wang, F. 2020. Zircon and apatite geochemical constraints on the formation of the Huojihe porphyry Mo deposit in the Lesser Xing'an Range, NE China. *American Mineralogist: Journal of Earth and Planetary Materials*, *105*(3), 382-397.

Zafar, T., Leng, C. B., Zhang, X. C., & Rehman, H. U. 2019. Geochemical attributes of magmatic apatite in the Kukaazi granite from western Kunlun orogenic belt, NW China: Implications for granite petrogenesis and Pb-Zn (Cu-W) mineralization. *Journal of Geochemical Exploration*, *204*, 256-269.

Zhao, J., Brugger, J., & Pring, A. 2019. Mechanism and kinetics of hydrothermal replacement of magnetite by hematite. *Geoscience Frontiers*, *10*(1), 29-41.

Zhao, G., Sun, M., Wilde, S. A., & Li, S. 2003. Assembly, accretion and breakup of the Paleo-Mesoproterozoic Columbia Supercontinent: records in the North China Craton. *Gondwana Research*, *6*(3), 417-434.

Zhao, J., Brugger, J., & Pring, A. 2019. Mechanism and kinetics of hydrothermal replacement of magnetite by hematite. *Geoscience Frontiers*, *10*(1), 29-41.

Zhao, T. P., Zhou, M. F., Zhai, M., & Xia, B. 2002. Paleoproterozoic rift-related volcanism of the Xiong'er Group, North China craton: implications for the breakup of Columbia. *International Geology Review*, *44*(4), 336-351.

Zirner, A. L., Marks, M. A., Wenzel, T., Jacob, D. E., & Markl, G. 2015. Rare earth elements in apatite as a monitor of magmatic and metasomatic processes: The Ilímaussaq complex, South Greenland. *Lithos*, *228*, 12-22.

Appendix I

Table I.1 – EMPA for apatite (in wt. %).

Sample_ID	F	Si	Mg	Na	Ca	P	Cl	Fe	Mn	Ce	La	Nd
B6_ap_1_1	3.51	0.08	0.02	0.27	37.76	17.56	0.10	0.25	0.84	0.19	0.06	0.08
B6_ap_1_2	4.04	0.11	0.04	0.20	37.68	17.82	0.10	0.19	1.02	0.24	0.06	0.11
B6_ap_2_1	3.64	0.03	0.03	0.25	37.57	17.49	0.15	0.29	1.09	0.16	0.05	0.11
B6_ap_3_1	3.85	0.08	0.04	0.24	37.25	17.88	0.19	0.31	1.17	0.16	0.07	0.11
B6_ap_3_2	3.69	0.13	0.04	0.17	37.53	17.56	0.17	0.26	1.03	0.16	0.04	0.12
B6_ap_4_1	3.91	0.05	0.04	0.16	37.60	17.67	0.20	0.29	1.13	0.14	0.06	0.08
B6_ap_5_1	3.99		0.01	0.10	38.86	18.21	0.06	0.07	0.65	0.08		0.06
B6_ap_6_1	4.04	0.03	0.03	0.11	37.97	17.92	0.16	0.20	1.03	0.14	0.05	0.08
B6_ap_6_2	4.10	0.02	0.03	0.12	38.33	17.77	0.11	0.20	0.84	0.11	0.05	0.07
B6_ap_7_1	3.78	0.02	0.01	0.14	38.48	18.10	0.11	0.07	0.64	0.16	0.05	0.08
PTO19_ap_22	3.27	0.12	0.05	0.15	38.50	17.79	0.18	0.16	0.09	0.40	0.18	0.18
GT-2_ap_1_1	2.57	0.10		0.11	39.40	17.73	0.69	0.04	0.09	0.12		0.04
GT-2_ap_1_2	2.45	0.04	0.01	0.07	39.50	18.03	0.72	0.07	0.07	0.05	0.04	0.03
GT-2_ap_1_3	2.74	0.07		0.07	39.66	18.02	0.52	0.02	0.07	0.09		0.04
GT-2_ap_2_1	2.69	0.09	0.01	0.12	39.76	17.83	0.64	0.04	0.10	0.08	0.05	0.02
GT-2_ap_2_2	2.78	0.05		0.05	39.73	18.02	0.50	0.06	0.09	0.06	0.08	0.07
GT-2_ap_3_1	2.67	0.06	0.01	0.06	39.88	18.04	0.20	0.02	0.08	0.11	0.02	0.04
GT-2_ap_3_2	2.92	0.08		0.05	40.10	18.11	0.26	0.09	0.07	0.06	0.01	0.03
GT-2_ap_4_1	2.81	0.06		0.06	39.87	18.25	0.25	0.04	0.06	0.07	0.05	0.04
GT-2_ap_4_2	2.72	0.08		0.08	39.99	17.80	0.29	0.02	0.06	0.07	0.02	0.08
GT-2_ap_4_4	2.72	0.10		0.06	39.66	18.08	0.24	0.04	0.07	0.12	0.01	0.04
GT-2_ap_5_1	2.72	0.04		0.02	39.87	18.10	0.22	0.01	0.06	0.11		0.02
GT-2_ap_6_1	2.60	0.17	0.10	0.05	39.64	18.07	0.19	0.16	0.07	0.07		0.03
GT-2_ap_6_2	2.90	0.06	0.01	0.07	39.98	18.00	0.18	0.03	0.06	0.08	0.06	0.01
GT-2_ap_6_3	2.68	0.04		0.06	39.85	17.98	0.22	0.04	0.06	0.13	0.09	0.06
GT-2_ap_7_1	2.71	0.08		0.08	39.93	17.82	0.22	0.04	0.06	0.07		
GT-2_ap_7_2	2.67	0.08		0.09	39.47	18.04	0.21	0.12	0.06	0.16	0.06	0.08
GT-2_ap_8_1	2.90	0.02		0.02	40.08	18.31	0.17	0.05	0.08	0.13	0.02	0.05
GT-2_ap_8_2	2.90	0.06	0.01	0.04	39.86	18.00	0.14	0.02	0.08	0.04		0.02
GT-2_ap_9_1	2.75	0.08		0.08	39.79	18.21	0.27	0.03	0.07	0.06	0.04	0.05
GT-2_ap_9_2	2.88	0.06	0.01	0.04	40.04	18.29	0.19	0.07	0.07	0.09	0.04	0.05
PGD-1_ap_1_1	3.67			0.01	40.19	18.27	0.02	0.04	0.06	0.06		
PGD-1_ap_1_2	3.69	0.03		0.01	40.21	18.40	0.02	0.14	0.05	0.04	0.04	
PGD-1_ap_4_1	3.64	0.17	0.01	0.01	39.80	17.98	0.04	0.15	0.10	0.34	0.10	0.04
PGD-1_ap_4_2	3.72	0.10	0.01	0.02	40.03	18.13	0.04	0.21	0.10	0.14	0.03	0.03
PGD-1_ap_4_3	4.16	0.07		0.01	40.10	18.02	0.02	0.19	0.06	0.04	0.01	0.01
PGD-1_ap_4_4	3.74	0.06		0.01	39.91	18.18	0.03	0.15	0.08	0.05	0.06	0.01
PGD-1_ap_5_1	3.60	0.38			38.99	17.42	0.04	0.05	0.07	0.66	0.28	0.12
PGD-1_ap_5_2	3.60	0.06	0.01	0.02	40.06	18.34	0.03	0.13	0.08	0.07		0.02
PGD-1_ap_5_3	3.73	0.30			39.35	17.72	0.04	0.11	0.08	0.46	0.20	0.11
RA69_ap_1_1	3.55		0.03		38.71	17.76	0.24	0.08	0.16	0.45	0.19	0.13

Table I.1 *(Cont.)*

Sample_ID	F	Si	Mg	Na	Ca	P	Cl	Fe	Mn	Ce	La	Nd
RA69_ap_1_2	3.48		0.03		38.39	17.56	0.22	0.11	0.15	0.48	0.19	0.14
RA69_ap_2_1	3.63		0.02		38.28	17.85	0.23	0.08	0.13	0.46	0.17	0.12
RA69_ap_2_2	4.03		0.02		38.17	17.55	0.19	0.10	0.12	0.54	0.16	0.20
RA69_ap_3_1	3.95		0.03		37.50	17.11	0.25	0.46	0.14	0.74	0.30	0.33
RA69_ap_3_2	3.79		0.02		38.47	17.47	0.19	0.25	0.14	0.41	0.21	0.16
RA69_ap_3_3	3.31		0.03		38.04	17.32	0.20	0.91	0.13	0.58	0.25	0.13
RA69_ap_4_1	4.04		0.02		38.36	17.69	0.23	0.09	0.15	0.38	0.18	0.15
RA69_ap_5_1	3.56		0.03		38.63	17.62	0.24	0.28	0.16	0.44	0.17	0.18
RA69_ap_5_2	3.66		0.04		38.33	17.54	0.20	0.37	0.12	0.54	0.23	0.23
RA69_ap_5_3	3.71		0.03		38.65	17.55	0.22	0.12	0.16	0.43	0.19	0.19
RA69_ap_7_1	3.97		0.04		38.09	17.59	0.14	0.12	0.15	0.50	0.21	0.13
RA69_ap_7_2	3.84		0.03		38.67	17.52	0.23	0.09	0.15	0.43	0.20	0.16
RA69_ap_7_3	3.97		0.04		38.60	17.75	0.14	0.11	0.15	0.44	0.19	0.16
RA69_ap_8_1	3.82		0.03		38.54	17.82	0.16	0.09	0.14	0.47	0.14	0.19
RA69_ap_8_2	4.09		0.04		38.60	17.77	0.21	0.16	0.14	0.50	0.15	0.19
RA69_ap_8_3	3.92		0.03		38.51	17.48	0.24	0.27	0.15	0.44	0.17	0.16
RA69_ap_9_1	3.19		0.02		38.12	17.65	0.24	0.13	0.13	0.34	0.17	0.18
RA69_ap_9_2	3.67		0.02		38.59	17.74	0.16	0.15	0.16	0.42	0.14	0.19
RA69_ap_9_3	3.60		0.03		38.68	17.58	0.24	0.11	0.16	0.48	0.25	0.18
RA69_ap_10_1	3.70		0.03		38.50	17.71	0.21	0.13	0.16	0.50	0.20	0.23
RA24_ap_1_1	3.71		0.01		39.44	18.22	0.02	0.17	0.09		0.02	
RA24_ap_3_1	3.78		0.01		39.44	17.93	0.01	0.07	0.06	0.03	0.02	0.06
RA24_ap_4_1	3.90		0.01		39.64	18.29	0.01	0.12	0.07	0.01		0.02
RA24_ap_5_1	4.08		0.01		39.18	17.81	0.01	0.21	0.09	0.06	0.01	0.02
RA24_ap_5_2	3.86		0.04		39.41	18.09	0.01	0.40	0.07	0.04		0.01
SPQ1_ap_10_1	3.55		0.05		38.70	17.78	0.01	0.26	0.05	0.45	0.21	0.05
SPQ1_ap_10_2	3.52		0.33		38.11	17.66	0.01	0.81	0.06	0.22	0.11	0.10
SPQ1_ap_10_3	3.56				39.09	17.95	0.01	0.08	0.04	0.41	0.21	0.05
SPQ1_ap_11_1	3.96				39.76	18.15		0.03	0.04	0.20	0.11	0.06
SPQ1_ap_11_2	3.74				39.74	17.92	0.01	0.05	0.04	0.23	0.11	
SPQ1_ap_11_3	4.05				39.67	17.88		0.13	0.03	0.27	0.18	0.02
SPQ1_ap_11_4	3.58				39.63	18.09		0.06	0.03	0.22	0.12	0.02
SPQ1_ap_12_1	3.56		0.01		39.79	18.18		0.03	0.03	0.23	0.10	
TP01_ap_1_1	3.95				38.87	17.68		0.53	0.12	0.24	0.07	0.12
TP01_ap_2_1	3.71		0.01		39.04	18.01		0.15	0.10	0.48	0.13	0.11
TP01_ap_2_2	3.93		0.01		39.08	17.84	0.01	0.31	0.10	0.43	0.18	0.13
TP01_ap_2_4	4.05				39.32	17.72	0.01	0.09	0.12	0.33	0.15	0.15
TP01_ap_4_1	3.91				39.10	17.84	0.02	0.10	0.09	0.40	0.21	0.09
TP01_ap_4_3	4.05				39.11	17.92		0.09	0.10	0.30	0.12	0.10
TP01_ap_4_4	3.66		0.01		39.21	17.94		0.19	0.08	0.26	0.10	0.10
TP01_ap_4_5	4.42				39.14	17.84		0.39	0.11	0.40	0.16	0.11
TP01_ap_4_6	4.26		0.01		38.77	17.97	0.01	0.44	0.12	0.32	0.15	0.08
BS07_ap_1_1	3.33	0.25			38.63	17.29	0.04	0.04	0.04	0.34	0.22	0.06

Table I.1 *(Cont.)*

Sample_ID	F	Si	Mg	Na	Ca	P	Cl	Fe	Mn	Ce	La	Nd
BS07_ap_2_1	3.87	0.15		0.04	39.33	17.65	0.04	0.14	0.04	0.20	0.08	0.11
BS07_ap_6_1	4.13	0.27		0.01	38.81	17.47	0.02	0.02	0.05	0.38	0.22	0.09
BS07_ap_6_2	4.51	0.05		0.04	39.26	17.75	0.01	0.23	0.02	0.09	0.06	0.08
BS07_ap_7_1	4.00	0.10		0.01	39.11	17.60	0.02	0.06	0.04	0.12	0.08	0.06
BS07_ap_7_2	4.03	0.09		0.01	39.07	17.66	0.04	0.05	0.04	0.13	0.05	0.04
BS07_ap_7_3	3.75	0.06		0.01	39.40	17.59	0.03	0.05	0.05	0.05	0.04	0.04
BS07_ap_7_4	4.08	0.12			39.23	17.59	0.03	0.12	0.02	0.13		0.04
BS07_ap_7_5	4.25	0.10	0.01	0.01	38.99	17.66		0.38	0.04	0.10	0.06	0.06
BS07_ap_7_6	4.06	0.16		0.01	39.16	17.65	0.04	0.08	0.05	0.23	0.08	0.05
BS07_ap_8_1	3.61	0.36	0.02	0.04	39.31	17.06	0.04	0.11	0.03	0.12	0.09	0.07
BS07_ap_10_1	3.63	0.07	0.01	0.04	39.77	17.80	0.05	0.04	0.07	0.14	0.03	
BS07_ap_10_2	3.82	0.08		0.02	39.34	17.81	0.05	0.02	0.07	0.12		0.05
BS07_ap_10_3	3.90	0.04		0.02	39.78	17.95	0.03	0.04	0.06	0.09	0.08	0.04
BS07_ap_10_4	4.12	0.05		0.01	39.53	18.28	0.02	0.06	0.04	0.05	0.04	0.05
BS07_ap_10_5	3.84	0.12		0.02	39.63	17.85	0.03	0.11	0.05	0.11	0.03	0.07
RA73_ap_1_1	3.32	0.08		0.09	39.20	17.96	0.05	0.05	0.03	0.16	0.08	0.07
RA73_ap_1_2	3.51	0.02		0.05	39.37	18.02	0.06	0.18	0.07	0.11	0.04	0.03
RA73_ap_2_1	3.72	0.09		0.12	39.12	17.80	0.05	0.20	0.06	0.09	0.05	0.04
RA73_ap_3_1	3.56	0.06		0.01	39.40	17.91	0.05	0.02	0.05	0.09	0.02	0.07
RA73_ap_3_2	3.54	0.08		0.09	39.44	17.84	0.04	0.26	0.06			0.03
RA73_ap_4_1	3.66	0.08		0.10	39.72	17.50	0.10	0.12	0.05			
RA73_ap_5_1	3.44	0.07	0.01	0.06	39.43	18.03	0.06	0.07	0.06	0.02		0.02
RA73_ap_5_2	3.60	0.01			39.49	18.14	0.03	0.13	0.07	0.05		0.02
RA73_ap_5_3	3.58	0.09		0.09	39.68	17.80	0.05	0.11	0.08	0.02	0.03	0.06
RA73_ap_5_4	3.67	0.04		0.03	39.52	17.89	0.05	0.06	0.06	0.03	0.03	0.03
RA73_ap_7_1	3.40	0.04		0.01	39.75	18.02	0.05	0.07	0.05		0.02	0.05
RA73_ap_7_2	3.52	0.03		0.04	39.76	18.47	0.04	0.17	0.06	0.02		0.01
RA73_ap_7_3	3.30	0.05		0.06	39.68	18.08	0.04	0.03	0.06	0.04		0.04
FD20-7_ap_2_1	3.74	0.03		0.04	39.55	18.15	0.01	0.18	0.08	0.09	0.06	0.05
FD20-7_ap_3_1	3.47	0.05	0.01	0.11	39.54	17.83	0.02	0.08	0.07	0.11	0.03	
FD20-7_ap_3_2	4.06	0.01		0.02	39.51	18.19	0.01	0.02	0.10	0.11	0.02	0.02
FD20-7_ap_3_3	3.72	0.04		0.04	39.27	18.12	0.01	0.06	0.09	0.08	0.01	0.01
FD20-7_ap_4_1	3.91	0.02		0.02	39.89	18.15	0.01	0.03	0.07	0.06	0.03	0.03
FD20-7_ap_5_1	3.76	0.07	0.01	0.08	39.67	17.79	0.01	0.02	0.08	0.06		0.01

Appendix II

Table II.1 – LA-ICP-MS analyses for apatite (ppm). From B to Sr.

Sample_ID	B	Mg	Si	Sc	Ti	V	Mn	Fe	Ga	Ge	As	Rb	Sr
B6_ap_2_1	3	389	2761	4	811	5	11560	2344		84	10		337
B6_ap_3_1	2	668	2536	3	779	4	11781	2997		93	12		342
B6_ap_3_2	5	393	2409	3	785	9	11679	2267		97	9		332
B6_ap_4_1	3	395	2373	2	782	4	10798	1969		71	4		317
B6_ap_5_1	3	129	2744		790	0	6218	1179		39	6		315
B6_ap_6_1	3	380	2845	2	759	3	10220	2565		87	8		338
B6_ap_6_2	3	302	2878	2	751	3	7473	2236		57	6		317
GT-2_ap_3_1	3	331	5176		841	6	729	944		118	20		295
GT-2_ap_3_2	3	290	9249		784	10	653	565		46	20		303
GT-2_ap_4_2	5	2294	11240		937	25	727	3867		56	16		303
GT-2_ap_4_4	4	3249	55776		782	7	704	643	2	72	10	3	314
GT-2_ap_5_1	8	231	5480		789	13	640	675		40	29		308
GT-2_ap_6_1	8	258	1528		789	24	691	823		39	8		464
GT-2_ap_6_2	9	232	2017		846	25	708	801		47	4		482
GT-2_ap_6_3	3	191	5387		805	25	715	499		59	7		413
GT-2_ap_7_1	14	69	16540		780	10	547	648		38	14	4	371
GT-2_ap_7_2	12	687	3197		2211	19	503	765		42	18		350
GT-2_ap_8_1	3	77	2096		826	10	682	496		30	31		326
GT-2_ap_8_2	12	142	2084		788	9	650	411		26	14		283
PGD-1_ap_1_1	3	122	2454		782	3	551	304		10	23		216
PGD-1_ap_1_2	5	200	4892	4	1157	8	732	677		30	23		209
PGD-1_ap_4_1	4	108	4432		801	3	924	538		69	7		229
PGD-1_ap_4_2	5	70	4734		805	14	872	544		64	30		222
PGD-1_ap_4_3	4	96	4575		916	7	837	1927		64	15	5	216
PGD-1_ap_4_4	12	17	5182	4	805	15	638	362		41	29		223
PGD-1_ap_5_1	2	239	9047	6	783	0	1049	601		343	14		194
PGD-1_ap_5_2	3	59	2545	2	814	13	767	1019		83	11		215
PGD-1_ap_5_3	5	1633	4933	6	806	3	930	3787	3	223	14	7	213
RA69_ap_1_2	3	347	3504		799	4	1594	2728		273	18		295
RA69_ap_2_1	2	307	1679		772	4	2242	1359		278	12		299
RA69_ap_2_2	1	603	15078		746	3	1344	1127		230	16		368
RA69_ap_3_1	2	352	5258		913	11	1597	4323		367	20	7	317
RA69_ap_3_2	1	278	8227		794	10	1607	1131		247	12	3	315
RA69_ap_10_1	3	932	28226		796	4	1562	1112		244	12		310
RA24_ap_1_1	2	223	7562	2	809	4	685	1124		24	5		188
RA24_ap_3_1	3	315	10836		779	13	652	456		52	7		171
SPQ1_ap_11_2	8	10	17781		826	40	538	420		167	6	2	271
SPQ1_ap_11_3	11	2933	45141		842	31	526	1435	2	141	4		244
SPQ1_ap_11_4	7	42	32906		789	36	452	425		170	5		276
TP01_ap_2_1	3	134	1891		782	14	1118	1911		268	11		94

Table II.1 *(Cont.)*

Sample_ID	B	Mg	Si	Sc	Ti	V	Mn	Fe	Ga	Ge	As	Rb	Sr
TP01_ap_2_4	3	107	6740		771	5	1011	1077		212	8		116
TP01_ap_4_1	3	249	7589		799		1110	1084		272	13	2	81
TP01_ap_4_3	2	266	5521		1281	2	1015	1290		196	12	2	176
TP01_ap_4_5	6	320	4291		893	2	1283	2391	2	192	5	7	79
TP01_ap_4_6	16	104	16384	2	775	7	1130	1221		201	15	2	71
BS-07_ap_5	3	704	10354		745	12	461	1311		69	21	2	313
BS-07_ap_10	5	309	12818		749	21	434	1262		53	55		320
BS-07_ap_12	6	678	7906		717	14	567	2323		50	46	4	290
BS-07_ap_14	9	38	2913		790	5	526	459		46	20		335
BS-07_ap_15	5	111	3738		840	6	318	550		32	573		357
RA73_ap_1_1	7	7601	92017		880	12	501	578		63	7	3	768
RA73_ap_3_1	5	819	5584		829	6	605	530		39	6		499
RA73_ap_4_1	4	331	9795		794	12	553	457		22	6		501
RA73_ap_5_4	14	3895	66507		766	8	518	422		14	6		464
FD20-7_ap_3_1	2	804	2464		825	6	923	363		53	1		871
FD20-7_ap_3_2	5	158	2434		830	5	867	392		27	10		310
FD20-7_ap_3_3	5	28	2682		849	10	841	260		47	1		752

Table II.2 – LA-ICP-MS analyses for apatite (ppm). From Zr to Ho.

Sample_ID	Zr	Nb	Ba	La	Ce	Pr	Nd	Sm	Eu	Gd	Tb	Dy	Ho
B6_ap_2_1	2		2	585	1765	281	1448	521	31	618	121	823	175
B6_ap_3_1		2	7	630	1738	280	1475	500	25	569	105	688	140
B6_ap_3_2			1	644	1943	307	1554	561	31	595	116	734	149
B6_ap_4_1			3	450	1355	216	1111	357	29	380	70	444	87
B6_ap_5_1			2	192	717	121	637	269	20	333	62	414	75
B6_ap_6_1	2		2	524	1480	231	1088	358	32	354	66	390	75
B6_ap_6_2			1	346	1097	181	943	384	27	414	81	509	103
GT-2_ap_3_1	3		1	727	1775	231	1111	204	29	182	23	121	22
GT-2_ap_3_2	2		6	265	713	108	559	137	18	127	17	94	18
GT-2_ap_4_1	33	1	163	339	874	116	575	116	15	104	12	65	14
GT-2_ap_4_2	2		2	436	1020	137	676	147	15	118	16	70	14
GT-2_ap_4_4	4		68	441	1302	184	893	189	28	158	19	103	20
GT-2_ap_5_1	2		3	190	633	101	541	121	19	128	17	86	20
GT-2_ap_6_1	3		1	289	608	79	350	68	17	56	7	38	7
GT-2_ap_6_2	4		3	336	746	94	409	86	24	77	10	51	9
GT-2_ap_6_3	5		3	425	963	129	571	119	24	102	14	68	13
GT-2_ap_7_1	2		16	196	644	104	532	132	16	109	14	80	18
GT-2_ap_7_2	8	3	15	195	665	119	572	142	19	133	16	88	19
GT-2_ap_8_1			2	196	448	63	318	76	8	82	10	53	10
GT-2_ap_8_2			2	107	429	78	432	125	23	122	19	103	21
PGD-1_ap_1_1			1	100	182	20	86	15	3	18	3	12	2
PGD-1_ap_1_2			3	281	478	47	185	22	7	35	4	26	5
PGD-1_ap_4_1			2	606	1131	117	441	66	14	73	9	42	9
PGD-1_ap_4_2			2	578	1003	99	386	57	15	53	7	45	11
PGD-1_ap_4_3	2		3	641	1162	124	508	94	12	85	10	52	11
PGD-1_ap_4_4			3	479	794	76	327	46	7	62	7	35	9
PGD-1_ap_5_1	7		19	2556	5737	708	2922	510	77	474	68	386	82
PGD-1_ap_5_2			4	810	1450	157	626	102	20	103	13	77	15
PGD-1_ap_5_3	3		3	1966	3725	419	1707	283	50	273	35	198	39
RA69_ap_1_2			13	2025	5322	651	2849	541	35	444	56	325	61
RA69_ap_2_1			6	2144	5506	683	3134	601	42	510	68	369	64
RA69_ap_2_2	4		17	1542	3948	470	2238	410	32	345	46	259	46
RA69_ap_3_1	3		10	2502	6135	794	3759	709	46	563	79	424	77
RA69_ap_3_2	5		27	1799	4401	563	2647	488	36	402	57	303	57
RA69_ap_10_1	6		28	1776	4471	597	2910	535	39	472	61	353	62
RA24_ap_1_1	2		9	172	400	68	498	275	27	462	84	513	106
RA24_ap_3_1	2		1	300	970	182	1241	612	33	820	154	894	179
SPQ1_ap_4_2	38	2	202	835	2099	188	730	100	17	113	9	52	16
SPQ1_ap_11_1	32		101	918	2429	327	1479	235	23	126	19	110	28
SPQ1_ap_11_2			3	1551	3480	304	1140	185	17	131	12	69	17
SPQ1_ap_11_3			59	900	1719	169	674	81	12	80	11	39	8
SPQ1_ap_11_4			6	1466	3384	381	1593	199	32	157	25	122	31

Table II.2 *(Cont.)*

Sample_ID	Zr	Nb	Ba	La	Ce	Pr	Nd	Sm	Eu	Gd	Tb	Dy	Ho
TP01_ap_1_1	4		332	1155	3419	530	2659	635	21	612	102	571	128
TP01_ap_2_1			3	1876	4263	511	2333	430	7	378	57	292	61
TP01_ap_2_2			1	1819	4013	508	2262	432	7	376	58	313	65
TP01_ap_2_4			5	1451	3481	445	1983	404	6	376	56	310	64
TP01_ap_4_1	3		3	2028	4525	568	2497	487	8	415	63	363	71
TP01_ap_4_3		6	10	1442	3430	483	2239	489	9	445	69	385	81
TP01_ap_4_5		3	19	1355	3301	415	2062	430	6	409	62	356	74
TP01_ap_4_6			5	1529	3463	460	2027	424	7	373	59	346	67
BS-07_ap_5	2		11	551	1235	154	679	133	17	111	13	67	16
BS-07_ap_7			14	40	82	9	31	21	6	15	3	21	3
BS-07_ap_10			3	375	982	137	609	116	12	101	12	65	14
BS-07_ap_12			11	313	946	131	703	110	9	92	12	64	12
BS-07_ap_13	73	3	867	10	36	3	35	46	6	39	4	16	4
BS-07_ap_14			6	405	873	110	492	73	11	73	9	50	11
BS-07_ap_15			2	208	560	79	408	76	12	62	8	40	9
RA73_ap_1_1	4		33	437	1105	160	799	137	22	95	11	51	9
RA73_ap_1_2		3	419	276	610	75	337	98	10	31	8	19	6
RA73_ap_3_1	2		4	231	646	95	485	102	19	83	11	55	10
RA73_ap_3_2	96	4	382	84	165	29	134	28	7	12	5	25	5
RA73_ap_4_1	3		7	150	409	58	290	60	14	51	7	35	7
RA73_ap_5_2	7		25	138	338	43	251	49	11	43	5	33	6
RA73_ap_5_4			15	180	485	66	325	79	14	47	6	32	7
RA73_ap_7_1	2		796	12	25	4	32	23	8	15	2	6	2
FD20-7_ap_3_1	2		16	296	869	133	747	147	23	89	11	47	10
FD20-7_ap_3_2			1	244	544	66	293	37	8	26	3	18	3
FD20-7_ap_3_3			2	348	867	120	646	126	19	79	9	45	7
FD20-7_ap_4_1	345	635	45	457	860	93	401	51	65	41	5	20	4

Table II.3 LA-ICP-MS analyses for apatite (ppm). From Er to U.

Sample_ID	Er	Tm	Yb	Lu	Hf	Ta	Pb	Th	U
B6_ap_2_1	497	74	565	72	4		10	28	34
B6_ap_3_1	370	55	414	55	2		6	15	45
B6_ap_3_2	404	59	433	57	2		6	16	18
B6_ap_4_1	249	40	306	41	3		7	12	6
B6_ap_5_1	182	27	160	21	2		4	2	9
B6_ap_6_1	200	30	236	33			7	11	12
B6_ap_6_2	291	41	291	40	3		7	16	31
GT-2_ap_3_1	55	7	42	6			5	15	3
GT-2_ap_3_2	42	5	28	4			4	6	4
GT-2_ap_4_1	33	5	21	4	6		6	15	
GT-2_ap_4_2	37	4	21	4			4	10	
GT-2_ap_4_4	46	5	32	3			4	11	
GT-2_ap_5_1	46	6	38	5			5	12	10
GT-2_ap_6_1	18	2	13	2			4	2	3
GT-2_ap_6_2	26	3	19	2			4	3	
GT-2_ap_6_3	35	4	23	3			3	4	
GT-2_ap_7_1	41	5	27	4	2		4	6	6
GT-2_ap_7_2	46	5	31	4			4	9	
GT-2_ap_8_1	27	3	19	3			5	13	4
GT-2_ap_8_2	51	6	41	6			2	3	
PGD-1_ap_1_1	8	1	5	1			3	2	8
PGD-1_ap_1_2	13	2	16	2			5	13	21
PGD-1_ap_4_1	24	4	26	4			9	36	25
PGD-1_ap_4_2	26	3	22	5			9	36	25
PGD-1_ap_4_3	29	3	31	4			11	40	14
PGD-1_ap_4_4	22	2	24	5			8	32	21
PGD-1_ap_5_1	220	32	212	34	2		34	193	71
PGD-1_ap_5_2	48	6	44	9			15	46	42
PGD-1_ap_5_3	123	16	111	20			75	394	135
RA69_ap_1_2	137	16	81	12	0		9	9	5
RA69_ap_2_1	148	18	106	11			6	7	
RA69_ap_2_2	111	12	70	9	0		5	8	4
RA69_ap_3_1	197	22	135	14	2		14	29	
RA69_ap_3_2	140	16	88	11			7	15	4
RA69_ap_10_1	136	15	91	11			7	10	6
RA24_ap_1_1	282	39	258	36	4		20	44	10
RA24_ap_3_1	472	59	399	54	3		80	96	34
SPQ1_ap_4_2	50	4	40	3	43	3	8	9	
SPQ1_ap_11_1	96	17	85	13	3		18	49	14
SPQ1_ap_11_2	40	5	75	8			5	17	

Table II.3 *(Cont.)*

Sample_ID	Er	Tm	Yb	Lu	Hf	Ta	Pb	Th	U
SPQ1_ap_11_3	22	3	23	5			27	10	
SPQ1_ap_11_4	73	11	64	16			8	42	59
TP01_ap_1_1	364	51	363	55	4		48	63	
TP01_ap_2_1	145	18	94	12			5	6	
TP01_ap_2_2	163	18	109	14	2		6	6	
TP01_ap_2_4	160	21	118	15	3		8	13	
TP01_ap_4_1	172	20	124	14			8	11	
TP01_ap_4_3	210	27	167	23			8	18	
TP01_ap_4_5	182	22	133	17			8	6	
TP01_ap_4_6	175	21	127	14	3		6	6	
BS-07_ap_5	37	5	37	5			18	30	75
BS-07_ap_7	5		3		2		39		28
BS-07_ap_10	36	4	22	3			10	27	103
BS-07_ap_12	27	4	29	3	2		6	21	
BS-07_ap_13	12	3	24	5	22	4	31	1	
BS-07_ap_14	27	5	15	3			8	5	
BS-07_ap_15	26	3	16	3			13	24	
RA73_ap_1_1	22	2	16	2	2		4	5	6
RA73_ap_1_2	12	1	10	4	9		7	4	37
RA73_ap_3_1	28	3	24	4			3	7	
RA73_ap_3_2	9	2	14	2	6	2	21	3	
RA73_ap_4_1	20	3	18	4			6	5	17
RA73_ap_5_2	19	2	25	2	2		3	9	68
RA73_ap_5_4	14	3	13	1	3		5	3	
RA73_ap_7_1	6	3	14	3	4	3	4	1	
FD20-7_ap_3_1	21	2	12	1	2		3	2	
FD20-7_ap_3_2	9	1	15	3			5	10	
FD20-7_ap_3_3	20	2	12	2			4	3	
FD20-7_ap_4_1	12	2	21	5	59	4	67	287	

Appendix III

Table III.1 – EMPA for magnetite (in wt. %).

Sample_ID	Na	Al	Si	Mg	Ca	K	Ti	Fe	Mn
B6_mag_2_1	0.01	0.01			0.01	0.01	0.20	71.12	0.06
PTO19_mag_4_1	0.07	0.05	0.01	0.02	0.01	0.02	0.96	67.05	0.05
PTO19_mag_5_1	0.02	0.02	0.03		0.02		0.65	67.73	0.07
PTO19_mag_7_1	0.06	0.27	0.33	0.03	0.05	0.02	0.03	64.94	0.27
PTO19_mag_9_1	0.02	0.01	0.16		0.03	0.02		70.85	0.03
PTO19_mag_10_1	0.01	0.01	0.02				0.24	67.71	0.13
PTO19_mag_13_1	0.03	0.03	0.04	0.01	0.01	0.08	0.57	67.05	0.32
PTO19_mag_15_1	0.03	0.08	0.34			0.10	0.05	70.07	0.06
PTO19_mag_17_1	0.04		0.17			0.07	0.03	70.04	0.03
PTO19_mag_19_1	0.03	0.02	0.19		0.03	0.02	0.01	70.13	0.04
GT-2_mag_1_1	0.02	0.05	0.02	0.02	0.04		0.37	71.24	0.02
GT-2_mag_1_2	0.01	0.22	0.01				0.04	71.69	0.01
GT-2_mag_2_1		0.58	0.01	0.01	0.01		2.02	67.60	0.02
GT-2_mag_3_1		0.08	0.01		0.02		0.05	71.80	0.03
GT-2_mag_4_1	0.02	0.05	0.01		0.01		0.02	71.70	0.03
GT-2_mag_5_1		0.17	0.01				1.19	70.19	0.05
PGD-01_mag_1_1		0.01	0.01	0.01			0.01	71.70	0.03
PGD-01_mag_2_1		0.05		0.01	0.01		0.30	70.52	0.28
PGD-01_mag_2_2			0.02		0.02		0.01	71.73	0.04
PGD-01_mag_3_1	0.02	0.06	0.02	0.02	0.01		0.01	71.67	0.05
PGD-01_mag_4_1	0.03	0.03	0.01		0.04			71.72	0.04
PGD-01_mag_5_1		0.02	0.02					71.62	0.04
PGD-01_mag_6_1	0.02	0.02		0.01				72.08	0.03
PGD-01_mag_7_1	0.01	0.56	0.02	0.01		0.01	0.09	70.15	0.12
PGD-01_mag_7_2	0.02	0.01			0.01		0.01	71.14	0.05
PGD-01_mag_9_1	0.01	0.01	0.01	0.01	0.02			71.66	0.04
PGD-01_mag_10_1		0.08	0.01	0.01	0.04			72.01	0.03
PGD-01_mag_11_1		0.02	0.01		0.01			71.71	0.03
PGD-01_mag_13_1	0.01	0.01	0.01		0.01			71.55	0.02
PGD-01_mag_12_1	0.01	0.02	0.01				0.01	71.35	0.04
RA69_mag_2_1	0.06	0.44	0.04	0.01	0.07		3.91	61.93	0.06
RA69_mag_3_1	0.14	0.50	0.08		0.06	0.02	4.56	61.14	0.11
RA69_mag_3_2	0.14	0.33	0.05		0.04	0.01	4.30	61.25	0.09
RA69_mag_4_1	0.07	0.33	0.05		0.03	0.01	4.64	61.82	0.08
RA69_mag_4_2	0.27	0.67	0.90	0.44	0.06	0.02	0.77	62.76	0.24
RA69_mag_5_1	0.09	0.36	0.05		0.04		4.43	62.07	0.10
RA69_mag_5_2	0.10	0.34	0.05	0.01	0.07	0.01	4.43	61.31	0.11
RA69_mag_6_1	0.09	0.49	0.12	0.01	0.05		4.42	61.31	0.14
RA69_mag_6_2	0.07	0.50	0.06	0.01	0.05	0.01	4.47	61.97	0.09
RA69_mag_7_1	0.08	0.49	0.03		0.01		4.49	62.30	0.06
RA69_mag_8_1	0.11	0.42	0.03		0.03	0.01	4.50	61.67	0.08

Table III.1 *(Cont.)*

Sample_ID	Na	Al	Si	Mg	Ca	K	Ti	Fe	Mn
RA69_mag_9_1	0.05	0.51	0.02		0.04		4.54	61.74	0.08
RA69_mag_10_1	0.06	0.48	0.05	0.01	0.04	0.01	3.88	62.89	0.08
RA69_mag_12_1	0.05	0.53	0.03	0.01	0.02		4.47	62.18	0.08
RA69_mag_14_1	0.07	0.46	0.05		0.04		4.50	61.27	0.08
RA69_mag_15_1	0.15	0.38	0.07		0.09		4.25	60.73	0.11
RA24_mag_2_1	0.03	0.08	0.01	0.01	0.07	0.03	0.18	70.18	0.02
RA24_mag_2_2	0.02	0.08	0.02			0.04	0.13	70.40	0.01
RA24_mag_4_1	0.01	0.12	0.01		0.02		0.08	70.62	0.02
RA24_mag_4_2		0.12	0.01			0.01	0.07	71.12	0.03
RA24_mag_10_1		0.13	0.01		0.01	0.01	0.10	71.12	0.07
RA24_mag_11_1	0.03	0.10		0.01	0.02		0.09	70.94	0.02
RA24_mag_12_1	0.03	0.04	0.01		0.02		0.02	71.00	0.01
RA24_mag_13_1	0.05	0.11	0.02	0.01	0.01		0.13	71.01	0.02
TP01_mag_1_1			0.05		0.02		0.31	70.14	0.11
TP01_mag_2_1	0.01	0.04	0.04		0.01		0.55	70.55	0.17
TP01_mag_3_1	0.01	0.04	0.03		0.05		0.12	69.19	0.02
TP01_mag_4_1		0.01	0.02		0.06		0.24	71.54	0.05
TP01_mag_5_1	0.01	0.02	0.08	0.01	0.05		2.66	64.40	0.19
TP01_mag_7_1	0.03	0.10	0.03	0.01	0.01		0.67	70.44	0.30
TP01_mag_8_1	0.01	0.02	0.07		0.04		0.57	68.76	0.16
TP01_mag_10_1	0.01	0.03	0.03				1.18	69.26	0.43
TP01_mag_11_1	0.03	0.04	0.08		0.08		0.18	68.98	0.03
TP01_mag_12_1	0.02	0.04	0.08	0.01	0.01		0.15	67.80	0.04
TP01_mag_13_1	0.01	0.01	0.03		0.04		0.13	70.68	0.03
RA73_mag_1_1								71.07	
RA73_mag_2_1		0.16	0.01		0.02		0.11	70.81	0.12
RA73_mag_3_1	0.01	0.08	0.01				0.09	71.07	0.08
RA73_mag_4_1	0.02	0.17	0.01		0.01		0.15	70.85	0.15
RA73_mag_5_1		0.17	0.01	0.01	0.01		0.18	70.90	0.16
RA73_mag_6_1		0.19	0.02				0.26	70.69	0.20
RA73_mag_6_2	0.01	0.12	0.01		0.01		0.18	71.21	0.18
RA73_mag_6_3		0.13	0.01		0.01		0.12	71.04	0.13
RA73_mag_6_4	0.01	0.08	0.01		0.02		0.15	71.10	0.18
RA73_mag_8_1	0.02	0.11	0.02		0.01		0.09	71.49	0.10
RA73_mag_9_1	0.01	0.14	0.01			0.01	0.09	70.92	0.11
RA73_mag_10_1	0.01	0.07	0.01		0.01		0.15	71.21	0.12
RA73_mag_11		0.12			0.08		0.11	71.13	0.11
RA73_mag_13_1		0.25	0.01	0.01	0.01		0.20	70.95	0.23
RA73_mag_13_2		0.08					0.10	71.48	0.12
RA73_mag_13_3	0.01	0.12	0.02		0.02		0.05	71.89	0.07
RA73_mag_13_4	0.01	0.12	0.01	0.01	0.04		0.32	70.52	0.23
RA73_mag_14_1		0.21			0.02		0.13	71.05	0.15
RA73_mag_14_2	0.02	0.06	0.01		0.06		0.10	70.88	0.08

Table III.1 *(Cont.)*

Sample_ID	Na	Al	Si	Mg	Ca	K	Ti	Fe	Mn
VU20-4_mag_1_1	0.01	0.08	0.15	0.03	0.02	0.02	4.70	62.77	0.04
VU20-4_mag_2_1		0.16	0.06	0.01	0.03		2.49	65.43	0.03
VU20-4_mag_3_1		0.32	0.04	0.02	0.02		2.57	64.98	0.07
VU20-4_mag_4_1	0.03	0.38	0.25	0.01	0.03	0.04	2.87	64.66	0.06
VU20-4_mag_4_2		0.12	0.05	0.01	0.04		3.10	64.70	0.04
VU20-4_mag_5_1		0.12	0.14		0.03	0.02	2.49	66.12	0.04
VU20-4_mag_11_1	0.02	0.34	0.08	0.02	0.03		3.21	64.08	0.07
VU20-4_mag_11_2		0.07	0.30	0.01	0.04	0.02	2.48	65.71	0.06
VU20-4_mag_11_3	0.01	0.08	0.11	0.02	0.03		2.19	65.81	0.07
VU20-4_mag_13_1		0.11	0.06		0.03		2.47	65.33	0.05
VU20-4_mag_13_2	0.02	0.27	0.05	0.02	0.03		2.64	64.26	0.04
VU20-4_mag_15_1		0.29	0.06	0.02	0.02	0.01	2.74	64.79	0.06
VU20-4_mag_15_2		0.08	0.11	0.02	0.05		4.26	63.01	0.07
VU20-4_mag_15_3		0.39	0.05	0.01	0.03		3.44	63.97	0.05
FD20-7_mag_1_1	0.01		0.01		0.01			71.65	0.04
FD20-7_mag_2_1	0.02	0.02			0.01			71.29	0.06
FD20-7_mag_2_2		0.01					0.02	71.53	0.07
FD20-7_mag_3_1			0.01		0.02	0.01		71.75	0.07
FD20-7_mag_3_2				0.01	0.01			71.31	0.06
FD20-7_mag_3_3	0.01	0.03	0.01			0.01	0.02	71.34	0.06
FD20-7_mag_5_1	0.02	0.02			0.01		0.10	71.15	0.09
FD20-7_mag_5_2			0.01		0.02			71.46	0.07
FD20-7_mag_6_1	0.01							71.20	0.09
FD20-7_mag_7_1		0.02	0.01		0.01			71.46	0.13
FD20-7_mag_7_2		0.01	0.01	0.01	0.01		0.03	71.30	0.20
FD20-7_mag_7_3	0.01	0.01		0.01				71.21	0.13
FD20-7_mag_9_1	0.01	0.03					0.03	71.16	0.10
FD20-7_mag_9_2		0.01	0.01					71.64	0.06
FD20-7_mag_8_1	0.01	0.01			0.01		0.01	71.27	0.22
FD20-7_mag_15_1		0.01	0.01		0.01			71.10	0.13
FD20-7_mag_16_1		0.01			0.03			71.70	0.09
FD20-7_mag_16_2	0.01	0.01	0.01		0.02	0.01	0.01	71.46	0.06

Appendix IV

Table IV.1 – LA-ICP-MS analyses for magnetite (ppm). From Li to Ca.

Sample_ID	Li	Na	Mg	Al	Si	P	K	Ca^{42}	Ca^{44}
GT-2_mag_1_1	12	1231	3840	5937	11300	563	244	7580	6609
GT-2_mag_2_1	4	913	957	3739	4268	66	108	1465	1102
GT-2_mag_4_1	10	250	2083	3103	8903	107	62	584	453
GT-2_mag_5_1		376	296	1642	8188	48	53	3913	2900
PGD-01_mag_2_1		196	86	2277	4196	41	55	584	150
PGD-01_mag_2_2		1846	449	592	4642	43	469	660	1364
PGD-01_mag_3_1		554	346	957	3734	40	318	1179	395
PGD-01_mag_4_1		197	73	479	4941	1088	110	3450	3532
PGD-01_mag_5_1		270	63	475	3178	35	58	971	336
PGD-01_mag_6_1		1663	433	832	4239	42	107	608	1116
PGD-01_mag_7_1		185	114	960	3272	33	12	458	119
PGD-01_mag_9_1		108	15	259	2844	28	11	409	103
PGD-01_mag_10_1	2	5430	1974	2501	30388	47	867	3792	4191
PGD-01_mag_11_1		221	118	584	4053	42	125	568	313
PGD-01_mag_13_1	2	925	945	1420	4527	100	128	646	891
PGD-01_mag_12_1	1	303	82	276	3384	38	87	477	125
RA69_mag_2_1	6	65664	4475	5978	163569	100	1144	37608	42810
RA69_mag_3_1	2	22455	1665	5027	79849	268	625	19471	20630
RA69_mag_3_2	3	19110	2288	1944	77896	88	476	16672	17057
RA69_mag_4_1	2	2111	169	5419	4724	84	132	2409	1729
RA69_mag_4_2	16	3466	2892	6375	13659	66	193	3364	2587
RA69_mag_6_1		3297	395	5841	18185	63	249	3877	3678
RA69_mag_6_2	2	13800	732	5609	26504	615	196	6334	6637
RA69_mag_7_1		6951	660	4663	4310	76	425	5304	4641
RA69_mag_9_1	3	13237	1217	5158	51072	1129	310	11412	12116
RA69_mag_12_1	2	19566	2059	6478	87139	129	524	15763	17331
RA24_mag_4_1	2	531	134	1034	2700	156	55	2399	531
RA24_mag_4_2	2	560	149	1339	9761	274	88	2557	1049
RA24_mag_10_1	3	549	131	1445	3814	935	18	713	1876
RA24_mag_11_1	2	896	312	1369	4171	78	54	771	625
RA24_mag_13_1		1439	414	1521	2672	135	14	610	205
TP01_mag_2_1	3	49	78	822	3392	48	57	649	399
TP01_mag_3_1	2	75	152	1330	3624	50	90	6183	5428
TP01_mag_4_1	8	139	26	209	4088	59	40	785	773
TP01_mag_5_1		137	65	401	5971	539	77	2571	1564
TP01_mag_7_1	2	81	66	1956	3035	139	140	1187	379
TP01_mag_8_1	2	148	90	397	3747	55	48	715	1829
TP01_mag_10_1		275	143	824	7972	44	110	587	495
TP01_mag_11_1	5	490	836	2690	22372	49	293	15632	16506
TP01_mag_12_1	2	253	96	1316	2989	43	101	570	439
TP01_mag_13_1	4	1150	511	531	11252	1998	195	6435	6594

Table IV.1 *(Cont.)*

Sample_ID	Li	Na	Mg	Al	Si	P	K	^{42}Ca	^{44}Ca
RA73_mag_1_1	2	22084	4292	2252	87315	109	913	22676	15454
RA73_mag_3_1		2564	475	1219	12657	61	173	1595	2051
RA73_mag_4_1		1872	441	1833	6595	58	136	1831	1536
RA73_mag_6_1		2679	610	2053	9926	87	200	3651	2595
RA73_mag_6_2	2	17695	4469	2551	70202	107	837	13501	13346
RA73_mag_6_3		2011	399	1409	7834	62	107	2313	1438
RA73_mag_8_1	2	3015	566	1682	13147	741	140	3896	3735
RA73_mag_10_1		3108	694	1362	4604	4667	142	10326	10498
RA73_mag_11		1121	305	2170	12958	385	95	3165	2664
RA73_mag_13_1	2	9495	1831	2542	34068	140	879	8552	7774
RA73_mag_13_3		2326	458	1526	10550	14998	99	41191	39078
RA73_mag_14_1	2	17384	3852	2734	77422	78	806	13991	13919
FD20-7_mag_6_1		899	247	275	4052	53	130	540	753
FD20-7_mag_7_1		673	258	348	3031	46	95	988	578
FD20-7_mag_7_2		242	96	213	3534	48	36	493	135
FD20-7_mag_7_3		447	238	385	3351	44	75	1199	389
FD20-7_mag_9_1	3	2703	1044	1059	15302	46	276	2464	1907
FD20-7_mag_9_2		2524	786	744	11282	265	223	3320	2495
FD20-7_mag_8_1		378	107	387	2613	33	88	374	311
FD20-7_mag_15_1		1162	281	13	2067	23	132	1316	906
FD20-7_mag_16_1	2	1555	339	456	7161	88	197	1107	1040
FD20-7_mag_16_2		4365	1120	872	15899	175	355	3585	3940

Table IV.2 – LA-ICP-MS analyses for magnetite (ppm). From Sc to Se.

Sample_ID	Sc	Ti	V	Cr	Mn	Co	Ni	Cu	Zn	Ga	As	Se
GT-2_mag_1_1	3	5231	1399	735	703	36	41	241	586	7	2	13
GT-2_mag_2_1	4	3081	2374	1763	279	34	148	8	3232	5	2	10
GT-2_mag_4_1		276	1339	115	295	36	24	6	353	3	2	11
GT-2_mag_5_1		5687	1260	19	260	31	28	3	727	3		10
PGD-01_mag_2_1	2	1193	1683	287	1263	20	21		974	9	2	8
PGD-01_mag_2_2		229	1393	236	428	18	14	3	96	7	2	9
PGD-01_mag_3_1		239	1242	126	661	18	17	6	602	7		7
PGD-01_mag_4_1		299	1245	81	404	21	16	7	239	5		13
PGD-01_mag_5_1		169	1039	143	431	21	17		449	5		15
PGD-01_mag_6_1	2	300	1120	167	641	19	17		533	7		12
PGD-01_mag_7_1	5	439	1328	294	599	18	17		1444	7	2	10
PGD-01_mag_9_1		107	887	182	319	15	13		175	4		9
PGD-01_mag_10_1		183	1199	157	327	18	18	8	586	7		10
PGD-01_mag_11_1		247	1016	144	453	16	20		442	5		15
PGD-01_mag_13_1		424	1024	217	464	11	17	4	410	6	2	17
PGD-01_mag_12_1		185	879	127	381	14	22	2	70	9		10
RA69_mag_2_1	11	44316	382	17	632	7	11	7	4496	22	2	12
RA69_mag_3_1	13	48305	852	99	1106	8	28	7	5943	21	2	15
RA69_mag_3_2	5	13211	197	80	792	8	13		1121	10	2	15
RA69_mag_4_1	11	50503	961	62	918	9	33	4	6665	23	2	13
RA69_mag_4_2	7	33103	447	49	1424	9	15	5	4100	20		15
RA69_mag_6_1	12	46593	888	56	797	8	32	4	4439	18	2	15
RA69_mag_6_2	13	47249	848	57	787	9	24	4	4974	18		10
RA69_mag_7_1	14	52875	904	44	908	8	32	9	4408	18	2	16
RA69_mag_9_1	11	45082	758	61	924	10	32	2	5320	21	2	19
RA69_mag_12_1	12	45888	903	74	788	10	25	3	4555	24	2	28
RA24_mag_4_1	2	859	649	83	153	12	15		481	18		9
RA24_mag_4_2	3	949	885	118	277	16	21		524	37	2	13
RA24_mag_10_1	3	940	879	111	500	22	25		538	56	2	15
RA24_mag_11_1	5	1076	947	138	239	15	21		712	29	2	18
RA24_mag_13_1		1338	884	158	232	17	17	4	536	45	2	16
TP01_mag_2_1		16790	403	14	4799	12	7	2	1006	61	2	10
TP01_mag_3_1	3	7773	361	7	499	16	5	3	630	61	2	12
TP01_mag_4_1	2	71843	468	18	18427	16	1	5	844	46	2	12
TP01_mag_5_1	2	23380	501	21	1840	9	4		145	21		8
TP01_mag_7_1		58602	452	12	6777	16	7	6	2211	44	2	8
TP01_mag_8_1		5632	587	27	1064	9	3		131	16	2	11
TP01_mag_10_1	7	18062	489	16	4795	10	3	2	1249	37	2	8
TP01_mag_11_1	11	17493	618	41	703	11	8	2	572	20	2	9
TP01_mag_12_1	3	17840	498	21	3019	7	3	2	2044	23	2	8
TP01_mag_13_1		20354	451	37	4996	9	4		1173	15		9
RA73_mag_1_1		1085	1180	97	1111	39	15	2	1192	56	2	13

Table IV.2 *(Cont.)*

Sample_ID	Sc	Ti	V	Cr	Mn	Co	Ni	Cu	Zn	Ga	As	Se
RA73_mag_3_1		1418	1002	46	948	23	16		724	18		7
RA73_mag_4_1		1104	1529	110	889	21	13		905	14		6
RA73_mag_6_1	2	3520	1076	209	1880	36	18	2	1610	46	2	12
RA73_mag_6_2	2	1037	1157	294	697	31	20	3	1115	32	2	12
RA73_mag_6_3		1021	1091	136	988	30	17		1307	40	2	7
RA73_mag_8_1		931	1194	131	718	36	18		1522	40		7
RA73_mag_10_1		800	1328	117	813	37	15	2	454	45	2	8
RA73_mag_11	4	3382	1080	166	2271	41	19	2	1724	61	2	6
RA73_mag_13_1		1362	1377	993	1608	53	54	8	960	73		6
RA73_mag_13_3		1609	1262	370	1273	41	27	2	1113	56		7
RA73_mag_14_1	2	1394	1554	215	1463	38	20		1368	44	2	7
FD20-7_mag_6_1		26	678	59	686	27	12		82	12	2	11
FD20-7_mag_7_1		434	694	57	1970	30	11		439	31		13
FD20-7_mag_7_2		106	696	61	1658	34	12		248	26		6
FD20-7_mag_7_3		64	636	52	1314	33	13		381	31		9
FD20-7_mag_9_1		127	680	72	828	26	12		106	15	2	9
FD20-7_mag_9_2		167	658	47	657	24	11		95	12		9
FD20-7_mag_8_1		127	709	41	2048	37	11		402	30		5
FD20-7_mag_15_1		105	715	59	1254	26	11	13	314	29		5
FD20-7_mag_16_1		107	837	53	1033	35	15	2	208	36	3	12
FD20-7_mag_16_2		129	786	48	787	31	11	1	104	28	2	11

Table IV.3 – LA-ICP-MS analyses for magnetite (ppm). From Rb to Sm.

Sample_ID	Rb	Sr	Y	Zr	Nb	Mo	Cd	Sn	Cs	Ba	La	Ce	Pr	Nd	Sm
GT-2_mag_1_1		8		3		36	7	19		8	7	9	1	6	2
GT-2_mag_2_1		4		2			3	9		14					
GT-2_mag_4_1		2					4	7		5					
GT-2_mag_5_1		3					4	9		5		2			
PGD-01_mag_2_1							6	2		3				2	
PGD-01_mag_2_2		6		2			4	50		17				2	2
PGD-01_mag_3_1	6	2					4	12		11				2	
PGD-01_mag_4_1	2	3	8	5	2		5	6		2	14	37	4	15	
PGD-01_mag_5_1							2	7		1				3	2
PGD-01_mag_6_1		4		2			3	46		11					
PGD-01_mag_7_1							3	11							
PGD-01_mag_9_1							2	6							
PGD-01_mag_10_1	22	13	4	11			5	24		39	3	3		2	
PGD-01_mag_11_1							2	1		2	2	2			
PGD-01_mag_13_1		4					3	29		10		1			
PGD-01_mag_12_1							3	2		1					
RA69_mag_2_1	5	45	3	49	10	7	3	34		55	8	10	1	2	
RA69_mag_3_1	2	30	9	35	24	6	5	31		47	65	91	11	30	5
RA69_mag_3_2	2	50	7	41	9	3	4	17		64	11	15	2	7	
RA69_mag_4_1		8	2	15	24	9	3	31		16	18	29	3	12	
RA69_mag_4_2		22	3	12	21	6	3	21		24	14	15	2	8	
RA69_mag_6_1		20	1	14	20	6	4	27		22	1	4	2	5	2
RA69_mag_6_2		17	2	18	20	6	3	29		18	9	10	2	4	
RA69_mag_7_1		12	4	44	25	6	4	27		46	34	53	6	21	4
RA69_mag_9_1		33	11	34	24	5	5	28		25	15	34	5	21	
RA69_mag_12_1		25	3	26	21	2	7	32		24	3	6		6	3
RA24_mag_4_1			3				3	2		2				2	
RA24_mag_4_2			2				3	2		2					
RA24_mag_10_1			6				4	4		5		2		3	
RA24_mag_11_1				2			5	3		2				2	
RA24_mag_13_1		2	3				3	7		4					
TP01_mag_2_1	3	2		5	2	34	3	259		8	5	5		4	
TP01_mag_3_1	3	6	94	21	18	25	3	121	2	19	46	80	9	37	8
TP01_mag_4_1			18	4	53	21	3	96		1	7	17	3	11	2
TP01_mag_5_1		4	28	23	6	14	2	110		12	45	62	9	37	9
TP01_mag_7_1		2	21	8	70	27	3	244		5	22	22	4	15	3
TP01_mag_8_1	2	5	6	5	4	44	3	72		8	16	27	4	13	
TP01_mag_10_1	2	7	47	17	2	8	3	93		18	42	64	8	26	6
TP01_mag_11_1	7	11	275	31	156	28	4	109	3	23	57	159	29	138	37
TP01_mag_12_1		5	10			15	3	120		9	11	27	3	14	3
TP01_mag_13_1	2	10	97		1	5	3	75		12	84	158	21	93	22
RA73_mag_1_1	2	11		12			5	7		26	2	1			2

Table IV.3 *(Cont.)*

Sample_ID	Rb	Sr	Y	Zr	Nb	Mo	Cd	Sn	Cs	Ba	La	Ce	Pr	Nd	Sm
RA73_mag_3_1		1					3	6		4					
RA73_mag_4_1		2					2	5		5					
RA73_mag_6_1		2		2			7	4		4			z		
RA73_mag_6_2	2	10		15			4	16		33	7	3		3	2
RA73_mag_6_3		2					3	3		4					2
RA73_mag_8_1		9					2	3		9	2	1			
RA73_mag_10_1		33		2		0	4	2		7	23	23	5	17	
RA73_mag_11		4				2	2	5		1	2	2		1	2
RA73_mag_13_1		9		5		2	2	1		20				2	
RA73_mag_13_3		46	8				4	3		6	6	16	2	15	3
RA73_mag_14_1	2	8	1	3	1		3	6		27	3	3		2	
FD20-7_mag_6_1		3		2			4	13		10					
FD20-7_mag_7_1		2					2	13		9					
FD20-7_mag_7_2		1					4	8		1					
FD20-7_mag_7_3		2					4	9		8					
FD20-7_mag_9_1		10		4			4	28		20					
FD20-7_mag_9_2		10		4			5	22		20				3	
FD20-7_mag_8_1		1					3	9		5					
FD20-7_mag_15_1		5		2			2	24		9					
FD20-7_mag_16_1		5		2		2	6	39		9				2	2
FD20-7_mag_16_2		14		6			5	81		30				2	

Table IV.4 – LA-ICP-MS analyses for magnetite (ppm). From Eu for U.

Sample_ID	Eu	Gd	Tb	Dy	Ho	Er	Tm	Yb	Lu	Hf	Ta	W	Pb	Th	U
GT-2_mag_1_1												2			
GT-2_mag_2_1															
GT-2_mag_4_1															
GT-2_mag_5_1													2		
PGD-01_mag_2_1													3		
PGD-01_mag_2_2															
PGD-01_mag_3_1													5		
PGD-01_mag_4_1		2											5	5	4
PGD-01_mag_5_1										2					
PGD-01_mag_6_1															
PGD-01_mag_7_1															
PGD-01_mag_9_1															
PGD-01_mag_10_1													16	1	3
PGD-01_mag_11_1														5	
PGD-01_mag_13_1															
PGD-01_mag_12_1															
RA69_mag_2_1				3						2		3	62		
RA69_mag_3_1		2		3		2		2					757	1	8
RA69_mag_3_2												2	139	2	1
RA69_mag_4_1				2									265		4
RA69_mag_4_2		2											193		2
RA69_mag_6_1													468		
RA69_mag_6_2				2									116		1
RA69_mag_7_1		2										3	418		17
RA69_mag_9_1		4		2						3			120		3
RA69_mag_12_1												2	55		
RA24_mag_4_1															
RA24_mag_4_2															
RA24_mag_10_1				2											
RA24_mag_11_1															
RA24_mag_13_1													4		
TP01_mag_2_1		2		2									127		4
TP01_mag_3_1		5	2	10	3	8	7	8	2	1		2	224	13	20
TP01_mag_4_1		3		2							2				
TP01_mag_5_1		8		4		3		4					279	11	9
TP01_mag_7_1		4		5		4					2		169	4	5
TP01_mag_8_1		2						2					146		7
TP01_mag_10_1		5		8		6		4					743	4	17
TP01_mag_11_1	2	40	7	47	8	23	3	27	4	3	5	3	247	7	19
TP01_mag_12_1				4				2					395		13

Table IV.4 *(Cont.)*

Sample_ID	Eu	Gd	Tb	Dy	Ho	Er	Tm	Yb	Lu	Hf	Ta	W	Pb	Th	U
TP01_mag_13_1		19	2	17	3	9	1	10	2	1		1	189	4	5
RA73_mag_1_1		2								2					
RA73_mag_3_1												2			
RA73_mag_4_1												2			
RA73_mag_6_1												7			
RA73_mag_6_2												12	10		
RA73_mag_6_3												12			
RA73_mag_8_1												5			
RA73_mag_10_1		2										1	8		
RA73_mag_11												11	2		
RA73_mag_13_1												105			
RA73_mag_13_3		4				2		2				27	3	1	2
RA73_mag_14_1												19	56	7	2
FD20-7_mag_6_1															
FD20-7_mag_7_1															
FD20-7_mag_7_2															
FD20-7_mag_7_3															
FD20-7_mag_9_1															
FD20-7_mag_9_2															
FD20-7_mag_8_1															
FD20-7_mag_15_1															
FD20-7_mag_16_1		2											3		
FD20-7_mag_16_2													2		

Appendix V

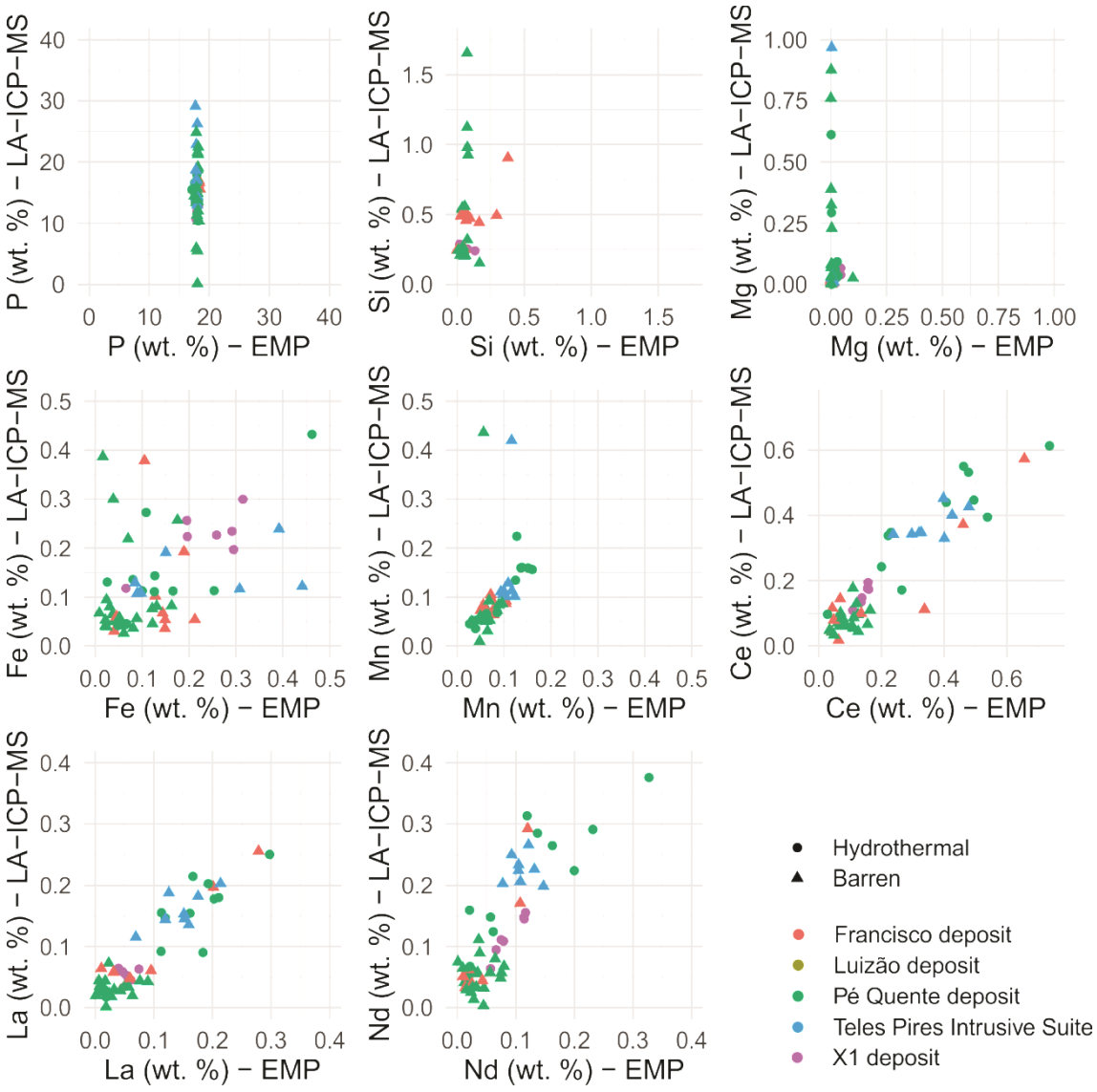

Figure V.1 – Comparison between EMP and LA-ICP-MS data for apatite analyses.

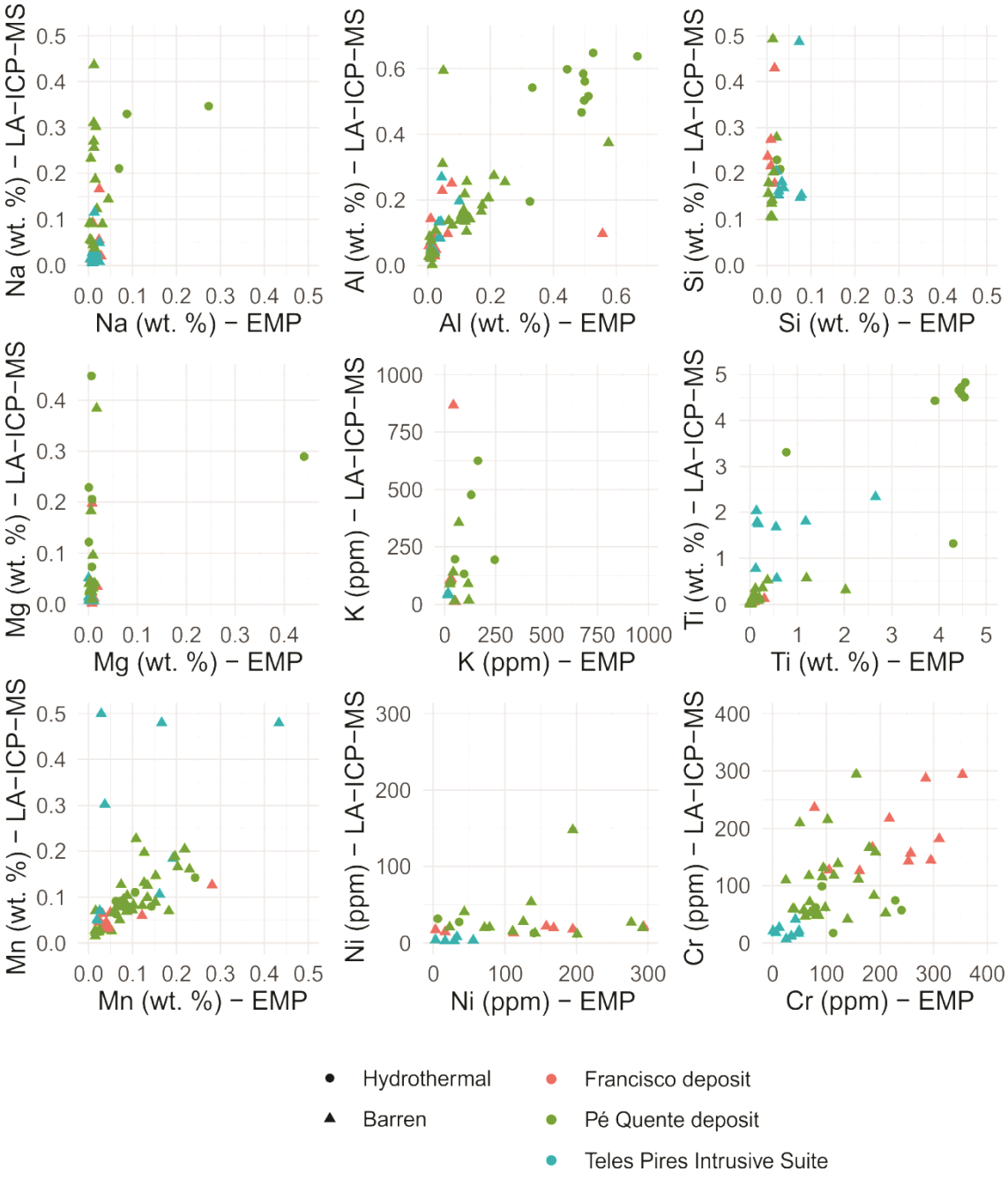

Figure V.2 – Comparison between EMP and LA-ICP-MS data for magnetite analyses.